

Probing Soft Interactions in Collider Experiments: From the Standard Model to Beyond

Dissertation

zur

Erlangung der naturwissenschaftlichen Doktorwürde
(Dr. sc. nat.)

vorgelegt der

Mathematisch-naturwissenschaftlichen Fakultät

der

Universität Zürich

von

Weijie Jin

aus

der V.R. China

Promotionskommission

Prof. Dr. Florencia Canelli (Vorsitz)

Prof. Dr. Thomas Gehrmann

Prof. Dr. Lea Caminada

Prof. Dr. Laura Baudis

Zürich, 2025



Abstract

In modern experimental particle physics with colliders, the most common particle collisions of interest are those containing hard interactions to probe physics at high energy scales, while the soft interactions are considered backgrounds. However, the soft interactions are related to many fundamental aspects of quantum field theory, which lead to rich experimental phenomena. Due to the non-perturbative nature of these interactions and difficulties in first-principle predictions, the theoretical description relies heavily on experimental inputs, which motivated the three analyses of experimental data in this thesis.

Inelastic proton-proton (pp) collisions are predominantly governed by quantum chromodynamics (QCD) interactions with low energy transfer, referred to as soft QCD interactions. The event shapes of these collisions encode key interaction properties through the kinematics of outgoing particles. The first analysis in this dissertation measures event shapes at a center-of-mass energy of 13 TeV using the pp collision data taken by the CMS detector in 2018, demonstrating the need for further theoretical developments to improve event shape predictions.

The second analysis examines the intrinsic k_T models in event generators, alongside the initial-state radiation in parton showers, to describe transverse recoils in the hard scattering process. The tuning of intrinsic k_T parameters to experimental data at center-of-mass energies from 38.8 GeV to 13 TeV taken by either fixed-target or collider experiments, along with their scaling behavior with regard to colliding energy and hard-scattering scales, provides insights into soft emissions not accounted for in parton showers.

The third analysis searches for new physics within hidden valley models, which predict exotic soft particle emissions through QCD-like extensions of the Standard Model. Sphericity, an event shape observable, along with multiplicity, is used to distinguish these soft unclustered energy patterns from the QCD multijet background. By leveraging the scouting stream of CMS Run 2 data (2016-2018) at 13 TeV, this search achieves high sensitivity across a broad range of signal hypotheses, placing constraints on signal parameters and excluding the models that are incompatible with the data.

Acknowledgments

I would like to express my deepest gratitude to my colleagues, friends, and family for their guidance, support, and love during my journey to the unknown. The work presented in this thesis would not have been accomplished without them.

I am grateful to my supervisors, colleagues and collaborators in University of Zürich and the CMS collaboration – to Prof. Florencia Canelli for giving me the opportunity to work in a group with a supportive environment and freely explore the topics I am interested in, and for guiding and encouraging me to pursue my ideas; to Dr. Kyle Cormier for the inspiring ideas and discussions during my projects, and for the help to solve many big and small problems and encouragements to overcome the difficulties; to Dr. Armando Martinez, Prof. Saptaparna Bhattacharya, Prof. Vitaliano Ciulli, Dr. Mikel Morentin, Dr. Chad Freer, Dr. Carlos Erice, Luca Lavezzo, Dr. Stefanos Leontsinis, Dr. Patrick Connor, Prof. Andrew Gilbert, Dr. Arne Reimers, Dr. Raffaella Tramontano and Dr. Louise Skinnari for the guidance and valuable suggestions to improve the data analyses and polish the papers; to Dr. Anna Macchiolo and Dr. Arash Jofrehei for the supervision and explanations in my work of module and disk testing in the phase-2 upgrade of CMS Tracker Endcap Pixel detector; to Fabian Stäger for the companionship, support and mental encouragement, which enabled me to pass over the difficult situations, personal or work-related; to Filip Bilandžija for his tasty coffee and apple pies to power me up in the work; to Dr. Pascal Bärtschi for the good or bad jokes and tips in the analyses; to Dr. Armin Ilg, Theresa Goldschmidt and Alessandra Lorenzetti for the chats and cakes – cakes are good for both stomach and soul; to Dr. Vinicius Mikuni, Dr. Sascha Liechti, Marc Huwiler, Fanqiang Meng, Anson Kwok, Eslam Shokr, Dr. Vagelis Gkougkousis, Dr. Valeriia Lukashenko and Dr. Izaak Neutelings for the information about the study in the university and workflow in the CMS collaboration, as well as tips to improve my presentation skills and to plan my career from various angles.

I am grateful to my friends during my study in Zürich and in the past – to Huan Liu and Shengyu Shan, who live together with me during my study, for sharing their experience and feelings in research and life, and for the nice and creative food and entertainments after work; to Xinlei Xi, Jing Wu, Jiawen Tian, Xinmei Huang, Ningzhou Gu, Zhongyu Zhang, Yu Yang, Botao Li and Jiapeng Wei for the survival guides in study and great holiday plans; to Dr. Fanyi Zhao, Dr. Zixuan Rao, Dr. Jiaxuan Wang, Yaixin Chang and Dr. Xin Huang for the friendship, mutual support and discussions about science when I was an undergraduate student, which affected my career decision to a large extent and also made me a well-rounded individual.

I am grateful to my family members – to my parents, Yongde Jin and Aimin Gu, and my grandparents, Yueping Chen and Ruikun Gu, for their unconditional love from my birth to the present and support behind me, like a steadfast harbor for a ship.

Special thanks to my cats, Orange and Flake, for a shoulder to cry on.

Contents

| | | |
|----------|--|-----------|
| 1 | Introduction | 1 |
| 2 | Theoretical background | 3 |
| 2.1 | The Standard Model of particle physics | 3 |
| 2.2 | Particle scattering | 9 |
| 2.3 | Non-perturbative particle interactions | 10 |
| 2.3.1 | Non-perturbative QCD from large coupling | 10 |
| 2.3.2 | Non-perturbative phenomena from topological structures of gauge fields | 11 |
| 2.4 | The physics of pp collisions | 13 |
| 2.5 | Beyond the Standard Model | 15 |
| 2.5.1 | Soft unclustered energy patterns from hidden valley models | 17 |
| 3 | The Compact Muon Solenoid Experiment at the Large Hadron Collider | 21 |
| 3.1 | The Large Hadron Collider | 21 |
| 3.2 | The CMS detector | 24 |
| 3.2.1 | Coordinate system | 24 |
| 3.2.2 | Tracking detectors | 27 |
| 3.2.3 | The preshower detectors and electromagnetic calorimeter | 28 |
| 3.2.4 | The hadronic calorimeter | 29 |
| 3.2.5 | The solenoid magnet & flux-return yoke | 30 |
| 3.2.6 | The muon system | 30 |
| 3.2.7 | The trigger system | 30 |
| 3.2.8 | The scouting stream | 31 |
| 3.3 | Object Definitions | 32 |
| 3.3.1 | Vertices | 32 |
| 3.3.2 | Tracks | 32 |
| 3.3.3 | Particle-flow candidates | 32 |
| 3.3.4 | Jets | 33 |
| 4 | Measurement of event shapes in minimum bias events | 35 |
| 4.1 | Motivation | 35 |
| 4.2 | Event shapes | 35 |
| 4.3 | Data and simulations | 37 |
| 4.4 | Event selections | 38 |
| 4.4.1 | Selections on detector-level objects | 38 |
| 4.4.2 | Selections on particle-level objects | 39 |
| 4.5 | Machine-learning based unbinned unfolding algorithm | 39 |
| 4.5.1 | Event-wise weighting with a binary classifier | 39 |
| 4.5.2 | Unfolding with iterative weighting | 40 |
| 4.5.3 | Additional steps for detector inefficiency and artifacts | 42 |

| | | |
|----------|--|-----------|
| 4.6 | Uncertainty estimation | 44 |
| 4.6.1 | Sources of uncertainty | 44 |
| 4.6.2 | Construction of uncertainty templates | 46 |
| 4.6.3 | Uncertainty estimation with toy experiments | 49 |
| 4.6.4 | Tests and validations | 50 |
| 4.7 | Results and interpretation | 57 |
| 4.7.1 | Unfolding results as one-dimensional histograms | 58 |
| 4.7.2 | Unfolding results as two-dimensional histograms | 58 |
| 4.7.3 | Interpretation | 59 |
| 5 | Investigation of intrinsic k_T in Drell–Yan events | 65 |
| 5.1 | Motivation | 65 |
| 5.2 | Data and simulations | 66 |
| 5.3 | Generator tuning strategy | 68 |
| 5.4 | Uncertainty estimation | 69 |
| 5.4.1 | Uncertainty from the choices of tune range | 69 |
| 5.4.2 | Uncertainty from the interpolation | 70 |
| 5.4.3 | Uncertainty from MC statistics | 70 |
| 5.4.4 | Uncertainty from the measured data | 71 |
| 5.5 | Results and discussion | 71 |
| 5.5.1 | Validations of the tunes | 71 |
| 5.5.2 | Energy scaling behaviors | 73 |
| 5.5.3 | Impacts of the hard-scattering scale | 76 |
| 5.5.4 | Interpretation | 78 |
| 6 | Search for soft unclustered energy patterns | 80 |
| 6.1 | Motivation | 80 |
| 6.2 | Data and simulations | 81 |
| 6.2.1 | Scouting data | 81 |
| 6.2.2 | Simulations of background and signals | 81 |
| 6.3 | Event selection | 84 |
| 6.3.1 | Scouting strategy and pre-selections | 84 |
| 6.3.2 | Selection on charged particle-flow candidates | 86 |
| 6.3.3 | SUEP candidates as large radius jets | 87 |
| 6.3.4 | Analysis selection | 91 |
| 6.4 | Data-driven background estimation | 95 |
| 6.4.1 | Modified ABCD method | 95 |
| 6.4.2 | Signal injection test | 98 |
| 6.4.3 | Validation of the background estimation in data | 100 |
| 6.5 | Uncertainty estimation | 103 |
| 6.5.1 | Integrated luminosity | 103 |
| 6.5.2 | Trigger efficiency | 103 |
| 6.5.3 | Clustering of AK4 jets | 103 |
| 6.5.4 | Pileup effect | 104 |
| 6.5.5 | Track reconstruction | 104 |
| 6.5.6 | Pre-firing | 105 |

| | | |
|----------|---|------------|
| 6.5.7 | Higgs reweighting | 105 |
| 6.5.8 | Non-closure of the ABCD method | 105 |
| 6.5.9 | Impacts of the uncertainties | 107 |
| 6.6 | Results | 108 |
| 6.6.1 | Maximum likelihood estimation | 108 |
| 6.6.2 | Derivation of upper limits | 109 |
| 6.6.3 | Upper limits of the SUEP signals | 110 |
| 7 | Conclusion | 112 |
| | References | 113 |
| A | Additional material for the measurement of event shapes in minimum bias events | 128 |
| A.1 | Generator settings | 128 |
| A.1.1 | PYTHIA A3 tune | 128 |
| A.1.2 | PYTHIA CP1 | 129 |
| A.1.3 | EPOS-LHC | 129 |
| A.1.4 | PYTHIA CP5 | 129 |
| A.1.5 | PYTHIA CUEPT8M1 | 130 |
| A.1.6 | PYTHIA A14 Tunes | 130 |
| A.2 | Systematic weighting plots | 132 |
| A.2.1 | Truth-level weighting to estimate the bias | 132 |
| A.2.2 | Two-step weighting to estimate the uncertainty of migration between dif- ferent MC models | 138 |
| A.2.3 | Truth and detector level weighting to estimate the track reconstruction efficiency uncertainty | 148 |
| A.3 | More Validation Tests of Unfolding Pseudo-data | 152 |
| A.4 | More plots of bias and coverage test | 177 |
| A.5 | Correlation matrices | 179 |
| A.6 | Uncertainty breakdown | 183 |
| B | Additional material for the energy scaling Behaviour of intrinsic k_T in Drell–Yan events | 185 |
| B.1 | Decoupling the underlying-event and Drell–Yan dilepton transverse momentum descriptions | 185 |
| B.2 | Validation of the tunes | 187 |
| B.3 | Tuning results | 187 |
| C | Additional material for the SUEP search | 213 |
| C.0.1 | Bias test of the signal extraction | 213 |

In memory of Dr. Fanyi Zhao.

1 Introduction

Understanding the fundamental structure of matter and modeling its origins and interactions mathematically is a central goal in physics. In high-energy physics experiments, probing smaller structures is achieved by colliding particles at increasingly higher energies and analyzing the resulting collision products. The Standard Model (SM) of particle physics emerged from a synthesis of theoretical modeling and experimental discovery. In SM, fundamental particles are modeled as eigenstates of wave functions that exhibit symmetry under spacetime transformations as well as specific phase (gauge) transformations described by the $SU(3) \times SU(2) \times U(1)$ group. The interactions and transformations of these particles arise naturally from these underlying symmetries.

At the Large Hadron Collider (LHC), protons or heavier ions are accelerated to the highest achievable energies on Earth and collided head-on within sophisticated particle detectors. These detectors are meticulously designed to identify and precisely measure the properties of the resulting particles. Because protons are composite particles with complex internal structures, their collisions exhibit a rich array of phenomena arising from multiple interactions across a broad energy spectrum. This complexity poses challenges for experimentalists in disentangling the various components of the collisions and the theorists in modeling these interactions and their mutual influences across different energy scales, particularly in the regime of soft interactions, which are particle interactions with low energy transfer.

In this thesis, the properties of soft interactions are examined from multiple perspectives.

- The event shapes of inelastic proton-proton (pp) collisions capture the momentum distribution of outgoing particles, which predominantly result from soft interactions. By comparing these experimental event shapes with theoretical predictions, we gain a powerful tool to probe and refine models of soft interactions and proton structure. In this work, I present precise, simultaneous measurements of multiple event shape observables using a machine-learning-based event-wise unfolding algorithm, followed by detailed interpretations derived from data-model comparisons.
- Recoils from hard interactions, characterized by clear signatures, serve as standard candles for probing the soft interactions present in pp collisions. In this work, I leverage the Drell-Yan (DY) process to reconstruct the transverse particles recoiling as protons approach one another and examine the scaling behavior of these transverse recoils with respect to collision energy and the dynamics of the hard interactions, providing valuable insights into soft parton motions, emissions, and their interplay with the hard process.
- A deep understanding of soft pp interactions is essential for accurately analyzing hard processes. Soft underlying events (UE) not only serve as backgrounds to hard interactions but also generate cascades of soft particles that reflect the characteristics of these interactions. In this work, I present a study aimed at enhancing our understanding of such events, which is critical for developing searches for new physics models that predict soft unclustered energy patterns (SUEPs) emerging from QCD-like extensions of the SM. This

work employs event-shape techniques to model soft emissions and effectively distinguish them from the SM background.

This dissertation has the following structure: Section 2.1 discusses the theoretical models involved in this thesis, including the SM, the modeling of pp collisions, and the new physics model for SUEPs. Section 3 describes the LHC, the Compact Muon Solenoid (CMS) detector, and the reconstruction of detector-level objects. Section 4 describes the measurement of event shapes of inelastic pp collisions. After that, Section 5 discusses the energy scaling behavior of intrinsic k_T in DY processes. Section 6 presents the search for SUEPs using event shapes and particle multiplicities. The summary is given in Section 7.

2 Theoretical background

This chapter introduces theoretical models that describe elementary particles – the smallest building blocks of the universe – and their interactions. These models form the foundation of hadron collision experiments at the LHC, as the experiments bring us closer to understanding the fundamental nature of the universe and predicting its fate.

The SM of particle physics provides a precise and consistent framework for describing elementary particles and their electromagnetic, weak and strong interactions. It has been rigorously tested across numerous aspects by high-energy particle collision experiments. Section 2.1 briefly introduces the SM, while Section 2.2 outlines the corresponding particle scattering model. Although perturbative quantum field theory is widely applicable to particle scatterings, there remain interactions where this approach is ineffective due to large coupling constants or discontinuous gauge transformations. Such non-perturbative interactions occur both within the SM – most notably in the quantum chromodynamics (QCD) sector – and in several SM extensions, such as QCD-like dark matter models that predict SUEPs, which are investigated in this thesis. Section 2.3 discusses these non-perturbative interactions. Section 2.4 describes the physics of pp collisions, which involves both perturbative and non-perturbative processes. Finally, Section 2.5 examines the limitations of the SM and explores beyond the Standard Model (BSM) theories, with a particular focus on the hidden valley models that may lead to SUEP production in pp collisions.

2.1 The Standard Model of particle physics

In the SM, the matter and its interactions are described by fields with respect to spacetime, and the elementary particles are excitations of the fields. The Lagrangian density \mathcal{L} as a function of the fields is required to satisfy the Poincaré spacetime symmetry, and the fields after quantization into operators are required to satisfy the commutation rules and spin properties of the corresponding particles. As a result, the spin 1/2 fermions are represented as spinor fields, the spin 0 bosons are represented as scalar fields, and the spin 1 bosons are represented as vector fields in spacetime. In addition, inspired by the fact that the absolute phase of a wave function in quantum mechanics is not a physical observable, the gauge field theory requires the \mathcal{L} to be invariant under some specific unitary transformations of the fields as functions of the spacetime, organized by gauge groups. In the SM, the fields of elementary fermions and Higgs boson transform as representations of the $SU(3)_C \times SU(2)_L \times U(1)_Y$ gauge group, leading to the modification of the spacetime derivative to gauge covariant derivative on the fields in \mathcal{L} .

The SM Lagrangian density is given by

$$\mathcal{L} = \underbrace{\sum_{\psi_f} i\bar{\psi}_f \gamma^\mu D_\mu \psi_f - \frac{1}{4} G_{\mu\nu}^a G_a^{\mu\nu} - \frac{1}{4} W_{\mu\nu}^i W_i^{\mu\nu} - \frac{1}{4} B_{\mu\nu} B^{\mu\nu}}_{\text{gauge}} + \underbrace{|D_\mu \phi|^2 - \mu^2 \phi^\dagger \phi - \lambda(\phi^\dagger \phi)^2}_{\text{Higgs}} - \underbrace{\bar{\psi}_i y_{ij} \psi_j \Phi}_{\text{Yukawa}} + h.c.. \quad (2.1)$$

The variables and terms in Eq. 2.1 are listed as follows.

- γ^μ : The generators of Clifford algebra, which satisfy $\{\gamma^\mu, \gamma^\nu\} = 2\eta^{\mu\nu}I$ for unit matrix I . $\mu = 0, 1, 2, 3$ is the spacetime index, and we choose the metric $\eta_{\mu\nu} = \text{diag}(+1, -1, -1, -1)$
- ψ_f : The spinors in gauge field representations describing quark or lepton fields. $\bar{\psi}_f := \psi_f^\dagger \gamma^0$.
- D_μ : Gauge covariant derivative. In the SM $SU(3)_C \times SU(2)_L \times U(1)_Y$ gauge group, it is explicitly written as

$$D_\mu = \partial_\mu + ig_s \frac{\lambda^a}{2} G_\mu^a + ig \frac{\tau^i}{2} W_\mu^i + ig' \frac{Y}{2} B_\mu. \quad (2.2)$$

In eq. 2.2, λ^a are the eight Gell-Mann matrices, τ^i are the three Pauli matrices, corresponding to $\frac{\lambda^a}{2}$ and $\frac{\tau^i}{2}$ as the generators of the $SU(3)_C$ and $SU(2)_L$ groups, respectively. Y are constants depending on the fermion or Higgs boson fields. Accordingly, the gauge fields G_μ^a , W_μ^i and B_μ as the connection components of gauge transformations are in adjoint representations of the $SU(3)_C$, $SU(2)_L$ and $U(1)_Y$ groups, respectively. The gauge fields correspond to vector bosons (gluons, Z , W^\pm and photons) that are exchanged in strong and electroweak interactions.

- $G_{\mu\nu}^a$, $W_{\mu\nu}^i$, $B_{\mu\nu}$: the field strength tensors for G_μ^a , W_μ^i and B_μ , respectively. The explicit expressions are

$$G_{\mu\nu}^a = \partial_\mu G_\nu^a - \partial_\nu G_\mu^a - g_s f_{abc} G_\mu^b G_\nu^c, \quad (2.3)$$

$$W_{\mu\nu}^i = \partial_\mu W_\nu^i - \partial_\nu W_\mu^i - g \epsilon_{ijk} W_\mu^j W_\nu^k, \quad (2.4)$$

$$B_{\mu\nu} = \partial_\mu B_\nu - \partial_\nu B_\mu, \quad (2.5)$$

where f_{abc} and ϵ^{ijk} are the structure constants of the $SU(3)_C$ and $SU(2)_L$ groups, respectively.

- ϕ : Scalar fields describing the Higgs boson.
- y_{ij} : Complex matrix with values depending on the indices of fermion fields i and j .
- Φ : Higgs (ϕ) or conjugate Higgs field (ϕ^c) depending on the fermion fields in the term, such that the term $\bar{\psi}_i y_{ij} \psi_j \Phi$ is gauge invariant.

The fields of fermions, gauge vector bosons and scalar bosons and their representations are given in Table 2.1. The interpretations of the gauge, Higgs and Yukawa sectors are given as follows.

Gauge sector

The gauge sector describes the kinetics of the fermions and gauge bosons, as well as their interactions. The fermion and gauge boson propagation is encoded in the spacetime derivatives. The interactions between the fermions and gauge bosons arise from the covariant derivative D_μ . The self-interaction of non-Abelian gauge bosons comes from the third terms of eq. 2.3 and 2.4.

The $SU(3)_C$ gauge symmetry and the strong interaction arising from this symmetry is described by QCD. Each quark field $\psi \in u_L, d_L, u_R, d_R$ is a spinor triplet of the $SU(3)_C$, denoted

Table 2.1: SM fields and their representations in the gauge group $SU(3)_C$ and $SU(2)_L$, as well as the hypercharges Y quantifying the effects of the $U(1)_Y$ transformation on the corresponding fields. The bold numbers denote the dimensions of the representations. **2** of $SU(2)_L$ and **3** of $SU(3)_C$ are the fundamental representations, **3** of $SU(2)_L$ and **8** of $SU(3)_C$ are the adjoint representations, while **1** singlet is the trivial representation, which is invariant under the transformation. For each quark or lepton in the table, there are three generations of fields.

| Spin | Field name | Label | $SU(3)_C$ repre. | $SU(2)_L$ repre. | Y |
|---------------|-------------------------|---|------------------|------------------|----------------|
| $\frac{1}{2}$ | Quark doublet | $Q_L = \begin{pmatrix} u_L \\ d_L \end{pmatrix}$ | 3 | 2 | $\frac{1}{3}$ |
| | Up-quark singlet | u_R | 3 | 1 | $\frac{4}{3}$ |
| | Down-quark singlet | d_R | 3 | 1 | $-\frac{2}{3}$ |
| | Lepton doublet | $L_L = \begin{pmatrix} \nu_L \\ e_L \end{pmatrix}$ | 1 | 2 | -1 |
| | Lepton singlet | e_R | 1 | 1 | -2 |
| 1 | Gluon field | G_μ^a | 8 | 1 | 0 |
| | Weak gauge field | W_μ^i | 1 | 3 | 0 |
| | Hypercharge gauge field | B_μ | 1 | 1 | 0 |
| 0 | Higgs doublet | $\phi = \begin{pmatrix} \phi^+ \\ \phi^0 \end{pmatrix}$ | 1 | 2 | 1 |
| | Conjugate Higgs doublet | $\phi^c = -i\tau^2\phi^* = \begin{pmatrix} -\phi^{0*} \\ \phi^{+*} \end{pmatrix}$ | 1 | 2 | -1 |

as

$$\psi = \begin{pmatrix} \psi_R \\ \psi_G \\ \psi_B \end{pmatrix}. \quad (2.6)$$

The corresponding quantum numbers are named as "colors", varying from red (R), green (G) and blue (B). The local gauge transformation can be written as an $SU(3)$ matrix

$$U(x) = e^{ig_s \frac{\lambda_a}{2} \alpha_a(x)}, \quad (2.7)$$

where $\alpha_a(x), a \in \{1...8\}$ are spacetime-dependent phase factors. The quark fields transform under the $SU(3)_C$ as

$$\psi(x) \rightarrow U(x)\psi(x). \quad (2.8)$$

The 8 gluon fields G_μ^a transform as

$$\lambda_a G_\mu^a \rightarrow U(x)(\lambda_a G_\mu^a)U^{-1}(x) + \frac{2i}{g_s}(\partial_\mu U(x))U^{-1}(x), \quad (2.9)$$

such that the Lagrangian density is invariant under the $SU(3)_C$ transformation. The terms $-\frac{g_s}{2}\bar{\psi}\gamma^\mu\lambda^a G_\mu^a\psi$, $\frac{1}{2}(\partial_\mu G_\nu^a - \partial_\nu G_\mu^a)g_c f_{abc}G_b^\mu G_c^\nu$ and $-\frac{1}{4}g_c^2 f_{abc}f_{ab'c'}G_\mu^b G_\nu^c G_{b'}^\mu G_{c'}^\nu$ indicate the quark-quark-gluon, three-gluon and four-gluon interactions.

The $SU(2)_L \times U(1)_Y$ gauge symmetry is used to describe the electroweak interactions. To describe the charged weak force that only couples to the left-handed chiral states, the left-handed and right-handed chiral projections of the quark and lepton fields are put in different representations, so that their behaviors under the gauge transformation can lead to different interactions. The chiral components of the fermion fields are projected out as $\psi_{L,R} = \frac{1}{2}(1 \mp \gamma^5)\psi$ for $\psi \in u, d, e, \nu$. e refers to electron, muon and tau fields, ν refers to electron, muon and tau

neutrino fields; u represents up, charm and top quark fields; and d represents down, strange and bottom quark fields. The left-handed quark and lepton fields are spinor doublets of the $SU(2)_L$ group, and their gauge covariant derivative term in the Lagrangian density gives the coupling to the weak gauge bosons

$$-\frac{g}{2}\bar{L}\gamma^\mu\tau^iW_\mu^iL, L \in \{Q_L, L_L\}. \quad (2.10)$$

Changing the basis of Pauli matrices τ^1, τ^2 into

$$\tau^\pm := \frac{1}{2}(\tau^1 \pm \tau^2), \quad (2.11)$$

and defining

$$W_\mu^\pm := \frac{W_\mu^1 \mp iW_\mu^2}{\sqrt{2}}, \quad (2.12)$$

the coupling term 2.10 becomes

$$-\frac{g}{\sqrt{2}}\bar{\nu}_L\gamma^\mu W_\mu^+e_L - \frac{g}{\sqrt{2}}\bar{e}_L\gamma^\mu W_\mu^-\nu_L - \frac{g}{2}\bar{\nu}_L\gamma^\mu W_\mu^3\nu_L + \frac{g}{2}\bar{e}_L\gamma^\mu W_\mu^3e_L \quad (2.13)$$

and

$$-\frac{g}{\sqrt{2}}\bar{u}_L\gamma^\mu W_\mu^+d_L - \frac{g}{\sqrt{2}}\bar{d}_L\gamma^\mu W_\mu^-u_L - \frac{g}{2}\bar{u}_L\gamma^\mu W_\mu^3u_L + \frac{g}{2}\bar{d}_L\gamma^\mu W_\mu^3d_L \quad (2.14)$$

for the leptons and quarks, respectively. The first two terms in the expressions 2.13 and 2.14 represent the charged weak interaction between electrons (muons, taus) and electron (muon, tau)-neutrinos, or up-type and down-type quarks by exchanging charged W^\pm bosons. The last two terms represent the neutral current interaction, and should be considered together with the coupling to the hypercharge gauge field B_μ . The right-handed quarks and leptons do not have charge weak interaction, and are modeled as $SU(2)_L$ singlets, such that the infinitesimal transformation from the $SU(2)_L$ generators τ^i on the fields vanishes.

The coupling between the fermions and hypercharge gauge field B_μ also comes from the gauge covariant derivative

$$-g'\frac{Y}{2}\bar{\psi}\gamma^\mu B_\mu\psi, \psi \in \{u_L, d_L, u_R, d_R, \nu_L, e_L, e_R\}. \quad (2.15)$$

The mixture of the neutral current interaction from B_μ and W_μ^3 models the electromagnetic interaction from the photon field A_μ and the Z boson field. Given the fact that neutrinos are neutral particles not interacting with photons, the neutral current coupling between neutrinos represents the Z boson interaction. Therefore, the Z boson and photon fields as orthogonal basis of the vector space spanned by W_μ^3 and B_μ are

$$Z_\mu = W_\mu^3 \cos \theta_W - B_\mu \sin \theta_W, A_\mu = W_\mu^3 \sin \theta_W + B_\mu \cos \theta_W, \quad (2.16)$$

where θ_W is the Weinberg angle given by $\sin \theta_W = \frac{g'}{\sqrt{g^2+g'^2}}, \cos \theta_W = \frac{g}{\sqrt{g^2+g'^2}}$. To recover the electromagnetic interaction in the SM Lagrangian, the electromagnetic coupling e is defined as

$$e := \frac{gg'}{g^2 + g'^2}, \quad (2.17)$$

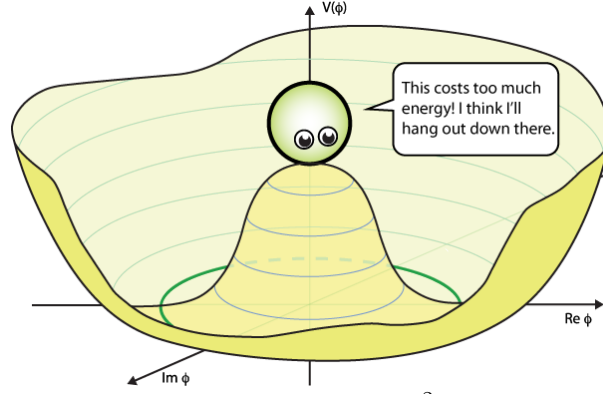


Figure 2.1: The Higgs potential when $\lambda > 0$ and $\mu^2 < 0$. The figure is taken from [1].

and the electric charge Q is defined as

$$Q = T_3 + \frac{Y}{2}, \quad (2.18)$$

where T_3 are the quantum numbers of the fields under the $SU(2)_Y$ generator $\frac{\tau^3}{2}$, i.e. $T_3 = \frac{1}{2}$ for u_L and ν_L , $T_3 = -\frac{1}{2}$ for d_L and e_L , and $T_3 = 0$ for u_R , d_R and e_R . The neutral current coupling terms are written as

$$-\frac{g}{\cos \theta_W} (T_3 - \sin^2 \theta_W Q) \bar{\psi} \gamma^\mu Z_\mu \psi - e Q \bar{\psi} \gamma^\mu A_\mu \psi. \quad (2.19)$$

The electric charges of the left-handed and right-handed projections of fermion fields are the same, because the electromagnetic interaction conserves parity.

Higgs sector

The Higgs sector describes the kinetics and self-interactions of the scalar Higgs field. The spontaneous symmetry breaking (SSB) of the field to its vacuum expectation value (vev) mass terms of the Higgs, Z and W^\pm bosons and explains the massive Z and W^\pm bosons in the experiment. To construct the Z and W^\pm mass terms, the Higgs field ϕ is an $SU(2)_Y$ doublet complex scalar field, such that the covariant derivative of ϕ gives the coupling between ϕ and $SU(2)_L$ gauge bosons.

In the Higgs sector of the Lagrangian, the potential of the Higgs doublet $\phi = \begin{pmatrix} \phi^+ \\ \phi^0 \end{pmatrix}$ is

$$V(\phi) = \mu^2 \phi^\dagger \phi + \lambda (\phi^\dagger \phi)^2. \quad (2.20)$$

For parameters $\lambda > 0$ and $\mu^2 < 0$, $V(\phi)$ is a quartic function of $|\phi|$ like a Mexican hat, as sketched in Figure 2.1. This implies a non-zero vev of the Higgs field when the potential is at the minimum. The choice of the vacuum has three degrees of freedom. The $SU(2)_L$ gauge symmetry is broken by the Higgs field falling into a specific vacuum. In the following, we choose the vacuum

$$\phi_v = \frac{1}{2} \begin{pmatrix} 0 \\ v \end{pmatrix}, \quad (2.21)$$

in which the constant $v := -\frac{\mu^2}{\lambda}$. At this vacuum value, the Higgs field kinetic term $|D_\mu \phi|^2$

becomes

$$|(ig\frac{\tau^i}{2}W_\mu^i + ig'\frac{Y}{2}B_\mu)\frac{1}{\sqrt{2}}\begin{pmatrix} 0 \\ v \end{pmatrix}|^2 \quad (2.22)$$

$$= \frac{v^2}{8}(2g^2W_\mu^+W^{-\mu} + (Yg'B_\mu - gW_\mu^3)^2). \quad (2.23)$$

The first term explains the W^\pm boson mass, while the second term gives the Z boson mass when the hypercharge Y of ϕ is set to 1, so that photons remain massless. The spin degrees of freedom of the W^\pm and Z bosons increase from two to three when the vector bosons become massive, absorbing the three degrees of freedom in the choice of vacuum. To describe the remaining one degree of freedom of the Higgs doublet around the vacuum, the doublet is written as

$$\phi(x) = \frac{1}{\sqrt{2}}\begin{pmatrix} 0 \\ v + h(x) \end{pmatrix}, \quad (2.24)$$

in which $h(x)$ is a real scalar field. The potential term $V(\phi)$ in the Lagrangian density gives quadratic, cubic and quartic terms of $h(x)$, corresponding to the mass, three-particle and four-particle interactions. Therefore, the $h(x)$ describes a massive scalar boson named as the "Higgs boson". The SM Lagrangian predicts the Higgs interactions with W^\pm and Z , and the measurements at the LHC agree with these predictions under the current precision. The three- and four-Higgs boson interactions are also predicted by the Higgs potential terms, which are under investigation in the current and future LHC experiments.

Yukawa sector

The Yukawa sector involves the coupling between the fermions and the Higgs field. After the SSB of the Higgs field, the Yukawa sector gives fermion mass terms and the coupling between the Higgs boson and fermions.

Constrained by the gauge symmetry, the Yukawa sector has the following terms

$$-y_{ij}^e\bar{L}_{Li}\phi e_{Rj} - y_{ij}^d\bar{Q}_{Li}\phi d_{Rj} - y_{ij}^u\bar{Q}_{Li}\phi^c u_{Rj} + h.c., i, j \in \{1, 2, 3\}. \quad (2.25)$$

After fixing ϕ to its vev eq. 2.21, the Yukawa sector turns into quadratic terms of the fermion fields. By diagonalizing the y_{ij}^e , y_{ij}^d and y_{ij}^u matrices, we can get the mass terms of fermion fields in their physical mass eigenstates. The mixture between the weak eigenstates and mass eigenstates is described by the Cabibbo-Kobayashi-Maskawa (CKM) matrix for the quark fields and the Pontecorvo-Maki-Nagawa-Sakata (PMNS) matrix for the lepton fields. The CKM and PMNS matrices are $U(3)$ matrices with each element denoting the projection of a mass eigenstate to a weak interaction eigenstate, thus describing the weak charged current coupling among these mass eigenstates. The off-diagonal components and non-trivial complex phases of these matrices explain the flavor mixing and CP violation of the weak interaction.

The SM particles in their mass eigenstates are summarized in Figure 2.2. While the neutrinos in the SM are massless and always left-handed, the observation of neutrino flavor oscillation gives evidence for non-degenerate neutrino masses. Extensions in the SM Lagrangian are necessary to explain the neutrino masses.

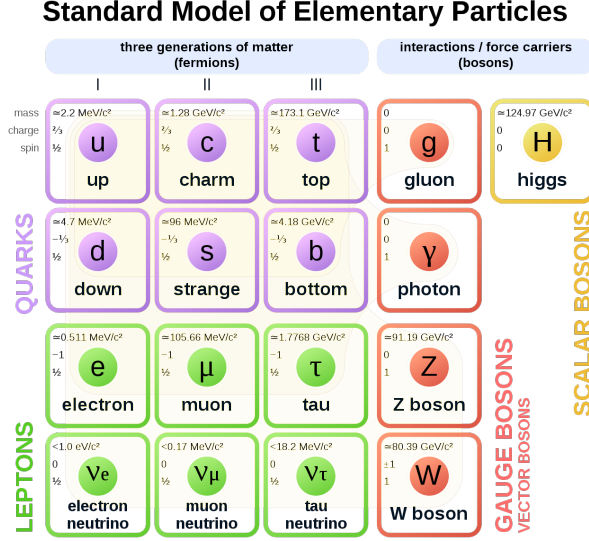


Figure 2.2: Summary of SM particles [2].

2.2 Particle scattering

The SM Lagrangian is used to describe the observations in the particle scattering experiment. The scattering process is considered as a transition from an initial state of particles to a final state. The most common observable is the differential cross section $\frac{d\sigma}{d\Omega}$, defined as

$$\frac{d\sigma}{d\Omega} := \frac{\text{Scattering rate per solid angle of final state particles}}{\text{Incoming particles per unit time per unit area}}. \quad (2.26)$$

Alternatively, the cross section differential in a general observable x is defined as

$$\frac{d\sigma}{dx} := \frac{\text{Scattering rate per unit of } x}{\text{Incoming particles per unit time per unit area}}. \quad (2.27)$$

In an ultra-relativistic $2 \rightarrow N$ particle scattering from the incoming particles A, B to the final-state particles $i \in \{1, 2, \dots, n\}$, the differential cross section is given by

$$d\sigma = \frac{1}{2s} |\mathcal{M}|^2 d\Phi_N, \quad (2.28)$$

in which $s = (p_A + p_B)^2$ is the Mandelstam variable as the square of the center-of-mass energy of the initial particles, $|\mathcal{M}|^2$ is the squared matrix element describing the dynamics of the process depending on $p_A^\mu, p_B^\mu, p_i^\mu$, and $d\Phi_N$ is the N-body phase space

$$d\Phi_N = (2\pi)^4 \delta^4(p_A + p_B - \sum_i p_i) \prod_{i=1}^n \frac{d^3 \vec{p}_i}{(2\pi)^3 2E_i}. \quad (2.29)$$

The matrix element $\mathcal{M}(p_A^\mu, p_B^\mu, p_i^\mu)$ controlling the dynamics can be computed from "Feynman rules" derived from the Lagrangian density. In brief, the Lagrangian density is split into kinetic terms describing free-propagating fermion and boson fields and interaction terms describing state transitions. The interaction terms are assumed to be weak enough that they can be considered as perturbations to the kinetic terms for free propagation. The matrix element \mathcal{M} is the transition amplitude from the initial state to the final state by a unitary time-evolution operator determined by interaction terms. The order-by-order expansion of the time-evolution operator can be used to calculate \mathcal{M} in increasing precision if the couplings in the interaction terms are weak. The

ordered series of \mathcal{M} can be organized in a graphical representation of particle interactions as "Feynman diagrams", and the \mathcal{M} computation is performed by applying the Feynman rules to these diagrams. In practice, the calculations are often performed in a fixed order for matrix element prediction at a certain precision. The "resummation" technique is sometimes used to systematically include logarithmic terms of the energy scale at all orders, which is more precise than fixed-order calculations when the contributions from these logarithmic terms are relatively large at higher orders.

2.3 Non-perturbative particle interactions

2.3.1 Non-perturbative QCD from large coupling

In the calculation of the matrix elements by order expansions, divergences appear in higher-order calculations and regularizations are necessary to cure the divergences. A procedure named as "renormalization" is used to eliminate the diverging terms by redefinition of the Lagrangian parameters and absorption of the divergences into the new definitions. The redefinition is based on the fact that these Lagrangian parameters are not physical observables. Instead, they are input parameters from the theory, which are related to the experimental measurements by the cross-section calculation via the Feynman diagrams. Therefore, these parameters can be tuned to reproduce the experimental observables. The divergences in the redefined parameters are not problematic, as they do not directly correspond to experimental observations, but are either interpreted as mathematical manipulations or the breakdown of low-energy theories when the undiscovered heavy particles are not considered in the calculation.

After the regularization, the theoretical parameters in the Lagrangian are constants with divergences, while the experimental observables are finite quantities depending on experimental conditions (e.g. the energy scale of the processes). As a result, the experimental observables under different conditions can be connected through their shared dependence on the same theoretical parameters. The relation between the coupling parameters g at different energy scales μ is described by renormalization group equations

$$\frac{\partial g}{\partial \ln \mu} = \beta(g), \quad (2.30)$$

in which the β -function only depends on the value of g but not μ , indicating the self-similarity of the system among all the scales.

The "running" of the couplings in the SM, governed by the renormalization group equations, has been tested and verified in the experiments [3, 4] In the QED part of SM, the coupling constant at energy scale μ defined as $\alpha(\mu^2) = \frac{e^2(\mu)}{4\pi}$ is approximately

$$\alpha(\mu^2) = \frac{\alpha(\mu_0^2)}{1 - \frac{\alpha(\mu_0^2)}{3\pi} \ln \frac{\mu^2}{\mu_0^2}}. \quad (2.31)$$

The coupling increases with the energy scale logarithmically. While in the QCD, the self-interaction of gluons leads to different behaviors in the running of the strong coupling constant

$$\alpha_S(\mu^2) := \frac{g_c^2}{4\pi} = \frac{\alpha_S(\mu_0^2)}{1 + \alpha_S(\mu_0^2) \frac{\beta_0}{4\pi} \ln \frac{\mu^2}{\mu_0^2}}, \quad (2.32)$$

in which β_0 depends on the number of colors N_C and quark flavors N_f as follows

$$\beta_0 = \frac{11N_C - 2N_f}{3}. \quad (2.33)$$

In the SM, $N_C = 3$ and $N_f \leq 16$ give a positive β_0 and decreasing coupling with increasing energy. The asymptotic freedom of QCD implies that QCD interactions at high energy scales can be modeled by perturbative calculations, and the quarks and gluons in hadrons can be treated as quasi-free particles in collisions with high momentum transfer.

On the other hand, perturbative calculations are not always applicable for predicting QCD interactions. For example, the strong coupling constant blows up at low energy scales. At $\alpha_S(1 \text{ GeV}^2) \simeq 0.5$, the perturbative calculation is not able to give precise predictions, as the higher-order contributions to the matrix elements become large. Tools such as lattice QCD [5–13], effective theories [14] or string-based approaches [15–17] are usually used for theoretical predictions in this region. The non-perturbative nature of QCD at low energy gives explanations for the color confinement and formation of hadrons in the experimental observations. The increasing coupling at a lower energy scale corresponds to a larger force between colored particles mediated by gluon exchange at a longer range. As a result, the potential energy between separated colored particles would increase until sufficient to create quark-anti-quark pairs. The newly formed quark pairs can combine with the original ones to form hadrons in color singlets. The absence of free quarks or gluons is called "color confinement". The formation of hadrons from quasi-free quarks and gluons in high-energy collisions is named "hadronization" or "fragmentation". In experiments, the hadrons originating from a high-energy quark or gluon form a collimated spray recognized as "jets".

2.3.2 Non-perturbative phenomena from topological structures of gauge fields

The non-Abelian $SU(2)_L$ and $SU(3)_c$ gauge fields in the SM have topologically non-trivial vacuum structures. To illustrate this feature, consider the pure gauge sectors in the Lagrangian density

$$-\frac{1}{4}F_{\mu\nu}^a F_a^{\mu\nu} \in \mathcal{L}, \quad (2.34)$$

in which $F_{\mu\nu}^a \in \{G_{\mu\nu}^a, W_{\mu\nu}^i\}$ corresponds to the field strength of the gauge field $A_\mu^a \in \{G_\mu^a, W_\mu^a\}$. In the following, the gauge field in each spacetime dimension is written as a vector in the space spanned by the $SU(2)_L$ or $SU(3)_c$ generators: $A_\mu = A_\mu^a T^a$, where $T^a = \frac{\tau^a}{2}$ in the $SU(2)_L$ case and $T^a = \frac{\lambda^a}{2}$ in the $SU(3)_c$ case. The vacua of gauge fields with zero field strength are

$$A_i = \frac{i}{g} U^\dagger(\vec{x}) i \partial_i U(\vec{x}), i \in \{1, 2, 3\}, A_0 = 0 \quad (2.35)$$

for U as $SU(2)$ or $SU(3)$ matrices and g as the coupling strength. In the case where U is a constant matrix with respect to \vec{x} , the vacuum of the gauge field is trivial $A_i = 0$. The topological effects of vacuum appear for some non-trivial cases of $U(\vec{x})$. Assuming the matrix $U(\vec{x})$ becomes identical at infinity $|\vec{x}| \rightarrow \infty$, it is a map from the 3-sphere $\vec{x} \in S^3$ to the gauge group. For example, the "hedgehog" form of U in the $SU(2)$ gauge group case satisfies this requirement

$$U = \exp \left[i \frac{\vec{r} \cdot \vec{\tau}}{r} P(r) \right] \quad (2.36)$$

for continuous function $P(r)$ satisfying $P(0) = 0$ and $P(\infty) = \pi n, \forall n \in \mathbf{Z}$. A gauge transformation

$$A_\mu \rightarrow V(x_\mu)A_\mu V^{-1}(x_\mu) + \frac{i}{g}(\partial_\mu V)V^{-1} \quad (2.37)$$

corresponds to $U \rightarrow VU$ in the gauge field vacua 2.35. A gauge transformation V smooth in spacetime and continuously deformable into identity represents a continuous deformation on U , which does not change the homotopy class of $U : S^3 \rightarrow SU(2)$ or $U : S^3 \rightarrow SU(3)$. The topological effect is quantified by the Chern-Simons number

$$N_{CS} = \frac{1}{24\pi^2} \int d^3x \epsilon^{ijk} (U^\dagger \partial_i U)(U^\dagger \partial_j U)(U^\dagger \partial_k U) \in \mathbf{Z}, \quad (2.38)$$

known as the "winding number" when one uses a 3-sphere to cover the gauge group. Since these classical vacua cannot be transformed into each other via gauge transformations that are continuous deformations, their topological distinctions are not gauge artifacts, but rather physical barriers that require intermediate fields with non-zero field strength and energy to go through.

This energy barrier can be penetrable by quantum tunneling, and the analytical solution of the tunneling path is given by Belavin, Polyakov, Schwartz, and Tyupkin in 1975 [18], known as the BPST instantons. The tunneling rate is approximately

$$\Gamma \sim e^{-\frac{8\pi^2}{g^2(\rho)}} \quad (2.39)$$

for the coupling strength g at the energy scale ρ . The tunneling rate can be non-negligible in QCD with large g , while highly suppressed in the electroweak sector as the coupling strength is small.

In the prediction of the QCD instanton production, the quark-gluon interactions and perturbative corrections need to be taken into account. The instanton-induced interaction can be effectively written as extra $2N_f$ -quark interaction terms ('t Hooft vertex) in the Lagrangian for N_f light quark flavors with all the masses approximately the same [19]. The instanton-induced interaction vertex has very different chirality structures from the gluon-induced interactions: the instanton-induced vertex includes a quark-anti-quark pair for each flavor with the same chirality, thus violating the chiral symmetry, while the gluon-induced interactions preserve chirality. The instanton-induced interactions have rich phenomena in hadronic physics: they induce mass corrections to mesons and provide explanations for the decay modes of the $0^- \eta_c$ charmonium [20]

$$\eta_c \rightarrow \eta\pi\pi, \eta'\pi\pi, K\bar{K}\pi, \quad (2.40)$$

by effective interaction term $\mathcal{L}_{eff} \sim (\bar{c}c)(\bar{u}u)(\bar{d}d)(\bar{s}s)$ and generally the large probability of charmonium three-body decays [21]. It is also predicted that the instanton-induced process can affect the decay modes of glueballs [21], and its chirality violation leads to spin-polarization effects in the hadrons from non-central heavy ion collisions [22].

Experimental searches for QCD instanton productions in deep-inelastic electron-proton (ep) scatterings have been performed in the HERA and ZEUS experiments without finding evidence of instanton-induced processes [23–26], while still compatible with theoretical predictions [27, 28]. The instanton-induced process has been predicted to be abundant in pp collisions at the LHC [29–31], for example, from the gluon-gluon fusions to N_f pairs of free light flavor quark-anti-quarks and multiple gluons via an effective instanton vertex, as shown in Figure 2.3. The

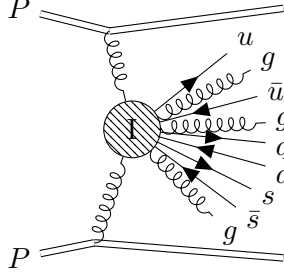


Figure 2.3: Dominant instanton-induced process in pp collisions at the LHC [31] from gluon fusions and decays into one $q\bar{q}$ pair of each of the N_f kinematically accessible quark flavors (e.g. u, d, s in the figure) and several gluons.

multiple-particle interaction vertex results in a constant matrix element $\mathcal{M} = \text{const}$ in this process, and the differential cross section eq. 2.28 is flat in the N-body phase space. This feature of instanton kinematics indicates a more isotropic distribution of instanton products than those from non-instanton QCD processes, and becomes one of the motivations of the event-shape measurement in pp collisions presented in this thesis (Section 4).

2.4 The physics of pp collisions

Protons, initially known as hydrogen ions, are composite particles of quarks and gluons. These spin 1/2 hadrons with electrical charge 1 can be considered as bound states of two up quarks and one down quark, named as "valence quarks", interacting by exchanging gluons. Due to the quantum fluctuations from the QCD interactions, quark-anti-quark pairs are created and annihilated in the protons, named as "sea quarks". The quark and gluon sub-constituents are referred to as "partons". pp collisions have diverse behaviors across different energy scales and impact parameters. A large part of the collisions are elastic scatterings, in which the colliding protons are only scattered through an angle, staying intact and preserving the energy and momentum of the incoming protons. The elastic scatterings happen at low energy scales. In inelastic scatterings, the strong force approaches the internal structure of hadrons at shorter length scales. In the pp collision experiments considered in this thesis, the elastic collisions are discarded, and the inelastic collisions are analyzed as "minimum bias" data.

The kinematics of inelastic pp collisions are dominantly affected by the running strong coupling constant at the energy scales of the collisions. Most of the inelastic collisions happen at a relatively low energy scale corresponding to large QCD couplings, in which the order expansion of perturbative predictions is not precise enough to describe the experiment. A small fraction of interactions involves large momentum exchange. At high energy scales, the partons become quasi-free particles because of the asymptotic freedom of QCD. These hard collisions can be modeled as scatterings of two quasi-free partons from each of the protons at a high energy scale and the rest of the protons undergoing soft interactions. The partons in hard collisions are approximately collinear with the incoming protons, and carry a fraction of the proton momenta. The probability distributions of the parton momentum fractions are described by parton distribution functions (PDFs). As the partons are probed by higher energy, the quantum corrections on the partons can be resolved, so that the PDFs depend on the energy scale of the probe Q^2 . Estimating the quantum corrections by perturbative expansions, the dependence of PDFs on Q^2 can be derived via the renormalization group equations of fixed-order perturbative expansions, denoted

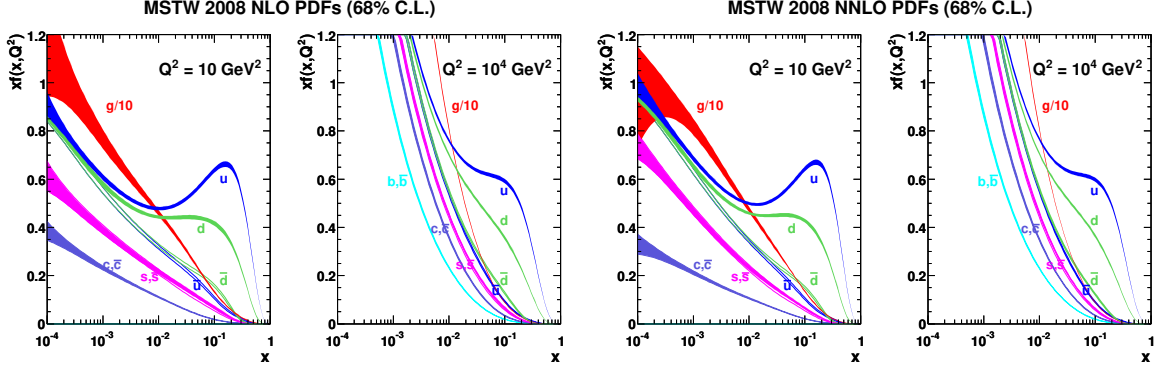


Figure 2.4: MSTW 2008 PDFs of various parton species at next-to-leading order (NLO) (left) and next-to-next-to-leading order (NNLO) (right) at $Q^2 = 10 \text{ GeV}^2$ and $Q^2 = 10^4 \text{ GeV}^2$.

as the DGLAP (Dokshitzer–Gribov–Lipatov–Altarelli–Parisi) evolution equations 2.41 [32–34].

$$\frac{\partial f_i(x, Q^2)}{\partial \ln Q^2} = \frac{\alpha_S(Q^2)}{2\pi} \sum_j \int_x^1 \frac{dz}{z} P_{j \rightarrow i}(z, \alpha_S(Q^2)) f_j\left(\frac{x}{z}, Q^2\right), \quad (2.41)$$

in which $P_{j \rightarrow i}(z, \alpha_S(Q^2))$ is the splitting function of a parton type j to a parton type i , carrying fraction z of the momentum of the parent parton j and quantifying the probability of the parton branching. The splitting functions are derived from the cross section of the corresponding decays at the collinear limit, as the soft and collinear emissions are dominant, and the dependence of the PDFs on soft non-perturbative emissions is to be extracted from experimental data.

The PDFs are determined by a multi-step procedure, involving the empirical and theoretical modeling of the PDFs, experimental data from a variety of processes e.g. deep inelastic ep scattering, DY processes, jet production from pp collisions, W^\pm and Z production, heavy quark production and small- x physics, and global fits to the data. The procedure starts by parameterizing the PDFs at an initial scale Q_0^2 with functional forms, then the PDFs are evolved to higher energy scales using DGLAP equations to predict the experimental observables depending on the PDFs at certain scales. Finally, numerical minimization is applied to find the best-fit values of the parameters to the data. The fitted PDFs and their uncertainties are necessary for simulations of hadron collisions. Figure 2.4 shows the MSTW 2008 PDFs [35–37] depending on the perturbative expansion order and energy scales Q^2 .

The differential cross section of a hard scattering process can be approximately factorized by convoluting the PDFs of the incoming partons with the cross section of the parton scattering process. Assume the ultra-relativistic colliding protons have momenta

$$P_1^\mu = \frac{\sqrt{s}}{2}(1, 0, 0, 1), P_2^\mu = \frac{\sqrt{s}}{2}(1, 0, 0, -1), \quad (2.42)$$

and the hard scattering protons i and j carry fraction x_1 and x_2 of the proton momenta P_1 and P_2 , respectively. The squared center-of-mass energy of the parton-parton system is

$$\hat{s} := (x_1 P_1 + x_2 P_2)^2 \simeq x_1 x_2 s. \quad (2.43)$$

The differential cross section is

$$d\sigma(P_1 P_2 \rightarrow X) = \sum_{i,j} \int dx_1 \int dx_2 f_i(x_1, \mu_F^2) f_j(x_2, \mu_F^2) \hat{\sigma}_{ij \rightarrow X}(x_1 x_2 s, \mu_F^2, \mu_R^2), \quad (2.44)$$

in which the f_i and f_j are the PDFs of i and j , μ_F is the energy scale of the hard scatterings

probing the protons, referred to as the "factorization scale" and the energy scale of computing the hard-scattering cross sections μ_R is denoted as the "renormalization scale".

Monte Carlo simulations of hard-scattering events start from calculating the differential cross section from perturbative order expansions on the phase space of X depending on the kinematics of initial-state partons. The initial states are sampled from PDFs and the kinematics of hard-scattering final states are sampled from the differential cross section on the phase space. The evolution of the PDFs from a low energy scale (when the protons are far away) to the factorization scale is modeled by exclusive parton emissions, referred to as "initial-state radiations", and generated for each event using the parton shower (PS) algorithms. In PS, a cascade of partons is generated in a Markov process from the factorization scale to a low energy cutoff referred to as the ISR starting scale and often set close to Λ_{QCD} where $\alpha_S(\Lambda_{QCD}^2) \sim 1$. This mimics the back-evolution of DGLAP equation from the factorization scale to the ISR starting scale. The partons generated from PS then go through hadronization and turn into stable hadrons. The simulation of the final states of the hard scattering to stable particles is realized by the final state radiation (FSR), simulated by a similar PS and hadronization procedure.

Soft QCD interactions dominate in inelastic pp collisions and contribute significantly to the remnants accompanying parton-parton hard scatterings – collectively known as the UE.

Phenomenological models are typically employed to simulate these soft QCD processes. Within the UE of many commonly used models, additional parton scatterings beyond the primary hard collision are modeled using multiple-parton interaction (MPI) frameworks, while the non-interacting remnants are represented as beam remnants (BR). Simulations of MPI and BR rely on parameterized models that incorporate the proton mass distribution, the intrinsic transverse momentum (intrinsic k_T) of partons, MPI kinematics, the PS and hadronization. These parameters are generally determined by generating events over a range of values, analyzing how observables depend on these parameters through simulations, and fitting the model predictions to experimental data. The resulting parameter sets are referred to as "tunes".

The UE encompasses a rich array of non-perturbative phenomena that are probed through various processes during parameter tuning. UE-related measurements and tuning efforts can uncover these phenomena and provide crucial experimental inputs for refining theoretical models. This motivation underlies the event-shape measurements in minimum bias events (Section 4) and the study of the intrinsic k_T tuning in DY events (Section 5) presented in this thesis.

Moreover, these models and parameters are integral to describing hard-scattering processes. Therefore, dedicated investigations of UE models and the precise determination of phenomenological parameters are essential for accurate predictions of hard-scattering phenomena. Understanding and controlling the impact and uncertainties associated with soft physics is vital for disentangling these effects from contributions at the high-energy frontier, such as those arising from SM extensions.

2.5 Beyond the Standard Model

Despite the remarkable success of the SM in describing and predicting the electroweak and strong interactions up to top and Higgs mass scale (~ 100 GeV) and the confirmations from experimental tests with high precision, there are indications from both theory and experiment side that the SM is not the final theory to completely describe all the fundamental particles and their interactions, but instead a low-energy effective theory.

Given that the matter composed of SM particles has gravitational interactions, a complete theory should include the SM and gravity consistently, and describe the quantum effects from gravitational interactions. In the quantization of the classical general relatively similar to electromagnetic force, the gravitational interaction is interpreted as the exchange of massless spin-2 bosons, named as gravitons. However, the perturbative expansions of such interactions have issues in renormalization – the ultraviolet divergences cannot be absorbed similarly to the SM renormalization. As a consequence, the quantum corrections to gravity cannot be predicted properly in this framework. In practice, the gravity is much weaker than the electroweak and strong interactions, thus the quantum effects from gravity are negligible at the scale probed by current LHC experiments. At the Planck scale $\sim 1.2 \times 10^{19}$ GeV, the quantum gravity effects are expected to be visible, and experimental observables would require the description from a theory superseding the SM. One candidate is string theory, in which particles are modeled as vibrations of extended objects (strings) instead of point-like objects, and general relativity appears to be its low-energy limit. The Feynman diagrams of string scatterings are not only renormalisable, but also finite. Therefore, string theory provides a solution to unify gravity and the SM. For its mathematical consistency, the string theory requires supersymmetry (SUSY) and extra spacetime dimensions, both have been extensively searched at LHC experiments [38, 39]. Although the experimental results do not show significant evidence, the majority of parameters remain unconstrained due to the flexibility and variety of models in the string theory.

The experimental conflicts with the SM mainly come from neutrino experiments, as well as astrophysical observations. Neutrino flavor oscillations when propagating through space have been discovered and measured in plenty of experiments [40–52]. This phenomenon originates from quantum superposition of flavor states when the neutrinos propagate on their mass eigenstates, which indicates non-zero and distinct neutrino masses and necessitates modifications to the SM, such as the seesaw mechanism [53–58], sterile neutrinos [59–62], or lepton-number-violation processes [63–66]. The concept of dark matter is motivated by evidence from multiple independent astronomical observations, pointing to the existence of unknown matter with gravitational effects. The observations include the inconsistency between spiral galaxies’ rotational curves and predictions with the distributions of observed matter [67–69], the disagreement between the mass distribution in Bullet Cluster reconstructed from gravitational lensing and X-ray data [70–72], the discrepancy between the power spectrum of cosmological microwave background (CMB) anisotropies and the prediction assuming only the baryonic matter [73, 74], the simulations of large cosmic structures (galaxies, clusters) aligning with observations only when dark matter is included [75], and the difference between the gravitational potential inferred from X-ray emissions from thermal bremsstrahlung of clusters of galaxies and that expected from optical observations [76]. The dark matter is compatible with some SUSY models, in which the dark matter particles are stable partners of SM particles, and these models can also be adapted to explain the Higgs mass hierarchy problem [77]. The searches for dark matter have been carried out in both hadron colliders [78] and dedicated dark-matter detector experiments [79–82] assuming non-gravitational interactions between dark matter and SM particles. Another concept of dark energy is motivated by the accelerated expansions of the universe supported by the redshift measurement of supernova [83, 84], CMB measurements [74], baryon-acoustic-oscillation measurements [85] and galaxy cluster observations [86–88].

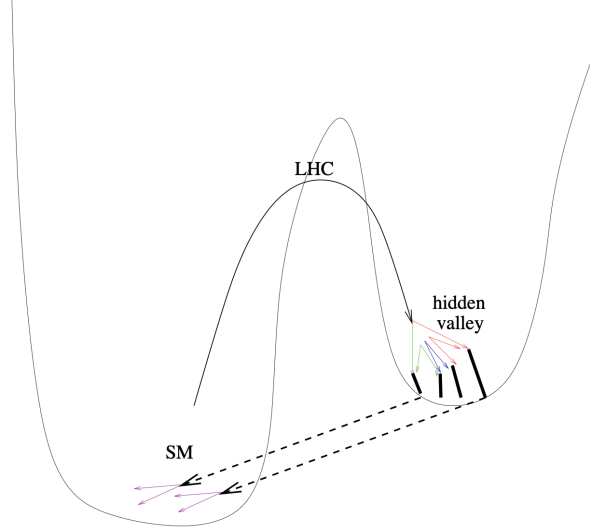


Figure 2.5: Depiction of the hidden valley scenario, where the SM particles need to go over a high energy barrier to access the particles in the hidden sector (the valley).

2.5.1 Soft unclustered energy patterns from hidden valley models

The searches for dark matter and SUSY in collider experiments have not shown evident deviations from the SM predictions, and strict limits have been put on the simplest SM extensions and their signatures in the current collider environment at \sim TeV scale. To fully exploit the discovery potential of the available data, the searches are turned towards unconventional signatures from more complex models, which could have escaped the previous searches. A class of well-motivated models are hidden valley models, which can appear either in some top-down string theory constructions [89, 90] or bottom-up solutions to the hierarchy problem e.g. the twin Higgs model [91], the Randall-Sundrum scenarios [92, 93], models with a decoupled SUSY sector or models with sterile neutrinos interacting with SM neutrinos. In these scenarios, the SM is extended by a hidden sector and the particles in this sector are feebly coupled to SM particles via a heavy neutral mediator e.g. Higgs boson, Z boson, or unknown neutral particles. The hidden sector is often featured as extended non-Abelian gauge groups containing various particle species with wide ranges of mass, different stability depending on the dynamics and symmetries, and rich phenomena, such as confinement similar to QCD or exotic decays. The heavy mediator production is followed by multiple-particle productions in the hidden sector. These particles in the hidden sector can have low masses, but are only accessible from the SM particles via portals of heavy mediators, thus the models gain the name of "hidden valley", as shown in Figure 2.5.

Depending on the details of the hidden sector, the particles in the hidden valley can undergo dark hadronization similar to the QCD hadronization or a chain of decays to either stable dark matter particles or SM particles, which could be realized by mixing of gauge bosons in the hidden sector with SM gauge bosons. The decay kinematics lead to distinct detector anomalies requiring dedicated searches, e.g. displaced decay vertices or emerging jets if the dark hadrons have a long lifetime before decaying to SM particles, semi-visible jets if partially decaying to stable hidden sector particles, missing energy if all the decay products are invisible.

In the scenario considered in this thesis (Section 6), the hidden sector particles from the heavy mediator form bounded states (dark hadrons) through confinement, and then promptly decay to light SM particles. The large amounts of soft decay products distribute isotropically

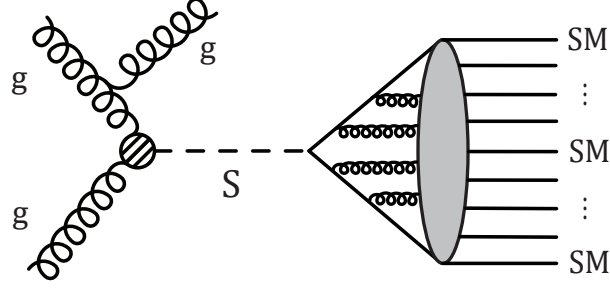


Figure 2.6: Schematic Feynman diagram of SUEP production from gluon-gluon fusions and decay into SM particles.

in the rest frame of the heavy mediator, resulting in a novel signature of SUEPs, as sketched in Figure 2.6. The explicit models in the search are discussed as follows.

Extended gauge group

In this hidden valley model, the gauge group is extended by an $SU(N)$, $N \geq 3$ hidden group. Similar to the QCD sector in the SM, non-trivial representations of this hidden group correspond to fundamental particles in the hidden sector. The spin 1/2 fermions, denoted as dark quarks, interact by exchanging spin 1 gauge bosons, denoted as dark photons. The dark-photon kinetic terms give self-interactions among these dark photons, as well as the dark hadronization behaviors due to confinement. The dark quarks promptly turn into dark hadrons as singlets of the hidden group. There can be possible kinetic mixing between dark photons and SM gauge bosons similar to the mixing between SM hypercharge gauge boson Y^μ and the weak neutral boson W_3^μ . The dark hadrons can decay to SM particles through the kinetic mixing of gauge bosons for the realization of the SUEP signatures [94].

Heavy mediator production as a portal to the valley

To activate the SUEP production, the portal connecting the SM and the hidden sector is charged in both gauge groups. The portal is effectively written as a heavy (pseudo)scalar mediator with coupling terms to particles in both sectors. We target the heavy mediator production from the gluon-gluon fusion mode via an effective coupling

$$\frac{c}{\Lambda} S G_{\mu\nu} G^{\mu\nu} \subset \mathcal{L} \text{ or } \frac{c}{\Lambda} S G_{\mu\nu} \tilde{G}^{\mu\nu} \subset \mathcal{L}, \quad (2.45)$$

in which S is the scalar field for the heavy mediator, $G_{\mu\nu}$ is the gluon field strength tensor, $\tilde{G}_{\mu\nu} = \epsilon_{\mu\nu\alpha\beta} G^{\alpha\beta}$ is the dual field of $G_{\mu\nu}$, Λ is the energy scale where this effective coupling become relevant, and c parametrizes the coupling strength. In the case the heavy mediator is the Higgs boson, the effective coupling is realized by a quark loop, as shown in Figure 2.7.

Dark hadron production

The decay from the mediator particle S to dark quarks is modeled by an interaction term

$$-iy_\psi S \bar{\psi}_D \gamma_5 \psi_D \subset \mathcal{L} \text{ or } -iy_\psi S \bar{\psi}_D \psi_D \subset \mathcal{L}, \quad (2.46)$$

in which the y_ψ parametrizes the coupling strength, similar to the Yukawa coupling between Higgs and fermions, ψ_D represents the dark quark fields.

Analogously to QCD, the pair of dark quarks from the heavy mediator decay undergo a dark

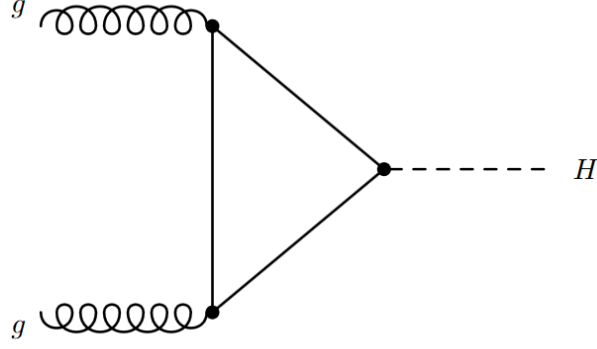


Figure 2.7: Effective coupling of a Higgs boson to two gluons realized by a quark loop.

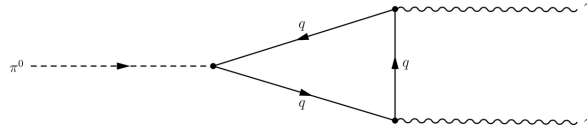


Figure 2.8: The Feynman diagram from the dominant decay channel of neutral pions π^0 to a pair of photons.

PS to a large multiplicity of softer dark partons until reaching the confinement scale of the hidden sector Λ_D . Then the particles turn into bound states of dark hadrons with masses close to Λ_D . Most of these dark hadrons are pseudoscalar dark mesons, denoted as ϕ_D with mass m_ϕ as an analogy to the π^0 's dominant in QCD hadronization. Following the models proposed in Ref. [94, 95], we assume a large 't Hooft coupling in the hidden sector, defined as $\lambda := g_D^2 N$, where g_D is the gauge coupling strength similar to the g_c , g and g' in the SM, and N is the dimension in the $SU(N)$ gauge group. Under this assumption, large-angle emissions in the dark shower are not suppressed, and the momentum distributions of dark hadrons can be described by the particle distribution in a thermal equilibrium, modeled by the relativistic Boltzmann equation

$$\frac{dN}{d^3\vec{p}} \sim \exp\left(-\frac{\sqrt{|\vec{p}|^2 + m_\phi^2}}{T}\right), \quad (2.47)$$

in which the temperature T describes the energy scale where the dark hadrons become unstable. It is in the same order as Λ_D and m_ϕ .

Dark hadron decay

To realize the prompt decay of the dark hadrons to SM particles, a ϕ_D decay into a pair of dark photons via the effective operator $\phi_D A'^{\mu\nu} A'_{\mu\nu}$ or $\phi_D A'^{\mu\nu} \tilde{A}'_{\mu\nu}$, analogous to the $\pi^0 \rightarrow \gamma\gamma$ process in the QCD sector (Figure 2.8). The dark photon pair decays to SM particles by the kinetic mixing with the SM hypercharge gauge bosons via the operator $\epsilon A'^{\mu\nu} B_{\mu\nu}$ with a small coupling parameter ϵ . A dark photon decays to a pair of charged pions $\pi^+\pi^-$ or leptons e^+e^- , $\mu^+\mu^-$, the branching ratio depending on the dark photon mass $m_{A'}$.

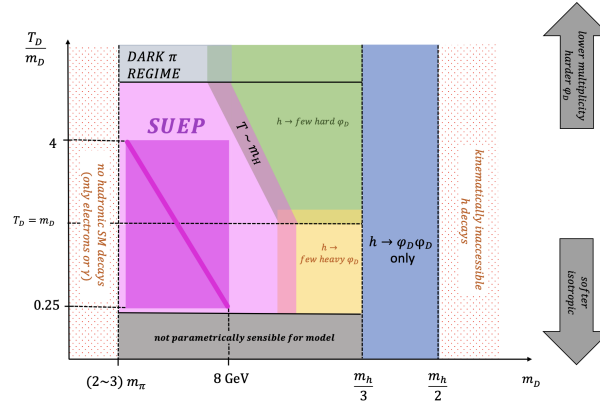


Figure 2.9: The parameter space of SUEP produced from prompt Higgs decays to dark hadrons and then to SM charged pions via dark photons, taken from [95]. The m_D and T_D in the figure are synonyms of the dark meson mass m_ϕ and temperature T in the context, respectively. m_h denotes the Higgs boson mass.

Parameter space of SUEPs

The parameters in the SUEP realization above are constrained by consistency with previous experiments, decay kinematics and model stability. The constraints are partially demonstrated in Figure 2.9, taking the example of the heavy mediator S as the Higgs boson h and the dark photon with mass $m_{A'} = 1$ GeV and decaying to charged pion pairs with 100% branching ratio.

In the heavy mediator production from gluon-gluon fusion eq. 2.45, the coupling strength is constrained by exotic Higgs searches at the LHC, as summarized in the LHC Higgs Working Group Yellow Report [96]. The highest dark hadron mass m_ϕ is constrained by the kinematics of the on-shell heavy mediator decay to a pair of dark quarks via interaction terms eq. 2.46 and the following hadronization to dark hadrons. Furthermore, the large multiplicity of dark hadrons from S decay requires $m_\phi \ll m_S$, and the on-shell decay $m_\phi \rightarrow A'A'$ kinematics requires $m_\phi > 2m_{A'}$. The model with a higher m_ϕ has S decay to few heavy ϕ_{DS} , as shown in the yellow and blue parts of Figure 2.9, and models with $m_\phi > m_S/2$ or $m_\phi < 2m_{A'}$ are not kinematically accessible, as shown in the dotted parts.

The temperature T controls the momentum distribution of decay products. Models with high T have higher ϕ_D momentum and hard emissions, as shown in the green and light gray regions of Figure 2.9. By definition, T is at the same order as m_ϕ , and $m_\phi \gg T$ indicates unstable ϕ_D at energy T , which conflicts with the model assumption, corresponding to the dark gray region in Figure 2.9.

The $T/m_\phi - m_\phi$ parameter space sensible for SUEP production is shown as the dark pink region in Figure 2.9. An additional model parameter is the dark photon mass $m_{A'}$. The decay mode $A' \rightarrow \pi^+\pi^-$ is only possible if $m_{A'} > 2m_{\pi^\pm}$, and the scenario with 100% branching ratio of this mode is the most difficult case in the experimental search because of the large QCD background also with multiple hadron products. To cover the $A' \rightarrow \pi^+\pi^-$ scenario in the search, we assume $m_{A'} \sim 1$ GeV and analyze various benchmark models with different $m_{A'}$ decay modes, together with the benchmarks with T/m_ϕ and m_ϕ on the grid points of their SUEP parameter space. The details of signal simulation are discussed in Section 6

3 The Compact Muon Solenoid Experiment at the Large Hadron Collider

The pp collision data analyzed in this thesis were produced by the LHC and collected by the CMS experiment. The LHC accelerates protons to the highest energies achieved to date, enabling the exploration of proton structure and elementary particle interactions at the smallest length scales. The state-of-the-art CMS detector captures collision products with exceptional precision and granularity, facilitating detailed reconstruction of the stable particles generated in these events.

3.1 The Large Hadron Collider

The LHC as the largest and most powerful particle collider is used to focus and accelerate hadron beams to high energies in both directions of the circular accelerator and produce head-on collisions at four interaction points for the four large particle detectors: A Toroidal LHC Apparatus (ATLAS), Compact Muon Solenoid (CMS), LHC Beauty (LHCb), and A Large Ion Collider Experiment (ALICE). The LHC machine is located at CERN near Geneva, Switzerland, in a circular tunnel at 100 meters underground with a 27 km circumference to accelerate protons and heavy ions, such as lead, xenon and oxygen ions.

As shown in Figure 3.1, the proton beam starts from ionizing hydrogen atoms to get protons and accelerating them at the LINear ACcelerator (LINAC2) with an electric field to 50 MeV energy. The protons are then passed through the Proton Synchrotron Booster, the Proton Synchrotron (PS), and the Super Proton Synchrotron (SPS) to be accelerated to an energy of about 450 GeV. At the next step, the proton beams from the SPS are injected into the LHC for further acceleration and the energy is ramped up to several TeV. At the final step, the beams are squeezed and adjusted at the collision points, and the detectors are turned on for data taking. At the LHC, the proton beams are bent by dipole magnets with a strong magnetic field at 8.3 T, generated by circular currents in superconducting niobium-titanium alloy at a low temperature achieved by liquid helium. In-between the dipole magnets, quadrupole magnets are added for focusing the beams and mitigating the beam losses. In the data-taking from 2015 to 2018, referred to as the "Run 2", the proton beam energy reached 6.5 TeV and the center-of-mass energy of the collisions is 13 TeV. The Run 2 data is used for the analyses in this thesis. In the new data-taking period from 2022, the beam energy increased to 6.8 TeV and the collision energy reached 13.6 TeV. More details about the LHC are given in [97].

The collision rate per cross section is quantified by the "instantaneous luminosity" \mathcal{L}_{inst} . In the head-on collision of two beams of particle bunches with Gaussian profiles in all the dimensions, the \mathcal{L}_{inst} is defined as

$$\mathcal{L}_{inst} = \frac{N_1 N_2 f}{4\pi\sigma_x\sigma_y}, \quad (3.1)$$

in which N_1 and N_2 are the number of particles per bunch for the two beams, f is the bunch crossing frequency (40 MHz for the LHC at Run 2), and σ_x and σ_y are the widths of the bunches in the two transverse dimensions, given by the root-mean-square of particles per bunch. In reality, corrections are applied to \mathcal{L}_{inst} to take into account the effects of crossing angles, beams offset, Hourglass effect from the change of beam density in the longitudinal direction, the non-Gaussian beam profiles, etc. [99]

The total number of collisions in a certain data-taking period is denoted as the "integrated luminosity", defined as the integration of the instantaneous luminosity in the corresponding period

$$L := \int_{\text{data taking}} \mathcal{L}(t) dt. \quad (3.2)$$

According to the definition, the integrated luminosity has a unit of inverse area. Figure 3.2 shows the integrated luminosity of pp collisions versus time in each year from 2015 to 2018.

The data from each bunch crossing is processed as an "event". Due to the large amount of particles in each bunch, multiple interactions are expected per bunch crossing. The number of inelastic collisions in each bunch crossing is named as "pileup", and estimated by

$$\text{pileup} = \frac{\mathcal{L} \sigma_{in}^{pp}}{f}, \quad (3.3)$$

in which σ_{in}^{pp} is the inelastic cross section of pp collisions. The pileup distributions in each year of CMS Run 2 from 2015 to 2018 are shown in Figure 3.3

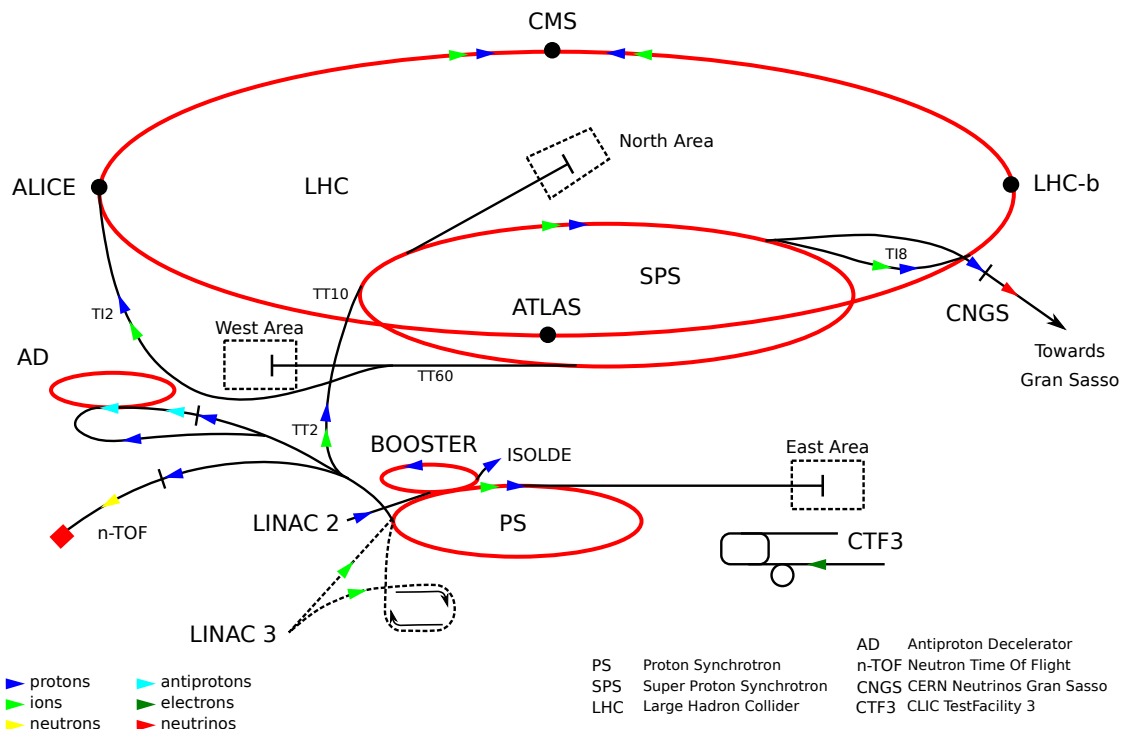


Figure 3.1: The CERN accelerator complex, taken from [98]. The protons start from LINAC2 and go through several steps of acceleration in circular accelerators until filled into the LHC, which ramps up the energy to several TeV for the collision experiment.

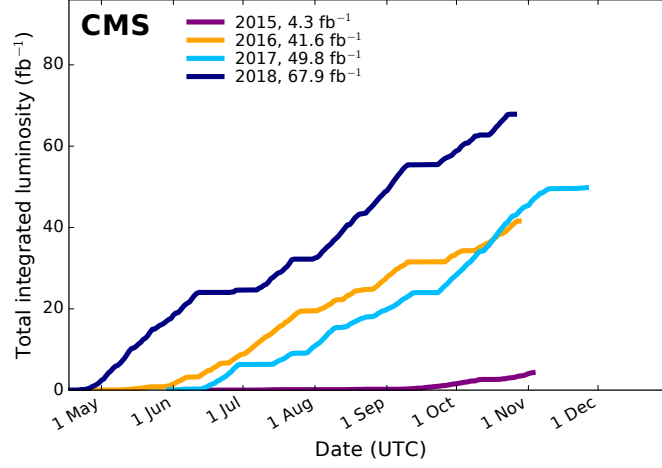


Figure 3.2: Integrated luminosity collected by CMS at $\sqrt{s} = 13$ TeV from 2015 to 2018. The figure is from [100].

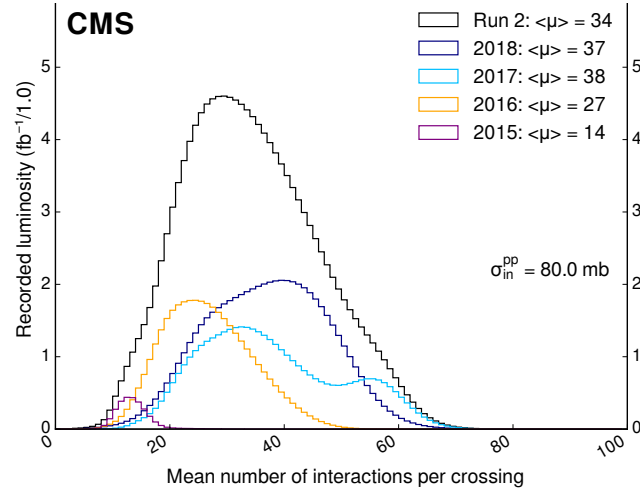


Figure 3.3: Distributions of pileups in proton-proton collisions at the CMS from 2015 to 2018, assuming an inelastic cross section of 80 mb. The figure is from [100].

3.2 The CMS detector

The 15 meters high, 21 meters long Compact Muon Solenoid (CMS) detector is one of the two general-purpose detectors, sitting at one of the interaction points at the LHC [104]. A sketch of the detector is shown in Figure 3.4.

The Compact Muon Solenoid (CMS) detector [104] is located at an interaction point at the LHC (Figure 3.1) for one of the two multipurpose experiments. A sketch of the CMS detector is shown in Figure 3.4. The cylindrical detector is about 15 meters high and 29 meters long and composed of the silicon trackers, preshower detector, electromagnetic calorimeter, hadron calorimeter, superconducting solenoid, muon chambers and forward calorimeter from inner to outer layers. The sub-detectors are discussed in the following sections.

3.2.1 Coordinate system

This thesis uses the conventional coordinate system to describe the CMS detector and the objects in the lab frame, as shown in Figure 3.5. The coordinate system was chosen to reflect the cylindrical symmetry of the detector and the collisions. The origin of the coordinate is in

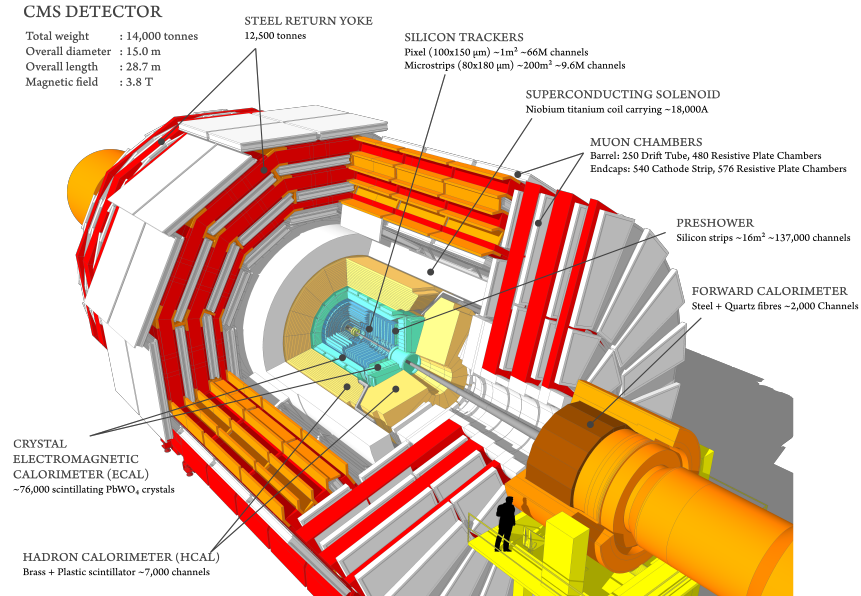


Figure 3.4: The CMS detector [101].

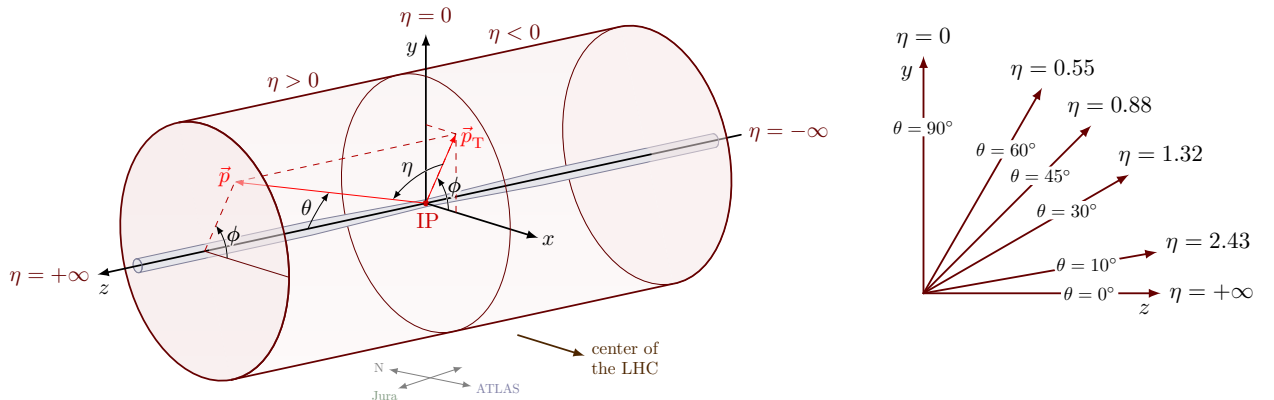


Figure 3.5: **Left:** The coordinate system of CMS and the momentum \vec{p} of an example object from the interaction point (IP), taken from [102]. **Right:** Sketch of pseudorapidity and the correspondence to θ , taken from [103].

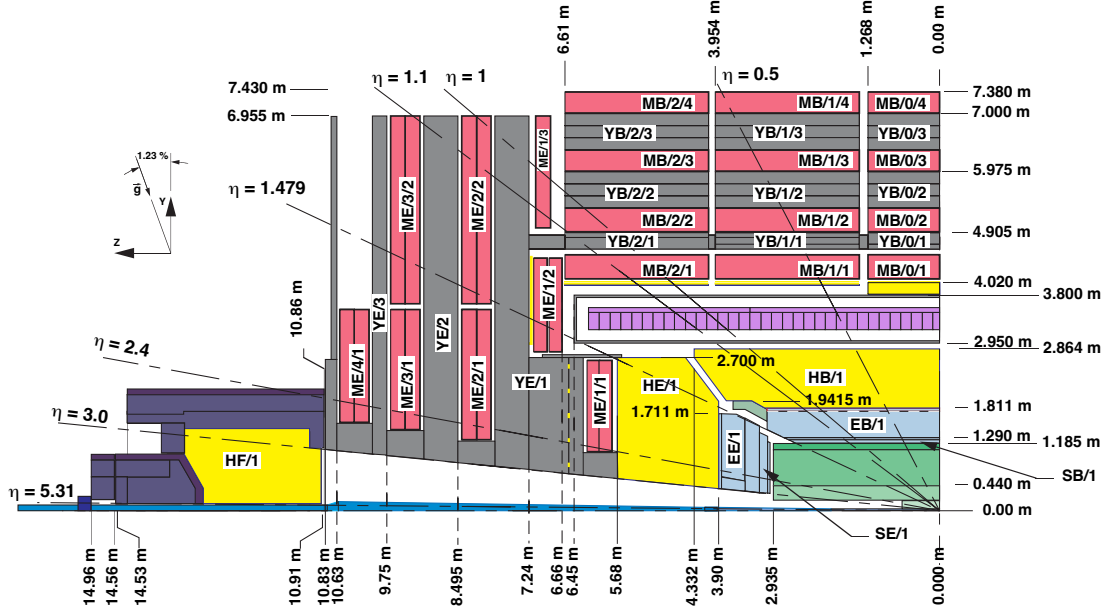


Figure 3.6: Schematic of one quadrant of the CMS detector in the positive zy -plane. Adapted from Ref. [105].

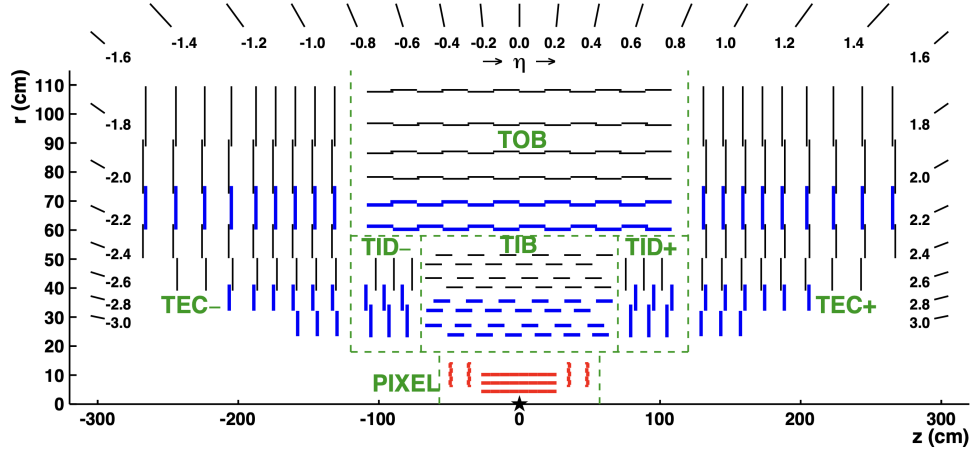


Figure 3.7: Cross section of the the CMS Phase-0 tracking system in the rz -plane, in which each line represents a layer of modules. Only the top half of the tracker is shown, as the detector is symmetric with respect to the z -axis. The figure is taken from from [106].

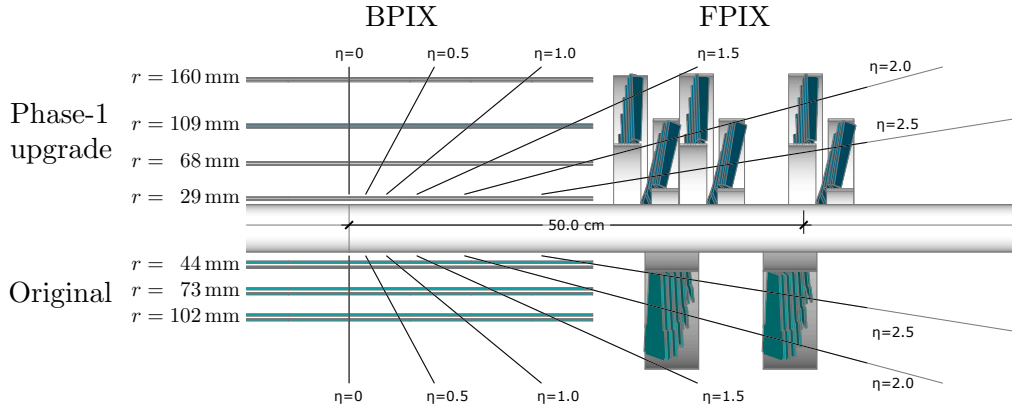


Figure 3.8: Layout of the CMS pixel detector in the rz -plane, comparing the Phase-0 pixel detector (lower half) and the Phase-1 upgrade (upper half). The original beam pipe with a 30 mm radius was replaced by a pipe with 23 mm radius. The figure is taken from [107].

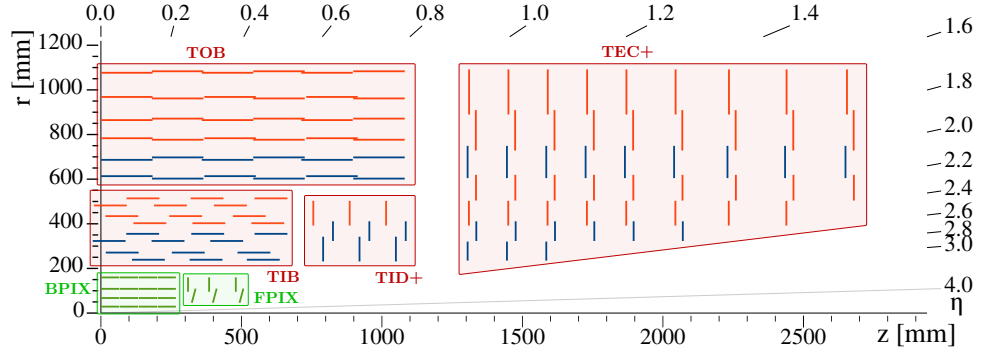


Figure 3.9: Cross section of one quadrant of the CMS Phase-1 tracking system in the rz -plane. The figure is adapted from [108].

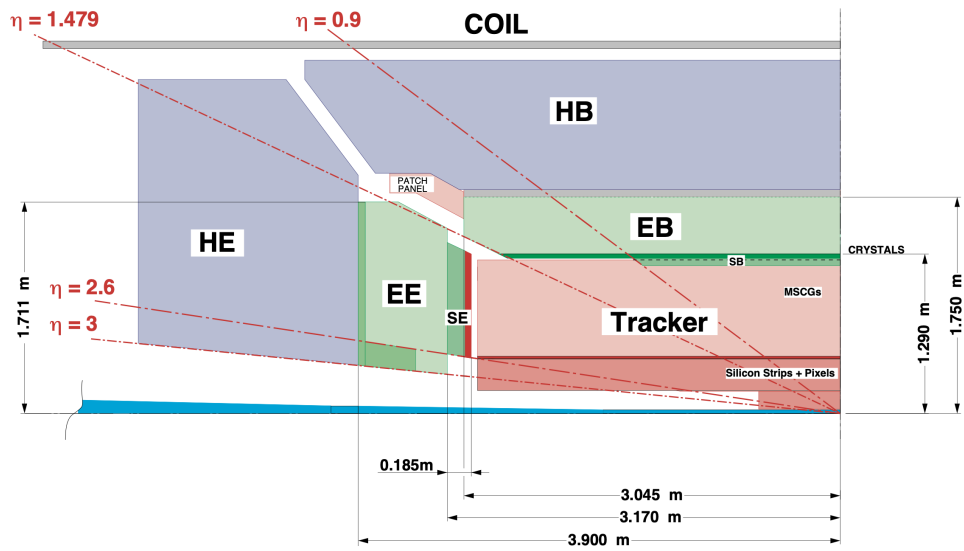


Figure 3.10: Cross section of one quadrant of the CMS ECAL outside of the tracker in the rz -plane. The figure is adapted from [109].

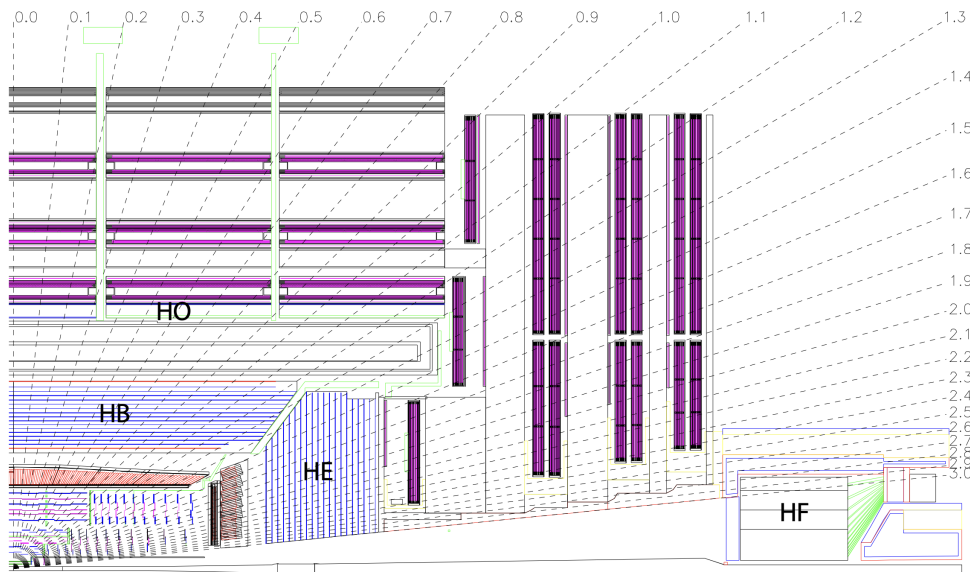


Figure 3.11: Cross section of one quadrant of the CMS HCAL in the rz -plane, consisting of the hadron barrel (HB), endcap (HE), outer (HO) and forward (HF) calorimeters. The figure is taken from [109].

the center of the detector. The z -axis is aligned with the anticlockwise beam direction (viewed from above) and points towards the Jura mountains. The y -axis is orthogonal to the ground and points to the sky. The x -axis is parallel to the ground and points to the center of the LHC. A cylindrical coordinate is defined accordingly, in which the positive direction of the z -axis defines the longitudinal direction, and the xy plane becomes the transverse plane. The azimuthal angle $\phi \in [0, 2\pi)$ is the angle in the transverse plane with respect to the positive direction of the x -axis. The polar angle $\theta \in [0, \pi]$ is the angle with respect to the z -axis.

The coordinate system is used to describe the kinematics of the objects in the collision events. The transverse momentum p_T of a particle is the projection of the momentum \vec{p} on the transverse plane, while the longitudinal momentum p_z is the projection of the momentum onto the z -axis. In high-energy hadron collisions, the collision products tend to be more aligned with the beam axis rather than distributing spherically, and the quantity "pseudorapidity" η is more commonly used than θ

$$\eta := -\frac{1}{2} \ln \left(\tan \left(\frac{\theta}{2} \right) \right). \quad (3.4)$$

The pseudorapidity of a particle becomes

$$\eta = \frac{1}{2} \ln \left(\frac{p + p_z}{p - p_z} \right). \quad (3.5)$$

As shown in Figure 3.5 (right), the η can be used to describe vectors with small θ more conveniently. Furthermore, it is a Lorentz-invariant measure of the opening angles between objects, thus often used in jet clustering algorithms.

Figure 3.6 shows one quadrant of the CMS detector in the positive zy -plane in this coordinate system. Cross sections of the sub-detectors, magnets and the iron flux return yoke are represented by different colors. The coverage of η by the sub-detectors is also sketched in the plot.

3.2.2 Tracking detectors

The tracking system is the innermost part of the CMS detector. It has a silicon pixel tracker close to the interaction point as the inner part, and a silicon microstrip tracker as the outer part, aiming to measure the trajectories of charged particles via the hits in the silicon sensors. As the tracker is immersed in a co-axial 3.8 T magnetic field from the solenoid, the trajectories of charged particles are bent by the magnetic field, and the particle momentum can be reconstructed from the curvatures of the trajectories.

Figure 3.7 shows the layout of the CMS Phase-0 tracker in the rz -plane, which has been used for the data-taking from 2008 to 2016. The pixel tracker has three cylindrical barrel layers (BPix) at radii 44, 73 and 102 mm, and two endcap layers (FPix) on each side at $z = \pm 34.5$ cm and ± 46.5 cm, covering a pseudorapidity range $-2.5 < \eta < 2.5$. The layers are composed of modular detector units. Each module consists of a sensor plate of $100 \times 150 \mu\text{m}^2$ pixel cells, which are bump-bonded to corresponding pixel unit cells in the readout chips. The sensors adopt the n -on- n concept [110], consisting of high-dose n -implants introduced to a n -substrate, the backside being p -doped. In data-taking, these pn -junctions are inverse-biased by a high voltage, and electron-hole pairs are created by the hits from charged particles in the depletion zones and are measured by the readout electronics. The positions of the pixels detecting the hits in different layers can be used for three-dimensional imaging of the charged particle trajectories. This pixel

tracker has 1440 sensor modules and about 66 million readout channels for the pixels. The high resolution pixel detector close to the interaction region allows for the precise reconstruction of impact parameters of the trajectories, and the reconstruction of secondary or displaced vertices from decaying b , τ and potential long-lived new physics particles, which is essential for the measurement of CP violation, top quark physics and new physics search.

At the end of 2016, the CMS pixel tracker was upgraded (Phase-1 upgrade) and replaced by four layers in BPix and 3 layers on each side of FPix (Figure 3.8) due to the accumulated radiation damage to the original detector [107, 111]. Figure 3.9 shows the sketch of the tracker after the upgrade. The upgraded pixel detector is designed to deal with the increased instantaneous luminosity achieved by the LHC upgrade in 2013-2014, and thus the increased data volumes and requirements on the radiation tolerance. The Phase-1 detector has the same pixel size as the Phase-0, consisting of 1856 modules with 124 million readout channels. A higher tracking efficiency and resolution are achieved by the increased number of layers and improved readout electronics. More details about the upgrade are found in [112, 113].

The silicon strip tracker [106] is located outside of the pixel tracker, dedicated to measuring the curvature of the charged-particle trajectories in the magnetic field for the momentum measurement. As shown in Figure 3.7 and 3.9, the strip tracker consists of four parts with different layouts. The Tracker Inner Barrel (TIB) and Disk (TID) cover the region $r < 55$ cm and $|z| < 118$ cm with four layers of modules in the barrel and three disks in the endcap on each side. The Tracker Outer Barrel (TOB) covers the region $55 < r < 110$ cm and $|z| < 118$ cm with 6 layers in the barrel. The Tracker EndCaps (TEC) cover the region $124 < |z| < 282$ cm with 9 disks on each side. The strip tracker consists of 15148 modules in total and 9.3 million strips with a hit resolution of 10-50 μm . Combining the information from the four parts, it achieves the coverage $|\eta| < 2.5$.

3.2.3 The preshower detectors and electromagnetic calorimeter

The preshower detectors and electromagnetic calorimeter (ECAL) are located outside of the tracking system to distinguish and measure the energies of electrons, positrons and photons [109]. Figure 3.10 shows the layout of the preshower detectors (labeled as SB and SE) and the ECAL (labeled as EE and EB) in between the tracker and the hadronic calorimeter. These detectors are optimized to resolve the photons from the $H \rightarrow \gamma\gamma$ process and precisely measure their energies, which are essential for the Higgs boson search and mass reconstruction.

The ECAL consists of a cylindrical barrel (EE) covering the region $|\eta| < 1.479$ and two endcaps (EB) covering the region $1.479 < |\eta| < 3.0$. About 78000 lead tungstate (PbWO_4) crystals are used as scintillators to create electromagnetic showers as a cascade of secondary photons, electrons and positrons from bremsstrahlung and photon conversions, and then convert all their energies into light. The PbWO_4 was chosen as the scintillating material because of its short radiation length, small Molière radius (transverse dimension of the electromagnetic showers) and fast response, allowing for the high spatial and time resolution of showering particles within a compact detector. The crystal front face has the dimension of 22×22 mm to match with the Molière radius of 21.9 mm, corresponding to the granularity $\Delta\eta \times \Delta\phi = 0.0175 \times 0.0175$ in the barrel, and progressively increases to a maximum $\Delta\eta \times \Delta\phi = 0.05 \times 0.05$ in the endcaps. The calorimeter thickness is about 26 radiation lengths at $\eta = 0$, corresponding to a crystal length of 23 cm in the barrel and 22 cm in the endcaps in the presence of the preshower detectors. Photodetectors are placed at the end of the crystals to convert the scintillations into electrical

signals. Considering the magnetic field and radiation environment in CMS, silicon avalanche photodiodes are used in the barrel, and vacuum phototriodes are used in the endcaps. The ECAL achieves the energy resolution from 0.4% to 1% for the energy scale of photons from $H \rightarrow \gamma\gamma$ process.

The preshower endcap detectors (ES) are placed in front of the ECAL in the endcaps, covering the region $1.653 < |\eta| < 2.6$. The detector contains two layers of thin lead converters followed by silicon strip detector planes. The first lead layer is about $2X_0$ in thickness, followed by a layer of about 2 mm pitch silicon strips. A second lead layer with $1X_0$ is placed behind, followed by another layer of silicon strips orthogonal to the first silicon strip layer. The two sampling layers can determine the impact positions and profiles of the electromagnetic showers with fine granularity, which enables the separation between single photons and two close photons from π_0 decays. The preshower detectors compensate for the low resolution of ECAL in the forward region of the endcaps, and especially resolve forward photons in the $H \rightarrow \gamma\gamma$ process. The barrel part (SB) with range $|\eta| < 0.9$ is not present for the Run 2 data used in this thesis, and will be installed in the high-luminosity runs in the future.

3.2.4 The hadronic calorimeter

The hadronic calorimeter (HCAL) [104] is outside of the ECAL layer as the last subdetector inside the solenoid, and extends to the forward region and the region outside of the solenoid. It is designed to measure the energy of hadrons by inducing hadronic showers through nuclear interactions between the incoming hadrons and absorbers. As shown in Figure 3.11, the HCAL has four parts: the hadron barrel (HB), endcaps (HE), outer hadron calorimeter (HO) and forward hadron calorimeters (HF).

The cylindrical HB and HE are located between the ECAL and the solenoid, and cover the pseudorapidity range $|\eta| < 1.3$ and $1.3 < |\eta| < 3$, respectively. They are sampling calorimeters, built from alternative layers of brass absorbers to induce the shower and plastic scintillators, which consist of scintillating tiles with embedded wavelength-shifting fibers, transferring the energy to light and guiding it to hybrid photodiode detectors (HPDs) for readout. The HB is segmented into 36 identical azimuthal (ϕ) wedges, each has flat brass absorber plates parallel to the beam axis and is further segmented into 4 azimuthal sectors. The plastic scintillators are longitudinally divided into 32 sectors in η . The tower segmentation results in a granularity $\Delta\eta \times \Delta\phi = 0.087 \times 0.087$. Each side of the HE is also segmented into 36 azimuthal wedges and 14 longitudinal towers, achieving a granularity $\Delta\eta \times \Delta\phi = 0.17 \times 0.17$.

In the central pseudorapidity region $|\eta| < 1.3$, the stopping power of EB and HB is not sufficient to contain the whole hadron showers. Therefore, the HO is placed in the barrel outside of the solenoid to catch the shower tails penetrating the HB and solenoid. The sizes and positions of the HO segmentation are roughly mapped to the towers of HB in order to achieve the same granularity.

The forward hadron calorimeters (HF) are placed at 11.2 m from the interaction point on both sides and cover the forward region $3 < |\eta| < 5.2$. Each side of the HF consists of a steel absorber made of grooved plates. Radiation-hard quartz fibers are inserted in the grooves, which generate Cherenkov light from charged shower particles for readout. The azimuthal and longitudinal segmentation of HF leads to the approximate granularity $\Delta\eta \times \Delta\phi \sim 0.175 \times 0.175$.

3.2.5 The solenoid magnet & flux-return yoke

The superconducting solenoid magnet [104] is cylindrical outside of the HB with 6 m in diameter and 13 m in length. A 3.8 T magnetic field parallel to the beam axis inside the magnet is realized by the winding currents in the Nb-Ti superconductor. The magnetic flux is returned by the steel return yoke consisting of 5 layers of barrel wheels and 3 layers of disks on each endcap. It is placed outside of the solenoid and in between the layers of muon chambers, as shown in Figure 3.4. The strong and uniform magnetic field from the solenoid magnet bends the trajectories of high-energy charged particles in the transverse plane such that their momenta can be precisely measured from the curvatures.

3.2.6 The muon system

The muon system is outside of the solenoid as the outermost part of the CMS detector. As indicated by the experiment's name, the muon detection function is of central importance to CMS, as high-energy muons are the key signatures of many interesting processes but rarely appear in the QCD background, and thus can be used for both online and offline event selections. The muon system in CMS is optimized for precise and robust muon measurement, responsible for muon identification, momentum measurement and triggering.

The muon system consists of several layers of muon stations interspersed among the flux return plates, including four barrel wheels and four endcap disks on each side, shown as "ME" and "MB" layers in Figure 3.6. In the barrel region with low expected muon rate and low magnetic field outside of the return yoke, drift-tube (DT) chambers are used for muon tracking, covering the pseudorapidity range $|\eta| < 1.2$ with resolution about $200\,\mu\text{m}$. A DT chamber consists of two or three superlayers, each made of four layers of staggered rectangular drift cells with wires either parallel or orthogonal to the beam axis, to measure the muon trajectories in three dimensions. In the endcap regions with high rates and radiation in a large and non-uniform magnetic field, cathode strip chambers (CSCs) are used for muon tracking in the region $0.9 < |\eta| < 2.4$ with resolution about $100\text{--}200\,\mu\text{m}$. The CSCs are trapezoidal and overlapped for a continuous ϕ -coverage; each consists of 6 anode wire planes interleaved among 7 cathode panels. The anode wires are arranged azimuthally to define the radial coordinate, while the cathode panels are milled with radial strips with constant gaps in ϕ , so that the azimuthal (ϕ) coordinates can be obtained by interpolating charges induced on the strips. Both the DT chambers in the barrel and CSCs in the endcaps are accompanied by Resistive Plate Chambers (RPC), which provide a time resolution of an ionizing event shorter than the time between two consecutive bunch crossings (25 ns). Based on the time tagging of the RPCs, dedicated muon triggers are developed, which can assign the triggering muons to the corresponding bunch crossing event.

Combining the information from all the subdetectors, the CMS achieves the momentum resolution 1-6% for muons with $p_T < 100\text{ GeV}$, and less than 10% for muons $p_T < 1\text{ TeV}$. The identification and reconstruction rate is over 95% for muons with p_T above a few GeV. More details about the muon system can be found in [104, 114].

3.2.7 The trigger system

With the 40 MHz proton beam bunch crossing rate at the LHC and high pileup, it is impossible to store and process all the events. Therefore, the trigger system is implemented to apply online

selections on specific signatures, which drastically reduces the event rate for storage and offline processing of the potentially interesting events. The CMS trigger system works in two tiers: the Level-1 (L1) trigger system and the High-Level Trigger (HLT) system.

The L1 trigger system uses hardware-based decisions implemented in Field-Programmable Gate Arrays (FPGAs) for the flexibility of the algorithms, while Application-Specific Integrated Circuits (ASIC) and programmable memory LookUp Tables (LUT) are used when speed, density and radiation resistance are required. Due to the high event rate and stringent limit on the L1 latency, the L1 decisions are only based on the coarsely segmented data from the calorimeters and the muon system. The L1 trigger works in a 4-level architecture: the Trigger Primitive Generators (TPGs) based on energy deposits in calorimeter trigger towers or hit patterns in muons chambers, the Regional Triggers (RTs) combining the TPG information to determine physics objects in limited spatial regions, the Global Calorimeter and Muon Triggers determining the global calorimeter objects (total transverse energy, missing transverse energy, jet counts and H_T as the scalar sum of the transverse energy of all jets above a programmable threshold) or muon objects across the entire experiment, and the Global Triggers deciding to reject or accept an event for further evaluation in HLT. The L1 trigger system reduces the event rate to 100 kHz within a few μs .

The HLT is a software system implemented in a filter farm of commercial processors. Each HLT path takes events accepted by several L1 trigger paths for further processing. With access to the complete read-out data and more relaxed latency limit, the HLT system can reconstruct physics objects with information from all the subdetectors, and perform complex calculations for specific signatures and selections. The HLT system outputs events at about 1 kHz for offline processing. Additional events from the HLT are saved at a few kHz in the Scouting stream without saving the raw data, and the Parking stream saves the raw data directly to the tape with delayed reconstruction. Details of the trigger system can be found in [104, 115]

3.2.8 The scouting stream

The data-scouting strategy at the CMS [116] involves non-standard usages of the trigger, data acquisition and offline computing to overcome the constraints from the limited bandwidth to write data to permanent storage. By storing only the high-level physics objects from HLT in the reduced event contents, the scouting strategy allows for significantly looser HLT thresholds, which enhances the sensitivity to new physics with unconventional signatures at low energy.

The implementation of the data-scouting in CMS started from Run 1, when the particle-flow (PF) algorithm (discussed in Section 3.3.3) was introduced in the online reconstruction at the HLT, and the scouting strategy was designed to keep the low threshold in the PF jet algorithm for the sensitivity in the low-mass region of the dijet resonance search, while satisfying the constraints on the trigger bandwidth. In Run 2, dimuon algorithms were implemented into the scouting stream in addition to the hadronic algorithms, the "Calo" scouting using the calorimeter information, and the "PF" scouting using the online-reconstructed PF candidates. In this thesis, the search for SUEPs (Section 6) uses the data from the PF scouting stream in Run 2. In this PF scouting stream, the information stored per event includes all PF candidates with $p_T > 0.6 \text{ GeV}$, PF jets, leptons and electrons that are reconstructed at the HLT, as well as the missing transverse momentum p_T^{miss} from all the PF candidates, the average energy density per unit area ρ , and the collection of the primary vertices. The event size of the PF scouting stream at 14.8 kB is about 100 times smaller than that stored for standard offline processing (0.87 MB).

3.3 Object Definitions

3.3.1 Vertices

The primary vertices are estimates of the positions of the pp collisions reconstructed from the detector objects. We use the standard CMS Run 2 vertex reconstruction algorithm [117]. The algorithm first selects the tracks compatible with being produced promptly from the primary interaction region by requirements on the transverse impact parameter to the center of the beam spot and the fitting quality of the trajectories. Then these tracks are clustered into groups and assigned to primary vertices (PVs) using a *deterministic annealing* (DA) algorithm [118], the splitting of vertices and association of tracks to PVs analogous to finding the configuration of a statistical mechanics system that minimizes the free energy in a gradually decreasing temperature. After the clustering, the positions of the PVs are further fitted with an *adaptive vertex fitter* [119] to calculate the positions, covariance matrices and the indicators for the success of the fits, such as the number of degrees of freedom. The tracks are softly assigned to the vertices with weights between 0 and 1, and the number of degrees of freedom of a PV is defined as

$$n_{\text{dof}} = -3 + 2 \sum_{i=1}^{\text{\#tracks}} w_i \quad (3.6)$$

with w_i the weight of the i th track associated to this vertex. The selection on n_{dof} is often applied for a good quality of vertex reconstruction and the match to true pp collisions.

3.3.2 Tracks

The charged particles produced from the proton collisions leave hits in the CMS pixel and strip trackers, which are input into the track reconstruction algorithm [117] to be grouped and recover the charged-particle trajectories. The algorithm then reconstructs the charged particles responsible for the hits (tracks) and estimates their momentum and position parameters. In the track finding stage, the collection of trajectories is reconstructed by running the Combinatorial Track Finder (CTF) [120] based on the combinatorial Kalman filter [121–123] and assigning the hits to tracks iteratively (*iterative tracking* algorithm). After getting the full information of the trajectories with all the hits, the trajectories are refitted with a Kalman filter and smoother in the track fitting stage. To reject the fake tracks not associated with charged particles, a selection is applied on the tracks, including the requirements on the number of layers with hits, the χ^2/dof of the fit and the compatibility of their positions with the primary vertices. The selection criteria are labeled as *loose*, *tight* and *high-purity* from the minimum requirements to progressively more stringent ones, where the high-purity tracks are used for most physics analysis.

3.3.3 Particle-flow candidates

The particle-flow (PF) event reconstruction algorithm [124, 125] combines the signals from various parts of the sub-detectors in CMS to reconstruct stable particles in the event and determine their types, momenta and energies. Besides the charged particle tracks from the tracker signals, the algorithm also recognizes energy clusters in the ES, ECAL, HCAL and HF as basic elements in the reconstruction. These elements are linked into blocks and interpreted as particles to be used in the data analyses.

The linking from a charged particle track to energy clusters is realized by extrapolating from

the last measured hit in the tracker to the ES, ECAL and HCAL at the typical longitudinal depth of electron or hadron showers, and the link is assigned if the extrapolated position is within the cluster boundaries. The links between the ES and ECAL clusters are considered if there are overlaps of the clusters in the (η, ϕ) plane. Particle identification algorithms are applied to the linked objects to identify and reconstruct the kinematics of electrons, muons, photons, charged and neutral hadrons as PF candidates, based on their different behaviors in the sub-detectors. Furthermore, the compatibility between the energy of tracks and clusters is checked for cleaning the spurious links, and patterns from detector noise are identified and removed.

Besides the offline PF candidate reconstruction, the PF algorithm is also implemented in the online reconstruction at the HLT. Due to the timing constraints, the HLT uses a simplified PF algorithm compared to the offline version: the identification and reconstruction of electrons and isolated photons are not performed, and the reconstruction of tracks from nuclear interactions in the tracker material is not included.

3.3.4 Jets

Jets are sprays of particles that originate from quarks and gluons produced by particle collisions. Due to the color confinement nature of QCD, the quarks and gluons as colored particles cannot propagate freely through space. These energetic particles first go through PS and split into bunches of collinear and softer partons, and then turn into color-neutral hadrons through the hadronization process. To analyze the primary interaction before PS and hadronization, the sprays of particles are clustered into jets based on their directions and energies, aiming to recover the kinematics of the quarks or gluons generating the jets. The clustering can also be applied to objects reconstructed by detector signals, e.g. tracks or PF candidates, as detector-level proxies of stable particles.

An important property that should be satisfied by the clustering algorithms is infra-red and collinear (IRC) safety. The clustering results must be invariant when an extra soft gluon is radiated (infra-red safe), and be insensitive to the collinear splitting of particles (collinear safe). This requirement ensures the stability of the results under the real-life detector environment, where soft particles are detected less efficiently, and collinear particles can hardly be resolved due to the limited detector resolution.

The anti- k_T algorithm [126] is used in this thesis for the jet clustering. The algorithm sequentially clusters particles or physics objects into jets until all of them are uniquely assigned to jets. The metric of distance between objects i and j in the algorithm is defined as

$$d_{ij} := \min(p_{Ti}^{-2}, p_{Tj}^{-2}) \frac{\Delta R_{ij}^2}{R^2}, \quad (3.7)$$

in which $R_{ij} := \sqrt{(y_i - y_j)^2 + (\phi_i - \phi_j)^2}$ is the distance in the plane of rapidity y and azimuthal angle ϕ . The rapidity of an object is derived from the 4-momentum

$$y := \frac{1}{2} \ln \left(\frac{E + p_z}{E - p_z} \right). \quad (3.8)$$

R is a constant parameter defining the jet radius for clustering. The typical value of R is 0.4 for most common applications, and the jets are often denoted as "AK4 jets". In this thesis, the search for SUEPs uses $R = 1.5$ to tag large-radius jets, denoting the results as "AK15 jets".

The jet clustering starts from identifying the most energetic object in the event as a jet candidate, and then sequentially assign the object with the smallest d_{ij} between the object

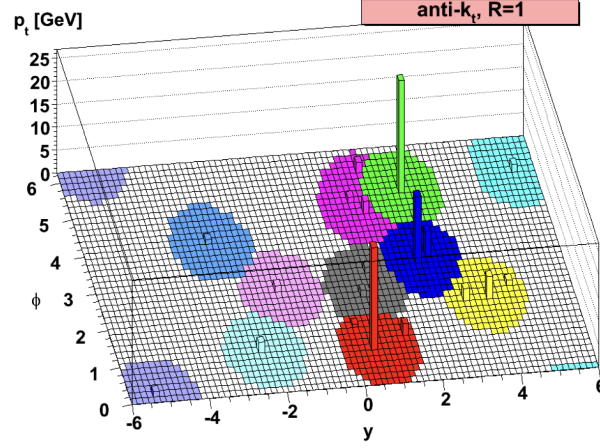


Figure 3.12: Example of an event with the jets clustered by the anti- k_T algorithm with $R = 1$. The p_T distribution of objects assigned to each jet is given concerning their ϕ and y . The jets are marked by various colors for distinction. The example is taken from [126]

and jet axis to the jet, and update the jet axis as the direction of the center-of-mass of all the constituents in the jet. The clustering of a jet stops when the smallest d_{ij} is larger than the distance between the jet axis and the beam direction: $d_{ij} > d_{iB} = p_{Ti}^{-2}$, with i representing the jet object. The objects already assigned to the jet are then removed from the list, and the clustering of the next jet continues from the rest of the objects. An example of the jet clustering results is shown in Figure 3.12.

4 Measurement of event shapes in minimum bias events

This chapter presents a measurement of observables that characterize event shapes in pp collisions, with sensitivity to soft and non-perturbative QCD effects. A machine-learning-based "multifold" algorithm is employed to unfold the high-dimensional distribution of these observables on a per-event basis. The results reveal that the observed events are more isotropic than predicted by various models, underscoring the need for refined theoretical descriptions of pp collisions.

The analysis was designed to advance our understanding of event shapes in minimum-bias events, providing valuable experimental input for nonperturbative modeling and offering potential insights into new effects such as QCD instantons. The author led this analysis in collaboration with a postdoctoral researcher from the UZH group, serving as the primary contact and spearheading the approval process. The results were first presented at the LHCP 2024 conference and have been submitted for publication in the Physics Review D journal.

4.1 Motivation

Shapes of the spatial distribution of final-state particles are basic properties of particle collisions to be understood. In pp collisions, the event shapes are predominantly affected by soft QCD processes, such as UE, which consist of MPI and BR, the initial- and final-state shower and hadronization, the modeling of which highly involves non-perturbative QCD.

The current phenomenological models of UE in general-purpose generators, for instance, PYTHIA and HERWIG, have discrepancies with some recent measurements of particle-pair correlations [127, 128] and the multiplicity of strange hadrons [129, 130] in pp collisions. The observations motivate the inclusion of new non-perturbative QCD effects into the models, such as collective flow, rope hadronization or QCD instanton effects. The measurement of the event shapes in minimum-bias events gives useful experimental inputs to the non-perturbative modeling and indications for the search for new effects.

4.2 Event shapes

To describe the spatial distributions of the detector-level objects or particles in the collision events, the following event shape observables are investigated: the number of tracks (correspondingly, the number of charged particles at the particle level), their invariant mass, the sphericity, thrust, broadening, transverse sphericity, transverse thrust and isotropy from the track momentum. Assume that the tracks associated with a collision have momenta \vec{p}_i , where i is the index for the tracks, \vec{p}_i has three components p_i^x , p_i^y and p_i^z . For each collision, the tracks are first boosted to their center-of-mass frame, and the event shape observables are defined based on the track momenta after boosting:

- **Sphericity:** measures how spherical (i.e. isotropically) the momenta are distributed in an event. First, the tensor S is defined with components

$$S^{\alpha\beta} = \frac{\sum_i |\vec{p}_i|^{r-2} p_i^\alpha p_i^\beta}{\sum_i |\vec{p}_i|^r} \quad (4.1)$$

and $\alpha, \beta = x, y, z$. Then the sphericity is constructed from the two smallest eigenvalues λ_2 and λ_3 : $\mathcal{S} = \frac{3}{2}(\lambda_2 + \lambda_3)$. This measurement uses the sphericity in the $r = 2$ case.

- **Thrust:** measures how highly collimated the momenta in an event are along one particular axis. It is defined as

$$\mathcal{T} = 1 - \max_{\vec{n}} \frac{\sum_i \vec{p}_i \cdot \vec{n}}{\sum_i |\vec{p}_i|} \quad (4.2)$$

where \vec{n} is a unit vector. In the maximization step [131], the thrust axis is defined as the \vec{n} at the maximum.

- **Broadening:** measures the fraction of energy which is perpendicular to the thrust axis. The thrust axis defines the left \mathcal{L} and right \mathcal{R} hemisphere of the event. The left and right broadening is defined as

$$\mathcal{B}_{\mathcal{L}} = \sum_{i \in \mathcal{L}} \frac{|\vec{p}_i \times \vec{n}|}{\sum_i |\vec{p}_i|}, \quad \mathcal{B}_{\mathcal{R}} = \sum_{i \in \mathcal{R}} \frac{|\vec{p}_i \times \vec{n}|}{\sum_i |\vec{p}_i|}. \quad (4.3)$$

The total broadening is defined as $\mathcal{B} = \mathcal{B}_{\mathcal{L}} + \mathcal{B}_{\mathcal{R}}$.

- **Transverse spherocity:** the spherocity in the transverse plane, a measure of how spread out the momentum is across directions in the transverse plane:

$$\mathcal{S}_0 = \frac{\pi^2}{4} \min_{\vec{n}=(n_x, n_y, 0)} \left(\frac{\sum_i |\vec{p}_{Ti} \times \vec{n}|}{\sum_i p_{Ti}} \right)^2 \quad (4.4)$$

- **Transverse thrust:** It is the transverse version of thrust by setting p_i^z to 0 in the thrust definition.
- **Isotropy:** is another measure of how isotropically energy is distributed in an event. It is defined as the Energy Mover's Distance (EMD) [132] from the spatial distribution of the tracks to a uniform radiation pattern [133]. The EMD is a collider-specific version of the "earth mover's distance", which measures the similarity of two distributions based on how much "work" would need to be done to transform one distribution into the other via an optimal transport technique. The detailed definition of this variable is given in [134], which also explores the efficacy of the isotropy to distinguish the isotropic events from the jetty ones.

4.3 Data and simulations

The measurement of event shapes in inclusive pp inelastic scattering requires an unbiased event selection in the high-level trigger, named the "ZeroBias" trigger, which is fired randomly regardless of the detector response of an event, with the trigger rate designed depending on the maximum recording rate of the CMS data acquisition system. An event from a proton bunch crossing can contain multiple proton collisions (pileup), and the products of the additional collisions can be mis-associated with the collision vertex relevant for the measurement. To mitigate the pileup effects, the low-pileup data in 2018 is used for the measurement, in which the average pileup is around 1.

Approximately 4.4 million data events are used for the analysis, corresponding to an integrated luminosity of $64.2 \mu b^{-1}$. The events are collected by the ZeroBias trigger, which selects events for storage and offline processing at a random rate without any requirements on the detector responses.

To remove the detector effects and unfold the particle-level event shape observables from the detector objects, Monte Carlo (MC) simulations of inelastic pp collisions and the detector responses, referred to as MC events, are used to derive the migration function from the particle-level event shape observables to the ones reconstructed from detector objects, which is defined as the conditional probability distribution function of the detector-level observables at given values of their particle-level correspondences. General-purpose event generators PYTHIA [135, 136], HERWIG [137] and EPOS-LHC [138] are employed to generate inelastic pp collisions with minimal selections (minimum bias), and GEANT4 [139–141] is used for simulating the detector responses of the CMS to these pp collisions.

Because of the large non-perturbative QCD contributions, the generators use phenomenological models to describe the minimum bias process in addition to first-principle predictions. The models vary among generators, including the PS, hadronization and kinematics of BR and MPI. The parameters in the phenomenological models are tuned to existing data, and resulting parameter sets are called "tunes". Several generator setups and UE tunes have been studied in the unfolding analysis, as listed in Tab. 4.1. More details about the parameter settings are given in Appendix A.1. The central values of the measurement come from unfolding with the nominal sample from the PYTHIA CP1 tune, in which the UE parameters are tuned to the CMS data. The simulations in "Systematic Uncertainty Samples" are used to estimate the unfolding uncertainty from the modeling of minimum bias events. They are chosen to cover different aspects of the modeling uncertainty. The PYTHIA A3 tune is based on different PDFs, and the UE parameters are tuned independently to the ATLAS data. The HERWIG CH3 sample has different PS and hadronization models from the nominal sample. The EPOS-LHC sample is generated from the hydrodynamic model, different from the PYTHIA and HERWIG models of two-to-two parton scatterings. The "Pseudodata Test Samples" are used to test and validate the unfolding method. The pseudodata samples from alternative simulations are unfolded with the nominal sample, and the results are compared with the particle-level distributions to confirm that the algorithm successfully recovers the truth. The samples listed in "Other checks and validations" are compared to the nominal sample and the data in detector-level distributions to evaluate the impacts of other modeling variations. The simulation with pileup drawn from a Poisson distribution with expectation 1, denoted $\sim \text{Poisson}(1)$ in the table, is used to check the impact of pileup on the observables. Other variations include the color-reconnection (CR) effects, the PDF choices, the strong coupling constant ($\alpha_S(M_Z)$) in PDF and the eigen-variations of the

tune uncertainties.

Table 4.1: The MC simulation of minimum bias events for the unfolding. The pileup in the table represents the number of collisions, in addition to the hardest collision generated. In the case of minimum bias simulation, the pileup equals the total number of collisions minus 1 for each event. For most samples, approximately 2M unweighted events are used.

| Generator | PDF | PDF $\alpha_s(M_z)$ | Pileup |
|--|--------------------------|---------------------|--------------------------|
| Nominal Sample | | | |
| PYTHIA8 (CP1) [142] | NNPDF3.1 QCD LO | 0.130 | 0 |
| Systematic Uncertainty Samples | | | |
| PYTHIA8 (A3) [143] | NNPDF2.3 QCD+QED LO | 0.130 | 0 |
| EPOS-LHC [138] | | | 0 |
| HERWIG 7 (CH3) [144] | NNPDF3.1 QCD NNLO | 0.118 | 0 |
| Pseudodata Test samples | | | |
| PYTHIA8 (CP5) [142] | NNPDF3.1 QCD+LUXQED NNLO | 0.118 | 0 |
| PYTHIA8 (CUETP8M1) [145] | NNPDF3.1 QCD LO | 0.130 | 0 |
| PYTHIA8 (A14) [146] | NNPDF2.3 QCD LO | 0.130 | 0 |
| Other checks and validation | | | |
| PYTHIA8 (CP5) | NNPDF3.1 QCD+LUXQED NNLO | 0.118 | $\sim \text{Poisson}(1)$ |
| PYTHIA8 (CP5) CR tunes [147] | NNPDF3.1 QCD+LUXQED NNLO | 0.118 | 0 |
| PYTHIA8 (CP5) α_s^{FSR} Variations [142] | NNPDF3.1 QCD+LUXQED NNLO | 0.118 | 0 |
| PYTHIA8 (CP2) | NNPDF3.1 QCD LO | 0.130 | 0 |
| PYTHIA8 (CUETP8M1) [145] | NNPDF2.3 QCD LO | 0.130 | 0 |
| PYTHIA8 (CUETP8M2T4) [145] | NNPDF3.0 QCD LO | 0.130 | 0 |
| PYTHIA8 (A14) eigenvariations | NNPDF2.3 QCD LO | 0.130 | 0 |
| PYTHIA8 (A14) CTEQL1 | CTEQL1 | 0.1298 | 0 |
| PYTHIA8 (A14) MSTW2008LO | MMSTW2008LO | 0.13939 | 0 |
| PYTHIA8 (A14) HERAPDF1.5LO | HERAPDF1.5LO | 0.130 | 0 |

4.4 Event selections

Selection criteria are designed to select well-reconstructed inelastic pp collision events by the CMS detector with little contamination from pileups.

4.4.1 Selections on detector-level objects

To minimize the effects of the pileup collisions on the event shape, we select the events with exactly one reconstructed primary vertex for the unfolding analysis.

The selections of primary vertices are $n_{dof} \geq 4$, $\rho \leq 2$ cm and $Z \leq 24$ cm, where n_{dof} is defined in eq. (3.6) and ρ and Z are the transverse and longitudinal distances between the vertex and the nominal beam spot. These criteria select on the quality of the vertex reconstruction and its position within the acceptance of the CMS detector.

Only well-measured tracks with sufficient transverse momentum and within the CMS tracker acceptance are used for the analysis. The selections on tracks are transverse momentum $p_T > 0.5$ GeV and pseudorapidity $|\eta| < 2.4$ for a sufficient track reconstruction efficiency and the "highPurity" tag (Section 4.4 of [117]) to reject fake tracks from poor reconstructions. We also require the association of the tracks to the primary vertex, discarding those loosely associated with the primary vertex or which are assigned to other vertices. Additionally, we put cuts on

the impact parameter significance, defined as the distance of the track impact parameter to the vertex in units of the vertex resolution. In the transverse direction, all tracks must have an impact parameter significance of less than 8, and in the longitudinal direction, they must have an impact parameter significance of less than 13. At least 3 tracks are required in each event.

4.4.2 Selections on particle-level objects

Particle-level selections are applied on the simulated samples to select inelastic collisions with final-state particles in the detector acceptance, in order to minimize the effects of extrapolating to particles which are not measured in the detector.

Charged particles are required to have transverse momentum $p_T > 0.5$ GeV and pseudorapidity $|\eta| < 2.4$, as the particle-level correspondences of tracks. At least three charged particles passing the p_T and η selections are required for each event.

The analysis is performed on the data events passing the detector-level selections and measures the observables in the fiducial phase space defined by the particle-level selections. The simulated events that pass the detector-level selections but fail the particle-level selections are used to estimate reconstruction artifacts, while those passing the particle-level selections but failing the detector-level selections are used to estimate reconstruction inefficiencies.

4.5 Machine-learning based unbinned unfolding algorithm

The event-wise simultaneous unfolding for the observables listed in Sec. 4.2 is realised by iterative weighting with machine-learning(ML)-based binary classifiers, originally proposed in Ref. [148], and then extended by Ref. [149] to take into account the detector inefficiency and artifacts. A few unfolding schemes were proposed, which differ in the input data structure and neural network architectures of the ML models. The "multifold" method is used in this analysis, taking an array of the observables of fixed length for each event and using fully-connected dense networks for the classification. Other schemes are "unfold", which unfolds the observables individually with simpler dense networks as an unbinned version of iterative Bayesian unfolding [150], and "omnifold", which unfolds the events at the particle level with Particle-Flow Networks [151, 152].

4.5.1 Event-wise weighting with a binary classifier

In a typical using scenario of binary classification, a ML-based classifier $s(\vec{x}) : \mathbb{R}^N \rightarrow [0, 1]$ is trained to distinguish two labeled sets A (labeled as 0) and B (labeled as 1) based on their features $\vec{x} \in \mathbb{R}^N$, assuming the probability distribution functions $f_A(\vec{x})$ and $f_B(\vec{x})$.

The two sets are normalized such that the prior probabilities are equal:

$$P(A) = P(B) = \frac{1}{2}. \quad (4.5)$$

An ideal classifier after the training predicts the probability of a given vector \vec{x} belonging to the set B

$$s(\vec{x}) = P(B|\vec{x}), \quad (4.6)$$

which can be further expressed as

$$\begin{aligned}
P(B|\vec{x}) &= \frac{P(B)f_B(\vec{x})}{P(A)f_A(\vec{x}) + P(B)f_B(\vec{x})} \\
&= \frac{f_B(\vec{x})}{f_A(\vec{x}) + f_B(\vec{x})}.
\end{aligned} \tag{4.7}$$

So the likelihood ratio between the two sets can be postulated from the classifier predictions:

$$\frac{\mathcal{L}(B|\vec{x})}{\mathcal{L}(A|\vec{x})} = \frac{f_B(\vec{x})}{f_A(\vec{x})} = \frac{s(\vec{x})}{1 - s(\vec{x})}. \tag{4.8}$$

In practice, the sets A and B are a finite number of independent and identically distributed random data points sampled from $f_A(\vec{x})$ and $f_B(\vec{x})$.

$$A = \{\vec{x}_{Ai} | \vec{x}_{Ai} \sim f_A(\vec{x}), i = 1 \dots p, p \in \mathbb{N}_+\}, \tag{4.9}$$

$$B = \{\vec{x}_{Bj} | \vec{x}_{Bj} \sim f_B(\vec{x}), j = 1 \dots k, k \in \mathbb{N}_+\} \tag{4.10}$$

The distributions $f_A(\vec{x})$ and $f_B(\vec{x})$ can be approximated by frequencies of these random data points in a small range $\Delta\vec{x}$, written as \tilde{f}_A and \tilde{f}_B . With large enough data sets, \tilde{f}_A and \tilde{f}_B converge to their expectations, and estimate f_A , f_B in the small range $\Delta\vec{x}$, respectively.

$$E(\tilde{f}_A) \simeq f_A(\vec{x}), \quad E(\tilde{f}_B) \simeq f_B(\vec{x}). \tag{4.11}$$

One can use the classifier to evaluate the set A , and derive the weights from the predictions

$$w(\vec{x}_{Ai}) := \frac{s(\vec{x}_{Ai})}{1 - s(\vec{x}_{Ai})} = \frac{f_B(\vec{x}_{Ai})}{f_A(\vec{x}_{Ai})}, \tag{4.12}$$

so that the weighted distribution of set A has the expectation close to $f_B(\vec{x})$ within the range $\Delta\vec{x}$:

$$E(\tilde{f}_{Aw}(\vec{x})) = E(w(\vec{x}_{Ai})\tilde{f}_A(\vec{x})) \simeq f_B(\vec{x}) \tag{4.13}$$

Therefore, the set A weighted by the binary classifier has a probability distribution function similar to the set B .

In this analysis, dense neural networks (DNNs) with 3 layers of 100 neurons are used for classification. The ensemble method is used to suppress the fluctuations induced by the randomly initialized network parameters, where multiple DNNs are initialized differently, trained to classify the same sets, and their evaluation results are averaged out. 4 ensembles of DNNs are used for each step of weighting.

4.5.2 Unfolding with iterative weighting

In the experiment, stable particles are generated in a collision event as the final state. Functions of the kinematics of these final-state particles can be used to define particle-level variables, e.g. number of charged particles, sphericity of the charged particles, etc., represented as a vector $\vec{t} \in \mathbb{R}^M$ with each element t^α from a particle-level variable. The final-state particles react with the detector and leave signals, which are used to reconstruct detector-level objects. Functions of the detector-level objects can be used to define detector-level variables, e.g. number of tracks, sphericity of tracks, etc., also represented as a vector $\vec{m} \in \mathbb{R}^N$, in which each element m^β represents a detector-level variable. The dimensions of particle-level variables M and detector-

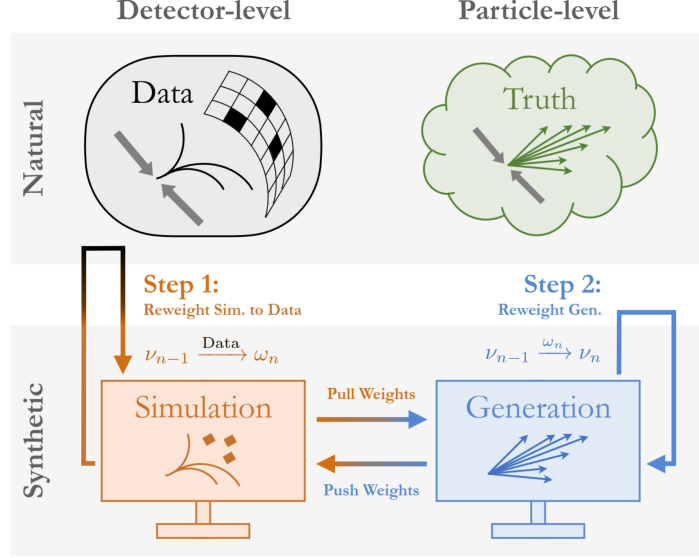


Figure 4.1: Sketch of the unfolding algorithm,

level variables N are not necessarily equal, though many unfolding analyses have the same dimension for the two levels.

The unfolding algorithm aims to estimate the particle-level distribution of the data $f_{\text{Data}}(\vec{t})$ from the detector-level distribution $g_{\text{Data}}(\vec{m})$, which is approximated by the detector-level variables in the data events. MC events are generated from theoretical predictions implemented in the event generators, and then detector simulations are applied to these events. Both the particle-level and detector-level variables of the MC events are used by the unfolding algorithm to extract the information of the detector response. In the following, we assume the MC distribution of the particle-level variables as $f_{\text{MC}}(\vec{t})$, the distribution of the detector-level variables as $g_{\text{MC}}(\vec{m})$, and the joint distribution as $F_{\text{MC}}(\vec{t}, \vec{m})$. They are related by

$$f_{\text{MC}}(\vec{t}) = \int F_{\text{MC}}(\vec{t}, \vec{m}) d^N m, \quad g_{\text{MC}}(\vec{m}) = \int F_{\text{MC}}(\vec{t}, \vec{m}) d^M t. \quad (4.14)$$

The detector response is modeled by the conditional probability distribution of the detector-level variables at given values of the particle-level variables $g_{\text{D|P}}(\vec{m}|\vec{t}) := \frac{F_{\text{MC}}(\vec{t}, \vec{m})}{f_{\text{MC}}(\vec{t})}$, named as the "migration function". The unfolding is based on the assumption that the migration function is properly modeled, and the data has the same migration function as the MC. The effects of mismodeling the migration function are discussed in Sec. 4.6, and considered as a systematic uncertainty.

As illustrated in Fig. 4.1, the unfolding consists of iterative weighting with the ML-based binary classifiers, and each iteration has two steps. In the following, we use $\omega^{(n)}(\vec{m})$ and $\nu^{(n)}(\vec{t})$ to denote the weights in the two steps in iteration n as function of detector-level variables and particle-level variables, respectively. $\omega^{(0)} = \nu^{(0)} = 1$ at the beginning. $f_{\text{MC}}^{(n)}(\vec{t})$ denotes the unfolded particle-level distribution given by the n -th iteration by the weighting procedure $f_{\text{MC}}^{(n)}(\vec{t}) := \nu^{(n)}(\vec{t}) f_{\text{MC}}(\vec{t})$. $g_{\text{MC}}^{(n)}(\vec{m})$ denotes the corresponding detector-level distribution in the n -th iteration $g_{\text{MC}}^{(n)}(\vec{m}) := \int f_{\text{MC}}^{(n)}(\vec{t}) g_{\text{D|P}}(\vec{m}|\vec{t}) d^M t$. $F_{\text{MC}}^{(n)}(\vec{t}, \vec{m})$ denotes the joint distribution after the weight in the n -th iteration $F_{\text{MC}}^{(n)}(\vec{t}, \vec{m}) := \nu^{(n)}(\vec{t}) F_{\text{MC}}(\vec{t}, \vec{m})$. Note that the migration function corresponding to $F_{\text{MC}}^{(n)}(\vec{t}, \vec{m})$ does not change along the iterations, because the weighting function $\nu^{(n)}(\vec{t})$ is independent of the detector-level \vec{m} .

At the first step of the n -th iteration, a classifier is trained to distinguish data and the MC

events from their detector-level variables, and then evaluate and weight the MC events to data distributions at the detector-level with the weighting function

$$\omega^{(n)}(\vec{m}) = \frac{g_{\text{Data}}(\vec{m})}{g_{\text{MC}}^{(n-1)}(\vec{m})}. \quad (4.15)$$

Applying the weights on the MC events leads to the joint distribution

$$\omega^{(n)}(\vec{m}) F_{\text{MC}}^{(n-1)}(\vec{t}, \vec{m}). \quad (4.16)$$

At the second step, another classifier is trained and weights the original MC events to the weighted MC events from the first step based on their particle-level variables. The weighting function is

$$\nu^{(n)}(\vec{t}) = \frac{\int \omega^{(n)}(\vec{m}) F_{\text{MC}}^{(n-1)}(\vec{t}, \vec{m}) d^N m}{f_{\text{MC}}(\vec{t})}. \quad (4.17)$$

Applying the weights on the MC events results in the particle-level distribution

$$\begin{aligned} \nu^{(n)}(\vec{t}) f_{\text{MC}}(\vec{t}) &= \int \omega^{(n)}(\vec{m}) F_{\text{MC}}^{(n-1)}(\vec{t}, \vec{m}) d^N m \\ &= \int g_{\text{Data}}(\vec{m}) \frac{F_{\text{MC}}^{(n-1)}(\vec{t}, \vec{m})}{g_{\text{MC}}^{(n-1)}(\vec{m})} d^N m, \end{aligned} \quad (4.18)$$

which estimates the data conditional probability distribution of particle-level variables \vec{t} under certain detector-level variables \vec{m} as the one given by the weighted MC events from the last iteration $\frac{F_{\text{MC}}^{(n-1)}(\vec{t}, \vec{m})}{g_{\text{MC}}^{(n-1)}(\vec{m})}$. It is a continuous version of the Iterative Bayesian Unfolding method [153], which is commonly used in experimental physics.

4.5.3 Additional steps for detector inefficiency and artifacts

The simulated events passing the particle-level selections can fail the detector-level selections with a small probability due to the detector inefficiency in reconstructing particles and associating them with the primary vertices. These events enter into the phase space of the particle-level variables in the measurement, so that the unfolding algorithm needs to take them into account by assigning weights depending on the particle-level variables in a way similar to that for the events passing the detector-level selections. On the other hand, the events passing the detector-level selections can also fail the particle-level selections because of detector artifacts, for example, recognizing detector noise as a particle. The unfolding algorithm needs to properly subtract the contribution of detector artifacts by weighting the corresponding simulated events at the detector level, since the particle-level variables are not available. The derivation of the weights is discussed below.

In the following, the MC events are divided into three exclusive sets:

- MC_{ineff} : the detector inefficiency part with the particle-level probability distribution function $f_{\text{ineff}}(\vec{t})$ with portion p_{ineff} ;
- MC_{arti} : the detector artifact part with the detector-level probability distribution $g_{\text{arti}}(\vec{m})$ with portion p_{arti} ;
- MC_{rest} : the rest of events passing both truth- and detector-level selections with particle-level distribution $f_{\text{rest}}(\vec{t})$, detector-level distribution $g_{\text{rest}}(\vec{m})$ and joint distribution $F_{\text{rest}}(\vec{t}, \vec{m})$

with portion $1 - p_{\text{ineff}} - p_{\text{arti}}$.

The MC particle-level distribution is contributed by the detector inefficiency part and the part passing both levels of selection

$$f_{\text{MC}}(\vec{t}) = \frac{p_{\text{ineff}} f_{\text{ineff}}(\vec{t}) + (1 - p_{\text{ineff}} - p_{\text{arti}}) f_{\text{rest}}(\vec{t})}{1 - p_{\text{arti}}}. \quad (4.19)$$

The MC detector-level distribution is contributed by the detector artifact part and the part passing both levels of selection

$$g_{\text{MC}}(\vec{m}) = \frac{p_{\text{arti}} g_{\text{arti}}(\vec{m}) + (1 - p_{\text{ineff}} - p_{\text{arti}}) g_{\text{rest}}(\vec{m})}{1 - p_{\text{ineff}}}. \quad (4.20)$$

The iterative weighting discussed in Section 4.5.2 are extended with extra steps in each iteration n .

Step 1: It is identical to step 1 in Section 4.5.2. The MC events passing the detector-level selections are weighted to data with a function of detector-level variables

$$\omega^{(n)}(\vec{m}) := \frac{g_{\text{Data}}(\vec{m})}{g_{\text{MC}}^{(n-1)}(\vec{m})}. \quad (4.21)$$

Step 1b: The detector inefficiency part cannot be weighted at the detector level in the last step. In this step, the particle-level weighting for MC_{ineff} is derived by training a classifier to weight the original MC_{rest} events to the weighted MC_{rest} from the last step at the particle level. The MC_{ineff} events are then evaluated by this classifier and assigned with weights

$$\nu_{\text{ineff}}^{1b(n)}(\vec{t}) := \frac{\int \omega^{(n)}(\vec{m}) F_{\text{rest}}^{(n-1)}(\vec{t}, \vec{m}) d^N m}{f_{\text{rest}}(\vec{t})}, \quad (4.22)$$

so that the weighting function $\omega^{(n)}(\vec{m})$ is effectively pulled back to the particle level to be applicable for MC_{ineff} .

Step 2: Similar to the step 2 in Section 4.5.2, a classifier is trained at the particle level to weight the original MC events passing the particle-level selections ($MC_{\text{rest}} + MC_{\text{ineff}}$) to the MC_{rest} weighted with $\omega^{(n)}(\vec{m})$ and MC_{ineff} weighted with $\nu_{\text{ineff}}^{1b(n)}(\vec{t})$.

$$\nu^{(n)}(\vec{t}) := \frac{(1 - p_{\text{ineff}} - p_{\text{arti}}) \int \omega^{(n)}(\vec{m}) F_{\text{rest}}^{(n-1)}(\vec{t}, \vec{m}) d^N m + p_{\text{ineff}} \nu_{\text{ineff}}^{1b(n)}(\vec{t}) f_{\text{ineff}}(\vec{t})}{(1 - p_{\text{arti}}) f_{\text{MC}}(\vec{t})}. \quad (4.23)$$

Step 2b: The detector artifact part cannot be weighted at the particle level in step 2. In this step, the detector-level weighting for MC_{arti} is derived by training a classifier with the detector-level variables to weight the original MC_{rest} events to the MC_{rest} events weighted by $\nu^{(n)}(\vec{t})$ at the last step. Then the MC_{arti} are evaluated and assigned weights

$$\omega^{2b(n)}(\vec{m}) := \frac{\int \nu^{(n)}(\vec{t}) F_{\text{rest}}^{(n-1)}(\vec{t}, \vec{m}) d^M t}{g_{\text{rest}}(\vec{m})}. \quad (4.24)$$

so that the weighting function $\nu^{(n)}(\vec{t})$ is effectively pushed to the detector level to be applicable for MC_{arti} .

4.6 Uncertainty estimation

The following section explains the uncertainty sources contributing to the unfolding results and the methods to estimate the uncertainties and the covariance in an unbinned way.

4.6.1 Sources of uncertainty

Several sources of uncertainty can contribute during the unfolding process and lead to results deviated from the truth.

The statistical uncertainty comes from fluctuations in the data events. The unfolding algorithm uses the distributions of data events to approximate the detector-level probability distribution functions of the target observables. The statistical uncertainty propagates to the parameters in the neural networks during the training, then further affects the weights when the neural networks are used to evaluate the MC events.

The systematic uncertainty comes from the following sources:

- **Monte Carlo Modeling:** The mismodeling of the physics process in the MC simulation causes the differences in the kinematics of the MC and data events at the particle-level. These differences affect the unfolding results in several ways.
 - In binned unfolding methods, the migration of events from particle-level bins to detector-level bins are described by conditional probabilities

$$P_{\text{MC}}(\vec{m} < \vec{m}' < \vec{m} + \Delta\vec{m} | \vec{t} < \vec{t}' < \vec{t} + \Delta\vec{t}) = \frac{\iint d^M t' d^N m' f_{\text{MC}}(\vec{t}') g_{\text{D|P}}(\vec{m}' | \vec{t}')}{\int d^M t'' f_{\text{MC}}(\vec{t}'')}, \quad (4.25)$$

which depend on the particle-level distribution $f_{\text{MC}}(\vec{t})$ given finite bin widths $\Delta\vec{t}$ and $\Delta\vec{m}$. Therefore, the unfolding results are altered by the mismodeled $f_{\text{MC}}(\vec{t})$ via the migration probabilities.

In unbinned unfolding, such an effect is largely mitigated as the bin sizes are infinitesimal in the ideal case, where the distributions are estimated by an infinite number of MC events. In reality, the equivalent bin sizes in unbinned unfolding are limited by the finite number of MC events, and this effect of mismodeled $f_{\text{MC}}(\vec{t})$ varies the migration function.

- The detector-level observables, as functions of the reconstructed objects, inherently depend on the momenta, positions and identities of the final-state particles at the particle level. The mismodeling of the particle-level event kinematics changes the detector response $g_{\text{D|P}}(\vec{m} | \vec{t})$ at certain values of particle-level variables. For example, the mismodeled identities of the final state particles can alter the average track reconstruction efficiency, because different particle species have distinct radiation patterns in the detector and reconstruction efficiencies. As a result, the mismodeling in particle identities changes the number of tracks and event shapes at the detector level, even though the particle-level distributions are not affected. As another example, the detector response varies across rapidity of the particles to be measured, and thus the mismodeled rapidity distribution in the simulation changes the migration probabilities of the observables of interest, even though the particle-level transverse event shape variables are not affected by the mismodeling. This uncertainty from mismodeling the underlying physics can be partially mitigated by the simultaneous unfolding

of multiple variables, in which the migration function deviations in low dimensions can be unrolled by the particle-level deviations in high-dimensional variables.

- In regularized unfolding, the results are generally biased towards the chosen nominal MC distributions, as the regularization penalizes the algorithm for overfitting to the data. In the iterative unfolding, the estimated unfolding result equals the particle-level distribution of the nominal MC at the beginning, and then iteratively moves away and approaches the particle-level data distribution, expected to converge to an unbiased estimation in the limit of an infinite number of iterations. The regularization of iterative unfolding is realized by stopping at a finite number of iterations, and the bias from the nominal MC needs to be considered as a source of systematic uncertainty.
- **Track reconstruction efficiency:** The track reconstruction efficiency in the simulation is not exactly the same as that in the experimental data. The deviation is assessed by measuring the branching ratio of D_0 decays [154, 155]

$$R = \frac{N(D_0 \rightarrow K\pi\pi\pi)\epsilon_{K\pi}}{N(D_0 \rightarrow K\pi)\epsilon_{K\pi\pi\pi}}, \quad (4.26)$$

where the D_0 mesons are selected by the $D_* \rightarrow D_0\pi$ decays for high purity, the $N(D_0 \rightarrow K\pi)$ and $N(D_0 \rightarrow K\pi\pi\pi)$ are the yields in data, and the $\epsilon_{K\pi}$ and $\epsilon_{K\pi\pi\pi}$ come from track reconstruction in simulation. The ratio between the charged pion reconstruction efficiency in data and simulation can be estimated by

$$\epsilon_{\text{rel}} = \sqrt{\frac{R}{R_{\text{PDG}}}}, \quad (4.27)$$

in which the R_{PDG} is the branching ratio given by the Particle Data Group (PDG) [156]. The uncertainty of the track reconstruction efficiency is estimated by the uncertainty on ϵ_{rel} .

- **Isolation of individual collisions:** In the low-pileup data, the actual number of collisions in each bunch crossing fluctuates according to a Poisson distribution with expectation around 1. While the nominal simulations consider one inelastic pp collision and its detector response for each event, without considering the effect of additional collisions in the same bunch crossing. In the analysis, this effect is controlled by requiring exactly one well-reconstructed primary vertex in each event, filtering out those with zero or multiple collisions. The remaining effect after the selection is evaluated by comparing the simulation with exactly one collision per event and that with several collisions sampled from the Poisson(1) distribution in the distributions of the observables of interest. The difference is found to be negligible.
- **Statistical uncertainty of the simulations:** Since the MC samples are used by the unfolding method to estimate the migration probabilities between particle-level and detector-level variables, the statistical uncertainty of the MC samples propagates into the migration function and leads to a systematic uncertainty in the unfolding results.

4.6.2 Construction of uncertainty templates

Considering the potential correlations among the uncertainty sources, toy experiments are used for the uncertainty estimation. Each toy experiment is an unfolding procedure with weighted MC or weighted data, and the weights deviated from one describe the combined impacts of all the relevant uncertainties on the input MC or data events. The unfolding results in the toy experiments deviating from those with nominal samples, which reflect the effects of the uncertainty sources propagated through the unfolding procedure.

To derive the weighted MC or data in the toy experiments, the uncertainty templates are constructed as sets of weights on nominal MC events or data events for individual uncertainty sources. These templates represent the alternative data or MC samples that lead to results deviating from the central values of the measurement because of the considered uncertainty sources. The weights for toy experiments are products of those in templates after being modulated by nuisance parameters as random numbers.

The uncertainty templates of the statistical uncertainty of data are constructed as the data events with weights sampled from the Poisson(1) distribution to mimic the data that would otherwise be recorded by the detector. Similarly, the templates of the statistical uncertainty of the simulations are constructed as nominal MC events with weights sampled from the Poisson(1) distribution.

Concerning the other uncertainties, the deviation from the nominal MC sample to each uncertainty template is expected to be modulated continuously by nuisance parameters to enable the uncertainty and covariance estimation from toy experiments, in which the unfolding is performed with MC samples corresponding to randomly sampled nuisance parameters to consider the effects of systematic deviations on the unfolding results. To realize this uncertainty estimation procedure, the uncertainty templates are constructed as the nominal MC sample with alternative weights using ML-based unbinned weighting as introduced in Section 4.5.1.

Weight templates of the Monte Carlo modeling uncertainty

The MC modeling uncertainty is estimated with the modeling differences between the nominal MC sample from PYTHIA 8 CP1 (PYTHIA 8 A3) and the alternative MC samples from PYTHIA 8 A3 tune (PYTHIA 8 CP1 tune), EPOS-LHC and HERWIG 7 CH3 tune in the unfolding for data (pseudodata from alternative MC samples). The differences between the samples are mixed effects of discrepancies in detector response and particle-level distributions, contributing to the second and third sources of the MC modeling uncertainty, respectively. The uncertainty templates are extracted by weighting at different levels between the nominal and alternative samples and disentangling the two effects into separate templates.

Weight templates of the particle-level distribution uncertainty

The templates of the deviations in particle-level distributions are derived by training a classifier to distinguish the nominal MC sample and an alternative sample with the input features as particle-level variables and using the classification scores to weight the nominal MC events to the alternative sample at the particle level for the events passing the particle-level selections. Assuming the particle-level distribution $f_{\text{Nom}}(\vec{t})$ and $f_{\text{Alt}}(\vec{t})$ for the nominal and alternative samples, respectively, according to the eq. 4.19 when $MC = \text{Nom}$ and $MC = \text{Alt}$, the nominal MC

events passing the particle-level selections ($Nom_{\text{rest}} + Nom_{\text{ineff}}$) are weighted with

$$\nu_{N \rightarrow A}(\vec{t}) := \frac{f_{\text{Alt}}(\vec{t})}{f_{\text{Nom}}(\vec{t})}. \quad (4.28)$$

The weights $\nu_{N \rightarrow A}(\vec{t})$ are only dependent on particle-level variables but not affected by the detector response. Therefore, the weighted events have the same particle-level distribution as the alternative sample, but the original detector response of the nominal sample.

The detector artifact events Nom_{arti} cannot be weighted at the particle level, so that an additional step is required to derive their weights from a function of detector-level variables. A classifier is trained with the detector-level variables to distinguish original Nom_{rest} events without weighting and the Nom_{rest} events with weights $\nu_{N \rightarrow A}(\vec{t})$, giving the weighting function

$$\omega_{N \rightarrow A}(\vec{m}) := \frac{\int \nu_{N \rightarrow A}(\vec{t}) F_{\text{rest}}^{\text{Nom}}(\vec{t}, \vec{m}) d^M t}{g_{\text{rest}}^{\text{Nom}}(\vec{m})}, \quad (4.29)$$

which effectively pushes the $\nu_{N \rightarrow A}(\vec{t})$ to the detector level. The Nom_{arti} are evaluated by the trained classifier and assigned weights $\omega_{N \rightarrow A}(\vec{m})$.

The closure of weighting the PYTHIA 8 A3 sample to the EPOS-LHC sample for the event sphericity and thrust is shown in Figure 4.2. The figure shows that the weighted sample can reproduce the particle-level distributions of the original sample. Validation of the weighting of other samples and for other observables is shown in Appendix A.2.1.

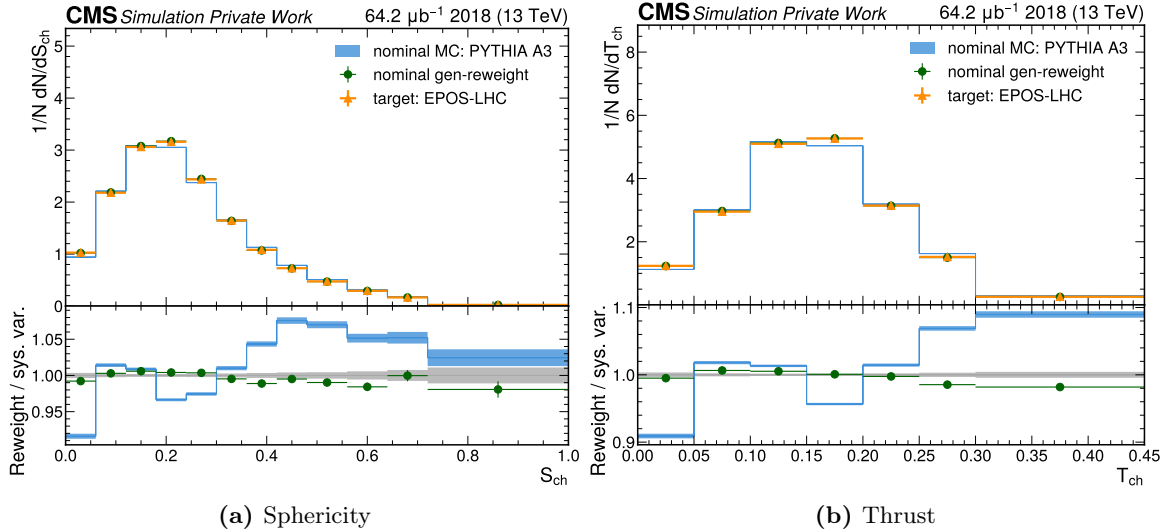


Figure 4.2: The event shape distributions of the EPOS-LHC sample as the target for the particle-level weighting, the PYTHIA 8 A3 tune (nominal MC) and the results after weighting. The ratio panels in the bottom show the ratio of the original nominal sample (step histogram) and the weighted nominal sample (green points) to the target alternative distribution.

Weight templates of the detector response uncertainty

The nominal MC sample weighted with these templates should keep the particle-level distribution of the nominal sample but have the detector response of the alternative samples. The weight templates are derived in two steps.

In the first step, the alternative sample is weighted to the nominal sample with the same procedure to derive the templates of the particle-level distribution uncertainty, but the samples

are in reverse. The alternative MC events passing the particle-level selections ($Alt_{\text{rest}} + Alt_{\text{ineff}}$) are weighted with

$$\nu_{A \rightarrow N}(\vec{t}) := \frac{f_{\text{Nom}}(\vec{t})}{f_{\text{Alt}}(\vec{t})}. \quad (4.30)$$

The detector artifact events of the alternative sample Alt_{arti} are weighted with

$$\omega_{A \rightarrow N}(\vec{m}) := \frac{\int \nu_{A \rightarrow N}(\vec{t}) F_{\text{rest}}^{\text{Alt}}(\vec{t}, \vec{m}) d^M t}{g_{\text{rest}}^{\text{Alt}}(\vec{m})}. \quad (4.31)$$

This results in a weighted alternative sample with the same particle-level distribution as the nominal sample and keeping the detector response of the alternative sample.

In the second step, another classifier is trained on both the truth and detector level variables to weight the nominal sample to the weighted alternative sample from the previous step at both levels, the weighting function as

$$w_{N \rightarrow A}(\vec{t}, \vec{m}) := \frac{p_{\text{ineff}}^{\text{Alt}} \delta(\vec{m}) \nu_{A \rightarrow N}(\vec{t}) f_{\text{ineff}}^{\text{Alt}}(\vec{t}) + p_{\text{arti}}^{\text{Alt}} \delta(\vec{t}) \omega_{A \rightarrow N}(\vec{m}) g_{\text{arti}}^{\text{Alt}}(\vec{m}) + (1 - p_{\text{ineff}}^{\text{Alt}} - p_{\text{arti}}^{\text{Alt}}) \nu_{A \rightarrow N}(\vec{t}) F_{\text{rest}}^{\text{Alt}}(\vec{t}, \vec{m})}{p_{\text{ineff}}^{\text{Nom}} \delta(\vec{m}) f_{\text{ineff}}^{\text{Nom}}(\vec{t}) + p_{\text{arti}}^{\text{Nom}} \delta(\vec{t}) g_{\text{arti}}^{\text{Nom}}(\vec{m}) + (1 - p_{\text{ineff}}^{\text{Alt}} - p_{\text{arti}}^{\text{Alt}}) F_{\text{rest}}^{\text{Nom}}(\vec{t}, \vec{m})} \quad (4.32)$$

in which 0 is assigned to \vec{m} for the detector inefficiency parts and \vec{t} for the detector artifact parts. The weighted nominal sample from this step has the same joint distribution of truth and detector-level variables as the weighted alternative sample from the last step. Therefore, the weight template shifts the detector response of the nominal sample towards that of the alternative sample and keeps the particle-level distribution of the nominal sample.

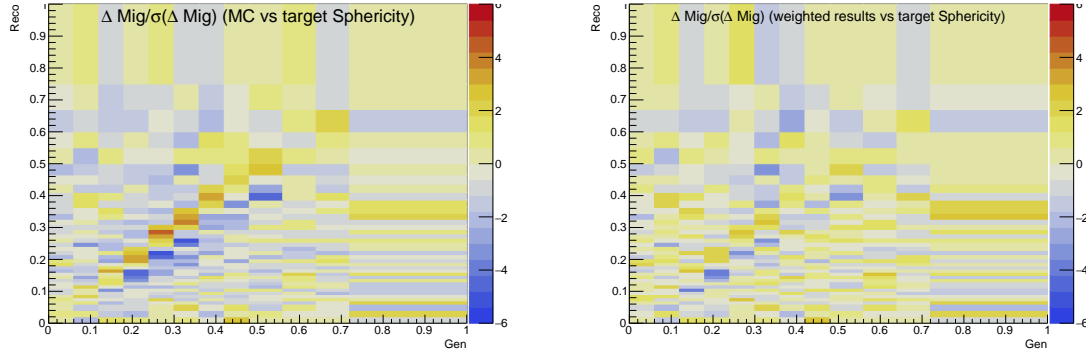
The closure of the weighting in the second step is shown in Figure 4.3, in which the nominal detector response comes from the PYTHIA 8 A3 sample and the alternative detector response comes from the EPOS-LHC sample. On the left, the initial differences between the migration matrices (detector responses projected onto the sphericity observable) of the two samples are shown. On the right, the differences between the weighted sample and the target are shown. After weighting, the remaining differences shown in the right plot are small fluctuations, as compared to the initial larger, structured differences visible in the left plot.

Further plots validating the weighting for other observables and other samples are given in Appendix A.2.2.

Weight template of the track reconstruction efficiency uncertainty

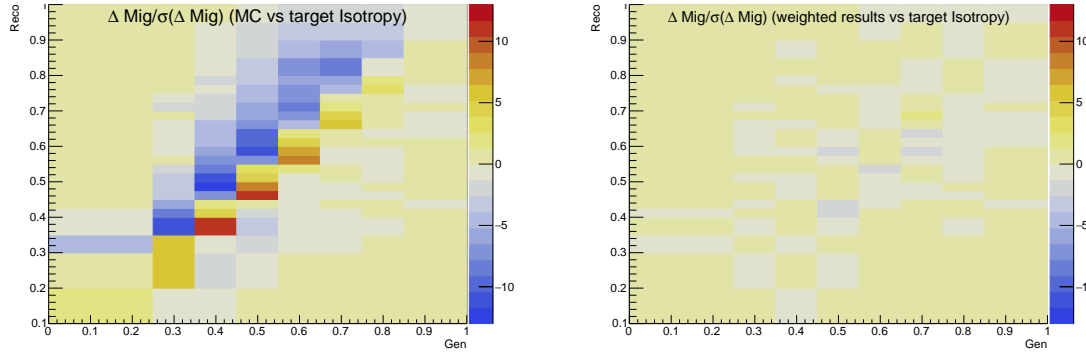
According to the track reconstruction efficiency evaluated in Ref. [154], the alternative sample is constructed by randomly dropping 2.1% of the tracks with $p_T < 20$ GeV and 1% of those with $p_T > 20$ GeV, which keeps the same particle-level variables of the nominal events and alters the detector response. The weighting procedure is similar to the second step of constructing the templates of the detector response uncertainty. A classifier is trained at both the truth and detector levels and weights the nominal sample to the alternative sample. The procedure results in a weighted sample with the same joint distribution at both levels as the alternative sample, indicating the unchanged particle-level distribution and alternate detector response.

The effect of the weighting on the detector response as a function of isotropy is shown in Figure 4.4. The differences in the migration matrix from randomly dropping tracks are clear before



(a) Sphericity migration matrix difference between the nominal MC and the target (b) Sphericity migration matrix difference between weighted results and the target

Figure 4.3: The closure to the target EPOS-LHC sample for the migration matrix after weighting the nominal PYTHIA 8 A3 sample to the weighted EPOS-LHC. The differences in the plot are shown in units of the statistical uncertainty of the difference between the two projected matrices.



(a) Isotropy migration matrix difference between the nominal MC and the target (b) Isotropy migration matrix difference between the weighted result and the target

Figure 4.4: The closure of migration matrices between the nominal MC/weighted results and the target PYTHIA 8 A3 sample with randomly dropped tracks.

weighting. After weighting, the differences in the migration matrix are only small fluctuations.

Further validations on other observables are shown in Appendix A.2.3

4.6.3 Uncertainty estimation with toy experiments

Toy experiments are employed for the uncertainty estimation, where the impacts of the uncertainty sources on the unfolding result are evaluated by the MC method. Due to the usage of neural networks in the unfolding, the uncertainty of the input MC and data samples can have nonlinear or correlated effects on the unfolding result, and the analytical error propagation is practically not applicable. Instead, these effects can be assessed properly by toy experiments on the alternative samples randomly deviated from the nominal samples under the considered uncertainties.

As introduced in Section 4.6.2, each toy experiment for the data statistical uncertainty includes assigning weights to data events independently sampled from the Poisson(1) distribution and unfolding the weighted data with the nominal MC sample. The statistical uncertainty of unfolding can be estimated by the weight variations on the nominal MC events from the ac-

cumulation of toy experiments. The standard deviation of the weights on each event is used to estimate the statistical uncertainty, and the covariance of the weights between each pair of events is used to estimate the covariance of the statistical uncertainty in the event-wise unfolding. When representing the unfolding results as histograms, the weight fluctuations among toy experiments result in variations of bin values in the histograms, so that the statistical uncertainty and the covariance are estimated as the standard deviations of values in each bin and the covariance between each pair of bins.

The systematic uncertainties are represented by the weight variations on the nominal MC events and the corresponding weight variations on the unfolding results. The nominal MC sample has a uniform weight of 1 for all the events, while the MC events in toy experiments have alternative weights, the weight on each event coming from the multiplication of weights given by different sources. Similar to the toy experiments for the statistical uncertainty from limited data events, the weights sampled from the Poisson(1) distribution are assigned to the nominal MC events to account for the impact of MC statistical fluctuations.

Concerning the uncertainty from MC modeling and track reconstruction uncertainty, the deviation from each source i is represented by the corresponding weight template w_i as explained by Section 4.6.2 and associated with a nuisance parameter $\theta_i \in \mathbb{R}$. To guarantee a non-negative probability distribution under systematic deviations, we assume a log-normal distribution of the weights in toy experiments. In each toy experiment, the MC weights for source i are $w_i^{\theta_i}$ with θ_i sampled from the normal distribution $\mathcal{N}(0,1)$. $\theta_i = 0$ represents the case of no systematic deviation, and uniform weights 1 are assigned. $\theta_i = 1$ as one standard deviation shift of the nuisance parameter represents the case of deviating to the systematic template, and weights w_i are assigned.

In each toy experiment for the systematic uncertainty, the final weight for an MC event is

$$w_{\text{tot}} = w_{\text{MCstat}} \prod_i w_i^{\theta_i}, \quad (4.33)$$

in which $w_{\text{MCstat}} \sim \text{Poisson}(1)$ is sampled independently for each event, and $\theta_i \sim \mathcal{N}(0,1)$ is sampled independently for each source i but invariant among all the MC events. The weighted MC sample is used to unfold the data, and the standard deviations and covariance between event (bin) pairs among the toy experiment results give the estimates of the unfolding systematic uncertainty and covariance event-wise (in histograms). Note that the weights w_{tot} can change the total normalization of the MC sample, although the systematic deviations only distort the shape of the probability distribution function and the detector response. To remove the undesired effects of shifted normalization, the unfolded events are normalized to a fixed value.

4.6.4 Tests and validations

This section describes a few important tests to validate the functionality of the unbinned unfolding algorithm.

In the closure test, alternative MC samples that are not used for constructing the nominal and systematic templates are used as proxies of real data and called "pseudodata". The unfolding is performed on the pseudodata, and the unfolding results can be compared with the known truth. This allows us to test if the unfolding can recover the truth, and to assess the performance when the true physics model in data is different from that considered in the nominal MC.

In the bias and coverage test, toy experiments are performed for the pseudodata unfolding,

which tests the variation of the unfolding results under uncertainties. The bias of unfolding represents the systematic deviations of the unfolding results from the truth, and the coverage represents the frequencies of the unfolding results being compatible with the truth. The bias and coverage are tested by comparing the accumulated results of toy experiments to the truth.

In the bottom-line test, the goodness-of-fit between the unfolded result and the nominal MC truth is compared to that between the data and the nominal MC at the detector level. This test ensures that the unfolding does not introduce additional discriminating power between the data and nominal MC.

Closure tests with pseudodata

The closure tests are performed for pseudodata sets from PYTHIA 8 CUETP8M1 tune (NNPDF3.1LO), CP5 tune and A14 tune with distinct PDF and parameterization of UE, shower and hadronization. The nominal MC sample for this test is generated by PYTHIA 8 A3 tune, and the systematic templates are derived as described by Section 4.6.2, among which the templates of MC modeling uncertainties are extracted from PYTHIA 8 CP1, HERWIG 7 CH3 and EPOS-LHC samples. The nominal MC sample and its systematic templates are input into the algorithm individually to unfold the pseudodata, aiming to recover the particle-level distributions within the uncertainty variations. The test results of unfolding PYTHIA 8 CUETP8M1 pseudodata are shown as follows. The results for the other pseudodata sets are given in Appendix A.3.

The unfolding lasts for 4 iterations, and the evolution of the performance is shown in Figure 4.5 and 4.6 as the particle-level and detector-level closure, respectively. The closure is measured by either χ^2 as the sum of squared differences weighted by the squared statistical uncertainties among all the bins, or the kolmogorov-smirnov distance (ks-distance) as the largest deviation between the empirical cumulative distribution functions of the two samples. To compare the closure evolution of different variables, the goodness-of-fit in the figures is displayed as the χ^2 or ks-distance relative to their initial values before unfolding (iteration 0). Therefore, the goodness-of-fit equals 1 in iteration 0 and decreases during the unfolding, as the agreement between the unfolded results and the pseudodata improves compared to the pre-unfolding agreement.

As shown in Figure 4.5 and 4.6, the goodness-of-fit stabilizes after 2 iterations at both truth and detector levels with some residual fluctuations in higher iterations. In the following, the weights after 2 iterations are considered as the unfolding result, and more detailed plots are shown comparing the unfolded distributions to the nominal MC and the pseudodata at both truth and detector levels. Figure 4.7 compares the unfolded distributions of charged particle sphericity and transverse sphericity, as well as the systematic variations, to the nominal MC and the pseudodata distributions at the particle level. Figure 4.8 compares the "refolded" distributions as the unfolding results at the detector level to the corresponding nominal MC and pseudodata distributions. Figure 4.9 and 4.10 show the comparisons in two-dimensional distributions of sphericity and transverse sphericity in slices of charged particle multiplicity. The comparisons in distributions of other variables are given in Appendix A.3. All these figures demonstrate that the unfolding reproduces the pseudodata distributions at both the truth and detector levels, and the discrepancies are covered by the considered uncertainties. The unfolding result and its systematic variations are much more compatible with the pseudodata than the nominal MC sample.

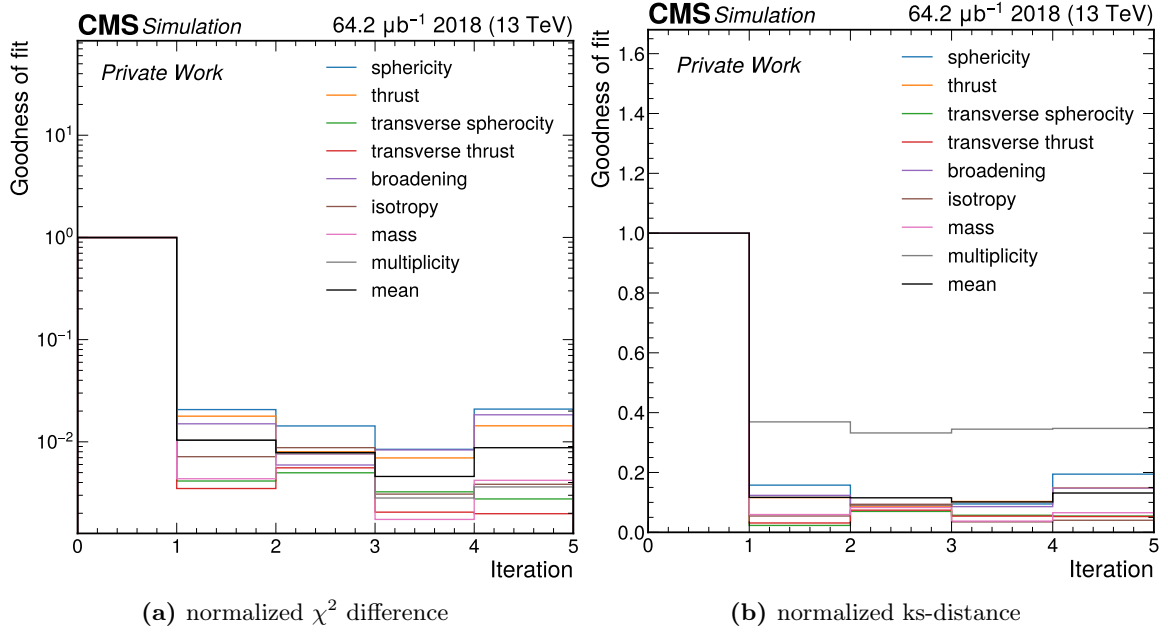


Figure 4.5: The unfolding closure to the pseudodata from PYTHIA 8 CUETP8M1 (NNPDF3.1LO) tune for the particle-level observables. The χ^2 includes only the pseudodata statistical uncertainty. The χ^2 and ks-distance values for each observable are normalized to those of the initial nominal MC and pseudodata samples before unfolding.

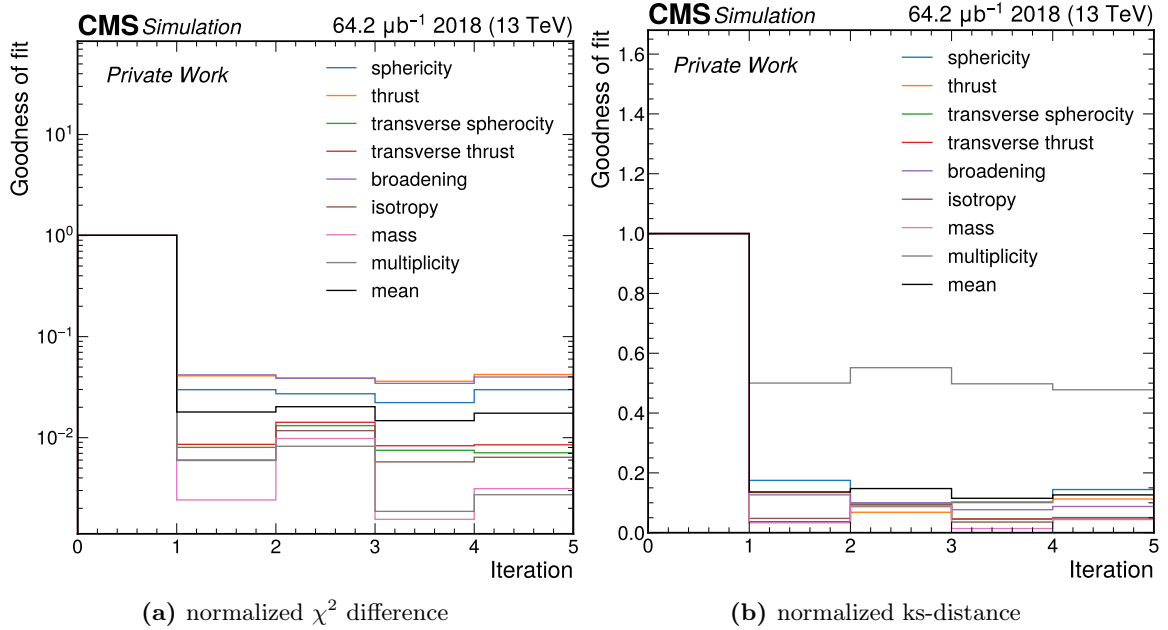


Figure 4.6: The unfolding closure to the pseudodata from PYTHIA 8 CUETP8M1 (NNPDF3.1LO) tune for the detector-level observables. The uncertainty in the χ^2 calculation includes only the pseudodata statistical uncertainty. The χ^2 and ks-distance values for each observable are normalized to those of the initial nominal MC and pseudodata samples before unfolding.

Bias and coverage tests

The unfolding for the pseudodata from PYTHIA 8 CUETP8M1 (NNPDF3.1LO) is used to test the bias of the unfolded results compared to the truth and to validate the coverage of the unfolding uncertainties. The tests use a frequentist framework, where multiple toy experiments of unfolding

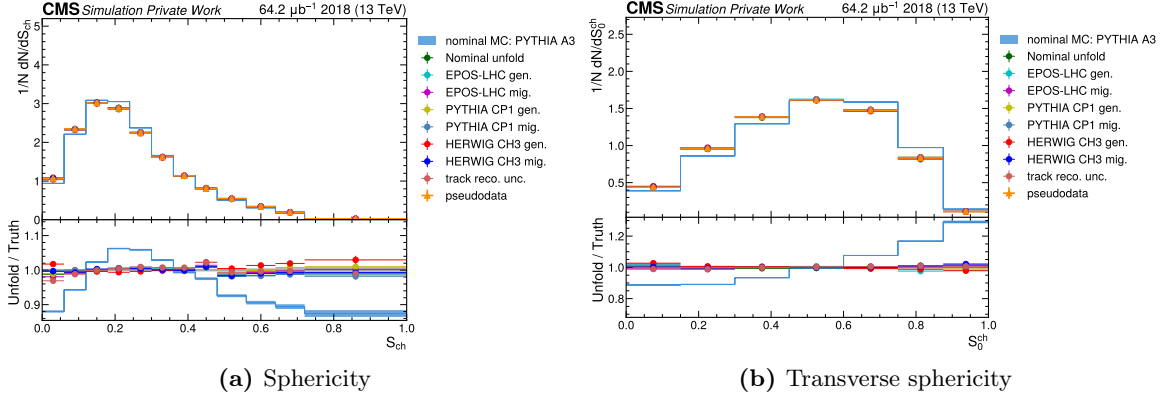


Figure 4.7: The event shape distributions of the PYTHIA 8 CUETP8M1 (NNPDF3.1LO) tune (pseudodata), the A3 tune (nominal MC) and the unfolding results at the particle level. The unfolding results using the systematic deviations of the MC are also shown in the plots.

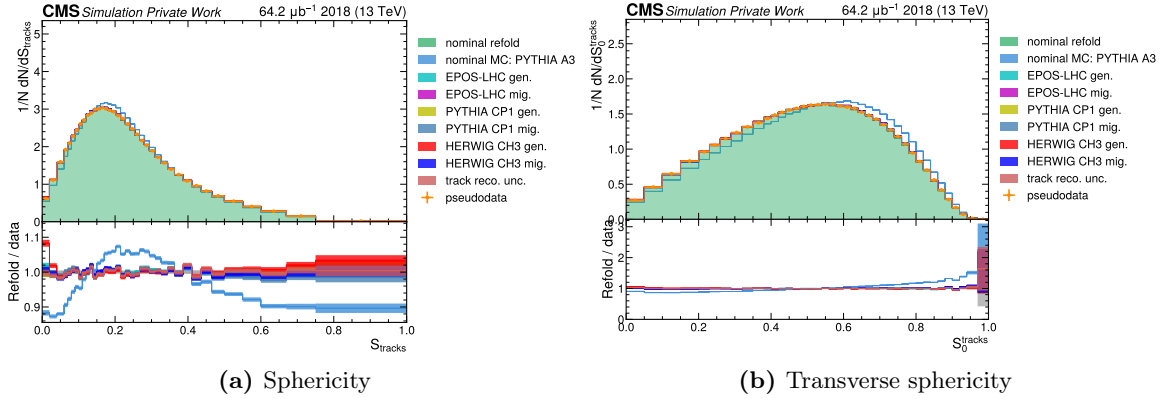
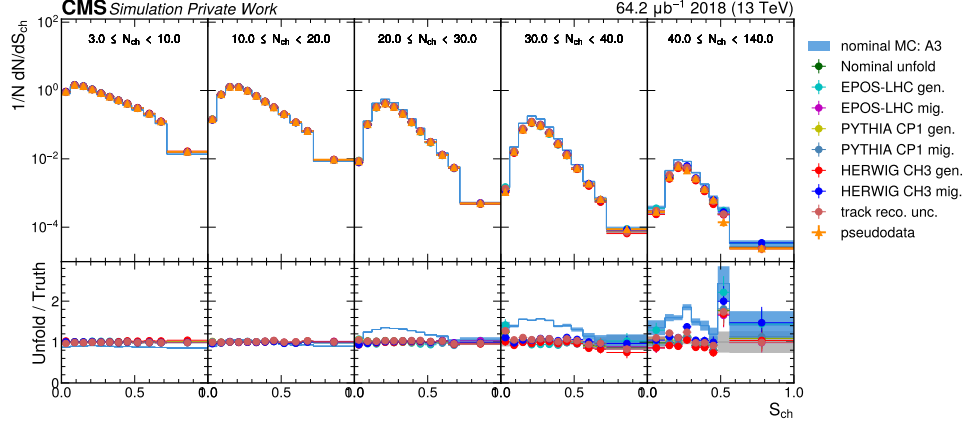


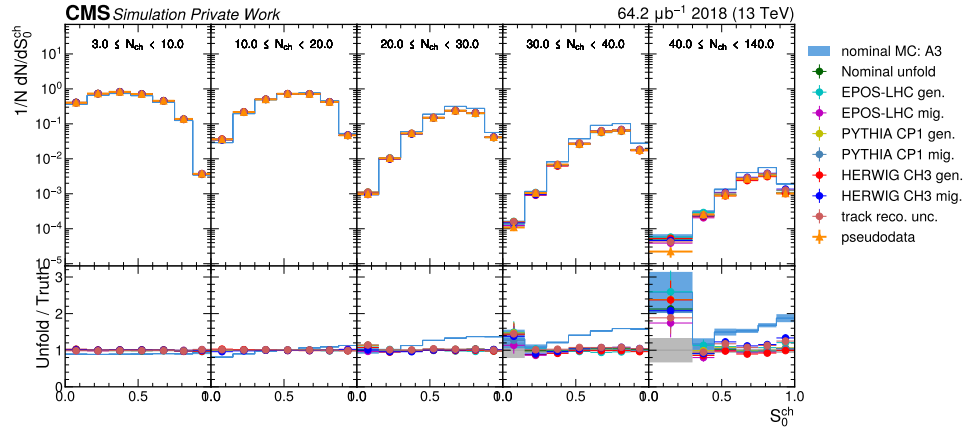
Figure 4.8: The event shape distributions of the PYTHIA 8 CUETP8M1 (NNPDF3.1LO) tune (pseudodata), the A3 tune (nominal MC) and the unfolding results at the detector level. The refolded results using the systematic deviations of the MC are also shown in the plots.

are performed for alternative models and observations that are randomly deviated from the original ones due to the considered uncertainty. The results of toy experiments indicate the accumulative behaviours of the unfolded distributions and their estimated confidence intervals, when the measurement is repeated a lot of times and fluctuates because of the uncertainties. The discrepancies between the central values in the toy experiments and the truth indicate the unfolding bias, and the frequencies of the unfolded results covering the truth are used to estimate the unfolding coverage.

In a toy experiment, the nuisance parameter θ_i for each source of the MC modeling uncertainty or track reconstruction efficiency uncertainty is drawn from the normal distribution $\mathcal{N}(0,1)$ independently, and the nominal MC sample is weighted as eq. 4.33, in which w_{MCstat} is drawn from Poisson(1) distribution independently for each event. The pseudodata events are also weighted with $w_{stat} \sim \text{Poisson}(1)$ independently for each event, to mimic an alternative sample due to the statistical fluctuations in the experiment. The central values of the toy experiment result are given by unfolding the toy pseudodata with the toy nominal MC. To estimate the uncertainty of a toy experiment in the same manner as Section 4.6.3, multiple toy experiments would be necessary, in which additional weights on nominal MC and pseudodata representing the uncertainty deviations are multiplied on top of the weights for deriving the central values of unfolding and unfold procedures are repeated. In practice, running toy experiments for uncer-



(a) Sphericity



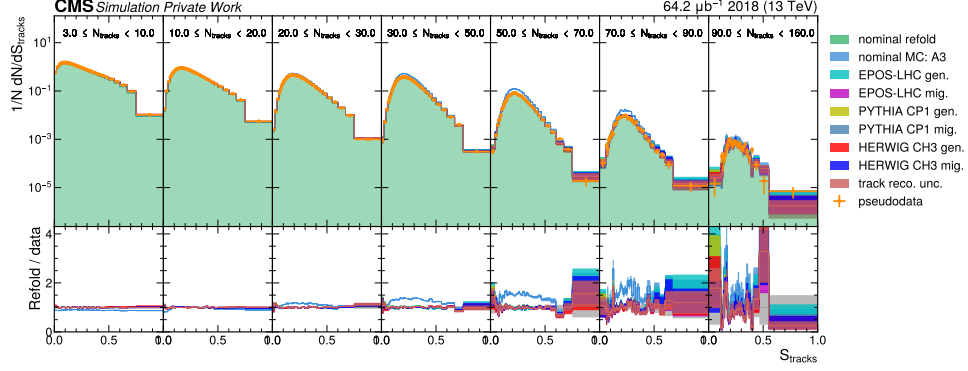
(b) Transverse sphericity

Figure 4.9: The event shape distributions of the PYTHIA 8 CUETP8M1 (NNPDF3.1LO) tune (pseudodata), the A3 tune (nominal MC) and the unfolding results at the particle level in slices of charged particle multiplicity. The unfolding results using the systematic deviations of the MC are also shown in the plots.

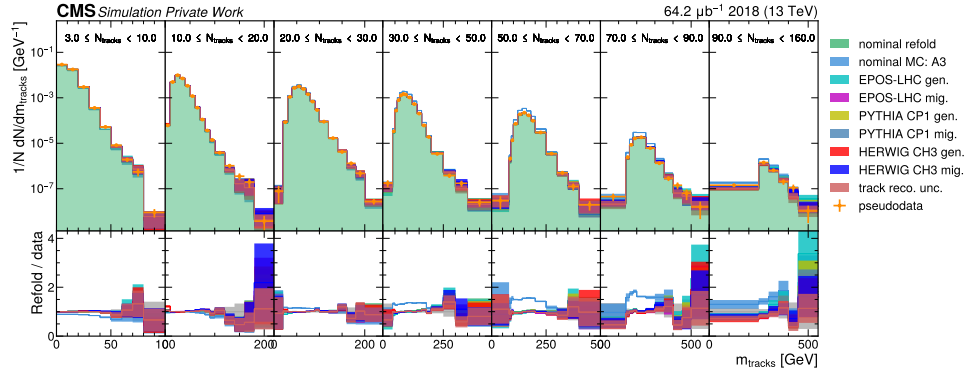
tainty estimation in each toy experiment of this test is computationally expensive. Therefore, we use the uncertainties and covariance from data unfolding (Section 4.7) as proxies of those in the toy experiments.

The ensemble of unfolded results in the toy experiments is compared to the pseudodata truth in histograms of the variables of interest. The bias is estimated as the ratio of the central values to the truth, as shown in Figure 4.11. The variations among the toy experiments are represented as box plots, and the unfolding uncertainties in the corresponding bins are overlaid on the plots. The average bias is found to be smaller than the variations of the toy experiments, as well as the unfolding uncertainty.

The coverage is estimated as the frequency of finding the toy experiment results compatible with the pseudodata truth, considering the unfolding uncertainty. As shown in Figure 4.12, the coverage is given in each bin, and the error bars as the 68.2% confidence interval of the estimations. The coverage across bins is compared to the dashed line at 68.2%. In ideal cases of unbiased unfolding, the expected values of toy experiment results would be equal to the pseudodata truth, and the truth would be in the range of 68.2% confidence interval for 68.2% of the experiments. An under-coverage would indicate the bias in the unfolding. The figure indicates that the coverage in most of the bins of these observables is compatible with 68.2%, given the statistical uncertainties from 50 toys.



(a) Sphericity



(b) Mass of the tracks

Figure 4.10: The event shape distributions of the PYTHIA 8 CUETP8M1 (NNPDF3.1LO) tune (pseudodata), the A3 tune (nominal MC) and the unfolding results at the reconstructed level in slices of track multiplicity. The refolded results using the systematic deviations of the MC are also shown in the plots.

The plots of testing the bias and coverage in distributions of other observables are given in Appendix A.4.

Bottom-line test

With the input from detector-level objects and detector responses to particle-level particles, the unfolded results cannot be more discriminative to the models than the detector-level data. Therefore, the differences between the unfolded result and the nominal MC sample at the particle level are expected to be no larger than those between the data and the nominal MC sample at the detector level. A violation of this relation happens when the unfolding algorithm attributes the data-MC discrepancies from statistical fluctuations to the differences in the particle-level models, and thus overfits the given samples, which is an undesired effect and should be avoided by regularization. In the bottom-line test, the χ^2 is used as the goodness-of-fit to measure the differences between two distributions. As shown in Figure 4.13, the test aims to ensure that the χ^2 between the unfolded result and the nominal MC at the particle level is less than or equal to the χ^2 between the (pseudo)data and the nominal MC at the detector level (labeled as "smeared MC"), which is visualized by the ratios between the values χ^2 at the two levels in the 4 iterations of unfolding the pseudodata from the sample PYTHIA 8 CUETP8M1 (NNPDF3.1LO). In the calculation of χ^2 between the unfolded result and the nominal MC at the particle level, the uncertainty in the χ^2 definition includes the bias from the particle-level modeling and the MC statistical uncertainty in the unfolded result, and the statistical uncertainty of the nominal

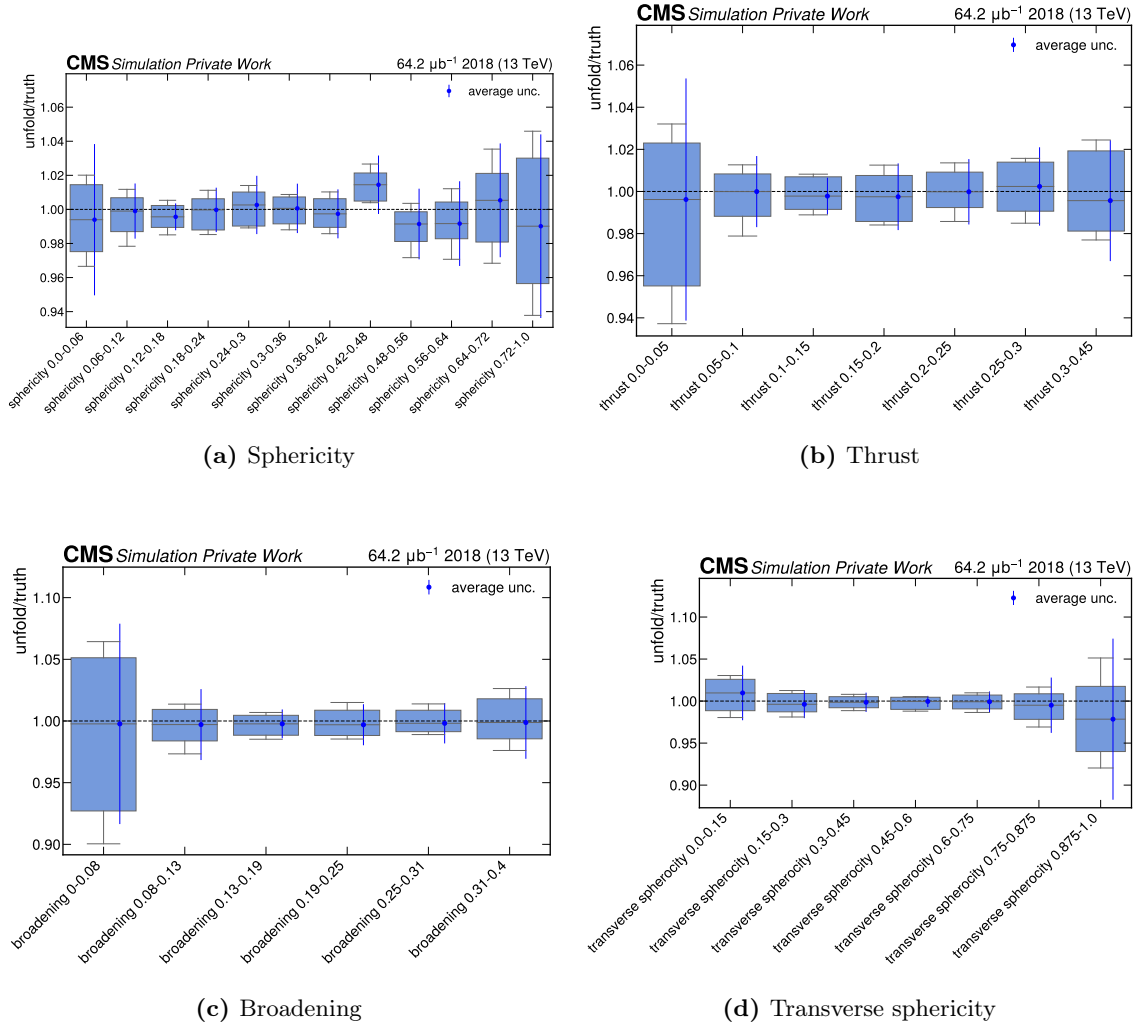


Figure 4.11: The bias of the unfolded results after 2 iterations, when unfolding the pseudodata from PYTHIA 8 CUETP8M1 (NNPDF3.1LO) tune with the nominal MC from the A3 tune. The boxplot shows the 25%, 50% and 75% quantiles of the ratio of the unfolded result over the corresponding pseudodata; the whiskers show the standard deviation. The uncertainty of the unfolding result in each bin is overlaid so that the size of the bias can be compared directly to the measurement uncertainty. The bias is estimated by 50 toy experiments with resampling of the uncertainty templates. The unfolding uncertainty is approximated by the uncertainty of unfolding the data.

MC sample. In the χ^2 between the pseudodata and the detector-level nominal MC, only the statistical uncertainties of the pseudodata and the MC are included. The unfolding bias from the particle-level modeling is included because it parametrizes the effects of the assumptions about the underlying physics model on the unfolding result. Therefore, this uncertainty is only present for the unfolded results, but does not affect the detector-level distributions. All other uncertainties affecting both the particle-level and detector-level quantities are ignored in this test. The histograms at the two levels use the same binning, so that the χ^2 values can be fairly compared by the ratios.

At iteration 0 before unfolding, the χ^2 at the particle-level equals 0 as expected, as the predicted particle-level distributions are the same as the nominal MC ones before unfolding. The ratios increase during the iterations, indicating the unfolded result leaving the nominal MC

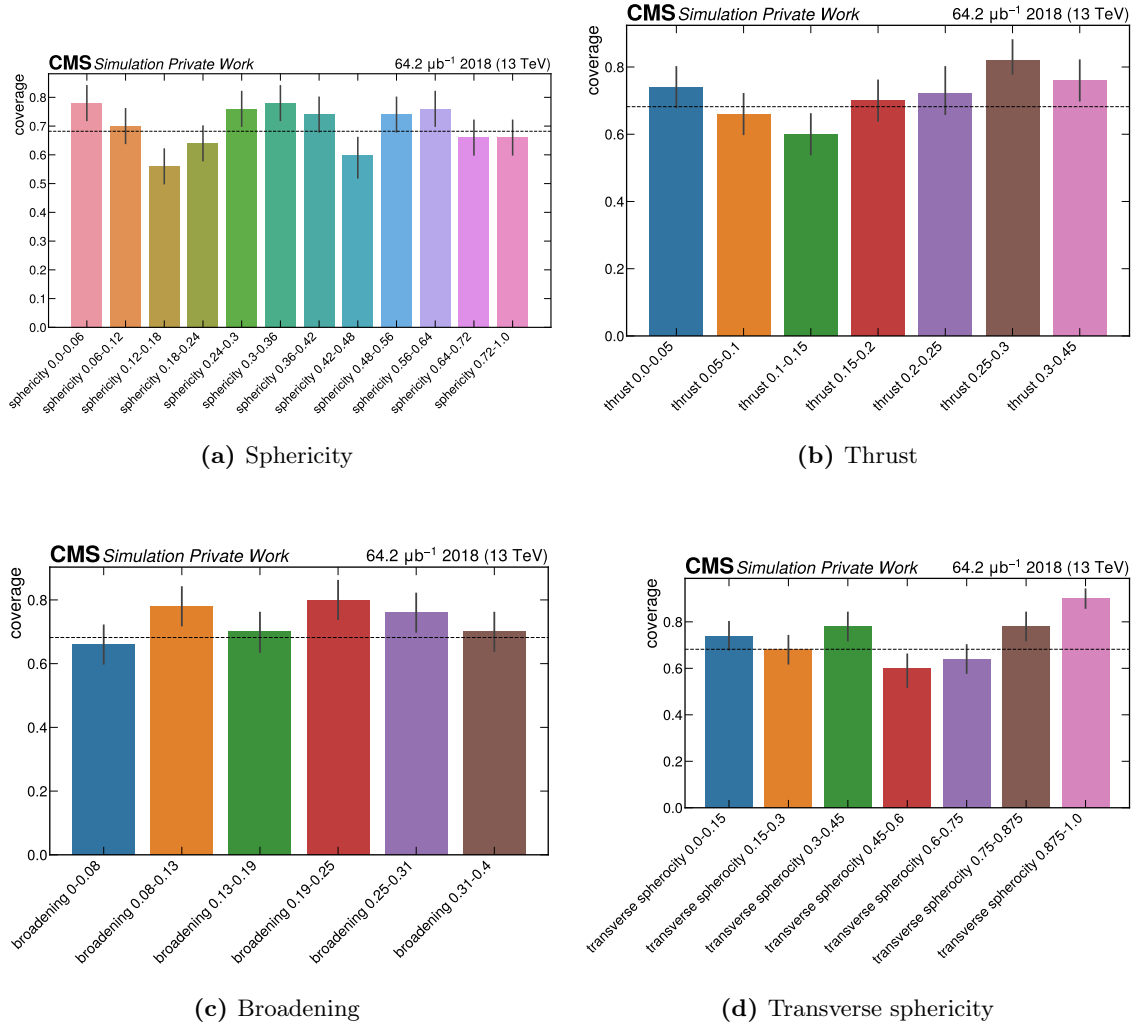


Figure 4.12: The coverage of the unfolded results after 2 iterations, when unfolding the pseudo-data from PYTHIA 8 CUETP8M1 (NNPDF3.1LO) tune with the nominal MC from the A3 tune. The coverage is estimated by 50 toy experiments with resampling of the uncertainty templates. The unfolding uncertainty is approximated by the uncertainty of unfolding the data.

model. The ratios are found to be less than one, as required by the test.

4.7 Results and interpretation

The unfolded results as weighted events at the particle-level are projected into one-dimensional or two-dimensional histograms of the event shape observables in this section. The sample from the PYTHIA 8 CP1 tune is used as the nominal MC sample in the unfolding, and the PYTHIA 8 A3 tune, EPOS-LHC and HERWIG 7 CH3 tune samples are used to derive the templates of MC modeling uncertainties. The unfolding is performed using 2 iterations, accompanied by uncertainties estimated by 100 toy experiments individually for the data statistical uncertainty and the systematic uncertainty from MC, as described by Section 4.6.3.

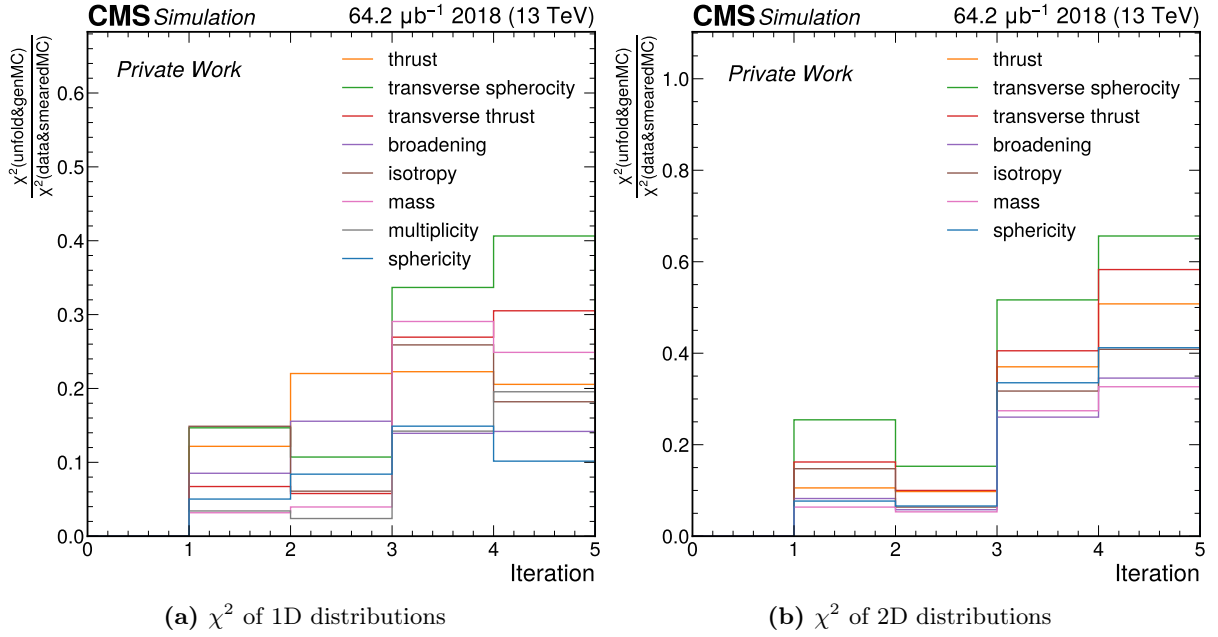


Figure 4.13: Ratios of the χ^2 difference between the unfolded results and MC truth to the χ^2 difference between the pseudo-data and MC distributions at the detector-level. The uncertainty in the χ^2 calculation includes the statistical uncertainty of the MC and the bias of the unfolding.

4.7.1 Unfolding results as one-dimensional histograms

The one-dimensional projections of the unfolded results are shown in Figure 4.14 and 4.15 as the histograms representing the probability distribution functions of the observables. The predictions from the nominal MC sample, as well as alternative models from PYTHIA 8 A3 tune, EPOS-LHC, PYTHIA 8 A14 and CP5 tune and HERWIG 7 CH3 tune are also given as references. Correlations of the uncertainty across the bins are given in Appendix A.5. The uncertainty contributions from individual sources are given in Appendix A.6. Discrepancies between the data and the predictions are observed, despite the variations among predictions due to the differences in modeling. A consistent trend of discrepancies is found for all the event shape observables among all the models, indicating that the data events tend to be more isotropic than the predictions. In the histograms of charged particle multiplicity and invariant mass, the deviations of the predictions from data are not monotonic. The MC models tend to overestimate the number of events with $N_{ch} < 10$ or $\sqrt{s_{ch}} < 20$ GeV, while underestimate the number of events with $10 < N_{ch} < 30$ or $20 \text{ GeV} < \sqrt{s_{ch}} < 70$ GeV. On the tail of high multiplicity ($N_{ch} > 30$) or mass ($\sqrt{s_{ch}} > 70$ GeV), the trends discrepancies varies among models. In general, none of the models is consistent with the data in describing these variables of charged particle multiplicity, invariant mass and event shape.

4.7.2 Unfolding results as two-dimensional histograms

Figure 4.16 and 4.17 show the two-dimensional projections of the unfolded result to the distributions of event shape observables and charged particle invariant mass in slices of charged particle multiplicity. Discrepancies between the predictions and the data are also observed in the slices of charged particle multiplicity, especially in the median N_{ch} region of $10 < N_{ch} < 30$, in which the data is generally more isotropic than the MC. This trend persists in the slices with controlled N_{ch} and occurs over multiple slices with different N_{ch} , which suggests that the mismodeling of

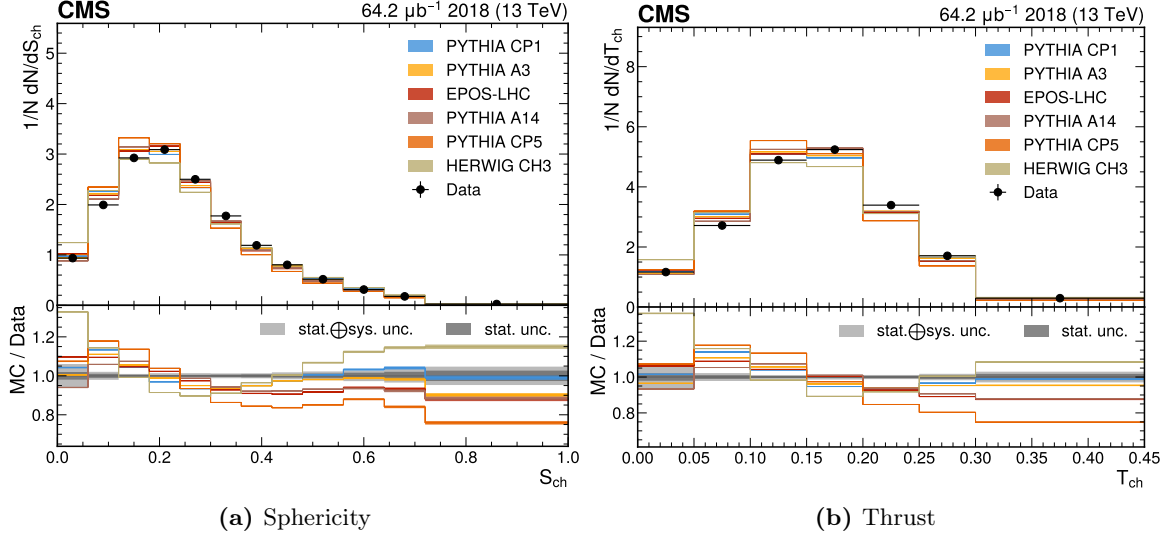


Figure 4.14: The event shape distributions of the unfolded results compared to the nominal MC from the PYTHIA 8 CP1 tune and the predictions from the PYTHIA 8 A3, A14 and CP5 tunes, the EPOS-LHC generator and the HERWIG CH3 tune.

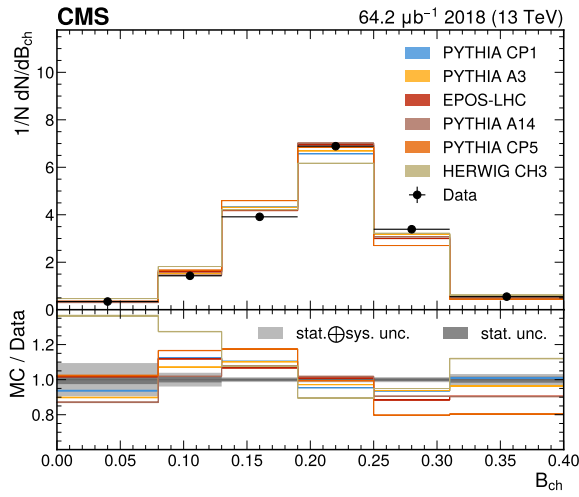
the event shape cannot be fully attributed to the mismodeled charge particle multiplicity.

4.7.3 Interpretation

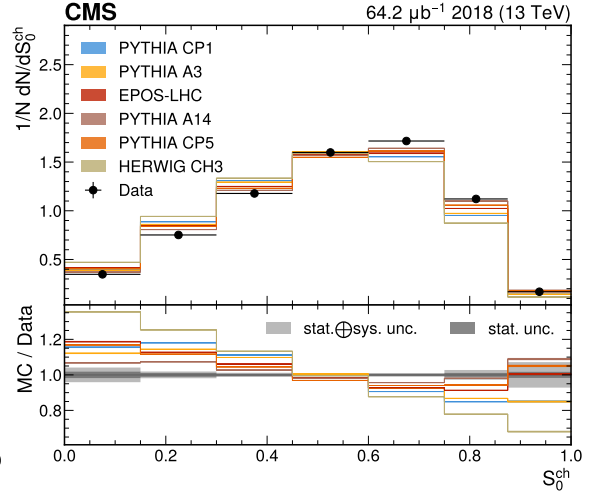
The description of event shape observables of inelastic pp collisions involves phenomenological models about the kinematics of soft parton scatterings and UE, e.g. MPI and BR. The MC predictions in Section 4.7.1 and 4.7.2 covers a large variety of the models with different PDFs, values of $\alpha_S(M_Z)$, showering, hadronization, UE parametrisations tuned to distinct experimental data, as well as the parton scatterings models in the proton environment. Nevertheless, the predictions from all these models deviate from the data consistently and show the same trend. The data events are more isotropic than the predictions of all these models, and the trend persists in multiple regions of controlled charged particle multiplicity. This indicates a common feature of mismodeling among all the considered models, which is not related to peculiarities of a particular generator or UE tune.

The discrepancies between MC predictions and data are different from the observations in Ref. [142], where the event shape predictions of PYTHIA CP2, CP3, CP5 and CUETP8M1 tunes are compared to LEP data in the $e^+e^- \rightarrow q\bar{q}$ process [157]. In the event shape distributions from e^+e^- collisions, the MC models either predict more isotropic events than data, or agree with data, the agreement mainly related to the strong coupling constant in the final state radiations α_S^{FSR} . This is opposite to the case of pp collisions in this analysis, where the MC models predicts less isotropic events than data in both cases of a large α_S^{FSR} value at 0.13 in the CP1 and CUETP8M1 tunes and a small α_S^{FSR} value at 0.118 in the CP5 tune. Therefore, the mismodeling of pp collision event shapes might not be related to the showering and hadronization models in the final state radiation.

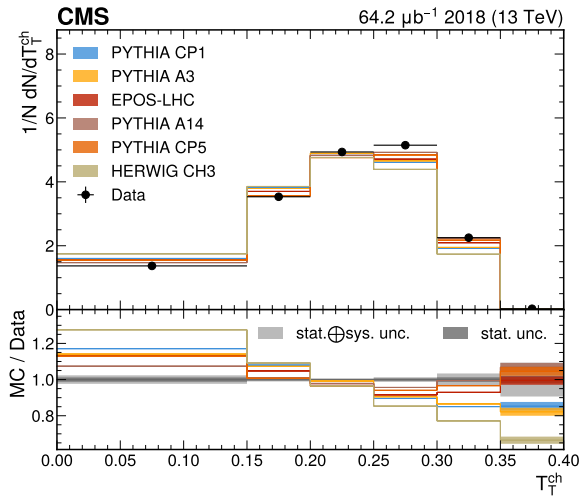
A factor that can alter the event shapes is the potential collective effects in the multiple scatterings in the pp collisions. The collective effects have been observed in relativistic heavy ion collisions [158–161], and considered as one of the typical signatures of quark-gluon plasma formation during the collisions. The collective effects have also been reported in pp collisions in the measurements of long-range near-side two-particle angular correlations [127, 162, 163]. The



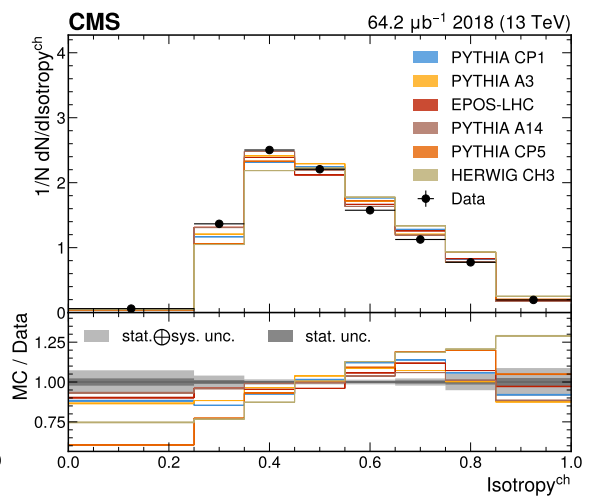
(a) Broadening



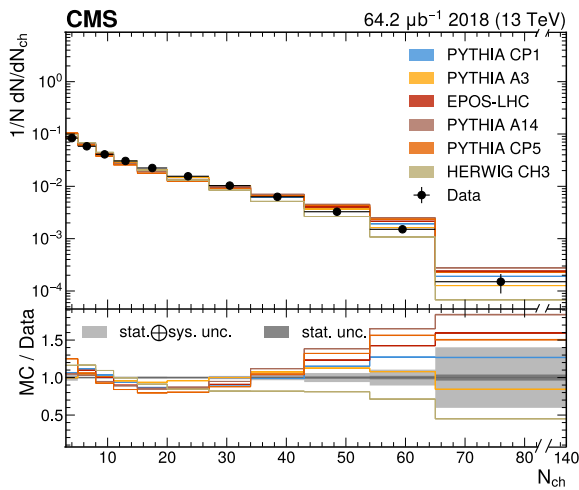
(b) Transverse sphericity



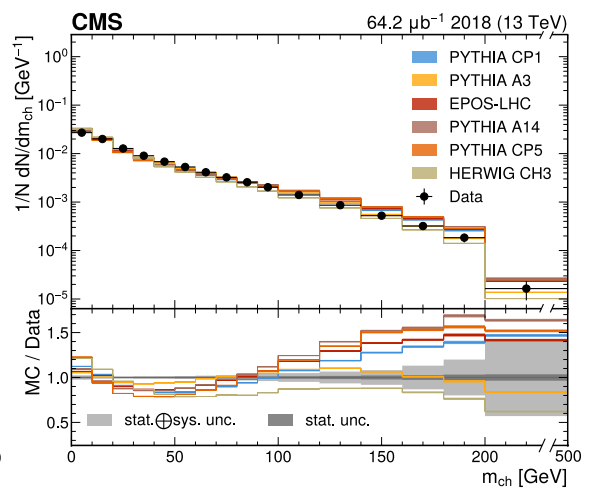
(c) Transverse thrust



(d) Isotropy



(e) Number of the charged particles



(f) Mass of the charged particles

Figure 4.15: The event shape distributions of the unfolded results compared to the nominal MC from the PYTHIA 8 CP1 tune and the predictions from the PYTHIA 8 A3, A14 and CP5 tunes, the EPOS-LHC generator and the HERWIG CH3 tune.

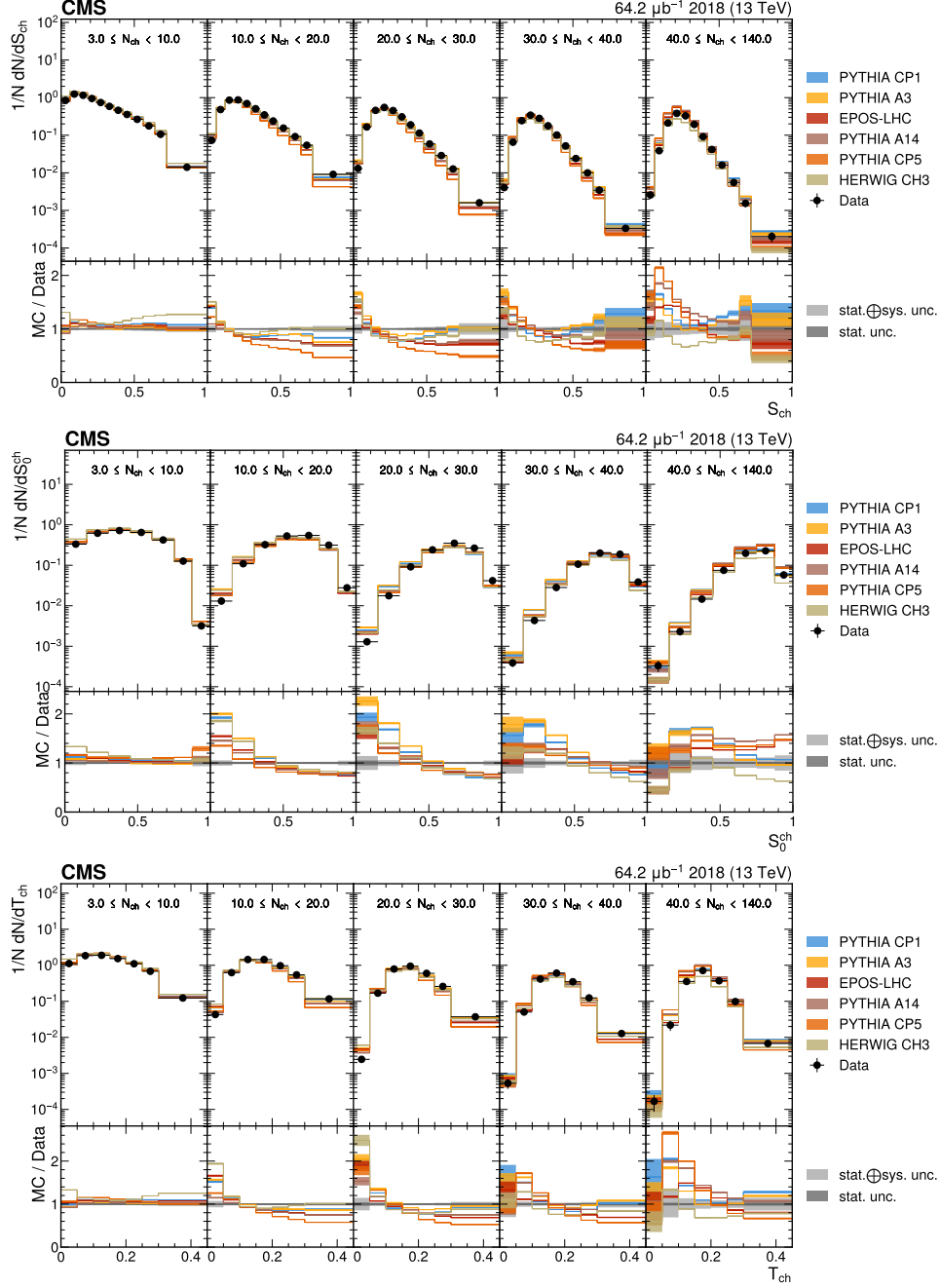


Figure 4.16: The unfolded distributions of sphericity, transverse sphericity and thrust in slices of charged particle multiplicity compared to the nominal MC from PYTHIA 8 CP1 tune and MC predictions from the PYTHIA 8 A14, CP5, A3 tunes, the EPOS-LHC generator and the HERWIG 7 CH3 tune.

EPOS-LHC uses the collective hadronization model to describe these collective behaviors in small collision systems, and is found describing the near-side ridge yield as a function of transverse momentum better than PYTHIA models [164]. However, the EPOS-LHC predictions show a similar trend of discrepancies to PYTHIA and HERWIG in the distributions of event shape observables in this analysis, indicating that the collective effects cannot fully explain the discrepancies.

The deviation of data from the MC predictions in the event shape measurement is qualitatively similar to the expectations of the QCD instanton contributions. According to the predictions [30, 165], instantons are characterized by soft isotropic events with relatively large multiplicities, which can alter the event shape distributions of inelastic pp collisions given their

large cross section around $\mathcal{O}(\text{mb})$, despite the accompanying large theoretical uncertainties [166].

For a preliminary interpretation of the event shape measurement concerning the instanton model, the events including instanton processes in pp collisions are simulated, and their event shape distributions are compared with the measured data. The instanton invariant masses (E_I) are sampled according to the linear interpolation of the cross sections at the center-of-mass energies of the incoming gluons given in Reference [30]. Similarly, the expected number of gluons ($\langle n_g \rangle$) is interpolated from the values in [30] to determine the $\langle n_g \rangle$ at each given E_I , then the number of outgoing gluons (n_g) are sampled from the Poisson distribution with expectation $\langle n_g \rangle$. Depending on the model, three flavors (u, d, s) or four flavors (u, d, s, c) of quark and anti-quark pairs are generated for each instanton event. The partonic cross sections are convoluted with the PDF via sampling, and the momenta of the outgoing quarks and gluons are generated with the RAMBO algorithm [167]. The parton-level instanton events are input into PYTHIA, which applies the PS and hadronization, and adds the UE, including MPI and BR from the pp collisions. The same PYTHIA settings as the CMS CP1 tune are used for the instanton simulation, except that MPI are allowed to be generated up to their kinematic limit. A threshold on the minimum instanton mass E_I is set to regularize the divergence in the cross section when E_I approaches zero [30] and the theoretical prediction is no longer valid. CMS detector simulation and reconstruction are applied to the instanton events [139–141], and detector-level observables are derived from the reconstructed tracks after the selections in Section 4.4.

Figure 4.18 compares a few instanton models with the minimum-bias prediction of PYTHIA CP1 tune, as well as the data in the normalized distributions of transverse sphericity and track invariant mass. The minimum instanton mass alters the average rapidity of the scatter producing the instantons, the gluon multiplicity and the kinematics of the outgoing partons, and the number of flavors alters the number of outgoing partons and their kinematics. Additionally, the kinematics of the instanton itself modify the impact parameter of the collisions as determined by PYTHIA, affecting the number of additional MPI that are generated. As shown in the figure, for some choices of parameters, the instanton models have the potential to compensate for the mismodeling of the current minimum-bias predictions in the event shape distributions. The histograms containing 30% instanton contribution with minimum E_I at 10 GeV in 4-flavor scheme and 70% contribution from minimum bias generated by PYTHIA CP1 tune are provided in the figure, which describe the data better than the minimum-bias predictions without instantons.

The inclusion of instantons in the UE model is well-motivated by the prediction of non-perturbative QCD, and for some reasonable parameter choices, improves the description of the minimum-bias data, but strong caveats must be taken into consideration about the interplay of the instanton simulation with the rest of the event and several theoretical aspects of the modeling. The impact parameter distribution and its effect on the number of additional MPI cannot be ignored, both due to the similar signature of instantons and MPI, and due to considerations about the instanton size for low mass instantons. Modifications to the traditional event generation in PYTHIA may be required. The experimental measurement of instantons is also limited by the ambiguities in the regularization model at the minimum E_I , the flavor scheme, the theoretical uncertainties of the instanton kinematics and the differential cross section $\sigma(E_I)$, and the modeling of potential multiple-instanton productions in pp collisions.

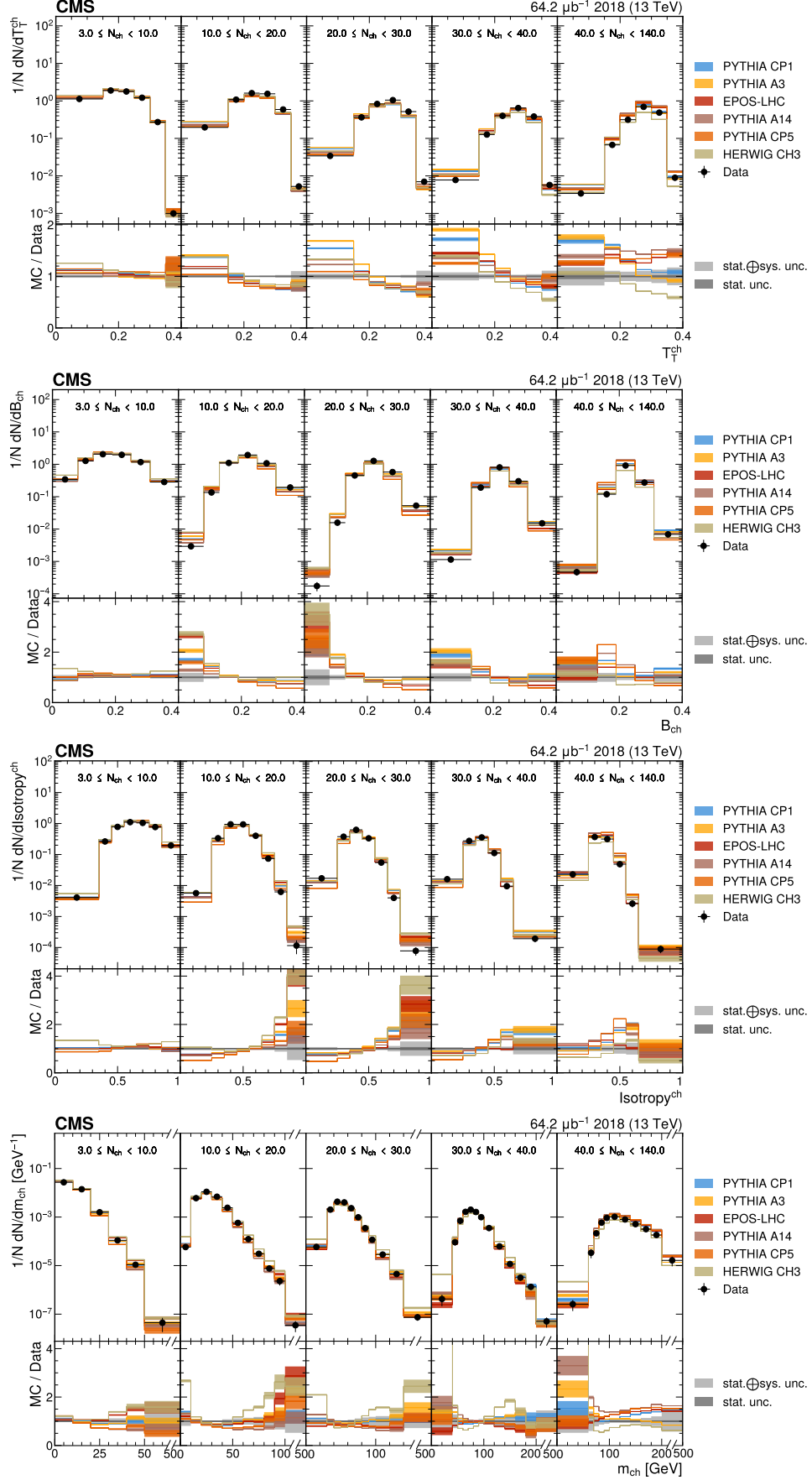


Figure 4.17: The unfolded distributions of transverse thrust, broadening, isotropy and charged particle invariant mass in slices of charged particle multiplicity compared to the nominal MC from PYTHIA 8 CP1 tune and MC predictions from the PYTHIA 8 A14, CP5, A3 tunes, the EPOS-LHC generator and the HERWIG 7 CH3 tune.

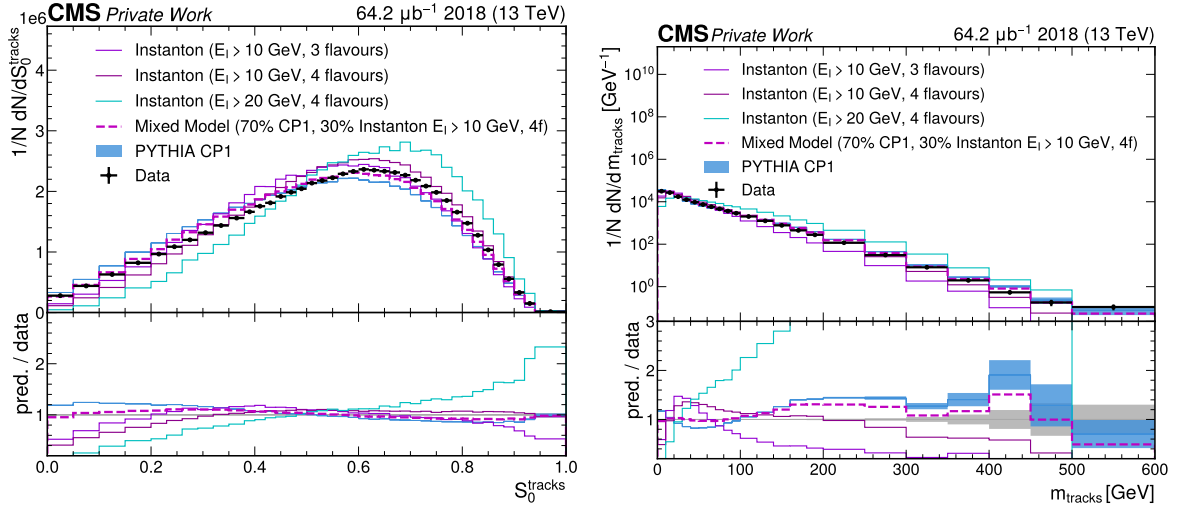


Figure 4.18: The transverse sphericity (left) and track invariant mass (right) distributions of instanton models with minimum $E_I = 10$ GeV in 3-flavor and 4-flavor scheme and minimum $E_I = 20$ GeV in 4-flavor scheme, compared to the minimum bias prediction of PYTHIA CP1 tune and the data. The distributions of the mixed model containing 30% instantons with minimum $E_I = 10$ GeV in 4-flavor and 70% PYTHIA CP1 minimum bias are provided as examples of improved descriptions of data by adding instantons.

5 Investigation of intrinsic k_T in Drell–Yan events

This chapter investigates intrinsic k_T models in hadron collisions by tuning generators to the differential cross section of the DY process with respect to the lepton-pair transverse momentum. The derived intrinsic k_T parameters exhibit a power-law scaling with collision energy and are independent of the lepton-pair invariant mass at a given collision energy within the measurement precision. These trends are consistent across various UE configurations in both PYTHIA and HERWIG generators, suggesting model-independent features of non-perturbative QCD effects in the initial state of hadron collisions.

Leveraging insights into soft interactions, UE, and MC generators developed in Chapter 4, the author independently led these studies within the CMS Generator group. The results were first presented at the Moriond 2024 conference and are now accepted for publication in Physics Review D.

5.1 Motivation

In the high-energy collision experiments, the transverse momentum (p_T) of the hard scattering process is one of the important kinematic variables for understanding the production and decay mechanisms of heavy particles, testing the SM prediction and searching for new physics. For example, the measurement of the W mass depends on the transverse momentum of the charged leptons from the W decay \vec{p}_T^l and the transverse momentum of the neutrinos from the W decay, inferred from the missing transverse momentum \vec{p}_T^{miss} , both relying on the p_T of the hard scattering processes producing the W bosons.

Due to the momentum conservation, the p_T of the hard scatters come from the p_T of incoming mother partons, which receive contributions from both the intrinsic transverse momenta of the partons inside the colliding hadrons (intrinsic k_T) from their Fermi motions and the initial state radiations (ISR) recoiling against the hard scatter. Several approaches exist to describe the intrinsic k_T , including those relying on the transverse-momentum-dependent (TMD) PDFs [168–170], and those based on first-principle calculations from lattice QCD [171–173]. The ISR is usually described by fixed-order or resummed perturbative QCD calculations, often combined with PS to generate fully exclusive events and to enable the predictions of observables at the (next-to-)leading-logarithmic order with the probabilistic Markov chain algorithm. PS algorithms are used in general-purpose MC event generators, such as PYTHIA [174, 175], HERWIG [176] and SHERPA [177], and optionally interfaced with fixed-order matrix element predictions to generate exclusive events for hadronization, detector simulation and direct comparison with experimental data. The cross-section calculation in parton showers becomes divergent in the limit of soft or collinear gluon emissions. Therefore, regularization on these divergences is implemented in the PS models of the MC generators, typically controlling the minimum p_T allowed for parton emissions. The intrinsic k_T is also taken into account during the event generation by the MC

generators for an accurate description of the event kinematics. Instead of using TMD PDFs or lattice QCD calculations, the MC generators are based on collinear PDFs and simply model the intrinsic k_T as a random variable with a Gaussian distribution, whose width is a tunable parameter. The intrinsic k_T model in the generators is not considered as the model for the transverse Fermi motions of the partons inside the hadrons, but rather a phenomenological model approximating the effects of both the transverse Fermi motions and the soft and collinear parton emissions regularized by the parton shower. The model parameter (width of the Gaussian distribution) is expected to be tuned to measured data to be able to describe the p_T of the hard scatters.

Besides the practical purpose of a better description of data, the tuning of intrinsic k_T can also give us hints about non-perturbative effects in the intrinsic motions of partons in hadrons, and both perturbative and non-perturbative effects in the ISR, since the tuned intrinsic k_T parameter compensates for the deficiencies in the parton showers inclusively. These considerations motivate the study of intrinsic k_T tunes and the investigation of various factors affecting the tunes.

5.2 Data and simulations

The DY process ends up with a lepton pair with opposite charges, which is a clean final state and can be reconstructed from detector signals with high resolution 3.2.2. The p_T of the lepton-pair system $p_T(\ell^+\ell^-)$ can be measured to probe the p_T of the incoming partons, and then used to tune the intrinsic k_T . The region of high $p_T(\ell^+\ell^-)$ (> 20 GeV) is dominated by large-angle emissions of hard partons of the ISR, and can be described by fixed-order calculations. The region of low $p_T(\ell^+\ell^-)$ around a few GeV is sensitive to soft or collinear ISR and intrinsic k_T , and thus suitable for the study of intrinsic k_T parameters. Previous studies have shown the sensitivity of this region [178] by illustrating the impact of high-order QCD contributions (soft or collinear ISR effects) to the low $p_T(\ell^+\ell^-)$ predictions. Treatments of the non-perturbative QCD effects have been proposed [179, 180].

The DY process has been widely studied in hadron collision experiments [181–193]. The measurements of the DY kinematics have been performed for various types of hadron collisions at different center-of-mass energies (\sqrt{s}) in either fixed-target or collider experiments. The $p_T(\ell^+\ell^-)$ measurement results from these previous experiments are used in this analysis to perform the intrinsic k_T tune and to study the interplay between the intrinsic k_T parameter and the perturbative evolution of ISR. The measurements of the differential cross sections of the DY process as a function of $p_T(\ell^+\ell^-)$ are summarized in Table 5.1.

The MC simulations of DY events are produced for each scenario in Table 5.1. Exceptionally, pp collisions are generated for comparison with the proton-lead (pPb) data with the cross section divided by 208 as the number of nucleons in a lead nucleus. The events are generated at next-to-leading order (NLO) using MADGRAPH5_aMC@NLO v3.4.1 [194] for the matrix-element computation and then matched to the PYTHIA 8 or HERWIG 7 generator for parton shower, hadronization and UE activity modeling. As introduced in Section 4.3, the parameters in the generators are set to UE tunes, coming from tuning to measurements of observables sensitive to UE. The usage of these UE tunes in DY simulations without further modification is justified by the observation that the UE parameters have a small impact on the DY $p_T(\ell^+\ell^-)$ distribution, and that the intrinsic k_T parameter used to modulate the DY $p_T(\ell^+\ell^-)$ also has a small impact on the UE observables, as shown in Appendix B.1. Various UE tunes have been used to generate

Table 5.1: Measurements of the Drell–Yan differential cross section as a function of $p_T(\ell^+\ell^-)$ at various center-of-mass energies \sqrt{s} from different hadron-collision processes used as inputs for the intrinsic k_T tunes. The \sqrt{s} in pPb collisions represents the nucleon-nucleon center-of-mass energy. The variable Q represents the energy scale of the hard scattering, approximated by the dilepton invariant mass.

| Experiment | Collision type | \sqrt{s} [GeV] | Q [GeV] |
|-----------------------|---------------------|------------------|--------------|
| E866/NuSea [181, 182] | pp/pd, fixed target | 38.8 | 4–12.85 |
| R209 [183] | pp | 62 | 5–8 |
| PHENIX [184] | pp | 200 | 4.8–8.2 |
| D0/CDF [185, 186] | p \bar{p} | 1800 | Z boson mass |
| D0/CDF [187, 188] | p \bar{p} | 1960 | Z boson mass |
| CMS [189] | pp | 2760 | Z boson mass |
| ATLAS [190] | pp | 8000 | 46–150 |
| CMS [191] | pPb | 8160 | 15–120 |
| CMS [192] | pp | 13000 | 50–1000 |
| LHCb [193] | pp | 13000 | Z boson mass |

the DY events, based on different PDFs, partonic emission orderings, and settings in MPI and BR modeling, as listed below:

- **PYTHIA 8 tunes:** The PYTHIA 8.243 generator is used for the p_T -ordered PS and hadronization, and the UE model is parameterized by the CP3, CP4, or CP5 tune [195]. The three tunes have the strong coupling constant $\alpha_S(m_Z)$ set to 0.118, use NLO strong-coupling evolution, and employ NLO or next-to-NLO (NNLO) PDFs in the hard scattering, parton showering, ISR, final-state radiations (FSR), MPI, and BR modelings.
- **HERWIG 7 tunes:** The HERWIG 7.1.4 generator is used for the angular-ordered PS and hadronization, and the CH2 and CH3 tunes [144] are used for the UE modeling. Both tunes use $\alpha_S(m_Z) = 0.118$ with NNLO strong-coupling evolution and the NNLO NNPDF3.1 PDFs for the parton shower, but different α_S and PDF sets in the MPI and BR modelings.

In these UE tunes, the relevant parameters have been tuned to measurements by the CDF and CMS experiments with \sqrt{s} ranging from 0.9 to 13 TeV. The performances of these tunes have been validated in modeling the UE-sensitive variables across all these energies, as well as the double-parton-scattering-sensitive variables and the kinematics of high p_T jet, $t\bar{t}$ and vector boson production at the CMS.

The intrinsic k_T is modeled similarly in PYTHIA and HERWIG by a Gaussian distribution in the transverse plane of the beams. The distribution is centered at 0, and the width is a tunable parameter to be studied, denoted as q_s . In PYTHIA, the width q_s of the Gaussian distribution is related to the parameter `BEAMREMNANTS:PRIMORDIALKTHARD` $\simeq q_s/\sqrt{2}$, whereas in HERWIG, it is given by the parameter `SHOWERHANDLER:INTRINSICPTGAUSSIAN` $= q_s$. In the following, we use q to refer to either the intrinsic k_T parameter `BEAMREMNANTS:PRIMORDIALKTHARD` in PYTHIA or the parameter `SHOWERHANDLER:INTRINSICPTGAUSSIAN` in HERWIG.

To find the values of the intrinsic k_T parameters with the best description of data, a scan in the tuning range is performed, and MC samples are generated for each grid point of the intrinsic k_T parameter.

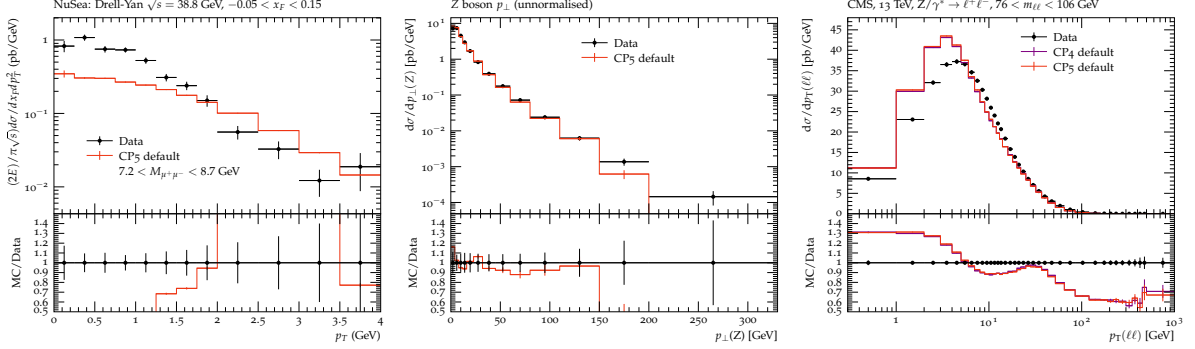


Figure 5.1: The MC predictions of the DY differential cross section as a function of $p_T(\ell^+\ell^-)$ with the PYTHIA intrinsic k_T model parameter set to the default value 1.8 and the UE parameters set to CP5 tune at various \sqrt{s} of pp or $p\bar{p}$ collisions compared to the corresponding measured data. The same selections on the final states are applied to the MC events as those in the measurements. Left: pp collisions at $\sqrt{s} = 38.8$ GeV with the dimuon final state and the invariant mass range of the muon pairs $7.2 < M(\mu^+\mu^-) < 8.7$ GeV. Middle: $p\bar{p}$ collisions at $\sqrt{s} = 1.96$ TeV with the di-muon final state and the mass range $65 < M(\mu^+\mu^-) < 115$ GeV. Right: pp collisions at $\sqrt{s} = 13$ TeV with the di-muon or di-electron final state and the mass range $76 < M(\ell^+\ell^-) < 106$ GeV.

5.3 Generator tuning strategy

In the default PYTHIA and HERWIG settings, the intrinsic k_T parameter q is set to a fixed value regardless of the collision energy \sqrt{s} . The PYTHIA predictions of the DY differential cross section versus $p_T(\ell^+\ell^-)$ in 3 of the scenarios in Table 5.1 are given by generating events of the corresponding hadron collision types and energies and passing the events to the RIVET routines [196], the results shown in Figure 5.1. In the MC simulations, the intrinsic k_T parameter is set to the default value `BEAMREMNANTS:PRIMORDIALKTHARD = 1.8`, and the rest of the settings are the same as the CP5 tune. Different trends of discrepancies are found between the MC predictions and data in the low $p_T(\ell^+\ell^-)$ region that is sensitive to the intrinsic k_T parameter. In the $\sqrt{s} = 38.8$ GeV pp collisions in the left plot, the MC underestimates the data; in the $\sqrt{s} = 1.96$ TeV $p\bar{p}$ collisions in the middle plot, the MC is approximately compatible with data; in the $\sqrt{s} = 13$ TeV pp collisions, the MC overestimates the data. These trends indicate that the best-fit values of the intrinsic k_T parameter are on different sides of the default value for the 3 scenarios, assuming that MC deviates from the data monotonically with respect to the intrinsic k_T parameter. Therefore, the intrinsic k_T parameter should be tuned separately for these scenarios for an optimal description of the measured data, and the figure suggests the dependence of the tuning results on the collision energy \sqrt{s} . The following tuning procedure is repeated for each scenario of hadron collisions and each generator setting individually.

As introduced in Section 5.2, we assume that the DY differential cross section versus $p_T(\ell^+\ell^-)$ depends on the intrinsic k_T parameter q and aim to find the value of q most compatible with the measured data. MC simulations of DY events are generated with different choices of the intrinsic k_T parameter q sampled from its tuning range, resulting in varied predictions of the differential cross section. In each bin i of $p_T(\ell^+\ell^-)$, the dependence of the cross section on q is extracted by interpolating the simulated values as a polynomial $f_i(q)$ of the corresponding values of q . The uncertainty of the cross section in bin i is also estimated by interpolating the uncertainty of the simulated values as a polynomial $u_{f_i(q)}$ of q . The interpolation allows us to estimate the response cross section as continuous functions of q and to search for the optimal q value with the gradient descent method. The compatibility between the model and data is

| Center of mass energy | Data histograms | Ranges |
|-----------------------|-----------------------------------|--------------|
| 38.8 GeV | /NUSEA_2003_I613362/d40-x01-y01 | 0 - 3.5 GeV |
| | /NUSEA_2003_I613362/d40-x01-y02 | 0 - 3.5 GeV |
| | /NUSEA_2003_I613362/d40-x01-y03 | 0 - 3 GeV |
| | /NUSEA_2003_I613362/d40-x01-y04 | 0 - 4 GeV |
| | /NUSEA_2003_I613362/d40-x01-y05 | 0.25 - 2 GeV |
| 62 GeV | /R209_1982_I168182/d02-x01-y01 | 0 - 5.2 GeV |
| 200 GeV | /PHENIX_2019_I1672015/d01-x01-y01 | 0 - 6 GeV |
| 1.8 TeV | /D0_2000_I503361/d01-x01-y01 | 0 - 10 GeV |
| | /CDF_2000_S4155203/d01-x01-y01 | 0 - 10 GeV |
| 1.96 TeV | /CDF_2012_I1124333/d02-x01-y01 | 0 - 10 GeV |
| 2.76 TeV | /CMS_2014_I1322726/d01-x01-y01 | 0 - 10 GeV |
| | /CMS_2014_I1322726/d02-x01-y01 | 0 - 10 GeV |
| 8 TeV | /ATLAS_2015_I1408516/d38-x01-y04 | 0 - 10 GeV |
| | /ATLAS_2015_I1408516/d39-x01-y04 | 0 - 10 GeV |
| | /ATLAS_2015_I1408516/d40-x01-y04 | 0 - 10 GeV |
| 8.16 TeV | /CMS_2021_I1849180/d04-x01-y01 | 0 - 10 GeV |
| | /CMS_2021_I1849180/d05-x01-y01 | 0 - 10 GeV |
| 13 TeV | /CMS_2022_I2079374/d01-x01-y01 | 0 - 10 GeV |
| | /CMS_2022_I2079374/d03-x01-y01 | 0 - 10 GeV |
| | /CMS_2022_I2079374/d05-x01-y01 | 0 - 10 GeV |
| | /CMS_2022_I2079374/d07-x01-y01 | 0 - 10 GeV |
| | /CMS_2022_I2079374/d09-x01-y01 | 0 - 10 GeV |
| 13 TeV | /LHCB_2021_I1990313/d19-x01-y01 | 0 - 10 GeV |

Table 5.2: The RIVET plugins [196] corresponding to the data histograms used in the tune, as well as the ranges for calculating and minimizing the goodness of fit.

quantified by the goodness-of-fit (GOF) function, defined as

$$\chi^2(q) = \sum_i \frac{(f_i(q) - d_i)^2}{u_{d_i}^2 + u_{f_i(q)}^2}, \quad (5.1)$$

where d_i and u_{d_i} are the cross section and its uncertainty measured in data in bin i , respectively. For the tuning in scenarios $\sqrt{s} > 1$ TeV, the value of $\chi^2(q)$ is obtained by summing over the bins i corresponding to the low $p_T(\ell^+\ell^-)$ range 0–10 GeV, which is sensitive to the intrinsic k_T model. In the scenarios $\sqrt{s} < 1$ TeV, the whole range of $p_T(\ell^+\ell^-)$ available in data, which is below 10 GeV, is taken into account to calculate the GOF. The histograms and $p_T(\ell^+\ell^-)$ ranges for tuning are summarized in Table 5.2. The tuned result of q is taken as the value that minimizes the GOF. The PROFESSOR 2 software [197] is used to interpolate and derive $f_i(q)$ and $u_{f_i(q)}$, compute the GOF as a function of q , and minimize the GOF with the MINUIT interface [198].

5.4 Uncertainty estimation

The uncertainty of the tuning results originates from the variations of the GOF (eq. 5.1).

5.4.1 Uncertainty from the choices of tune range

The choices of the tune range affect the bins entering the summation in the GOF. The nominal choices in Section 5.3 are based on the approximate energy scale of $p_T(\ell^+\ell^-)$ sensitive to the intrinsic k_T and soft ISR. To estimate the impact of the ambiguity in the choices on the tuning

result, alternative tune ranges are chosen, and the changes in the tuning results are considered as the uncertainty. The alternative tune range is set to $[0, 15]$ GeV for scenarios of $\sqrt{s} > 1$ TeV, as the transition from the non-perturbative to perturbative contributions takes place around 10 to 20 GeV. Concerning the $\sqrt{s} < 1$ TeV cases, the alternative range is $[0, 2]$ GeV (for $\sqrt{s} = 38.8$ GeV) or $[0, 4]$ GeV (for $\sqrt{s} = 62$ and 200 GeV), in which the higher boundaries of $p_T(\ell^+\ell^-)$ are about 2 GeV lower than the maximum $p_T(\ell^+\ell^-)$ in the corresponding measurements.

5.4.2 Uncertainty from the interpolation

The cross-section response $f_i(q)$ and its uncertainty $u_{f_i(q)}$ come from interpolating the responses of the simulation at the sampled values of q . They can be different from the true responses because of the interpolation uncertainty. This uncertainty is estimated by the differences in the tuning results from two choices of functional forms for the interpolation. The results using order-5 polynomials are considered as the central values, and the results using order-3 polynomials are used as alternative values for uncertainty estimation.

5.4.3 Uncertainty from MC statistics

The $f_i(q)$ values in GOF fluctuate by $u_{f_i(q)}$ due to the statistical uncertainty of the event generation, which can propagate into the GOF definition and affect the tuning result. By definition, the GOF function around its minimum is shaped by the MC uncertainty $u_{f_i(q)}$ and data uncertainty u_{d_i} in the denominators of eq.5.1. Therefore, the MC statistical uncertainty in the tuning results can be estimated from the GOF around the minimum.

To disentangle the MC statistical uncertainty and the data uncertainty in the GOF shape, we substitute the denominators of eq.5.1 by $u_{f_i(q)}^2$ to get the GOF considering only the MC statistical uncertainty

$$\chi^2(q) = \sum_i \frac{(f_i(q) - d_i)^2}{u_{f_i(q)}^2}. \quad (5.2)$$

The minimization of the $\chi^2(q)$ in eq. 5.2 is the maximum-likelihood estimation (MLE) of the parameter q assuming that the difference between the MC prediction and the data coming only from the MC statistical uncertainty $u_{f_i(q)}$ and that the difference in each bin follows a Gaussian distribution. The $\chi^2(q)$ is proportional to the negative log-likelihood

$$-\ln(L(q)) = \frac{1}{2}\chi^2(q). \quad (5.3)$$

Near the minimum of $\chi^2(q)$, denoted as χ_{min}^2 , the $\chi^2(q)$ can be approximated as the its order-2 Taylor series

$$\chi^2(q) \simeq \chi_{min}^2 + \frac{1}{2} \frac{d^2\chi^2}{dp^2} \big|_{q=q_{best}} (q - q_{best})^2, \quad (5.4)$$

in which q_{best} is the intrinsic k_T parameter that minimizes $\chi^2(q)$ and gives $\chi_{min}^2 = \chi^2(q_{best})$.

As the MLE of q , q_{best} is consistent and asymptotically normal, and thus follows a Gaussian distribution centered at the truth q_{true} . The variation of q_{best} is constrained by the Cramér-Rao bound [199–203]

$$\sigma^2(q_{best}) \leq \frac{1}{I(q_{best})}, \quad (5.5)$$

in which the Fisher information $I(q_{best})$ is defined as the second derivative of the negative log-likelihood

$$I(q_{best}) = \frac{-d^2 \ln(L(q))}{dq^2} \Big|_{q=q_{best}} = \frac{1}{2} \frac{d^2 \chi^2}{dq^2} \Big|_{q=q_{best}}. \quad (5.6)$$

Because of the asymptotic sufficiency of the MLE, the q_{best} variance can achieve the bound in eq. 5.5 in the limit of infinite MC statistics. Substituting eq. 5.5 and eq. 5.6 into eq. 5.4 and evaluating at $q = q_{true}$, we get

$$\chi^2(q_{true}) - \chi_{min}^2 \simeq \frac{(q_{true} - q_{best})^2}{\sigma^2(q_{best})}, \quad (5.7)$$

which follows a χ^2 distribution with one degree of freedom. Therefore, the range of q corresponding to $\chi^2(q) - \chi_{min}^2 < 1$ is the 68.2% confidence interval of the tuning result q_{best} , and considered as MC statistical uncertainty of the tune.

5.4.4 Uncertainty from the measured data

The measured data d_i in eq. 5.1 has uncertainty u_{d_i} from the measurement, and propagates through the GOF minimization to the tuning result. Correlations are expected among the data uncertainties of the different tunes to the same measurement. To evaluate the correlations, the data uncertainty in the tunes is not estimated in the same way as the MC statistical uncertainty in Section 5.4.3, but instead is estimated by toy experiments. In each toy experiment, the differential cross section to be tuned to is obtained by sampling from Gaussian distributions centered at the nominal values of measured cross sections and with the standard deviations equal to their uncertainties, then parameter tuning is performed for all the generator setups in the corresponding scenario. The covariance between the uncertainties contributed by the measured data in different generator setups is estimated by the covariance between the corresponding tunes in the toy experiments.

The uncertainties from other sources (choice of tune range, interpolation, MC statistics) are considered uncorrelated among the tunes under different generator setups and experiment scenarios. The contributions from these uncertainty sources to the total uncertainty are shown in Figure 5.2.

5.5 Results and discussion

5.5.1 Validations of the tunes

After tuning the PYTHIA and HERWIG intrinsic k_T parameters to the measurements, the tuned values are inserted into the generators to produce MC simulations under their corresponding generator settings and collision scenarios to validate the tuning results. The upper and lower bounds of the tuning uncertainties are also inserted into the generators to simulate their impacts on the predictions. Examples of the comparison between the predictions of the tuned values, the predictions of the default values, and measured DY $p_T(\ell^+\ell^-)$ are given in Figure 5.3. More results of the comparison are given in Appendix B.2. The ratios of the predictions to measurements in the tuning range are shown in Figure 5.4. The MC predictions generally agree with the measurements as expected, and describe the measured data better than the default. The remaining discrepancies between the predictions and the measurements show similar trends among

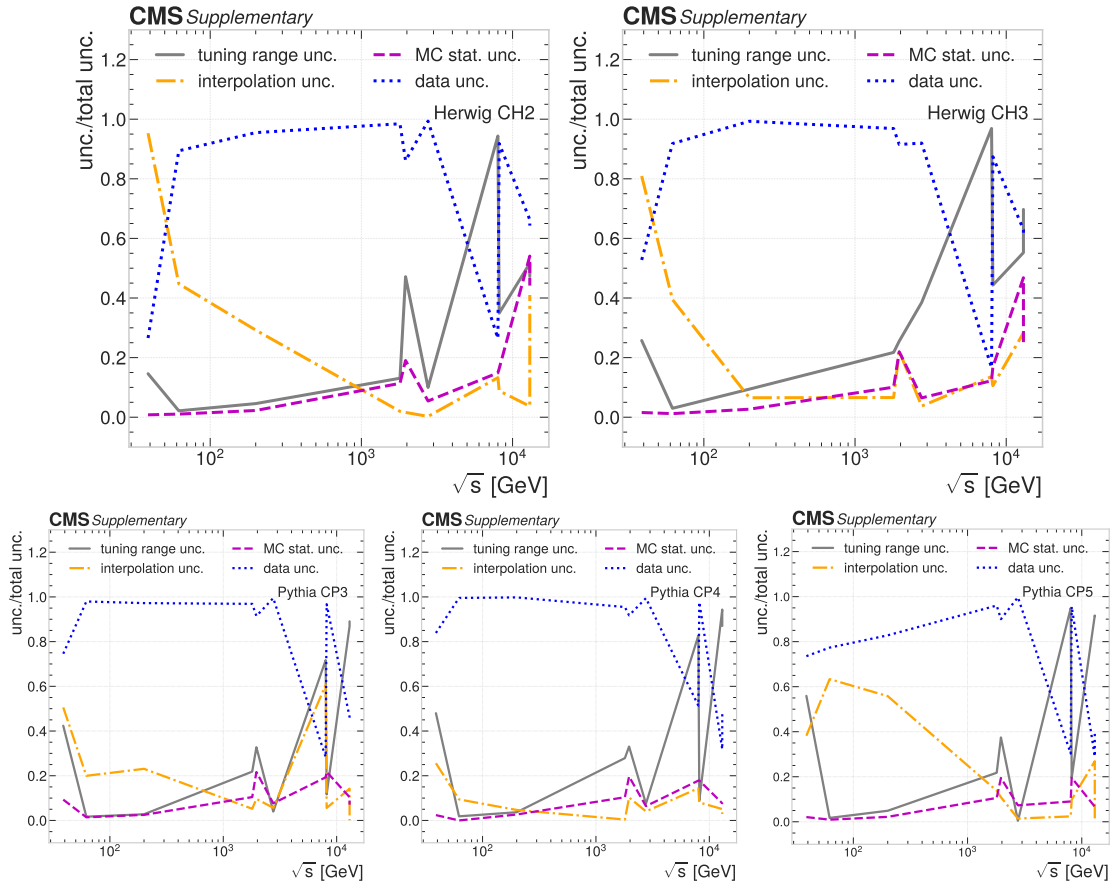


Figure 5.2: The ratio between the contributions from individual uncertainty sources to the total tuning uncertainties in the intrinsic k_T tunes under the UE tunes: HERWIG CH2 (upper left); HERWIG CH3 (upper right); PYTHIA CP3 (lower left); PYTHIA CP4 (lower center); PYTHIA CP5 (lower right).

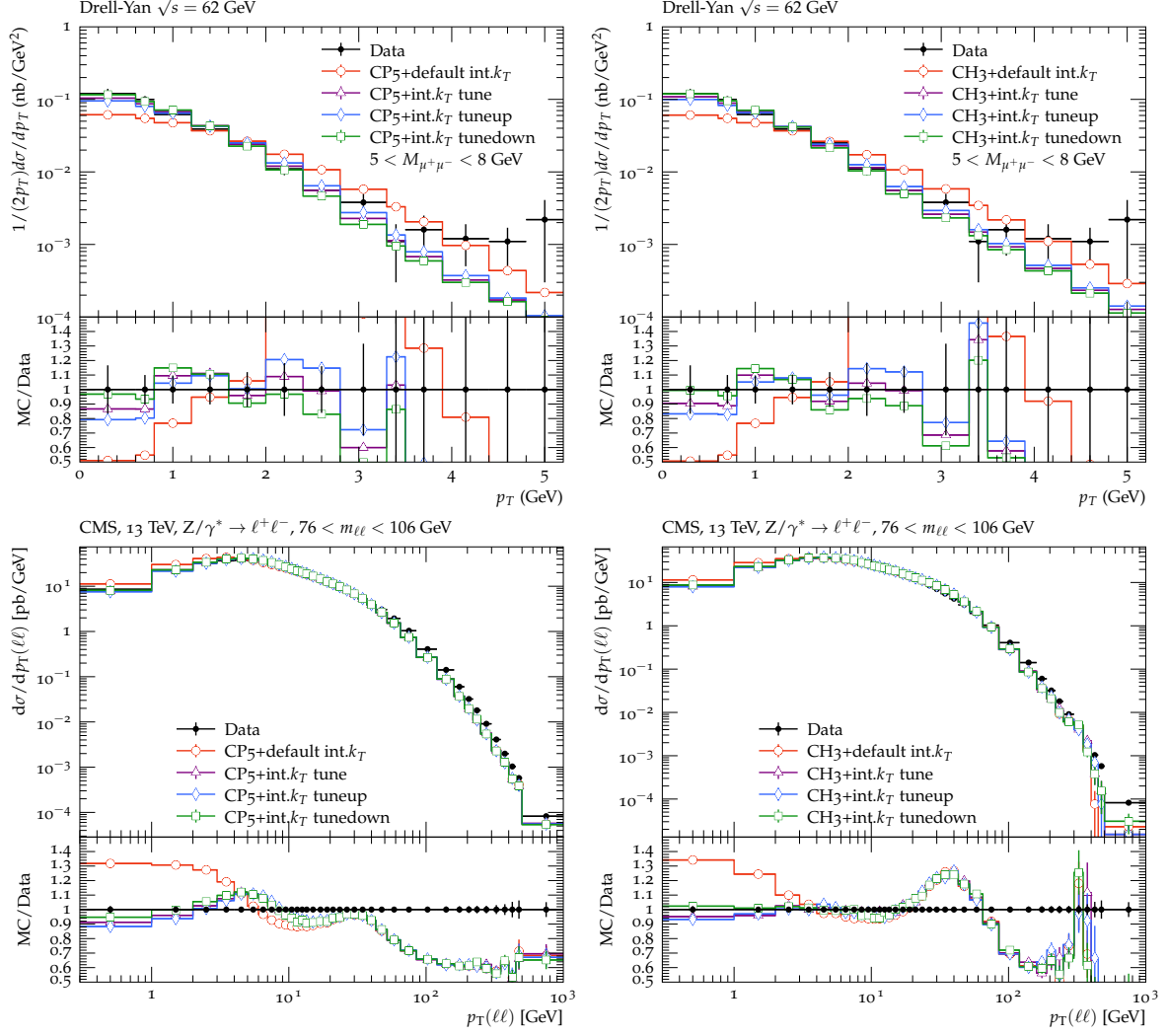


Figure 5.3: The predictions of the intrinsic k_T tunes of the DY $p_T(\ell^+\ell^-)$ under PYTHIA CP5 tune (left) and HERWIG CH3 tune (right) at 62 GeV compared to the R209 experiment (upper) and at 13 TeV compared to CMS measurement (lower).

the tunes for the same generators, indicating that they are probably due to the deficiencies of the phenomenological models in the generators.

5.5.2 Energy scaling behaviors

The tuned results versus the center-of-mass energies are illustrated in Figure 5.5. The tuned results of the CASCADE generator [204], given in Ref. [169, 170], are also shown as a reference. The figure shows an energy-scaling behavior of the intrinsic k_T parameter for both PYTHIA and HERWIG generators and all their setups. To quantify the scaling behaviors, the function $q(\sqrt{s}) = b\sqrt{s}^a$ is fitted to the tuned results, with fit parameters a and $\log_{10}(b)$ describing the slope and intercept of the function, respectively. Observing the similar trends for all the setups, we perform the combined fit assuming the same slope a for all the generator setups, in which the uncertainty correlations among the tunes are considered in the minimization of the sum of squared error weighted by the covariance of the tune uncertainties ($\chi^2_{\text{lin.}}$). The fit is supported by the minimized $\chi^2_{\text{lin.}}$ at 56.0 with the total number of degrees of freedom (NDF) at 44 (50 tuned results fitted to 6 parameters), and the corresponding p -value [205] of 0.11. The slope of the fitted function is found to be $a = 0.162 \pm 0.005$.

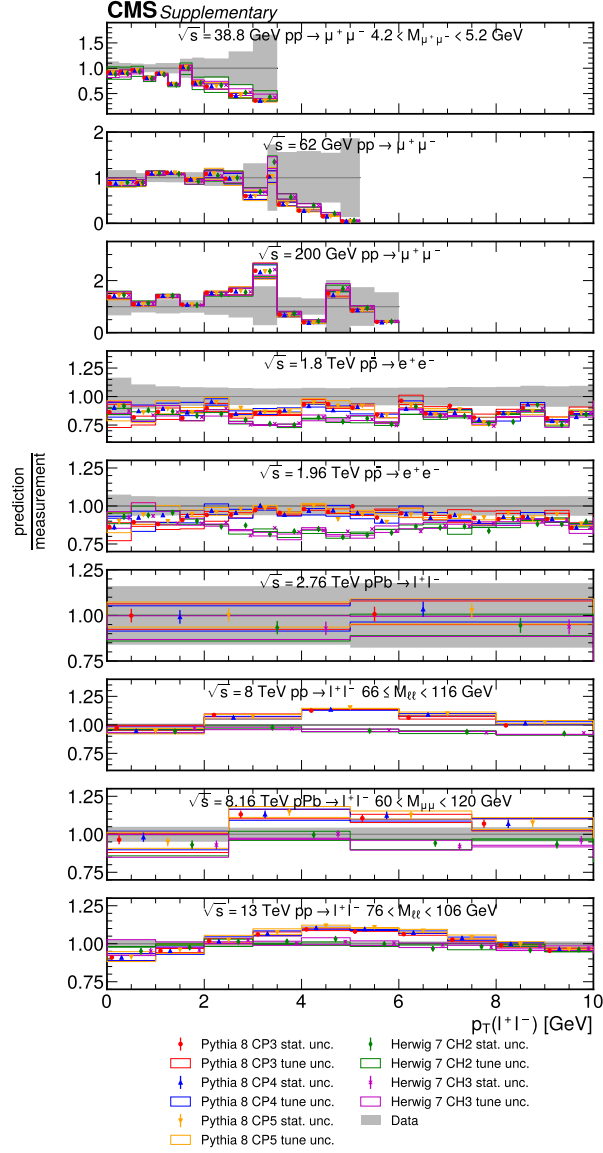


Figure 5.4: MC and data comparison for the intrinsic k_T after tuning. The tune uncertainty comes from the choice of $p_T(\ell^+\ell^-)$ range and the interpolation function in the tune. The last panel corresponds to the MC prediction compared to the CMS data measured at 13 TeV.

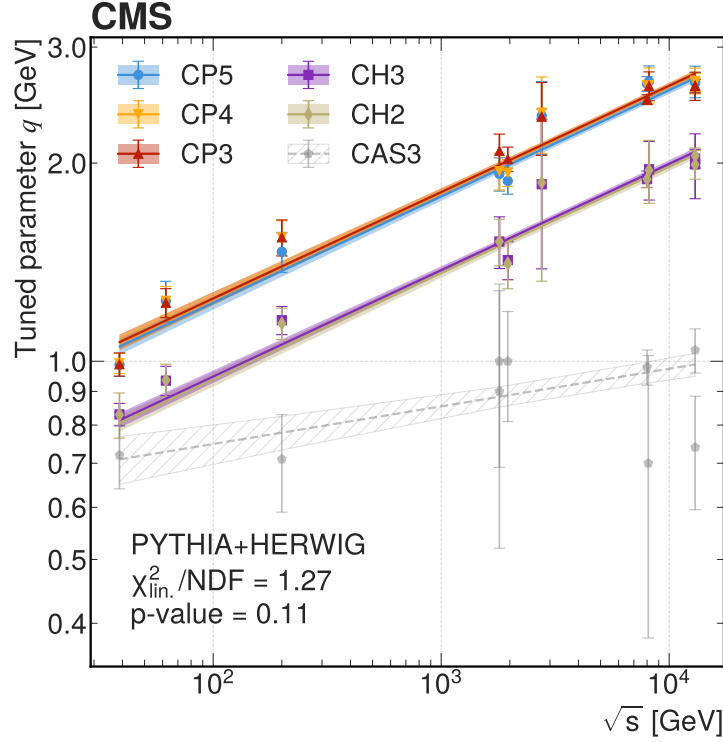


Figure 5.5: Tuned parameter q values for DY measurements at different center-of-mass energies (points) for various PYTHIA and HERWIG setups (colors). The error bars on the points represent the tuning uncertainties. The tuned values are given in Appendix B.3. For each generator setup, the function $b\sqrt{s}^a$ is fitted to the points and shown as a line, assuming the same slope a for all the settings. The $\chi^2_{\text{lin.}}/\text{NDF}$ and p -value of the combined linear fit is given in the plot. The uncertainty in each fit is shown as a colored band and corresponds to the up and down variations of the fit parameters, propagated from the tune uncertainties. The CASCADE predictions (CAS3) [169, 170] are also fitted separately with the function $b\sqrt{s}^a$ for comparison with PYTHIA and HERWIG.

Alternatively, the function $b\sqrt{s}^a$ is also fitted with free-floating slopes, and gives the resulting slopes 0.163 ± 0.006 , 0.164 ± 0.006 , 0.170 ± 0.008 , 0.160 ± 0.008 and 0.155 ± 0.007 for the CP3, CP4, CP5, CH2 and CH3 tunes, respectively, which are compatible with each other. Such an energy-scaling model of the intrinsic k_T parameter can be implemented into the generators for an improved description of data.

Besides the intrinsic movements of partons in colliding hadrons, the DY $p_T(\ell^+\ell^-)$ distribution is also contributed by the ISR. As a result, the tuned intrinsic k_T parameters practically compensate for the ISR contribution below the cutoff scale in describing the measured DY differential cross section. To investigate the impacts of the ISR cutoff scale on the intrinsic k_T tunes, we perform the tunes under shifted ISR cutoff scales, controlled by the regularization parameters `SPACESHOWER:PT0REF` in PYTHIA and `SUDAKOVCOMMON:PTMIN` in HERWIG. In PYTHIA, the `SPACESHOWER:PT0REF` parameter is changed from the default value 2 GeV to a lower value 1 GeV. In HERWIG, the `SUDAKOVCOMMON:PTMIN` parameter is changed from the default value 1.22 GeV to 0.7 GeV. The lower cutoff scales in the test induce more low-energy ISR contributions to the low $p_T(\ell^+\ell^-)$ DY distribution, but still allow the generators to have reasonable descriptions for the DY $p_T(\ell^+\ell^-)$ measurements after the intrinsic k_T tunes. Following the same tuning process and uncertainty estimation as the procedures used in Figure 5.5, the results are obtained in the PYTHIA CP5 and HERWIG CH3 setups with lower ISR regularization parameters, as shown in Figure 5.6.

As similar trends of energy scaling are shown in the tunes with lower ISR cutoff scales to the ones in Figure 5.5, the function $b\sqrt{s}^a$ is also fitted for the tunes with lower ISR cutoff scales. Figure 5.6 shows the combined fit for the tuned parameters under the PYTHIA CP5 setups in the two cases of the default and lower ISR cutoff scales, and the one under the HERWIG CH3 setups, also in the two cases of the default and lower ISR cutoff scales. The fits are performed allowing free-floating slopes a and offsets $\log_{10}(b)$ for all the lines. The slope parameters in the PYTHIA cases are 0.172 ± 0.009 (default) and 0.170 ± 0.009 (lower ISR cutoff), and the slopes for the HERWIG cases are 0.153 ± 0.007 (default) and 0.130 ± 0.009 (lower ISR cutoff). As measures of the fitting quality, the $\chi^2_{\text{lin.}}/\text{NDF}$ and p -values of the fits are 1.71 and 0.04 for PYTHIA (1.15 and 0.30 for HERWIG), respectively. The reported p -values are the significance of the χ^2 tests with 16 degrees of freedom from 20 tuned results and 4 parameters to be fitted, including 2 slope parameters and 2 offset parameters. The fitting results indicate that the variations of the ISR cutoff scales do not change the trends of the energy-scaling behaviors in the intrinsic k_T tunes, and only a mild change of the slope is found for very low values of the cutoff scale.

5.5.3 Impacts of the hard-scattering scale

The hard-scattering scale Q of the DY process can be approximated by the invariant mass of the lepton pairs $m_{\ell\ell}$. To explore the dependence of the intrinsic k_T parameters on Q , the tunes are performed to the DY differential cross section versus $p_T(\ell^+\ell^-)$ measured in exclusive ranges of the $m_{\ell\ell}$ for $\sqrt{s} = 38.8$ GeV, and 8, 8.16, and 13 TeV, in which measurements in multiple $m_{\ell\ell}$ ranges are available. The tuned results versus $m_{\ell\ell}$ in PYTHIA CP5 and HERWIG CH2 settings are shown in Figure 5.7, and the intrinsic k_T parameters are stable for various $m_{\ell\ell}$ ranges at the same \sqrt{s} . This leads to the hypothesis that the tuned parameters are identical for all the $m_{\ell\ell}$ ranges at a fixed \sqrt{s} . Based on the hypothesis, the results of constant fits to the tuned parameters for each \sqrt{s} and generator setting are also shown in Figure 5.7. The fits are compatible with the tuned results as indicated by the values of $\chi^2_{\text{const.}}/\text{NDF}$ close to 1. This investigation of the

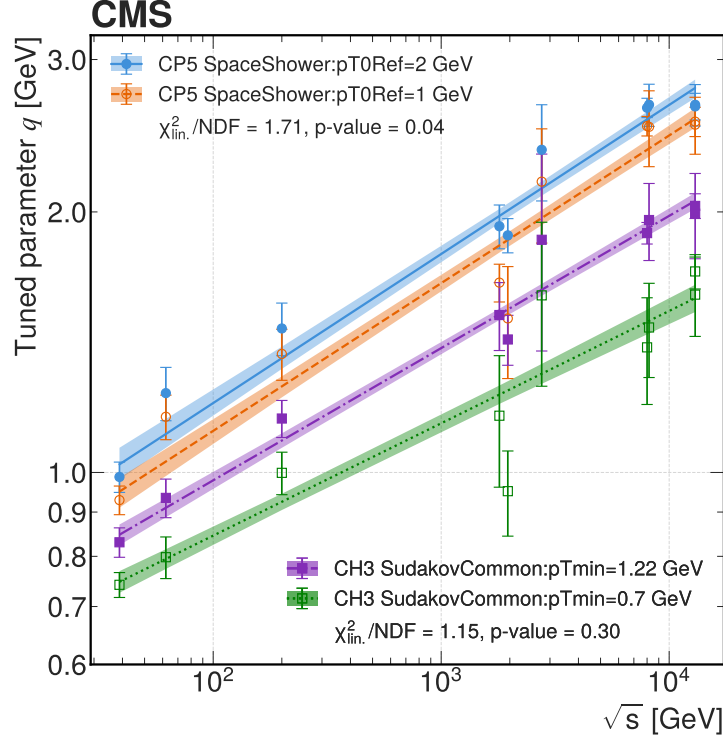


Figure 5.6: Tuned parameter q values for DY measurements at different center-of-mass energies (points) for various generator settings (lines and bands). The error bars on the points represent the tuning uncertainties. The tuned values are given in Appendix B.3. For the PYTHIA CP5 setup, the parameter SPACESHOWER:PT0REF is set to 1 GeV (orange dashed) or its default value of 2 GeV (blue solid). For the HERWIG CH3 setup, the parameter SUDAKOVCOMMON:PTMIN is set to 0.7 GeV (green dotted) or its default value of 1.22 GeV (purple dash-dotted). The function $b\sqrt{s}^a$ is fitted to the points of each generator setting and shown as a line, allowing free-floating slopes a and offsets $\log_{10}(b)$. The uncertainty in each fit is shown as a colored band and corresponds to the up and down variations of the fit parameters, propagated from the tune uncertainties.

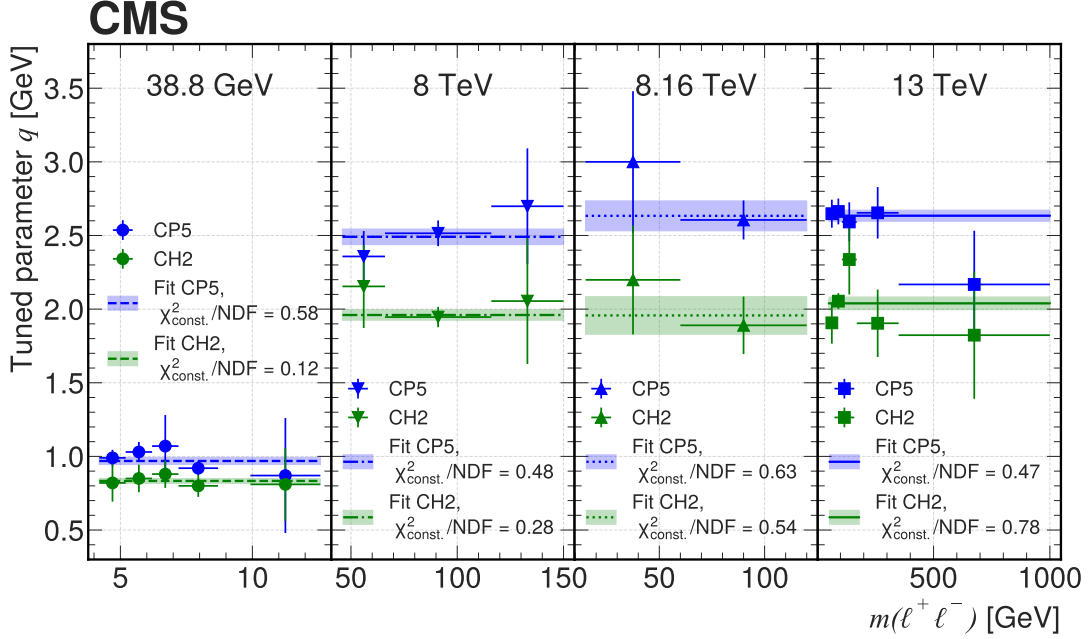


Figure 5.7: Tuned parameter values (points) for DY measurements with respect to the lepton-pair invariant mass at four different center-of-mass energies (panels) for the PYTHIA CP5 (blue) and HERWIG CH3 (green) setups. The error bars on the points represent the tuning uncertainties. The tuned values are given in Appendix B.3. For each generator setup, a constant is fitted to the points and shown as a line. The uncertainty in each fit, propagated from the tune uncertainties, is shown as a colored band.

Q -dependence of the tunes under fixed \sqrt{s} complements previous studies on the \sqrt{s} -dependence of the resummed non-perturbative Sudakov factor controlling the soft ISR under fixed Q , as summarized in Ref. [206].

5.5.4 Interpretation

The energy scaling behavior shown in Figure 5.5 and 5.6 can lead to deeper insights about the non-perturbative QCD contributions in the low $p_T(\ell^+\ell^-)$ region, as the perturbative effects can be extracted from the comparison among different generator setups. On one hand, the impacts of perturbative QCD models are demonstrated by the variations of intercepts in the fitting lines under different generator settings, which differ in perturbative modeling. For example, the PYTHIA and HERWIG generators use different PS models, PYTHIA using p_T -ordered showering, while HERWIG using angular-ordered showering, which results in more low-energy ISR in the DY events generated by HERWIG. Therefore, less compensation is needed from intrinsic k_T tunes in HERWIG to describe the low $p_T(\ell^+\ell^-)$ DY cross section, corresponding with the smaller intercepts in the fits to HERWIG tunes than the PYTHIA cases. On the other hand, the slopes of the linear fits of $\log_{10}(q) - \log_{10}(\sqrt{s})$ are similar for these PYTHIA and HERWIG tunes combined with the DY matrix elements computed at NLO, despite their diversity in the PDF, the order in the parton shower, and the lower cutoff scale of showering. In addition, the tuning results are not or weakly dependent on the hard-scattering scales under fixed collision energies within the measurement precision, as shown in Figure 5.7. This suggests the scaling behavior of the tuned q with increasing \sqrt{s} is not related to the hard-scattering scales. Stable under variations of perturbative QCD models and hard-scattering scales, the energy-scaling behaviors of the tunes potentially originate from non-perturbative QCD effects, and point to the need for

further theoretical investigations. In higher-order or resummed calculations of the DY $p_T(\ell^+\ell^-)$, the non-perturbative effects are increasingly incorporated into the matrix element calculation. Therefore, the energy-scaling behaviors of intrinsic k_T tunes can be different, and a weaker dependence on \sqrt{s} is expected.

The CASCADE generator [204] (“CAS3” in Figure 5.5) has a different approach in modeling the ISR, which accounts for the effect of low-energy gluons with a non-perturbative Sudakov form factor [180] using the parton branching method [168, 169], and results in behaviors of intrinsic k_T tunes different from those in PYTHIA and HERWIG. The intrinsic k_T parameter in CASCADE [169, 170] is less dependent on the collision energy than the other cases, as shown in Figure 5.5. The energy-scaling behavior observed in PYTHIA and HERWIG models may be necessary to account for the non-perturbative and soft gluon emissions not included in their parton shower.

To interpret the results in Figure 5.7, we define the fractions of the hadron longitudinal momentum carried by the incoming quarks in the DY process to be x_1 and x_2 . $m_{\ell\ell}$ is given by $m_{\ell\ell} = x_1x_2\sqrt{s}$ at leading order. Since the tuned results are stable versus $x_1x_2\sqrt{s}$ for given values of \sqrt{s} , the intrinsic parameters are independent of x_1x_2 within the present precision. The effect of x_1/x_2 on the intrinsic k_T tunes is demonstrated by the comparison of the tunes using the CMS and LHCb measurements at $\sqrt{s} = 13$ TeV, because the two detectors have different acceptance regions for the pseudorapidity of the lepton pairs from the DY process, which are correlated with the rapidity y of their center of mass, related to x_1/x_2 by $y = \frac{1}{2} \ln(x_1/x_2)$. As shown in Figure 5.5, the tunes using the two experiments agree within their uncertainties, and indicate that the intrinsic k_T tunes are stable under x_1/x_2 variations. The stability of results versus x_1x_2 and x_1/x_2 suggests the independence of the intrinsic k_T parameter from the momentum fractions x_1 and x_2 individually.

6 Search for soft unclustered energy patterns

This chapter presents a search for SUEPs in the gluon-gluon fusion channel of pp collisions using data collected by the scouting stream of the CMS experiment. The SUEPs are predicted by certain hidden-valley models, which extend the SM to include QCD-like dark sectors. These signatures arise from nonperturbative particle emissions in the dark sector, analogous to the parton shower and hadronization processes observed in QCD. The analysis leverages our understanding of event sphericity from Chapter 4 and employs it, alongside track multiplicity, as a key observable to distinguish SUEPs from the QCD background. A data-driven, extended ABCD method is used to estimate this background. The approach provides high sensitivity across a broad range of signal model parameter space.

The author has contributed significantly to all aspects of this work – from design to implementation – and currently serves as the contact person for the analysis, leading its approval within the EXOTIC Physics Analysis group at the CMS. The analysis has been unblinded and it is currently under the approval process, with a public release targeted for spring 2025 and subsequent publication planned in Physics Review Letter.

6.1 Motivation

The analysis on SUEPs is a search for unconventional signatures of BSM particle production based on event shapes of the pp collisions at the LHC. Besides the theoretical motivation of the existence of BSM particles, which is required for the puzzles not explained by the SM of particle physics such as the hierarchy problem and the dark matter, the search is also motivated by the current status of the LHC data taking and the its tight constraints set on many of the benchmark BSM theories with signatures such as missing transverse energy from long-lived particles, heavy resonances, displaced vertices or disappearing tracks from decay of BSM particles. As the LHC changes from increasing the collision energy to accumulating higher luminosity, the searches for rare events with BSM signatures are able to detect the potential signals with high sensitivity, but have not discovered new physics so far. Attention has been paid towards challenging signatures quantified in phase spaces of unconventional observables, which might have escaped the previous LHC searches.

As discussed in Section 2.1, certain hidden-valley models with a dark QCD sector can lead to anomalous production of large multiplicity of soft isotropic particles from the decay of a heavy mediator, unsuppressed large-angle emission of dark mesons and their prompt transition into SM particles. The resulting signature is referred to as a soft-unclustered-energy pattern. Similar signatures are predicted by quantum black hole productions at the existence of extra dimensions, and the electroweak sphaleron productions. In the current LHC experiments, no dedicated trigger has been designed targeting such patterns, and the enormous pileup and QCD multijet background make it challenging to distinguish such signatures. From the side of signal simulation, difficulties are also faced in producing rigorous predictions of the SUEP signatures and simulating the signal events in detail. Besides the SUEP search for the heavy mediator

production from gluon fusions with the data collected by the offline stream, and the ongoing searches for the SUEP from a Higgs decay associated with a vector boson, the analysis presented in this section utilizes online-reconstructed physics objects from data collected by the CMS Run 2 scouting stream and targets the SUEP signals from gluon fusions in a phase space of data different from that used in the offline analysis. With the advantage of a lower trigger threshold enabled by the smaller event sizes in the scouting stream, the analysis on this dataset can probe signals with lower heavy mediator masses than the offline analysis.

To overcome the large QCD background, the track multiplicity and sphericity as a characteristic event shape variable of the SUEP candidate are used to discriminate the SUEP signal against the background. Furthermore, a data-driven background estimation method is used to extrapolate the signal-region background from the control region (CR) event yield and kinematics, in order to avoid using the poorly modeled MC simulation of the QCD background.

6.2 Data and simulations

6.2.1 Scouting data

This search for the SUEP signals is performed on the pp collision data of the CMS Run 2 (2016-2018) at $\sqrt{s} = 13$ TeV. As there is no dedicated trigger for the SUEP signature, and the heavy mediators in the signal models are produced at a relatively higher energy scale than the average pp collisions, the analysis uses the dataset collected by the `Scouting_PFHT410` high-level trigger (HLT), which selects the events with H_T larger than 410 GeV, the H_T defined as the scalar p_T sum of AK4 jets with $p_T \gtrsim 30$ GeV in the online reconstruction. The main unprescaled level-1 (L1) trigger seeding the HLT is `L1_HTT240`. A small part of the data in the 2018 run was removed from the analysis because of using the wrong L1 trigger on muons instead of H_T . This includes the data from runs 321712 to 322040 and an integrated luminosity of about 5 fb^{-1} .

The scouting stream only keeps the physics objects from online reconstruction by the Particle Flow (PF) algorithm [207] without saving the raw data from the detector. This significantly reduces the event size compared to the raw data events and allows for a higher event rate than the raw data, given the limited bandwidth of data transmission and storage. As a result, the H_T threshold of the scouting HLT used for this analysis is lower than that used in the offline analysis: $H_T > 900$ (1050) GeV for 2016 (2017 and 2018). The lower HLT threshold results in a higher acceptance of the SUEP signals, which is beneficial for the sensitivity of the search, especially to the signals with low mediator mass and thus relatively low H_T . The scouting stream includes the 4-momentum of all the particle flow candidates with $p_T > 0.6$ GeV reconstructed by the HLT and their associated primary vertices, which are input into the analysis. The datasets and corresponding integrated luminosities are listed in Table 6.1.

6.2.2 Simulations of background and signals

MC simulations are generated for both the background and signal processes for designing the background estimation strategy and deriving the expected exclusion limits of the search. The events are generated by the PYTHIA generator, and then input into the GEANT4 package [139] simulation of the CMS detector response.

The simulated events are passed to the same online reconstruction algorithm as used for scouting data, which gives trigger-level physics objects. The simulated events are from the

Table 6.1: Particle Flow Scouting datasets and luminosity

| Dataset | Luminosity (fb^{-1}) |
|-------------------------------|---------------------------------|
| /ScoutingPFHT/Run2016B-v2/RAW | 5.826 |
| /ScoutingPFHT/Run2016C-v2/RAW | 2.602 |
| /ScoutingPFHT/Run2016D-v2/RAW | 4.286 |
| /ScoutingPFHT/Run2016E-v2/RAW | 4.066 |
| /ScoutingPFHT/Run2016F-v1/RAW | 3.137 |
| /ScoutingPFHT/Run2016G-v1/RAW | 7.653 |
| /ScoutingPFHT/Run2016H-v1/RAW | 8.740 |
| /ScoutingPFHT/Run2017C-v1/RAW | 8.318 |
| /ScoutingPFHT/Run2017D-v1/RAW | 4.248 |
| /ScoutingPFHT/Run2017E-v1/RAW | 9.315 |
| /ScoutingPFHT/Run2017F-v1/RAW | 13.540 |
| /ScoutingPFHT/Run2018A-v1/RAW | 14.027 |
| /ScoutingPFHT/Run2018B-v1/RAW | 7.067 |
| /ScoutingPFHT/Run2018C-v1/RAW | 6.895 |
| /ScoutingPFHT/Run2018D-v1/RAW | 26.757 |
| 2016 total | 36.310 |
| 2017 total | 35.420 |
| 2018 total | 54.746 |
| Combined total | 126.476 |

following campaigns of the CMS sample production:

- 2016apv: RunIISummer20UL16MiniAODAPVv2
- 2016: RunIISummer20UL16MiniAODv2
- 2017: RunIISummer20UL17MiniAODv2
- 2018: RunIISummer20UL18MiniAODv2

The scouting simulation of 2016 and 2016apv background samples are not available in CMS central production, thus the background-to-data comparison is only given for the other years in the following sections. Additional interactions per bunch crossing (pileup) are also simulated, and the MC events are reweighted to have the same pileup distributions as the data for each year.

Signal modeling and simulations

In the signal models, the dark sector is coupled to the via a heavy (pseudo)scalar mediator (S), produced by gluon fusions through the effective coupling $SG_{\mu\nu}G^{\mu\nu}$ or $SG_{\mu\nu}\tilde{G}^{\mu\nu}$. The scalar mediator goes through a quasi-conformal showering to a large multiplicity of pseudo-scalar dark mesons (ϕ_D). In the signal generation, the momenta of the dark mesons are described by a Boltzmann distribution, as shown in eq. 2.47, in which the parameter m_ϕ is the mass of the dark meson, and the "temperature" parameter T describes the scale of the hadronization in the dark sector. The dark mesons subsequently decay into dark photon (A') pairs via the coupling operator $\phi A'^{\mu\nu} A'_{\mu\nu}$. The dark photon pairs kinematically mix with the SM sectors and promptly decay to pairs of SM particles.

The search is performed on a series of benchmark signal models with various heavy scalar masses m_S with negligible widths, dark meson masses m_ϕ , temperature T , the dark photon

masses $m_{A'}$ and decay modes of dark photons to SM particles. The masses of S in the benchmark models (m_S), as well as the cross sections and their uncertainties, are listed in Table 6.2 as recommended by the LHC Higgs Working Group Yellow Report [96]. Three scenarios of dark photon masses and decay modes are considered

- "Leptonic" mode: $m_{A'} = 0.5$ GeV, $A' \rightarrow e^+e^-, \mu^+\mu^-, \pi^+\pi^-$ with branching fractions 40, 40 and 20%.
- "Hadronic" mode: $m_{A'} = 0.7$ GeV, $A' \rightarrow e^+e^-, \mu^+\mu^-, \pi^+\pi^-$ with branching fractions 15, 15 and 70%.
- "Generic" mode: $m_{A'} = 1.0$ GeV, $A' \rightarrow \pi^+\pi^-$ with branching fractions 100%.

For each scenario and m_S , a scan on the grid points of the two-dimensional plane of m_ϕ and T is performed for the benchmark signal generation. The region of scan is $2m_{A'} \leq m_\phi \leq 8$ GeV and $0.25 \leq T/m_\phi \leq 4$.

The Ultra Legacy samples of benchmark signals are generated with a PYTHIA plugin [208] interfaced with the CMS Software (CMSSW). The program generates Higgs-like scalar particle S via gluon fusions with the given m_S and cross section, and then generates the 4-momenta of dark mesons one by one in the rest frame of S by sampling from the Maxwell-Boltzmann distribution eq. 2.47, until the energy sum of all the dark mesons equal to m_S . Afterwards, the 4-momenta of dark mesons are rebalanced for energy-momentum conservation, and then boosted to the lab frame. The kinematics of dark meson decay to dark photons $\phi \rightarrow A'A'$ and dark photon decay to SM particles are generated according to the three benchmark scenarios.

Table 6.2: Gluon fusion cross sections (N3LO) for BSM scalars in pp collisions at $\sqrt{s} = 13$ TeV

| m_S (GeV) | XS (pb) | Theory + (%) | Theory - (%) | TH Gaussian (%) | \pm (PDF+ α_s) (%) |
|-------------|----------|--------------|--------------|-----------------|------------------------------|
| 125 | 4.52e+01 | 1.7 | -3.7 | ± 2.1 | ± 3.2 |
| 200 | 1.69e+01 | 1.3 | -3.2 | ± 1.8 | ± 3.0 |
| 300 | 6.59e+00 | 1.5 | -3.2 | ± 1.8 | ± 3.0 |
| 400 | 3.16e+00 | 1.6 | -3.3 | ± 1.9 | ± 3.1 |
| 500 | 1.71e+00 | 1.7 | -3.5 | ± 2.0 | ± 3.3 |
| 600 | 1.00e+00 | 1.8 | -3.6 | ± 2.1 | ± 3.5 |
| 700 | 6.21e-01 | 1.9 | -3.7 | ± 2.1 | ± 3.8 |
| 800 | 4.02e-01 | 2 | -3.8 | ± 2.2 | ± 4.2 |
| 900 | 2.69e-01 | 2.1 | -3.8 | ± 2.2 | ± 4.6 |
| 1000 | 1.85e-01 | 2.2 | -4 | ± 2.3 | ± 5.0 |
| 1200 | 9.26e-02 | 2.3 | -4.1 | ± 2.4 | ± 5.9 |
| 1500 | 3.69e-02 | 2.4 | -4.3 | ± 2.5 | ± 7.3 |
| 2000 | 9.60e-03 | 2.6 | -4.5 | ± 2.6 | ± 9.7 |

Background simulations

The main background for the SUEP search comes from the QCD multijet process. Although the background simulations do not affect the data-driven background estimation, they are used to validate the distributions of the key variables in the data, and to design and optimize the background estimation strategy. The background samples are centrally produced by the CMS Collaboration, the sample names listed in Table 6.3, 6.4 and 6.5. The QCD samples are generated in slices of H_T by MADGRAPH5_amc@NLO [209], interfaced with PYTHIA 8 [210, 211] for parton showering and hadronization. The PYTHIA CP5 tune [142] is used to model the UE under the PDFs NNPDF 3.1 [212].

Table 6.3: Dataset names and cross sections for the QCD background in 2016.

| Process | Dataset Name | Cross Section [pb] |
|-------------------|--|--------------------|
| H_T -binned QCD | QCD_HT50to100_TuneCP5_PSWeights_13TeV-madgraphMLM-pythia8 | 186100000.0 |
| H_T -binned QCD | QCD_HT100to200_TuneCP5_PSWeights_13TeV-madgraphMLM-pythia8 | 236300000.0 |
| H_T -binned QCD | QCD_HT200to300_TuneCP5_PSWeights_13TeV-madgraphMLM-pythia8 | 1554000.0 |
| H_T -binned QCD | QCD_HT300to500_TuneCP5_PSWeights_13TeV-madgraphMLM-pythia8 | 323800.0 |
| H_T -binned QCD | QCD_HT500to700_TuneCP5_PSWeights_13TeV-madgraphMLM-pythia8 | 30280.0 |
| H_T -binned QCD | QCD_HT700to1000_TuneCP5_PSWeights_13TeV-madgraphMLM-pythia8 | 6392.0 |
| H_T -binned QCD | QCD_HT1000to1500_TuneCP5_PSWeights_13TeV-madgraphMLM-pythia8 | 1118.0 |
| H_T -binned QCD | QCD_HT1500to2000_TuneCP5_PSWeights_13TeV-madgraphMLM-pythia8 | 108.9 |
| H_T -binned QCD | QCD_HT2000toInf_TuneCP5_PSWeights_13TeV-madgraphMLM-pythia8 | 21.93 |

Table 6.4: Dataset names and cross sections for the QCD background in 2017.

| Process | Dataset Name | Cross Section [pb] |
|-------------------|---|--------------------|
| H_T -binned QCD | QCD_HT50to100_TuneCP5_PSWeights_13TeV-madgraph-pythia8 | 187300000.0 |
| H_T -binned QCD | QCD_HT100to200_TuneCP5_PSWeights_13TeV-madgraph-pythia8 | 235900000.0 |
| H_T -binned QCD | QCD_HT200to300_TuneCP5_PSWeights_13TeV-madgraph-pythia8 | 1555000.0 |
| H_T -binned QCD | QCD_HT300to500_TuneCP5_PSWeights_13TeV-madgraph-pythia8 | 324500.0 |
| H_T -binned QCD | QCD_HT500to700_TuneCP5_PSWeights_13TeV-madgraph-pythia8 | 30310.0 |
| H_T -binned QCD | QCD_HT700to1000_TuneCP5_PSWeights_13TeV-madgraph-pythia8 | 6444.0 |
| H_T -binned QCD | QCD_HT1000to1500_TuneCP5_PSWeights_13TeV-madgraph-pythia8 | 1127.0 |
| H_T -binned QCD | QCD_HT1500to2000_TuneCP5_PSWeights_13TeV-madgraph-pythia8 | 109.8 |
| H_T -binned QCD | QCD_HT2000toInf_TuneCP5_PSWeights_13TeV-madgraph-pythia8 | 21.98 |

6.3 Event selection

This section describes multiple levels of selections applied on the data and simulations to clean up the events 6.3.1, 6.3.2, reconstruct the detector-level correspondences of decay products from the heavy scalar particles in the signal models 6.3.3, and distinguish the signals from the background 6.3.4.

6.3.1 Scouting strategy and pre-selections

As introduced in Section 6.2.1, the analysis uses the H_T -based L1 triggers, which select the events depositing substantial energy in the calorimeter, followed by the H_T -based HLT, which selects the events based on the scalar p_T sum of online reconstructed AK4 jets. Figure 6.1(left) shows the distributions of H_T for the QCD MC and signals with $m_\phi = 3 \text{ GeV}$, $T = 3 \text{ GeV}$, $A' \rightarrow \pi^+ \pi^-$ in 2018 before applying the trigger selections. The H_T in the figure is the offline emulation of the HLT-level H_T , computed as the scalar p_T sum of the HLT-level AK4 jets with additional selections for noise and pileup removal, as recommended by the JETMET POG [213] and listed below.

- $|\eta| < 2.6$
- Neutral hadron energy fraction < 0.90
- Neutral electro-magnetic energy fraction < 0.90
- Muon fraction < 0.80
- Charged electro-magnetic fraction < 0.80
- Charged hadron energy fraction > 0.0
- Charged multiplicity > 0
- Total multiplicity > 1

Table 6.5: Dataset names and cross sections for the QCD background in 2018.

| Process | Dataset Name | Cross Section [pb] |
|-------------------|---|--------------------|
| H_T -binned QCD | QCD_HT50to100_TuneCP5_PSWeights_13TeV-madgraph-pythia8 | 187300000.0 |
| H_T -binned QCD | QCD_HT100to200_TuneCP5_PSWeights_13TeV-madgraph-pythia8 | 23590000.0 |
| H_T -binned QCD | QCD_HT200to300_TuneCP5_PSWeights_13TeV-madgraph-pythia8 | 1555000.0 |
| H_T -binned QCD | QCD_HT300to500_TuneCP5_PSWeights_13TeV-madgraph-pythia8 | 324500.0 |
| H_T -binned QCD | QCD_HT500to700_TuneCP5_PSWeights_13TeV-madgraph-pythia8 | 30310.0 |
| H_T -binned QCD | QCD_HT700to1000_TuneCP5_PSWeights_13TeV-madgraph-pythia8 | 6524 |
| H_T -binned QCD | QCD_HT1000to1500_TuneCP5_PSWeights_13TeV-madgraph-pythia8 | 1127.0 |
| H_T -binned QCD | QCD_HT1500to2000_TuneCP5_PSWeights_13TeV-madgraph-pythia8 | 109.8 |
| H_T -binned QCD | QCD_HT2000toInf_TuneCP5_PSWeights_13TeV-madgraph-pythia8 | 21.98 |

- In 2018 data taking eras B, C, and D, the endcaps of the hadron calorimeter failed to cover the phase space $-3 < \eta < -1.3$ and $-1.57 < \phi < 0.87$. Therefore, the jets in these regions and eras of data are vetoed.

The number of events drops rapidly with H_T , motivating the H_T cut to be set to the lowest threshold available. The PF scouting stream from the "DST_HT410_PFScouting_v*" trigger has the lowest unprescaled H_T threshold for the events with track information saved. Figure 6.1(right) shows the H_T distribution of the background and signals passing the trigger selection in 2018.

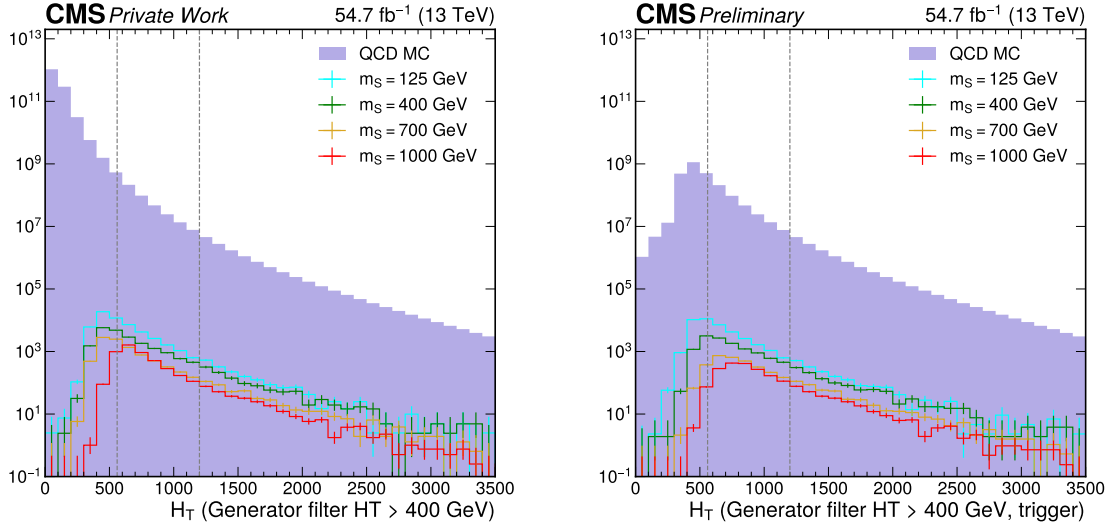


Figure 6.1: Left: H_T distributions of signals with various mediator masses passing the generator level selection $H_T > 400$ GeV and the QCD background. No trigger or offline cuts are applied. The requirement of $H_T > 560(1200)$ GeV is shown as a vertical gray line for the offline H_T cut for the scouting (offline) analysis. Right: H_T distributions of the QCD background and signals passing the trigger. The requirement of $H_T > 560(1200)$ GeV is shown as a vertical gray line.

In addition to the selection from the trigger, a selection on the offline emulated H_T is applied to avoid the potential bias from the variations in trigger performances along the data-taking periods. Figure 6.2 shows the trigger efficiency as a function of H_T in background and signal simulations and the reference data. The trigger efficiencies in data is measured from the `ScoutingPFCommissioning` dataset, in which the events are required to pass the `DST_DoubleMu3_noVtx_CaloScouting_v*` reference trigger, given that the selection on muons is irrelevant to H_T , thus the H_T distribution of these events is not biased by the reference trigger. In the $H_T > 500$ GeV region, the simulation of QCD background matches the data efficien-

cies and both are near 1. The discrepancies between the data and background efficiencies as a function of H_T are derived as the trigger scale factors to correct the signals by H_T -dependent weighting. Based on the trigger efficiency comparison, the $H_T > 560$ GeV requirement is used as an offline analysis selection.

In Figure 6.2(right), the trigger efficiencies have divergent behaviors for signals with different mediator masses. The signals with higher masses have a slower turn-on in the trigger efficiency as the H_T increases, because the heavier scalar mediators tend to be less boosted, and the decay products are more dispersed in the lab frame, thus the decay products are less likely to be clustered into jets in the online reconstruction and fire the H_T triggers.

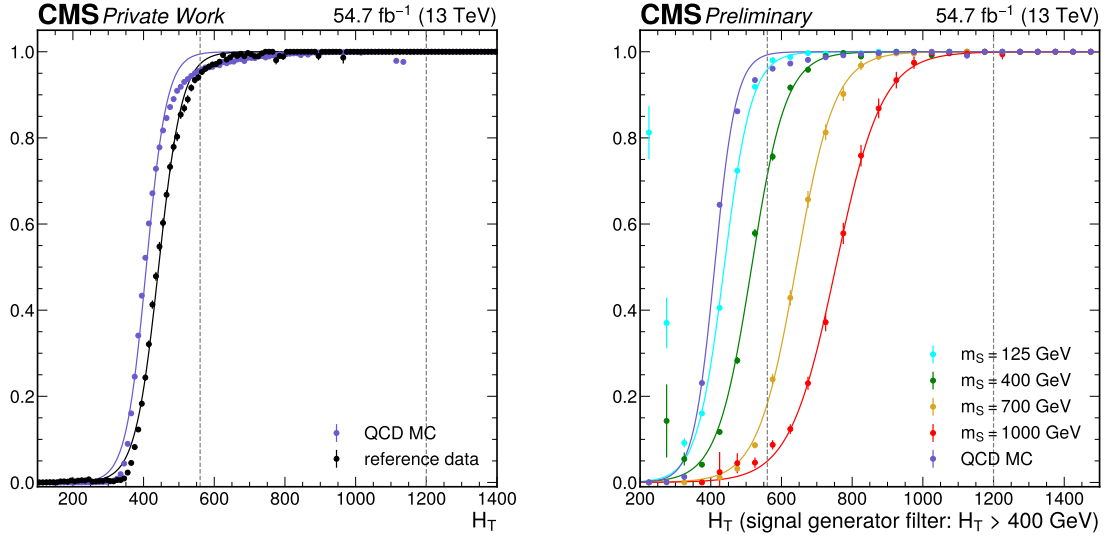


Figure 6.2: Left: Trigger efficiency for QCD MC (purple) and reference data (black) in 2018. Right: Trigger efficiency of QCD MC (purple) and signals in 2018. The fluctuations and large uncertainties at low H_T for signal samples are due to the inefficiency from the generator level filter $H_T > 400$ GeV.

The pre-selection also vetoes events with identified prompt muons and electrons, to search in a phase space exclusive to that investigated by other analyses searching for SUEPs from Higgs decays associated with vector bosons. The lepton veto criteria are listed as follows:

- Veto global muons with $p_T \geq 25$ GeV, $d_{xy} \leq 0.02$ cm, $d_Z \leq 0.1$ cm, $\chi^2 < 0.1$, $|\eta| < 2.4$.
- Veto electrons with $p_T \geq 25$ GeV, $d_{xy} < 0.05(0.1)$ cm, $d_Z < 0.1(0.2)$ cm in barrel (endcaps) with $|\eta| < 1.444(> 1.566)$, and $|\eta| < 2.5$.

6.3.2 Selection on charged particle-flow candidates

The dataset from the PF scouting stream has the information from individual final-state particles recorded as PF candidates. This collection contains PF candidates with $p_T > 0.6$ GeV with the following information for each candidate entry:

- Particle identity and charge
- 4-momentum
- Primary vertex association

In this analysis, the reconstruction of the SUEP candidates and the following definition of discriminating variables for background reduction use charged PF candidates, in which the tracker information is available to reconstruct the trajectories and determine the association with primary vertices. The reconstruction efficiency of charged PF candidates is investigated by assigning them to truth-level final-state charged particles with $p_T > 0.5$ GeV nearest in $\Delta R = \sqrt{\Delta\eta^2 + \Delta\phi^2}$ in a one-to-one matching procedure. The charged PF candidate – truth-level particle pairs are considered as properly matched if their $\Delta R < 0.02$. The charged PF candidates not matched to truth-level particles are considered as *fakes* from the detector noise, while the truth-level particles not matched to PF candidates originate from reconstruction inefficiency. Figure 6.3 shows the matching efficiency as a function of particle p_T , η and ϕ for some benchmark signals, the efficiency defined as the ratio of the number of charged particles matched to PF candidates to the total number of charged particles in each bin. While stable and high efficiencies are achieved with particle $p_T > 10$ GeV, the low- p_T particles are essential for distinguishing the signals from the QCD background. In the preliminary study shown in Figure 6.4, the charged PF candidates with $p_T > 0.6$ GeV and associated with the primary vertex of the hardest collisions in the events are clustered into AK15 jets and the jets with the highest multiplicity per event are considered as proxies for SUEPs from the scalar mediators decay. Above 0.7 of the sphericity in the jet rest frame, the signals have much higher charged PF candidates multiplicity than the background. However, a higher threshold for the p_T selection reduces the differences. As shown by the comparison among the plots in Figure 6.4, the differences between the background and signals in charged PF candidates multiplicity become smaller as the p_T threshold increases. To benefit the sensitivity to the SUEP signals, the search prefers a low- p_T threshold for the charged PF candidate selection. Taking into account that a $p_T > 0.75$ GeV cut eliminates looping tracks in the detector, and the signal-background differences are similar in charged PF candidate distributions with $p_T > 0.6$ GeV and $p_T > 0.75$ GeV in Figure 6.4, the final PF candidate p_T threshold is set to 0.75 GeV.

The selection criteria on the HLT-reconstructed PF candidates are summarized as follows:

- Associated with the primary vertex of the hardest collision for each bunch crossing;
- Electrical charge = ± 1 ;
- $p_T > 0.75$ GeV;
- $|\eta| < 2.4$ within the coverage of the CMS outer tracker.

Figure 6.5 shows the p_T , η , ϕ and multiplicity distributions of the PF candidates passing these selection criteria and the event-level selections on the trigger and offline-emulated H_T for signal, QCD and data. The shape of the signal events is consistent with that of the QCD distributions with the important exception of the PF candidate multiplicity, where signal events tend to have more PF candidates than the average QCD events, as expected.

6.3.3 SUEP candidates as large radius jets

The H_T requirement in triggers and analysis selects SUEP from the scalar mediator decay recoiled against a high-energy ISR system. The SUEP products tend to appear as a large-radius jet containing a large multiplicity of isotropic soft particles and back-to-back in ϕ against the ISR system from QCD processes. Figure 6.6 shows the radiation patterns of a typical signal event and a QCD background event as the charged PF candidate distribution in the ϕ - η plane

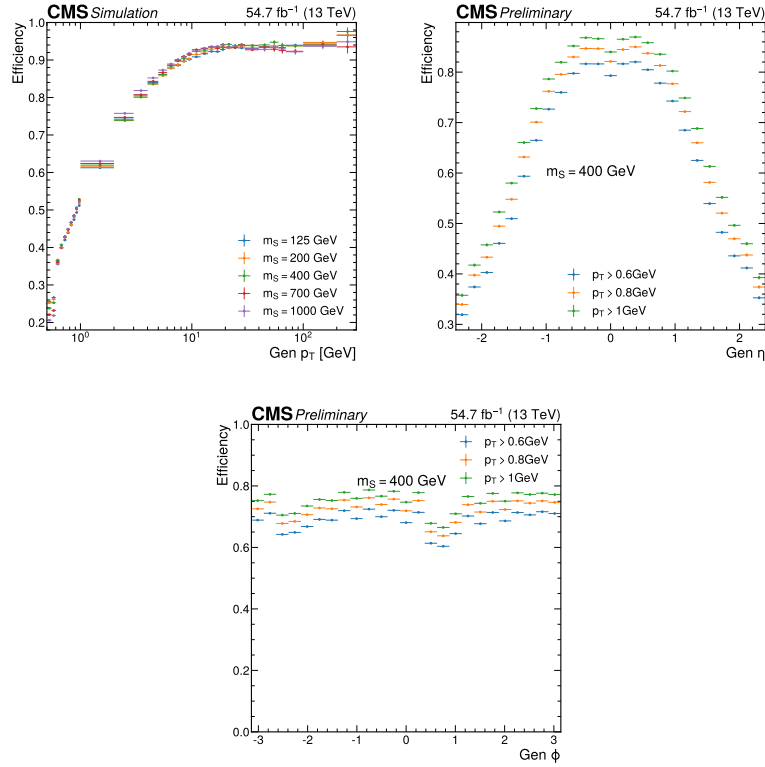


Figure 6.3: Scouting charged PF candidate efficiency with respect to p_T (left), η (middle) and ϕ (right). The efficiency is computed for different particle p_T thresholds by the ratio of truth-level charged particles passing the p_T cut that are additionally matched to a PF candidate to the total number of truth-level charged particles passing the p_T cut. Trigger selections, $H_T > 560$ GeV, particle $|\eta| < 2.4$ are required. The 2018 signals have $m_\phi = 3$ GeV, $T = 3$ GeV, and decay mode $A' \rightarrow \pi^+\pi^-$. The efficiencies versus η and ϕ are shown from the signal with $m_S = 400$ GeV. The signals with other m_S have similar behaviors.

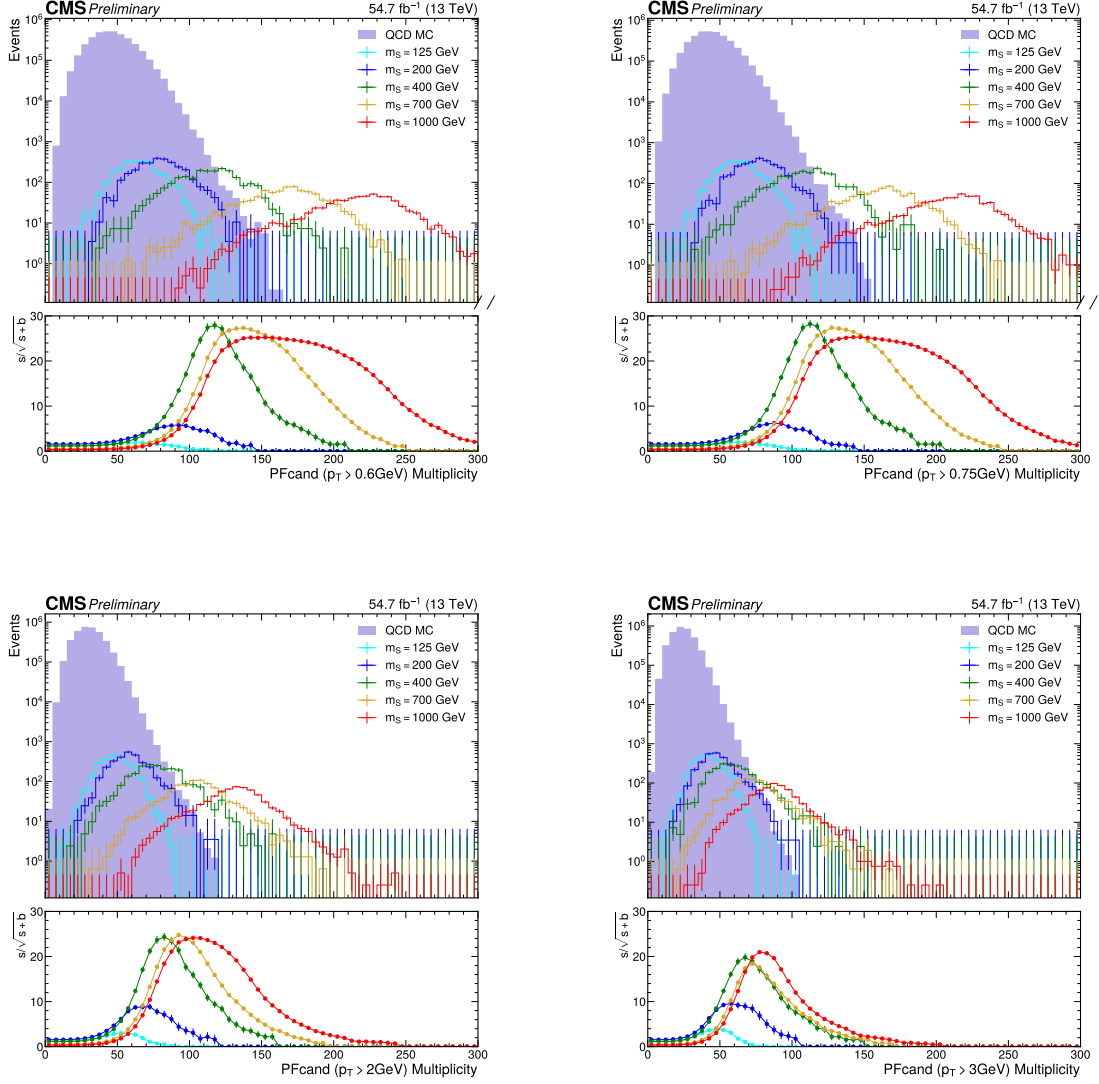


Figure 6.4: Event distributions and significances with various PF candidates p_T thresholds. Event pre-selection and SUEP jet selections are applied along with a cut of $sph_{boost}^{SUEP} > 0.7$. Upper left: $p_T > 0.6$ GeV; upper right: $p_T > 0.75$ GeV; lower left: $p_T > 2.0$ GeV; lower right $p_T > 3.0$ GeV.

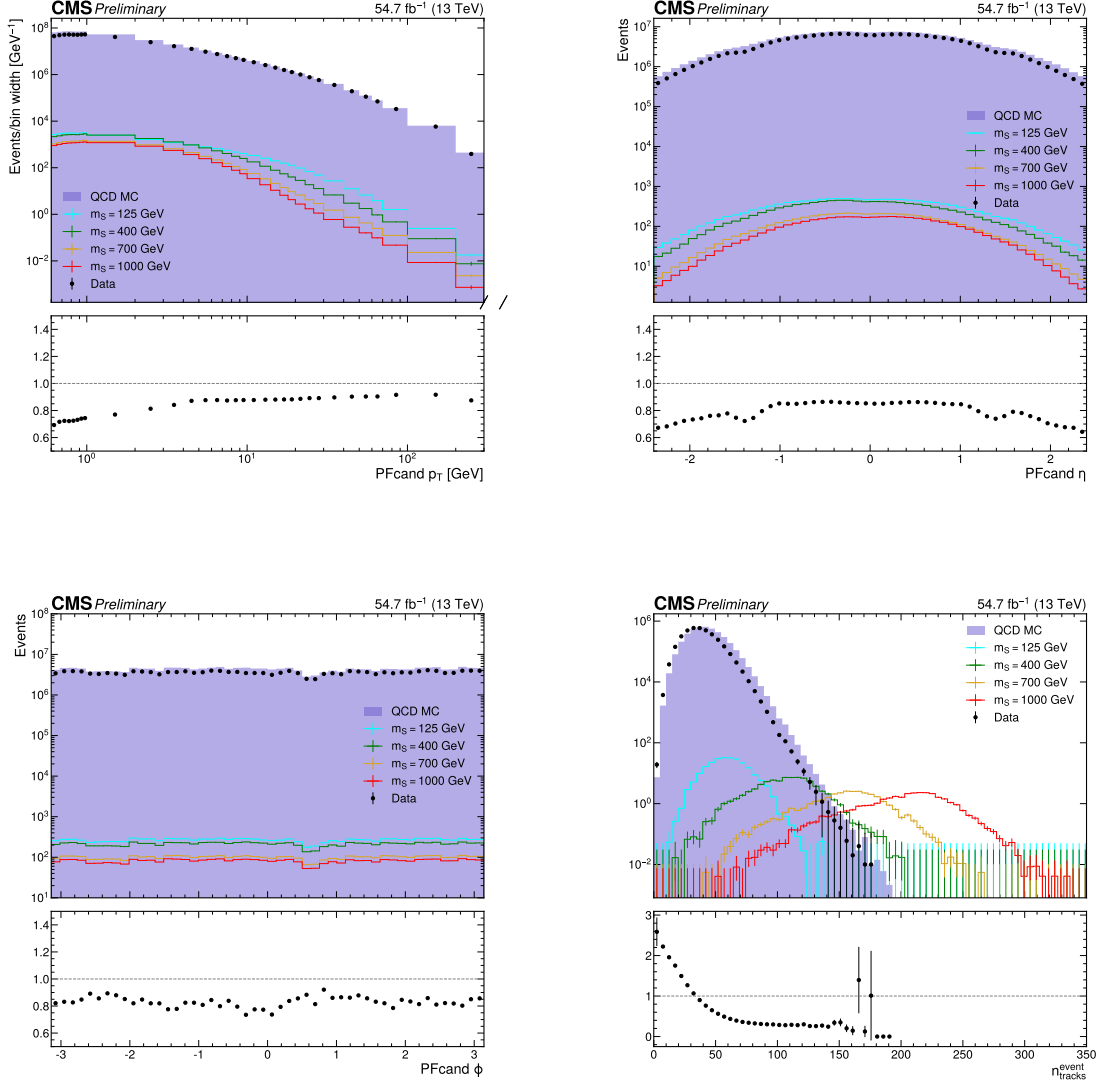


Figure 6.5: Comparison of PF candidate kinematic distributions in QCD background, signals and 1% of 2018 data: p_T , $\eta(p_T > 0.75 \text{ GeV})$, and $\phi(p_T > 0.75 \text{ GeV})$ for charged PF candidates in events passing the trigger and offline selection $H_T > 560 \text{ GeV}$, and PF candidate multiplicity in events passing additional selections on at least two AK15 jets with $p_T > 50 \text{ GeV}$. The simulations are scaled to 1% of the 2018 luminosity for comparison with 1% of the data.

of the lab frame. The difference between the two events is visible, especially in the distributions in the leading jet, originating from the differences in the radiation patterns of the signal dark sector and the SM QCD sector in the background. We use the anti- k_T algorithm with $R = 1.5$ to cluster the charged PF candidates passing the selections in Section 6.3.2. These jets are referred to as AK15 jets in the following sections. The positions and ranges within $\Delta R < 1.5$ of the jet centers are marked as circles in the figure.

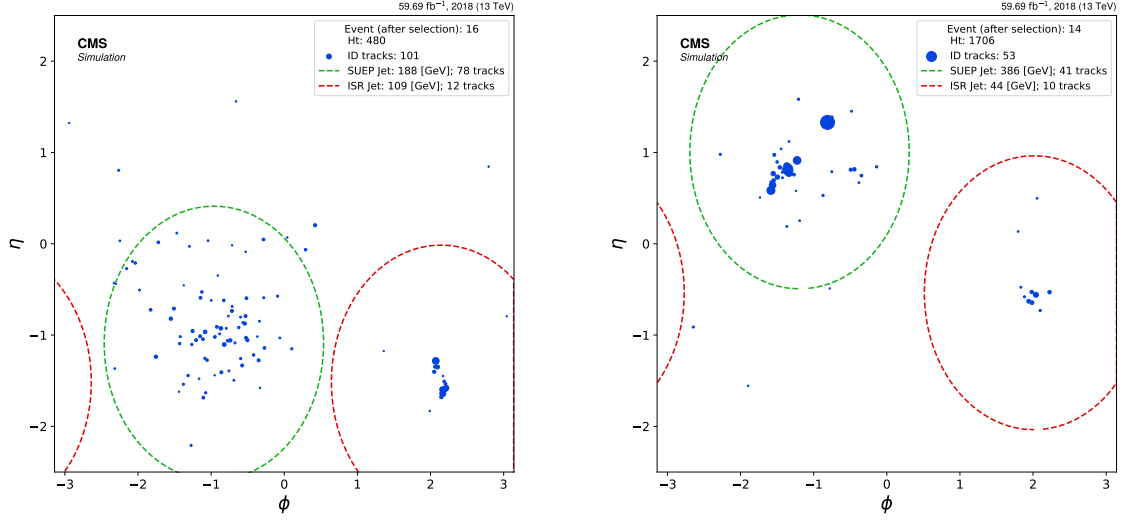


Figure 6.6: Example signal event display for a representative $m_S = 400$ GeV event and a QCD background event. Jets are clustered using the anti- k_T algorithm with $R = 1.5$. Size of the dots represents the charged PF candidate p_T .

To recover the isotropic feature of the SUEP in the leading large-radius jet, the PF candidates are boosted to the rest frame of the jet center-of-mass as an estimation of the scalar mediator momenta, and the resulting distributions are shown in Figure 6.7. The signal event shows a "ring of fire" pattern after boosting, in which the constituents in the leading jet evenly distribute in ϕ on a belt of η , while the background event does not have such a pattern. Therefore, the event shape of the jet constituents after boosting, as well as their multiplicity, can be used as discriminating variables to select the background-depleted and signal-enriched regions, and search for a potential excess in these regions.

6.3.4 Analysis selection

As discussed in Section 6.3.3, the event selection for the SUEP signature requires at least two AK15 jets from the charged PF candidates with $p_T > 50$ GeV. The two leading jets in p_T correspond to the SUEP and ISR system in the detector. The leading jet with a larger multiplicity of constituents is designated as the SUEP candidate, while the other leading jet is designated as the ISR jet. The SUEP-ISR tagging with jet clustering naturally separates the ISR systems from the SUEP candidates. The p_T cut on the jets ensures sufficient Lorentz boost of the SUEP system against the ISR, and the coverage of the SUEP jet radius to the SUEP decay products. As shown by the kinematics distributions in Figure 6.8, the p_T distributions of signal SUEP jets and ISR jets have peaks higher than 50 GeV, so that the $p_T > 50$ GeV selection keeps high signal acceptance. For all the simulated samples and data, the ISR jets tend to have lower p_T

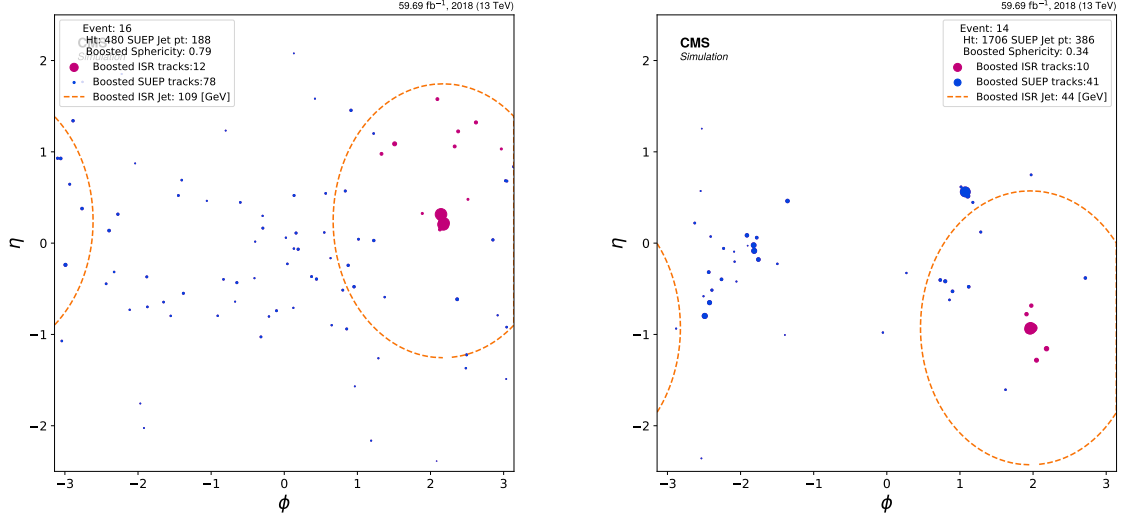


Figure 6.7: Example signal event display for a representative $m_S = 400$ GeV event and a QCD background event. Jets are clustered using the anti- k_T algorithm with $R=1.5$. The size of the dots represents the charged PF candidate p_T .

than the SUEP jets.

Figure 6.9 shows the resolutions of the SUEP candidate identification with the differences between p_T , η and ϕ of the leading multiplicity AK15 jets (SUEP jets) with regard to those of the scalar mediators in a few benchmark signal samples. The p_T difference distributions with peaks near zero suggest that the Lorentz boost of the SUEP system is accurate in most cases. The detector-level SUEP candidates tend to have lower p_T in most cases than the scalar mediators, mainly because the neutral particles from the scalar mediator decay are not taken into account in the jet clustering. The $\Delta\eta$ and $\Delta\phi$ between the SUEP jets and the scalar mediators also have peaks at zero, verifying that this method correctly selects the SUEP decay products in most cases. The events with $\Delta\phi$ near π for low mass signals come from misidentification of the ISR jet as the SUEP jet, but the fraction of the misidentified events is much smaller than the ones close to the scalar mediators.

As introduced in Section 6.3.3, the isotropic feature of the SUEP can be used to distinguish the signal from the QCD background. After boosting the constituents of the SUEP jet to the rest frame, the sphericity ($S_{boosted}^{SUEP}$) of these constituents is calculated to identify the "ring of fire" signature. The definition of the sphericity variable is found in Section 4.2, using the case $r = 1$, which has the advantage of being infrared and collinear (IRC) safe and thus less dependent on the details of the dark QCD models. As shown in Figure 6.10, the signals tend to have higher sphericity and number of constituents in the SUEP jet than the QCD background. Therefore, the sphericity and constituent multiplicity of the SUEP ($n_{constituent}^{SUEP}$) are used as the key discriminating variables to define the selection criteria for the signal region (SR). The SR requires $S_{boosted}^{SUEP} > 0.5$ and $n_{constituent}^{SUEP} > 50$.

Figure 6.11 shows the $n_{constituent}^{SUEP}$ distributions of the QCD background and signal simulations in 2018 after applying the $S_{boosted}^{SUEP} > 0.5$ selection, which largely reduces the background compared to Figure 6.10 (right) but has minor effects on the signal yields. The high $n_{constituent}^{SUEP}$ regions have higher signal yields than the background, and are thus sensitive to the SUEP signals.

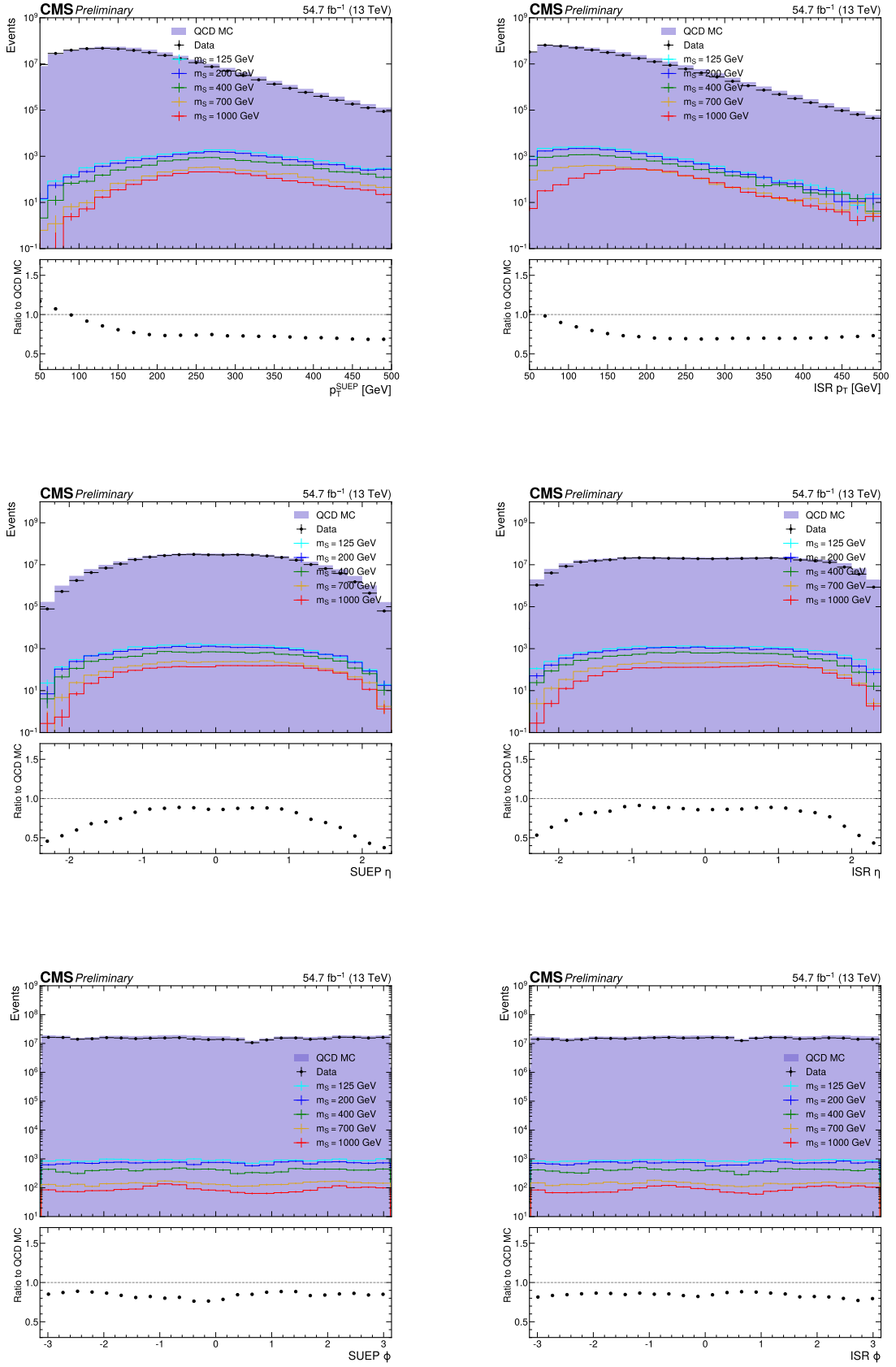


Figure 6.8: Distribution of the designated SUEP (left) and ISR (right) jets, corresponding to the leading and second leading multiplicity AK15 Jets, respectively. The simulations are normalized to 1% integrated luminosity of the 2018 run and compared to 1% of the 2018 data.

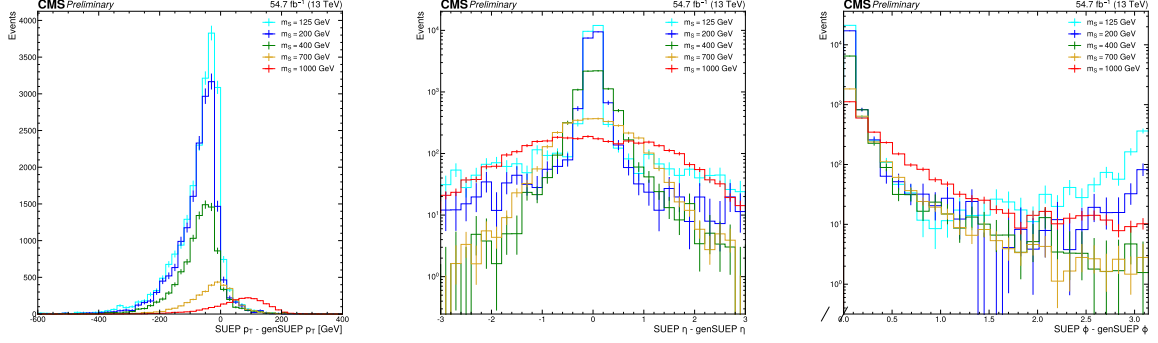


Figure 6.9: p_T (left), η (middle) and ϕ (right) differences between the SUEP candidates and the corresponding truth level scalars.

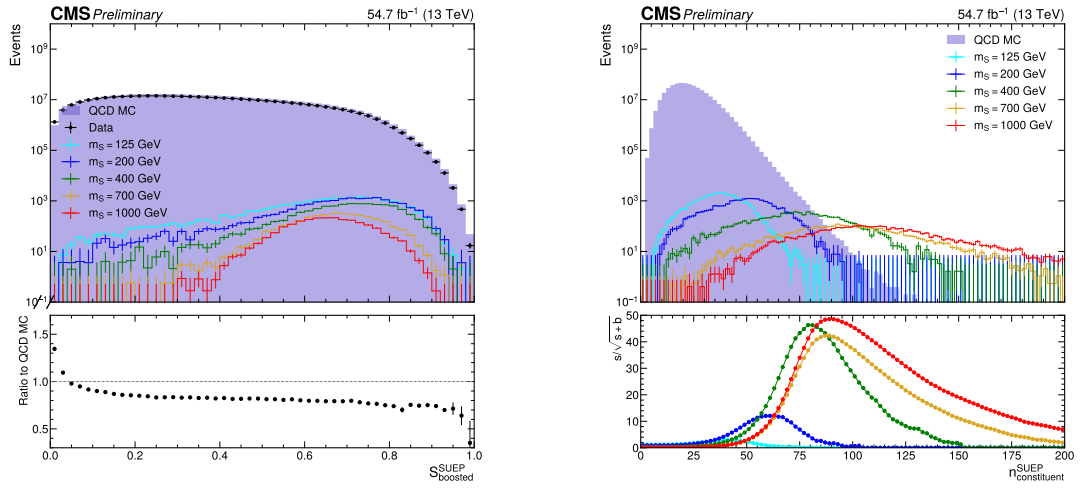


Figure 6.10: The sphericity (left) and number of constituents (right) of the SUEP jets for the data, QCD background and some benchmark signals with $m_\phi = 3$ GeV, $T = 3$ GeV, decay mode $A' \rightarrow \pi^+\pi^-$ and various $m_{S\phi}$.

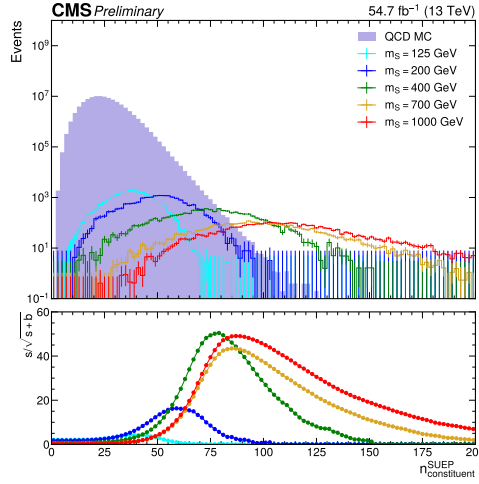


Figure 6.11: The number of constituents of the SUEP jets for the QCD background and some benchmark signals with $m_\phi = 3$ GeV, $T = 3$ GeV, decay mode $A' \rightarrow \pi^+\pi^-$ and various m_{GS} after the $S_{boosted}^{SUEP} > 0.5$ selection.

6.4 Data-driven background estimation

The high H_T and high multiplicity requirements lead to the dominant background from the QCD multijet process. However, the kinematics of the QCD multijet events are not well-modeled by the simulations as shown in Figure 6.8, and the central produced MC sets have lower statistics compared to the data. For an accurate background prediction, this analysis uses a data-driven background estimation with the modified ABCD method.

6.4.1 Modified ABCD method

The ABCD method relies on two discriminating variables that are approximately uncorrelated for the background. By cutting on each variable, the 2-dimensional plane of these variables can be split into background-enriched CRs and an SR containing significantly more signal than the background. The background contributions in the SR are estimated by extrapolating from the data distributions in the CRs. In the application in this analysis, the two approximately uncorrelated variables are the sphericity and constituent multiplicity of the SUEP jets. Figure 6.12(left) shows the normalized sphericity distributions of the 2018 background simulation in slices of constituent multiplicities. The distributions are similar in shape for cases of sphericity above 0.3, though differences are still observed from the mild correlations. The 2-dimensional background distribution of these two variables is shown in Figure 6.12 (right).

In the standard version of ABCD method, the 2-dimensional plane is divided into 4 regions as demonstrated in Figure 6.12 (right). In this example, the region D with high sphericity and high multiplicity is considered as the SR, while the others are CRs. Assuming the two variables are not correlated, the probability distributions of one variable should be independent of any selections applied to the second variable. Therefore, the probability distribution of multiplicity in the SR D is approximately equal to the distribution in the CR B , and their ratio of yields can be estimated by a transfer factor from the yield ratios in regions C and A . The expected

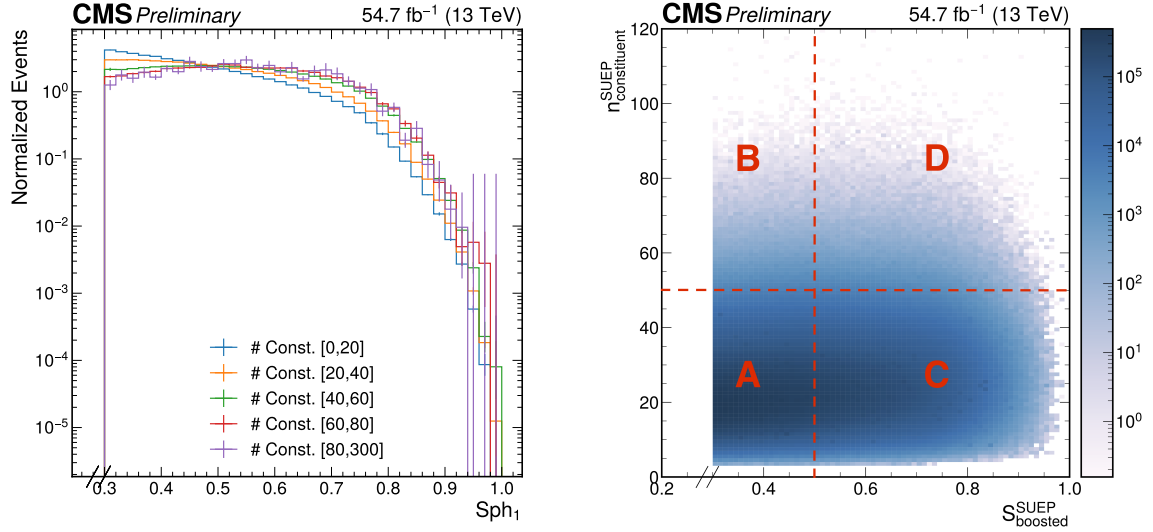


Figure 6.12: The SUEP jet sphericity distribution in slices of SUEP jet constituent multiplicities(left), and the 2-dimensional distribution of SUEP jet sphericity and constituent multiplicity distributions (right) in the 2018 background simulation, as well as the demonstration of the regions in the standard ABCD method.

background in a bin of multiplicity in region D (D_{bin}) is then

$$D_{bin} = \frac{C}{A} \times B_{bin}, \quad (6.1)$$

where B_{bin} denotes the data yield in the same bin of multiplicity in region B, and C and A represent the total data yield in region C and A, respectively. Figure 6.13 shows the comparison of the estimated SR distribution and the truth when applying the standard ABCD method on the QCD background simulations. Although the expected distributions have similar shapes to the truth, they generally underestimate the truth in the yield of each bin because of the undesired correlations between the two variables.

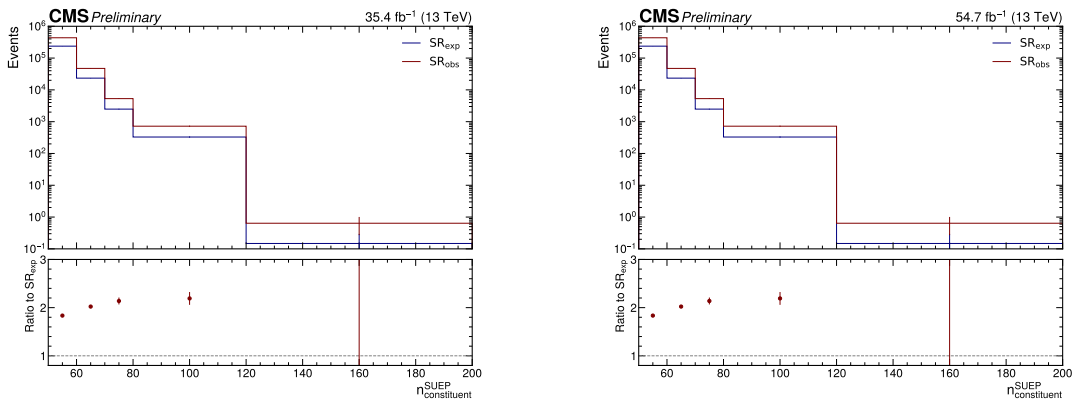


Figure 6.13: The expected SR $n_{constituent}^{SUEP}$ distribution (SR_{exp}) estimated by the standard ABCD method compared with the truth (SR_{obs}), when the ABCD method is applied on the 2017 (left) and 2018 (right) background simulation.

A modified version of ABCD method was proposed recently [214] as an improvement of the standard method. Instead of using one boundary point of division for each variable, it uses

2 boundary points per variable to divide the 2-dimensional plane into 9 regions, as shown in Figure 6.14. The sub-division of CRs in this method provides extra information about the correlation between the two variables to be input into the extrapolation and mitigate the non-closure of estimation from the correlations.

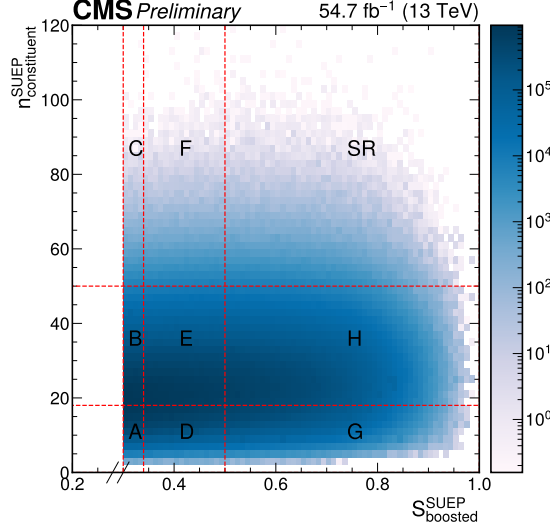


Figure 6.14: The 2-dimensional distribution of SUEP jet sphericity and constituent multiplicity distributions in the 2018 background simulation, and demonstration of the regions in the modified ABCD method.

In the modified ABCD method, the correlations between the two discriminating variables x and y can be evaluated by

$$1 + \epsilon(x, y) := \frac{P(x, y)}{P_x(x)P_y(y)}, \quad (6.2)$$

in which $P(x, y)$ denotes the joint probability distribution, and $P_x(x)$ and $P_y(y)$ are the probability distribution of x and y . The $\epsilon(x, y)$ represents the correlated part of the two variables and is assumed to be small: $|\epsilon(x, y)| \ll 1$. Under this assumption, the integral of $\epsilon(x, y)$ can be estimated by Taylor's series of x and y , and the yield of the SR can be expressed as

$$SR_{yield} = \frac{F^2 H^2 D^2 B^2}{G C A E^4} + \mathcal{O}(\Delta_x^2 \Delta_y^2), \quad (6.3)$$

in which A – F represent the yields in the corresponding CRs, and Δ_x and Δ_y represents the interval among the boundaries for x and y , respectively. The $\mathcal{O}(\Delta_x^2 \Delta_y^2)$ term represents the non-closure of the estimation from the variable correlations. As a comparison, the non-closure of SR yield in the standard ABCD method is $\mathcal{O}(\Delta_x \Delta_y)$. The modified method takes into account higher-order terms from the correlation, thus expecting a smaller non-closure of the estimation. The distribution of one variable in the SR can be estimated as the probability distribution of the same variable in the adjacent CR multiplied by SR_{yield} .

In this analysis, the multiplicity distribution in the SR is estimated as the probability distribution in the F region multiplied by the SR_{yield} . In each bin of multiplicity, the SR background

is approximately

$$SR_{bin} \simeq \frac{F^2 H^2 D^2 B^2}{G C A E^4} \frac{F_{bin}}{F}. \quad (6.4)$$

The dividing boundaries are optimized based on the estimation closure and signal significance using simulations, and chosen to be 0, 18, 50, ∞ for $n_{constituent}^{SUEP}$ and 0.3, 0.34, 0.5, 1 for $S_{boosted}^{SUEP}$. The SR of $n_{constituent}^{SUEP} \geq 50$ and $S_{boosted}^{SUEP} > 0.5$ is further divided into 5 exclusive bins of $n_{constituent}^{SUEP}$ when deriving the exclusion limits or the signal significances, in order for a high sensitivity to different signal hypotheses. The SR bins are chosen as $50 \leq n_{constituent}^{SUEP} < 60$, $60 \leq n_{constituent}^{SUEP} < 70$, $70 \leq n_{constituent}^{SUEP} < 80$, $80 \leq n_{constituent}^{SUEP} < 120$ and $n_{constituent}^{SUEP} \geq 120$. The first bin $50 \leq n_{constituent}^{SUEP} < 60$ is used as the validation region for the background estimation method applied on data (Section 6.4.3) and not used for the derivation of final results. Figure 6.15 shows the expected SR distributions and the truth when applying the modified ABCD method on the QCD background simulations. Compared with the results of the standard ABCD method in Figure 6.13, the modified method achieved a much better closure, as expected.

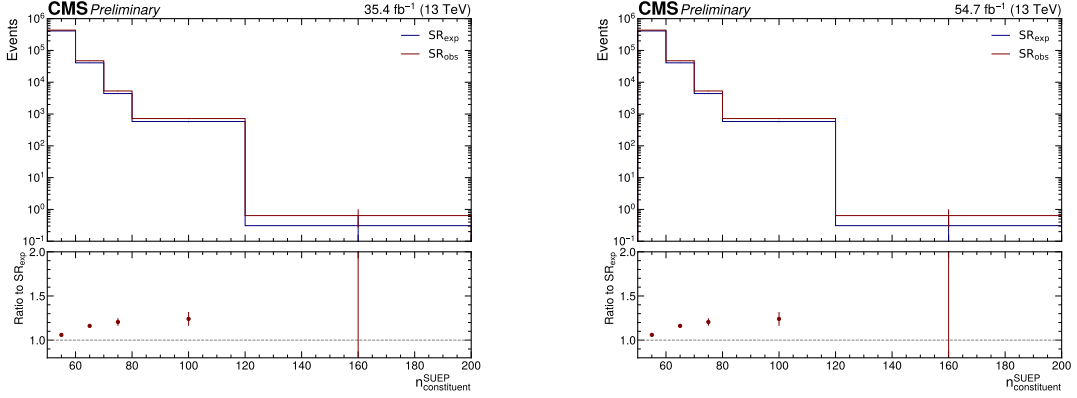


Figure 6.15: The expected SR $n_{constituent}^{SUEP}$ distribution (SR_{exp}) estimated by the modified ABCD method compared with the truth (SR_{obs}), when the ABCD method is applied on the 2017 (left) and 2018 (right) background simulation.

Figure 6.16 shows the distributions of the two discriminating variables in the QCD background and signal simulations.

In the data-driven background estimation with the modified ABCD method, the background yields and shapes of $n_{constituent}^{SUEP}$ distribution are estimated for the years 2016, 2017 and 2018 individually from the corresponding data in the CRs, and the residue of non-closure is covered by systematic uncertainties. The data distributions in the CR are compared with the background and signal simulations in Figure 6.17.

6.4.2 Signal injection test

As shown in Figure 6.16 and 6.17, the signal yields are much lower than the background in the CRs as required by the ABCD method. However, some high m_S signals have higher magnitudes than the background on the tail of the $n_{constituent}^{SUEP}$ distribution in the F region, which can alter the estimation of the yield and distribution shape of the SR background. In the signal injection test, the modified ABCD method is applied to the sum of background and signal distributions and estimate the SR background in the presence of signals. Figure 6.18 shows the signal injection

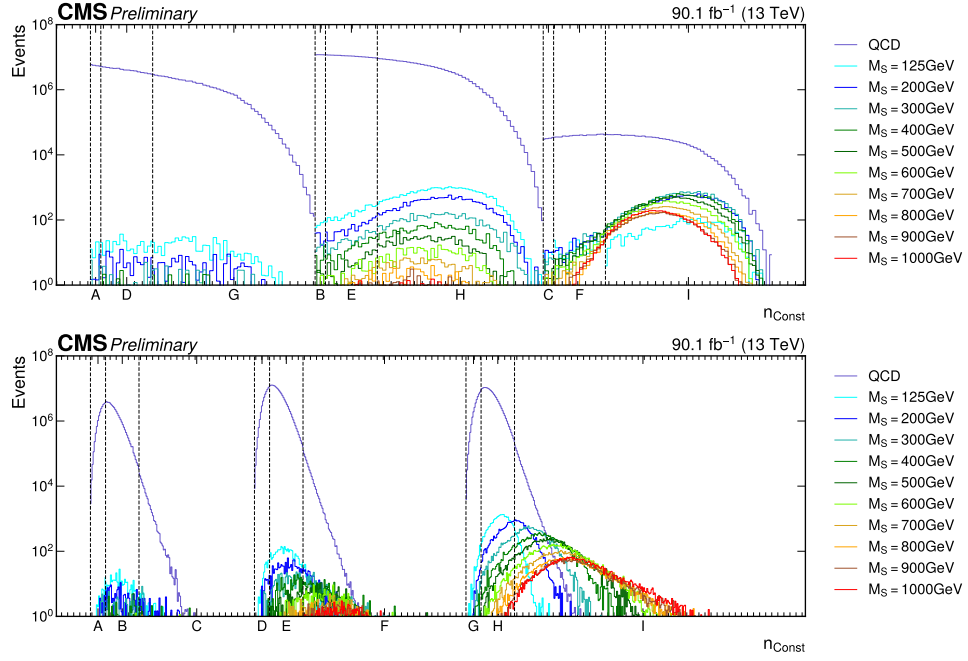


Figure 6.16: The $n_{constituent}^{SUEP}$ (upper) and $S_{boosted}^{SUEP}$ (lower) distributions in the 9 regions of the modified ABCD method from the QCD background and benchmark signals with $m_{\phi} = 3$ GeV, $T = 3$ GeV, decay mode $A' \rightarrow \pi^+ \pi^-$ in the 2017+2018 simulation.

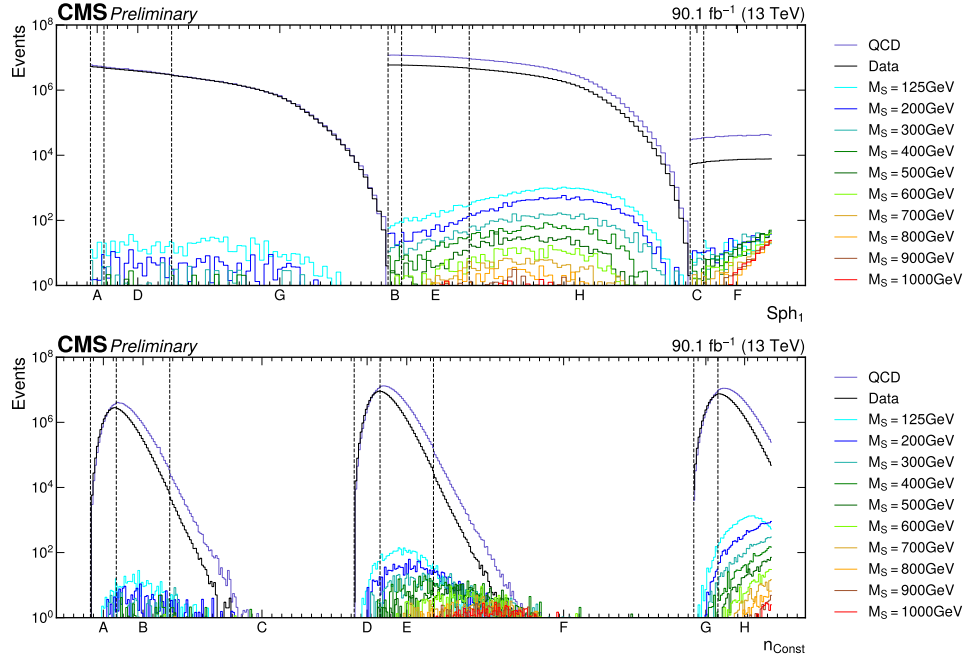


Figure 6.17: The $n_{constituent}^{SUEP}$ (upper) and $S_{boosted}^{SUEP}$ (lower) distributions in the 8 CR regions of the modified ABCD method from the QCD background and benchmark signals with $m_{\phi} = 3$ GeV, $T = 3$ GeV, decay mode $A' \rightarrow \pi^+ \pi^-$ in the 2017+2018 simulation, compared with the data distributions.

test results for the benchmark signals with $m_S = 400$ GeV and 1000 GeV. In the last bin of $n_{constituent}^{SUEP}$, the expected background in the presence of signals is larger than the case if the signals are absent. However, the observation remains significantly higher than the expected background if the signal is present, which verifies the discovery potential of the background estimation strategy if the signals are present and contaminate the CRs.

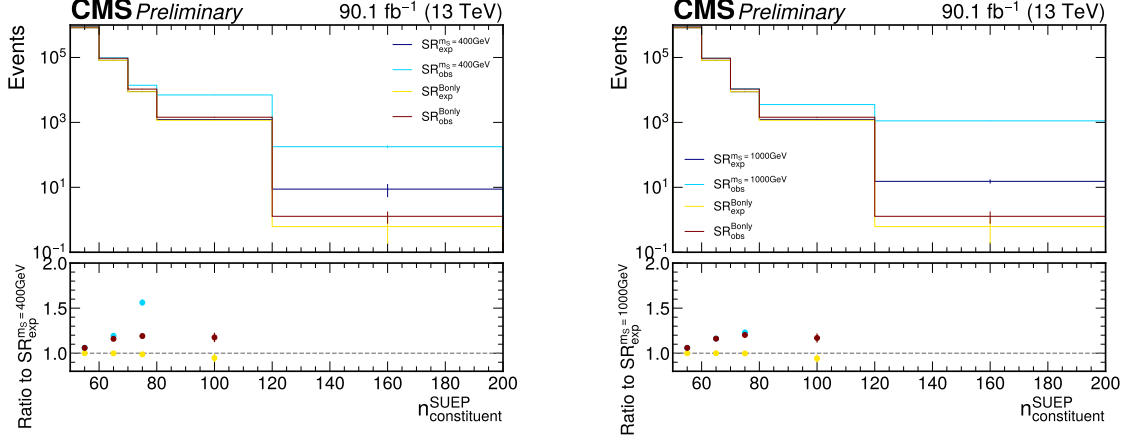


Figure 6.18: Background estimations of the modified ABCD method with (dark blue lines) and without (yellow lines) considering the signal contamination in the F region, compared with the observations under the background-only (dark red lines) or the signal+background (light blue lines) assumptions. The estimations use QCD background simulations and signals with $m_\phi = 3$ GeV, $T = 3$ GeV, decay mode $A' \rightarrow \pi^+\pi^-$, and $m_S = 400$ GeV or 1000 GeV in year 2017 and 2018.

To fully exploit the discovery potential from the observations and signal templates, we adopt a more sophisticated strategy to account for the signal contamination effects when deriving the final results of exclusion limits or discovery significances. Instead of assuming the observations are fully composed of QCD background in the CRs, we assume that both the background and hypothetical signal contribute to the CR observations, and the expected signal is determined by its template of distribution shapes and the rate as the parameter of interest to be fitted. By considering the potential signals in the CRs, the signal contamination tends to contribute to the sensitivity instead of leading to an overestimated background in the SR.

6.4.3 Validation of the background estimation in data

Developed based on the QCD multijet simulations, the background estimation strategy is verified for the data distributions while remaining blinded to the regions sensitive to the signal contributions. The application of the modified ABCD method to data is validated in two ways as follows.

Firstly, the modified ABCD method is applied with the input from the data in the CRs to estimate the background yields and shapes in the first bin $50 \leq n_{constituent}^{SUEP} < 60$ of the SR as the validation region, and compared with the observations. As shown in Figure 6.11 (right), the fraction of signals within this region is small enough such that the observations should be dominated by the background with little potential signal contamination. Figure 6.19 shows the estimations and observations in this validation region, as well as the potential signal contributions. The estimated background yields and distribution shapes are close to the observations, and the signal contributions are negligible.

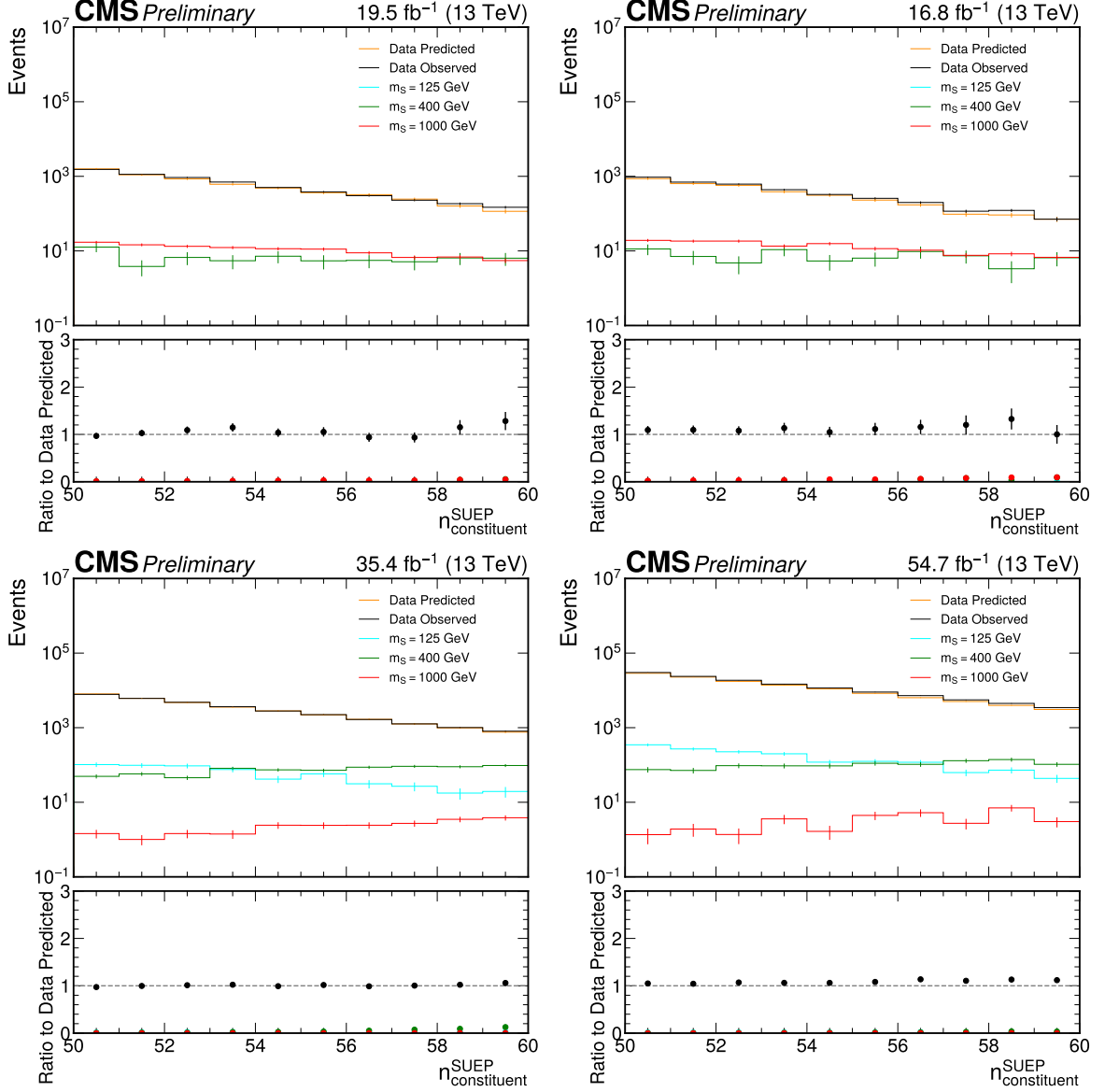


Figure 6.19: Validation of the ABCD method using Run 2 data (upper left: 2016 preVFP, upper right: 2016 postVFP, lower left: 2017, lower right: 2018) in the $50 \leq n_{constituent}^{SUEP} < 60$ bin of SR where the background would overwhelms the signals.

In the second validation method, the modified ABCD method is applied to the joint distribution of sphericity and constituent multiplicity of the ISR jets in data. Originating from QCD radiations, the ISR jets are expected to have similar kinematics to the QCD multijet background in the SUEP jets. The constituents in the ISR jets are analyzed in the same way as those in SUEP jets in multiplicity counting and sphericity computation in the rest frame of the corresponding ISR jets. By the definitions of the SUEP and ISR jets in the SUEP-ISR tagging, the ISR jets have fewer constituents than the SUEP jets. To test with sufficient statistics in the equivalent SR of ISR jets, the dividing boundaries of the ABCD methods are set to 0, 18, 35, ∞ for $n_{constituent}^{ISR}$, while keeping the same boundaries 0.3, 0.34, 0.5, 1 for $S_{boosted}^{ISR}$ as for the SUEP jets. Figure 6.20 shows the estimated $n_{constituent}^{ISR}$ distributions in each year and the full Run 2 compared with the observations. The agreement is at the same level as the test on the QCD background simulations in Figure 6.15.

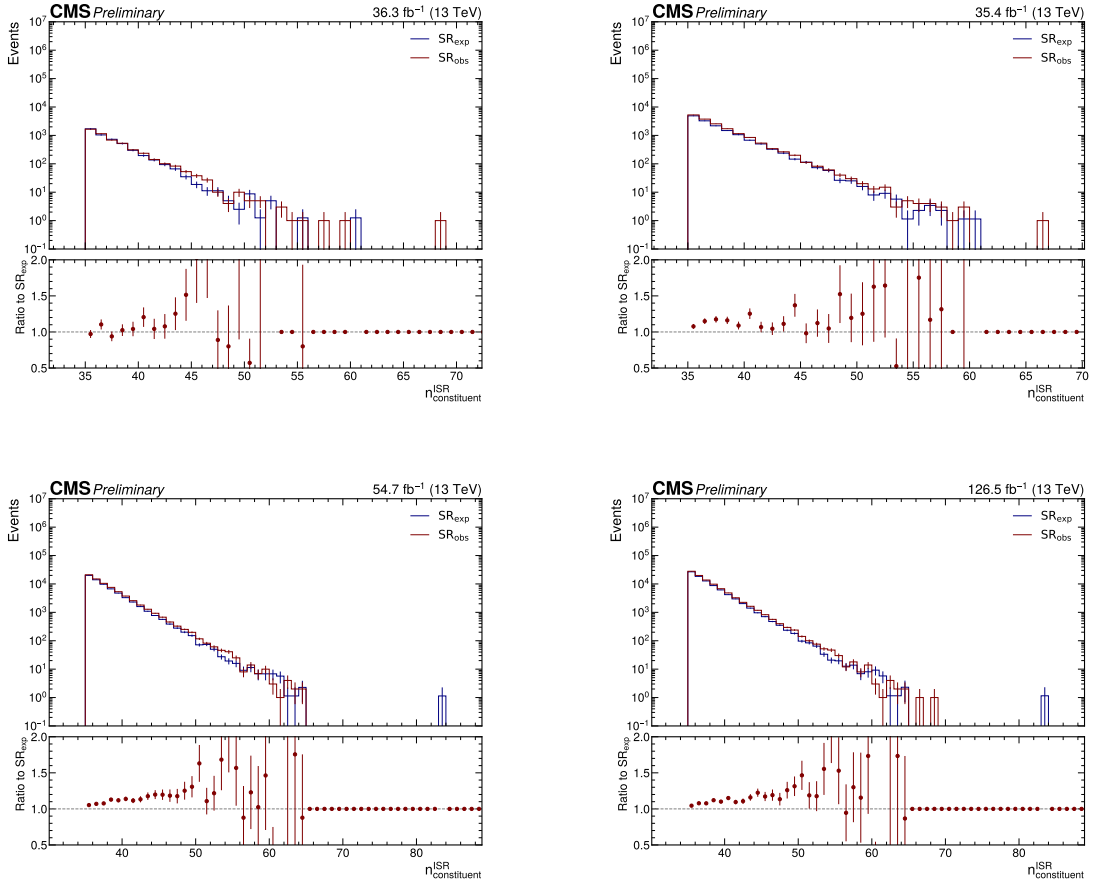


Figure 6.20: Validation of ABCD method using the Run-2 data within the ISR jet equivalent SR $n_{\text{constituent}}^{\text{ISR}} \geq 35$ and $S_{\text{boosted}}^{\text{ISR}} > 0.5$. Upper left: 2016 data. Upper right: 2017 data. Lower left: 2018 data. Lower right: full Run 2 data.

6.5 Uncertainty estimation

The systematic uncertainty of the analysis includes the modeling uncertainty of the signals and the non-closure uncertainty of the background estimation with the modified ABCD method. The statistical uncertainty comes from the limited statistics in the data taking. This section describes the sources and estimation methods for the systematic uncertainty, while all the statistical uncertainties on the expected yields are modeled with Poisson distributions.

6.5.1 Integrated luminosity

The integrated luminosity affects the normalization of the signals, and the uncertainty on the luminosity measurements in the data taking propagates into the uncertainty on the total signal yields.

The uncertainties of the integrated luminosity measurement are applied for each year according to the recommendations from the CMS lumi POG. The uncorrelated uncertainties are 1.0, 2.0 and 1.5 % for 2016, 2017 and 2018, respectively. The correlated uncertainties among the three years are 0.6, 0.9 and 2.0 % for 2016, 2017 and 2018, respectively. The corrected uncertainties between 2017 and 2018 luminosity are 0.6 and 0.2 for 2017 and 2018, respectively.

6.5.2 Trigger efficiency

The efficiency of the trigger as a function of the trigger-level H_T affects the acceptance of the analysis to the signals, thus the modeling of the trigger efficiency needs to be corrected to the truth. As described in Section 6.3.1, the trigger scale factors are derived as the ratio of the trigger efficiency measured in the reference data to that measured in the QCD background simulation in bins of the offline emulation of the trigger-level H_T . The trigger scale factors are derived for years 2017 and 2018 individually, and the simulated signal events are weighted by the trigger scale factors depending on their H_T as corrections. In 2016, the QCD simulations were not centrally produced by the CMS collaboration, and the trigger scale factors are not available. Therefore, the scale factors in 2017 are applied to the 2016 signal simulations. The uncertainty on the trigger scale factors is considered as a source of systematic uncertainty in the signal modeling.

6.5.3 Clustering of AK4 jets

As the H_T depends on the online reconstruction of AK4 jets, the mismodeling of AK4 jet reconstruction in the simulations affects the H_T computation, thus propagates through the $H_T > 560$ GeV pre-selection as a systematic uncertainty on the signals.

A standard procedure to deal with this effect in offline analyses is the jet energy correction (JEC) [215]. In this analysis on scouting data, the offline JEC is not applicable because of differences in the online and offline jet reconstruction procedures. Instead, the signal yields are computed with $H_T > 540$ GeV and $H_T > 580$ GeV in the pre-selection as the up and down variations of this systematic uncertainty, the nominal yields from the $H_T > 560$ GeV selection. The variations from shifting the H_T threshold are designed to be larger than those from offline JEC, in order to safely cover the AK4 jet clustering uncertainty in this analysis.

6.5.4 Pileup effect

To simulate the pileup effects on the reconstructed objects, the number of pileup collisions in each simulated event is sampled from a distribution roughly describing the pileup condition of the data taking in the corresponding year, and then the events are weighted according to the ratio of the pileup distribution in the data to that in the simulation. The simulated samples after weighting are expected to have the same pileup distribution as the data. The uncertainty of the pileup measurement in the data affects the weighting procedure and is considered as the up and down variations of pileup weights and signal distributions.

6.5.5 Track reconstruction

The track reconstructing efficiency uncertainty is estimated by a *track-killing* method similar to the strategy in the event shape measurement (Section 4.6). The uncertainties 2.5% (1%) for tracks with $p_T < 20$ GeV ($p_T > 20$ GeV) are only evaluated for offline reconstructions. The corresponding uncertainties for online-reconstructed tracks in the scouting stream are estimated by scaling up the offline uncertainties, in order to account for the lower precision and stability in the online reconstruction. It has been observed that the track multiplicity distributions shift across eras due to the changes in the detector performances. Table 6.6 summarizes the average track multiplicity per event for each era and their differences from the corresponding year averages. The largest difference is found in 2017F (6.9%). To cover this reconstruction efficiency uncertainty from variations of detector performances, the tracks are killed with a probability of 7% if $p_T (< 20$ GeV), and a probability of 2.8% otherwise. For the histograms concerning the computation of exclusion limits, the distributions after track killing are considered as the down variations of this uncertainty. The up variations are derived by inverting the down variations against the axis of symmetry as the nominal distributions.

| Year | era | average track multiplicity / event | difference from year average |
|--------------|-----------|------------------------------------|------------------------------|
| 2016 preVFP | inclusive | 32.24 | - |
| | 2016apvB | 33.80 | 4.85% |
| | 2016apvC | 32.27 | 0.09% |
| | 2016apvD | 32.03 | -0.66% |
| | 2016apvE | 30.75 | -4.63% |
| | 2016apvF | 30.55 | -5.23% |
| 2016 postVFP | inclusive | 31.10 | - |
| | 2016F | 31.67 | 1.83% |
| | 2016G | 30.79 | -0.99% |
| | 2016H | 31.37 | 0.86% |
| 2017 | inclusive | 34.39 | - |
| | 2017C | 35.05 | 1.91% |
| | 2017D | 35.83 | 4.19% |
| | 2017E | 35.64 | 3.63% |
| | 2017F | 32.02 | -6.90% |
| 2018 | inclusive | 37.48 | - |
| | 2018A | 38.31 | 2.23% |
| | 2018B | 38.16 | 1.83% |
| | 2018C | 38.07 | 1.57% |
| | 2018D | 36.72 | -2.02% |

Table 6.6: Comparison of average track multiplicity per event across eras.

6.5.6 Pre-firing

During the 2016 and 2017 data taking, the ECAL trigger primitives (TPs) located in the innermost rings of the endcap region ($2.5 < |\eta| < 3.0$) exhibited a timing drift leading to an increase of the L1 pre-firing rate for any calorimeter-based trigger. A given L1 trigger pre-fires when the decision of a mistimed TP, with energy above a minimum threshold required in the L1 menu, is wrongly assigned to the earlier interaction (BX1) compared to the current one (BX0). Due to the trigger rules, the interesting events in BX0 are discarded in favor of the previous one in BX1. The pre-firing issue reduces the efficiency of recording potentially interesting events. The pre-firing probabilities are centrally measured as a function of p_T and $|\eta|$ and are applied to the simulation samples.

6.5.7 Higgs reweighting

As recommended by Reference [216], additional corrections are applied to signal samples with $m_S = 125$ GeV, in which the heavy scalar is assumed to be the Higgs boson. Higher order corrections were calculated for the Higgs boson production cross section from gluon-gluon fusion, and the corrections are applied to the signal events generated at lower precisions as a function of generator-level Higgs p_T , denoted as the K_{EFT}^{NNLO} factors and listed in Table 6.7. The up and down variations of the K_{EFT}^{NNLO} factors are listed as the $+\sigma$ and $-\sigma$ columns in the table. After applying the K_{EFT}^{NNLO} factors or their variations on the event weights, the signal events are normalized to the same yield before the Higgs reweighting.

| Higgs p_T [GeV] | K_{EFT}^{NNLO} | $+\sigma$ | $-\sigma$ |
|------------------------|------------------|-----------|-----------|
| $p_T < 450$ | 1.25 | 9.2% | 12% |
| $450 \leq p_T < 500$ | 1.25 | 8.9% | 12% |
| $500 \leq p_T < 550$ | 1.25 | 8.8% | 11% |
| $550 \leq p_T < 600$ | 1.25 | 8.8% | 11% |
| $600 \leq p_T < 650$ | 1.24 | 8.8% | 11% |
| $650 \leq p_T < 700$ | 1.24 | 8.7% | 11% |
| $700 \leq p_T < 750$ | 1.24 | 8.7% | 11% |
| $750 \leq p_T < 800$ | 1.24 | 8.7% | 11% |
| $800 \leq p_T < 850$ | 1.24 | 8.7% | 11% |
| $850 \leq p_T < 900$ | 1.24 | 8.7% | 11% |
| $900 \leq p_T < 950$ | 1.24 | 8.5% | 11% |
| $950 \leq p_T < 1000$ | 1.24 | 8.6% | 11% |
| $1000 \leq p_T < 1050$ | 1.24 | 8.6% | 11% |
| $1050 \leq p_T < 1100$ | 1.24 | 8.6% | 11% |
| $1100 \leq p_T < 1150$ | 1.24 | 8.7% | 11% |
| $1150 \leq p_T < 1200$ | 1.24 | 8.7% | 11% |
| $1200 \leq p_T < 1250$ | 1.24 | 8.7% | 12% |
| $1250 \leq p_T$ | 1.24 | 8.6% | 12% |

Table 6.7: Summary of Higgs reweighting factors by bins of generator-level Higgs p_T .

6.5.8 Non-closure of the ABCD method

As demonstrated in Section 6.4, the estimation of SR background by the modified ABCD method can deviate from the truth because of higher-order correlations between the constituent multiplicity and sphericity of the SUEP jet in the background process. The non-closure of the

background estimation is considered as a systematic uncertainty when fitting the background and potential signal contributions to the observation.

The non-closure uncertainty on the inclusive background yield in the SR and the shape of the $n_{\text{constituent}}^{\text{SUEP}}$ distribution are considered separately in this analysis

Yield uncertainty of the non-closure

The yield uncertainty of the non-closure is estimated by the differences between the expected and observed yields in the ISR jet, when the modified ABCD method is applied to the sphericity and number of constituents in the ISR jet. Table 6.8 shows the predicted and observed SR yields in the ISR jets and their ratios in different years. Considering the large uncertainty of the ratios due to the limited statistics in the SR of the ISR jet, we assign a conservative uncertainty 50% as the yield uncertainty uncorrelated across the years.

| Year | 2016 | 2017 | 2018 |
|--------------|-------------------|-------------------|--------------------|
| SR | 18.00 | 72.00 | 423.00 |
| Predicted SR | 18.36 ± 14.44 | 74.87 ± 36.20 | 272.02 ± 45.80 |
| Ratio | 0.98 ± 0.81 | 0.96 ± 0.48 | 1.56 ± 0.27 |

Table 6.8: Comparisons of the predicted SR and observed SR yields when the ABCD method is applied to the sphericity and number of constituents in the ISR jet.

Shape uncertainty of the non-closure

The 9-region ABCD method uses the shape of the constituent multiplicity distribution in CR F to approximate the shape of the background distribution in SR. The SR background shape deviates from the F region shape due to the non-closure. The deviation is estimated by the differences between the F region and C region distribution shapes, quantified by the ratios of the normalized F region constituent multiplicity distribution to the one in the C region per bin. These ratios are multiplied by the estimated signal region distribution as corrections for their corresponding bins. In the estimation of the F to C region ratios, the insufficient statistical precision in the high multiplicity bins would cause unstable ratios with large uncertainties. Instead, we use a linear fit of the ratios versus the constituent multiplicity as the first-order approximation. For the stability of the linear fit, the histograms in F and C regions are obtained with finer bins, especially in the low multiplicity parts with higher statistical precision, and then a fit is performed on the ratios weighted by their inverse squared statistical uncertainties.

The constituent multiplicity bins in the linear fit are 50, 52, 54, 56, 58, 60, 62, 64, 66, 68, 70, 75, 80, 120, and F to C ratios in these bins are fitted as a linear function of multiplicity in the bin centers. The SR to F ratios in the bins for extraction of exclusion limits or discovery significances, 50, 60, 70, 80, 120, ∞ , are estimated as values of the resulting linear function in the corresponding bin centers. The estimated ratio for the last bin is taken at multiplicity 125. The linear fit is performed for each year of 2016, 2017 and 2018, individually, and the corresponding corrections to the SR shapes are also applied separately for each year. The F to C region ratios and the results of linear fits are shown in Figure 6.21.

In addition to the corrections to the SR distribution shapes, uncertainties are assigned to the expected SR background distribution shapes to account for the residues. The magnitudes of the uncertainties are estimated as those of the corrections to the SR shapes given by the

upper and lower bounds of the linear fits. 100% shape uncertainty is assigned to the last bin as a conservative estimation. These uncertainties are uncorrelated across the years and correlated across the bins. The nuisance parameters associated with the shape uncertainties are assumed to have log-normal distributions when fitting the models to observations.

Table 6.9 gives the values of corrections to the SR shapes, as well as the shape uncertainties, across the three years.

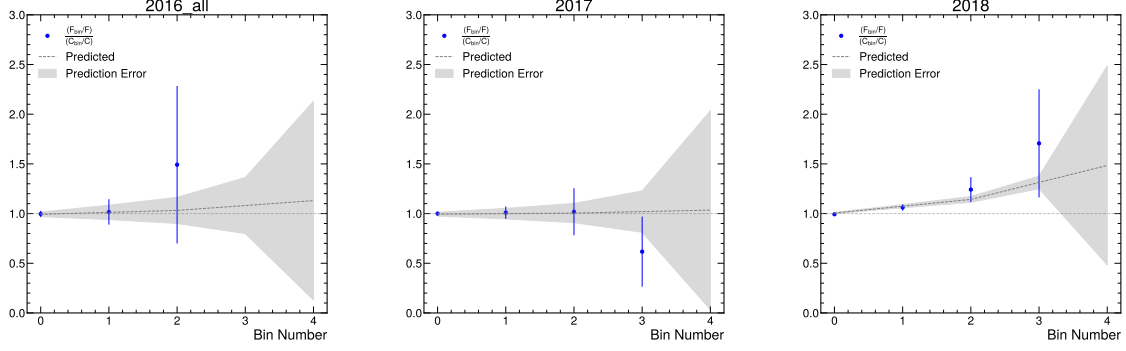


Figure 6.21: Bin-by-bin ratios of the normalized F region constituent multiplicity distribution to the C region constituent multiplicity distribution. The predicted ratios of the normalized SR to F region constituent multiplicity distribution are derived from the linear fits of the F to C region ratios in bins 50, 52, 54, 56, 58, 60, 62, 64, 66, 68, 70, 75, 80, 120 versus the bin centers, weighted by inverse squared ratio uncertainties.

| Bins | [50, 60) | [60, 70) | [70, 80) | [80,120) | [120,Inf) |
|------|-------------------|-------------------|-------------------|-------------------|-----------------|
| 2016 | 0.992 ± 0.023 | 1.012 ± 0.072 | 1.032 ± 0.131 | 1.081 ± 0.282 | 1.130 ± 1.0 |
| 2017 | 0.994 ± 0.019 | 0.999 ± 0.053 | 1.005 ± 0.097 | 1.020 ± 0.208 | 1.034 ± 1.0 |
| 2018 | 1.006 ± 0.005 | 1.074 ± 0.016 | 1.142 ± 0.029 | 1.313 ± 0.063 | 1.484 ± 1.0 |

Table 6.9: Summary of the shape corrections of the ABCD method non-closure and their uncertainties.

6.5.9 Impacts of the uncertainties

The effects of the systematic uncertainties are investigated by fitting the signal strength together with all the nuisance parameters for the systematic uncertainties and background rate parameters. In Figure 6.22, the fits are performed to Asimov data, in which the signal strengths are set to certain values and the observations are equal to the expected background plus the injected signals. The pull of the parameters reflects the constraints on them from the fit to observations, and the impacts of the parameters reflect the contributions of the corresponding uncertainty sources to the uncertainty on the signal strength. The nuisance parameters for the non-closure yield uncertainty (Closure_2016, Closure_2017, Closure_2018) have small uncertainty after the fits, which indicates that the 50% conservative pre-fit uncertainty gets well-constrained by the observations. When the signal is not injected, the non-closure shape uncertainty of the background estimation (Shape_2016, Shape_2017, Shape_2018) has larger impacts than the yield uncertainty. When the signal is injected, the uncertainty of the track reconstruction efficiency in 2017 and 2018 signal simulations (CMS_trk_kill_2017, CMS_trk_kill_2018) has a dominant impact.

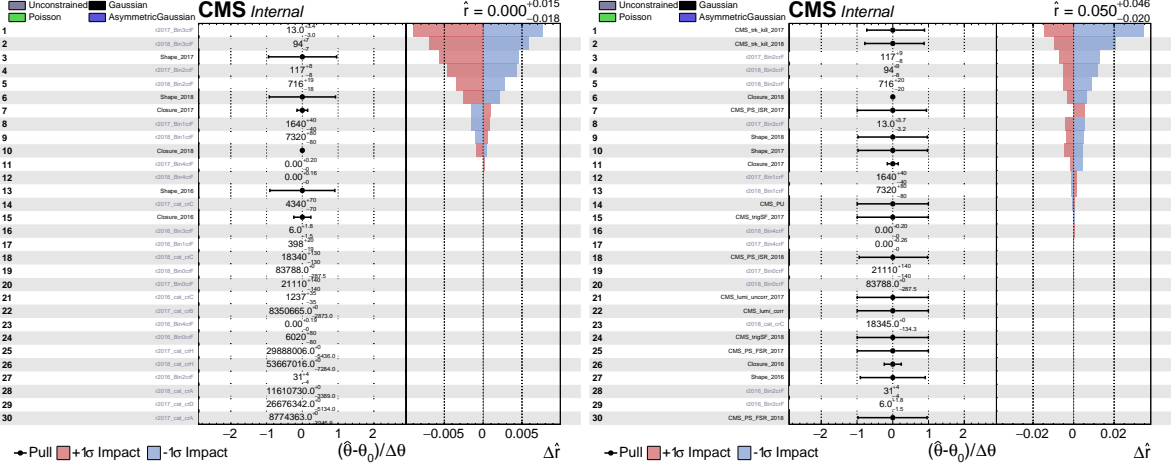


Figure 6.22: Impacts of the systematic nuisance parameters and background rate parameters on the fit result of the signal strength. The fit assumes the observation as the Asimov data with signal strength $r = 0$ (left) and $r = 0.05$ (right) for a benchmark signal $m_S = 400$ GeV, $m_\phi = 4$ GeV, $T = 4$ GeV and the leptonic decay mode of dark photons with mass $m_{A'} = 0.5$ GeV.

6.6 Results

As introduced in Section 6.4, the searching results are derived from the background estimations, signal simulations and observations in the 4 bins of $n_{constituent}^{SUEP}$ for discovery in the SR: $60 \leq n_{constituent}^{SUEP} < 70$, $70 \leq n_{constituent}^{SUEP} < 80$, $80 \leq n_{constituent}^{SUEP} < 120$ and $n_{constituent}^{SUEP} \geq 120$. A binned maximum likelihood estimation (MLE) is utilized to extract the possible signals over the expected background given the observations. All the uncertainties are considered in the MLE by their corresponding terms in the likelihood function. The fit results are used to compute the upper limits of the signal cross sections based on the CL_s criterion [217].

6.6.1 Maximum likelihood estimation

For each hypothetical signal model, the nominal cross section in the MLE is taken from the corresponding value in Table 6.2. The likelihood function is the product of independent Poisson likelihoods for the statistical uncertainties in the exclusive regions in the space space of $n_{constituent}^{SUEP}$ and $S_{boosted}^{SUEP}$, and the likelihoods to constrain the nuisance parameters controlling the deviations by the systematic uncertainties, expressed as

$$\mathcal{L}(\mu, \vec{\theta}_s, \vec{\theta}_b, b_i; N_i, N_j) = f_s(\vec{\theta}_s) \times f_b(\vec{\theta}_b) \times \prod_i^{CR} P(N_i | \mu s_i(\vec{\theta}_s) + b_i) \prod_j^{SR} P(N_j | \mu s_j(\vec{\theta}_s) + b_j(b_i, \vec{\theta}_b)). \quad (6.5)$$

The parameters and terms in eq.6.5 are defined as follows.

- μ : the signal strength parameter modulating the signal cross section. $\mu = 1$ represents the case of the nominal signal cross section, while $\mu = 0$ represents the case when the signal does not exist.
- i : the index of a CR in the $n_{constituent}^{SUEP} - S_{boosted}^{SUEP}$ phase space, defined by the modified ABCD method. As shown in eq. 6.4, the relevant indices for CRs are $A, B, C, D, E, F_{bin}, G, H$, in which $bin = 0, 1, 2, 3, 4$ represent the bins of sub-division $50 \leq n_{constituent}^{SUEP} < 60$, $60 \leq n_{constituent}^{SUEP} < 70$, $70 \leq n_{constituent}^{SUEP} < 80$, $80 \leq n_{constituent}^{SUEP} < 120$ and $n_{constituent}^{SUEP} \geq 120$, respectively.

- j : the index of a $n_{constituent}^{SUEP}$ bin in the SR. The relevant indices for j are SR_{bin} , in which $bin = 1, 2, 3, 4$ has the same definition as the one for the CR F. The $bin = 0$ in the SR is used for validating the background estimation method, and is not used in the signal extraction.
- $\vec{\theta}_s$: the array of nuisance parameters for the signal systematic uncertainties. It controls the deviation of the signal yields from their central values.
- $s_i(\vec{\theta}_s), s_j(\vec{\theta}_s)$: the signal yield in region i or j given the nominal signal cross section and the nuisance parameters $\vec{\theta}_s$ controlling the signal kinematics and detector response.
- b_i : the background yield in the CR i . These are free parameters without prior constraints.
- $\vec{\theta}_b$: the array of nuisance parameters for the systematic uncertainties in the background estimation in the SR. It refers to the nuisance parameters for the yield and shape uncertainties of non-closure.
- $b_j(b_i, \vec{\theta}_b)$: The estimated SR background yield in region j , estimated from the modified ABCD method as a function of the CR yields b_i and shifted by the nuisance parameters $\vec{\theta}_b$.
- $f_s(\vec{\theta}_s), f_b(\vec{\theta}_b)$: the prior joint probability distributions of the nuisance parameters $\vec{\theta}_s$ and $\vec{\theta}_b$.
- N_i, N_j : the observed number of events in regions i and j .
- $P(N_i | \mu s_i(\vec{\theta}_s) + b_i), P(N_j | \mu s_j(\vec{\theta}_s) + b_j(b_i, \vec{\theta}_b))$: the Poisson distribution function of N_i or N_j given the expectation $\mu s_i(\vec{\theta}_s) + b_i$ or $\mu s_j(\vec{\theta}_s) + b_j(b_i, \vec{\theta}_b)$.

Given the observation N_i and N_j , the maximization of eq. 6.5 gives the extracted signal strength $\hat{\mu}$ at the nuisance parameters $\hat{\vec{\theta}}_s, \hat{\vec{\theta}}_b$ and the background rates \hat{b}_i .

6.6.2 Derivation of upper limits

The likelihood function eq. 6.5 can be used to construct the test statistic to compute the p-values under the background-only and signal+background hypotheses, and derive the upper limits for the signals. In the following, the parameter θ is used to represent $\hat{\vec{\theta}}_s, \hat{\vec{\theta}}_b$ and \hat{b}_i .

The profile-likelihood test statistic q_μ is defined as

$$q_\mu(N_i, N_j) := -2 \ln \frac{\mathcal{L}(\mu, \hat{\vec{\theta}}_\mu; N_i, N_j)}{\mathcal{L}(\hat{\mu}, \hat{\vec{\theta}}; N_i, N_j)}. \quad (6.6)$$

The $\hat{\mu}(\hat{\theta})$ denotes the MLE of $\mu(\theta)$, while $\hat{\vec{\theta}}_\mu$ denotes the profiled MLE of θ conditioned on the given μ . To compute the one-sided limit, the value of q_μ is set to 0 in the case $\hat{\mu} > \mu$. To enforce the constraint $\mu > 0$ in the fit, q_μ is set to $-2 \ln \frac{\mathcal{L}(\mu, \hat{\vec{\theta}}_\mu; N_i, N_j)}{\mathcal{L}(0, \hat{\vec{\theta}}_0; N_i, N_j)}$ if $\hat{\mu}$ is negative. As a function of the observation N_i and N_j , the q_μ is a random variable with the probability distribution dependent on μ . Given the data observations N_i^{data} and N_j^{data} , the p-value of the hypothesis with signal strength μ is

$$p_\mu = \int_{q_\mu^{data}}^{\infty} f(q_\mu) dq_\mu, \quad (6.7)$$

in which the $f(q_\mu)$ is the probability distribution function of q_μ , and $q_\mu^{data} := q_\mu(N_i^{data}, N_j^{data})$.

| Year | Category | [60, 70) | [70, 80) | [80,120) | [120, ∞) |
|------|-----------------|------------------|----------------|--------------|------------------|
| 2016 | B-only pre-fit | 620 ± 360 | 49 ± 30 | 10 ± 7 | 0 |
| | B-only post-fit | 657 ± 26 | 53 ± 6 | 7 ± 2 | 0 |
| | Observed | 658 | 54 | 5 | 0 |
| 2017 | B-only pre-fit | 2493 ± 1168 | 179 ± 86 | 20 ± 11 | 0 |
| | B-only post-fit | 2662 ± 48 | 242 ± 12 | 24 ± 4 | 0 |
| | Observed | 2639 | 266 | 24 | 0 |
| 2018 | B-only pre-fit | 11315 ± 5971 | 1176 ± 623 | 178 ± 95 | 0 |
| | B-only post-fit | 12050 ± 109 | 1256 ± 30 | 167 ± 11 | 0 |
| | Observed | 12055 | 1262 | 157 | 0 |

Table 6.10: The observed yields in bins of SUEP jet constituent multiplicity in the signal region for the data collected in 2016, 2017 and 2018 individually. The observations are compared with the background predictions before fitting the background model to the data (B-only pre-fit), as well as the background predictions in the fits under the background-only hypothesis (B-only post-fit).

In the confidence level (CL) calculation, the CL_s criterion [218, 219] is commonly used in particle physics to avoid some undesirable properties of the standard methodology, which requires

$$p_\mu < 1 - CL \quad (6.8)$$

to exclude the hypothesis of signal strength μ . In the case when the experiment is almost not sensitive to the signal hypothesis, e.g. $f(q_\mu) \sim f(q_0)$, the standard criterion can set a limit on a small value of μ with the probability $1 - CL$ and undesirably exclude the signal. Instead, the CL_s criterion requires

$$\frac{p_\mu}{1 - p_b} < 1 - CL, \quad (6.9)$$

in which p_b is the p-value of the background-only hypothesis

$$p_b := \int_0^{q_\mu^{\text{data}}} f(q_\mu) dq_\mu. \quad (6.10)$$

This avoids the search from setting limits stricter than the experimental sensitivity.

The expected upper limits are computed to evaluate the sensitivity of the analysis to the signals and to compare with the limits from the data observation. In the expected limit, the observations are set to distribute under the background-only assumption, and the 2.5%, 16%, 50%, 84% and 97.5% quantiles of upper limits are computed, setting the median expected limits together with the uncertainty bands.

6.6.3 Upper limits of the SUEP signals

The unblinding of the signal region and the validation of the fits are in progress. Table 6.10 presents the observed yields in bins of SUEP jet constituent multiplicity in the signal region, compared with the background predictions before and after fitting to the background model. The values in Table 6.10 are illustrated as histograms of SUEP jet constituent multiplicity in Figure 6.23.

No significant excess is observed in comparison with the SM background prediction. 95% CL upper limits of signal cross sections are presented as constraints on the signal models by

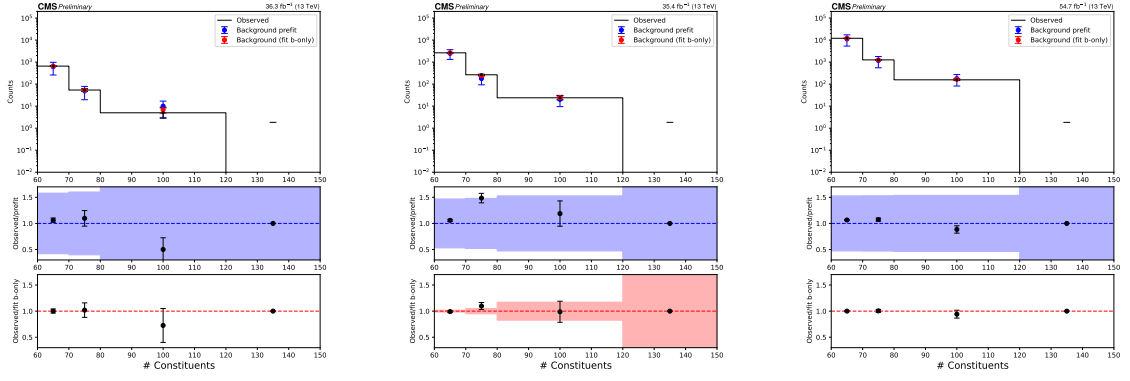


Figure 6.23: The observed, B-only pre-fit, B-only post-fit distributions of SUEP jet constituent multiplicity in the signal region for year 2016 (left), 2017 (middle) and 2018 (right).

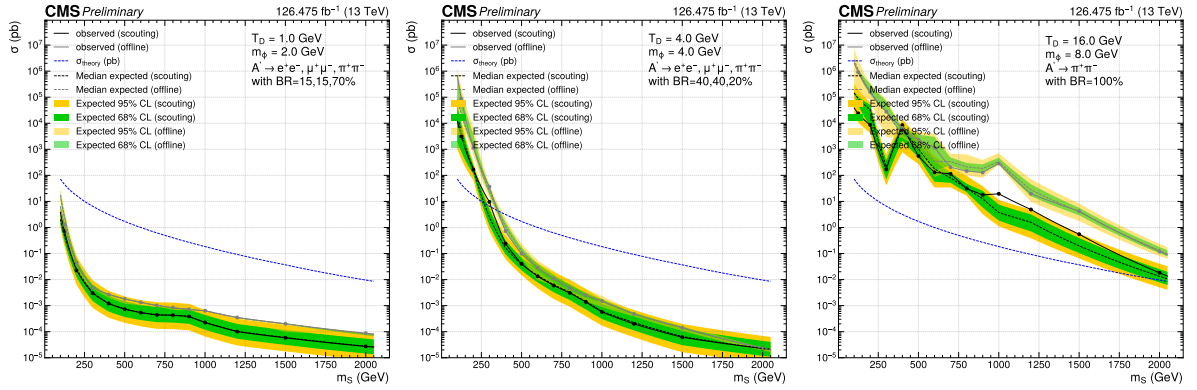


Figure 6.24: 95% CL upper limits on the production cross sections as a function of m_S for representative benchmark signals of m_ϕ , T and $m_{A'}$ from gluon-gluon fusion. Left: $m_\phi = 2$ GeV, $T = 1$ GeV, $m_{A'} = 0.7$ GeV. Middle: $m_\phi = 4$ GeV, $T = 4$ GeV, $m_{A'} = 0.5$ GeV. Right: $m_\phi = 8$ GeV, $T = 16$ GeV, $m_{A'} = 1$ GeV. The limits given by this analysis (scouting) are compared with those from the offline analysis [220] (offline).

the observed data. Figure 6.24 shows the 95% exclusion limits as a function of m_S for three benchmark sets m_ϕ , T and $m_{A'}$. The exclusion limits from analysis on offline-reconstructed data [220] are included in the figures for comparison. The lower limits given by this analysis (scouting) indicate its higher sensitivity to the SUEP signals and more stringent constraints on the signal cross sections.

7 Conclusion

This thesis presents studies on the soft interactions in pp collisions and their mutual influences with hard interactions from various aspects. Although the soft interactions play an important role in the modeling of pp collisions, the theoretical descriptions are faced with challenges due to their non-perturbative nature. This thesis encompasses experimental efforts aimed at deepening our understanding of these interactions and providing valuable input to refine theoretical models. Additionally, the analysis of these events is leveraged to investigate the potential existence of new physics within the sample.

The measurement of event shapes is performed for inelastic pp collisions at 13 TeV from CMS minimum bias data. The event shape observables are functions of outgoing particles' momenta per event to quantify the shapes. The measurement indicates that the data events are averagely more isotropic than predictions, consistently for all the models we considered, which have distinct UE models and parameterization. The multiple-dimensional measurement shows that the mismodeling in event shapes can not be explained by the mismodeling of particle multiplicity or invariant mass. The QCD-instanton interpretation is provided as a possible explanation of the data-simulation discrepancy. The measurement provides experimental inputs to future improvements in theoretical modeling of soft pp collisions.

The energy scaling behavior of intrinsic k_T tunes in various MC generators is investigated by analyzing DY data from a range of hadron collisions at different center-of-mass energies, along with corresponding simulations. This analysis extracts non-perturbative QCD information and examines the interplay between the intrinsic k_T parameter and the perturbative evolution, including ISR. In our approach, the intrinsic k_T is modeled as a Gaussian-distributed random variable that complements the ISR from parton showers in describing the transverse recoils in hard-scattering processes. The width of this distribution is tuned to match the transverse momentum spectra observed in the DY process. The study focuses on how the intrinsic k_T width scales with both collision energy and the hard scattering scale, offering insights into modeling soft parton emissions not captured by the ISR as collinear limits of perturbative QCD emissions.

A search for SUEP is performed on the CMS Run 2 data collected with the scouting strategy, corresponding to integrated luminosity 126 fb^{-1} . The soft particle emission not only arises in UE, but can also appear in certain BSM hidden-valley models featuring a dark QCD sector, where the decay of a heavy mediator can lead to an anomalously high multiplicity of soft, isotropic particles, as well as unsuppressed, large-angle emissions of dark mesons that promptly transfer into SM particles. The sphericity as an event shape observable is used to distinguish the soft, high-multiplicity emissions predicted by the model from the QCD background. The sphericity and multiplicity of wide jets are used as powerful discriminating variables in the search. Using the novel scouting strategy and the signal-background separation with the sphericity and multiplicity, the search shows high sensitivity to the signals. This work sets more stringent constraints on the signal models than the analysis with the offline-reconstructed data. Exclusion limits on the benchmark signals are provided, and the range of excluded signal parameter is derived.

References

- [1] “Why do we expect a Higgs boson? Part II: Unitarization of Vector Boson Scattering”.
<https://www.quantumdiaries.org/2012/02/14/why-do-we-expect-a-higgs-boson-part-ii-unitarization-of-vector-boson-scattering/>.
Accessed: 2020-04-08.
- [2] “Standard Model”. https://en.wikipedia.org/wiki/Standard_Model. Accessed: 2020-04-08.
- [3] **OPAL** Collaboration, “Measurement of the running of the QED coupling in small-angle Bhabha scattering at LEP”, *Eur. Phys. J. C* **45** (2006) 1–21, doi:10.1140/epjc/s2005-02389-3, arXiv:hep-ex/0505072.
- [4] A. Deur, S. J. Brodsky, and G. F. de Teramond, “The QCD Running Coupling”, *Nucl. Phys.* **90** (2016) 1, doi:10.1016/j.pnpnp.2016.04.003, arXiv:1604.08082.
- [5] K. G. Wilson, “Confinement of Quarks”, *Phys. Rev. D* **10** (1974) 2445–2459, doi:10.1103/PhysRevD.10.2445.
- [6] M. Creutz, “Monte Carlo Study of Quantized SU(2) Gauge Theory”, *Phys. Rev. D* **21** (1980) 2308–2315, doi:10.1103/PhysRevD.21.2308.
- [7] I. Montvay and G. Münster, “Quantum Fields on a Lattice”. Cambridge University Press, 1994. doi:10.1017/CB09780511470783, ISBN 9780521599177, 9780511470783,
- [8] H. J. Rothe, “Lattice Gauge Theories: An Introduction”, *World Sci. Lect. Notes Phys.* **74** (1997) 1–605, doi:10.1142/6103.
- [9] **HotQCD** Collaboration, “Equation of state in (2+1)-flavor QCD”, *Phys. Rev. D* **96** (2017) 074510, doi:10.1103/PhysRevD.96.074510, arXiv:1708.04897.
- [10] **BMW** Collaboration, “Ab-initio determination of light hadron masses”, *Science* **322** (2008) 1224–1227, doi:10.1126/science.1163233, arXiv:0906.3599.
- [11] G. Colangelo et al., “Hadron Spectroscopy with Lattice QCD”, *Rev. Mod. Phys.* **83** (2011) 1545–1579, doi:10.1103/RevModPhys.83.1545, arXiv:1011.4408.
- [12] J. Greensite, “The Confinement problem in lattice gauge theory”, *Prog. Part. Nucl. Phys.* **51** (2003) 1–83, doi:10.1016/S0146-6410(03)90012-3, arXiv:hep-lat/0301023.
- [13] T. DeGrand and C. DeTar, “Lattice Methods for Quantum Chromodynamics”, *World Scientific* (2006) doi:10.1142/6067.
- [14] H. Leutwyler, “On the Foundations of Chiral Perturbation Theory”, *Annals of Physics* **235** (1994), no. 1, 165–203, doi:https://doi.org/10.1006/aphy.1994.1094.
- [15] A. Migdal, “Loop equations and 1N expansion”, *Physics Reports* **102** (1983), no. 4, 199–290, doi:https://doi.org/10.1016/0370-1573(83)90076-5.

- [16] Y. Nambu, “QCD and the string model”, *Physics Letters B* **80** (1979), no. 4, 372–376, doi:[https://doi.org/10.1016/0370-2693\(79\)91193-6](https://doi.org/10.1016/0370-2693(79)91193-6).
- [17] I. R. KLEBANOV, “QCD AND STRING THEORY”, *International Journal of Modern Physics A* **21** (2006), no. 08n09, 1831–1843, doi:[10.1142/S0217751X06032794](https://doi.org/10.1142/S0217751X06032794), arXiv:<https://doi.org/10.1142/S0217751X06032794>.
- [18] A. A. Belavin, A. M. Polyakov, A. S. Schwartz, and Y. S. Tyupkin, “Pseudoparticle solutions of the Yang-Mills equations”, *Physics Letters B* **59** (1975), no. 1, 85–87.
- [19] G. t Hooft, “Computation of the quantum effects due to a four-dimensional pseudoparticle”, *Physical Review D* **14** (1976), no. 12, 3432–3450.
- [20] J. D. Bjorken, “Intersections 2000: What’s new in hadron physics”, *AIP Conf. Proc.* **549** (2000), no. 1, 211–229, doi:[10.1063/1.1345244](https://doi.org/10.1063/1.1345244), arXiv:[hep-ph/0008048](https://arxiv.org/abs/hep-ph/0008048).
- [21] V. Zetocha and T. Schäfer, “Instanton contribution to scalar charmonium and glueball decays”, *Phys. Rev. D* **67** (2003) 114003, doi:[10.1103/PhysRevD.67.114003](https://doi.org/10.1103/PhysRevD.67.114003), arXiv:[hep-ph/0212125](https://arxiv.org/abs/hep-ph/0212125).
- [22] J. I. Kapusta, E. Rrapaj, and S. Rudaz, “Hyperon polarization in relativistic heavy ion collisions and axial U(1) symmetry breaking at high temperature”, *Phys. Rev. C* **101** (2020), no. 3, 031901, doi:[10.1103/PhysRevC.101.031901](https://doi.org/10.1103/PhysRevC.101.031901), arXiv:[1910.12759](https://arxiv.org/abs/1910.12759).
- [23] T. Carli, J. Gerigk, A. Ringwald, and F. Schrempp, “QCD instanton induced processes in deep inelastic scattering: Search strategies and model dependencies”, in *Workshop on Monte Carlo Generators for HERA Physics (Plenary Starting Meeting)*, pp. 329–347. 4, 1998. arXiv:[hep-ph/9906441](https://arxiv.org/abs/hep-ph/9906441).
- [24] C. Adloff, H. Collaboration et al., “Search for QCD instanton-induced processes in deep-inelastic scattering at HERA”, *The European Physical Journal C-Particles and Fields* **25** (2002), no. 4, 495–509.
- [25] Z. collaboration et al., “Search for QCD-instanton induced events in deep inelastic ep scattering at HERA”, *The European Physical Journal C-Particles and Fields* **34** (2004), no. 3, 255–265.
- [26] H1 Collaboration, “Search for QCD instanton-induced processes at HERA in the high- Q^2 domain”, *Eur. Phys. J. C* **76** (2016), no. 7, 381, doi:[10.1140/epjc/s10052-016-4194-6](https://doi.org/10.1140/epjc/s10052-016-4194-6), arXiv:[1603.05567](https://arxiv.org/abs/1603.05567).
- [27] A. Hasenfratz and C. Nieter, “Instanton content of the SU (3) vacuum”, *Physics Letters B* **439** (1998), no. 3-4, 366–372.
- [28] Athenodorou, A and Boucaud, Ph and De Soto, F and Rodríguez-Quintero, José and Zafeiropoulos, Savvas, “Instanton liquid properties from lattice QCD”, *Journal of High Energy Physics* **2018** (2018), no. 2, 140.
- [29] V. V. Khoze, D. L. Milne, and M. Spannowsky, “Searching for QCD Instantons at Hadron Colliders”, *Phys. Rev. D* **103** (2021), no. 1, 014017, doi:[10.1103/PhysRevD.103.014017](https://doi.org/10.1103/PhysRevD.103.014017), arXiv:[2010.02287](https://arxiv.org/abs/2010.02287).
- [30] V. Khoze, F. Krauss, and M. Schott, “Large effects from small QCD instantons: making soft bombs at hadron colliders”, *Journal of High Energy Physics* **2020** (2020), no. 1911.09726, 1–29.

- [31] S. Amoroso, D. Kar, and M. Schott, “How to discover QCD Instantons at the LHC”, *Eur. Phys. J. C* **81** (2021), no. 7, 624, doi:10.1140/epjc/s10052-021-09412-1, arXiv:2012.09120.
- [32] V. N. Gribov and L. N. Lipatov, “Deep inelastic e p scattering in perturbation theory”, *Sov. J. Nucl. Phys.* **15** (1972) 438–450.
- [33] Y. L. Dokshitzer, “Calculation of the Structure Functions for Deep Inelastic Scattering and e+ e- Annihilation by Perturbation Theory in Quantum Chromodynamics.”, *Sov. Phys. JETP* **46** (1977) 641–653.
- [34] G. Altarelli and G. Parisi, “Asymptotic Freedom in Parton Language”, *Nucl. Phys. B* **126** (1977) 298–318, doi:10.1016/0550-3213(77)90384-4.
- [35] A. D. Martin, W. J. Stirling, R. S. Thorne, and G. Watt, “Parton distributions for the LHC”, *Eur. Phys. J. C* **63** (2009) 189–285, doi:10.1140/epjc/s10052-009-1072-5, arXiv:0901.0002.
- [36] A. D. Martin, W. J. Stirling, R. S. Thorne, and G. Watt, “Uncertainties on $\alpha(S)$ in global PDF analyses and implications for predicted hadronic cross sections”, *Eur. Phys. J. C* **64** (2009) 653–680, doi:10.1140/epjc/s10052-009-1164-2, arXiv:0905.3531.
- [37] A. D. Martin, W. J. Stirling, R. S. Thorne, and G. Watt, “Heavy-quark mass dependence in global PDF analyses and 3- and 4-flavour parton distributions”, *Eur. Phys. J. C* **70** (2010) 51–72, doi:10.1140/epjc/s10052-010-1462-8, arXiv:1007.2624.
- [38] A. Feike et al., “Combination and reinterpretation of LHC SUSY searches”, *JHEP* **07** (2024) 122, doi:10.1007/JHEP07(2024)122, arXiv:2403.11715.
- [39] N. Deutschmann, T. Flacke, and J. S. Kim, “Current LHC constraints on minimal universal extra dimensions”, *Physics Letters B* **771** (2017) 515–520, doi:https://doi.org/10.1016/j.physletb.2017.06.004.
- [40] R. J. Davis, D. S. Harmer, and K. C. Hoffman, “Search for Neutrinos from the Sun”, *Physical Review Letters* **20** (1968) 1205, doi:10.1103/PhysRevLett.20.1205.
- [41] Y. e. a. S.-K. C. Fukuda, “Measurement of the solar neutrino energy spectrum using neutrino electron scattering”, *Physical Review Letters* **81** (1998) 1158, doi:10.1103/PhysRevLett.81.1158.
- [42] Q. R. e. a. S. C. Ahmad, “Measurement of the Rate of $\nu_e + d \rightarrow p + p + e^-$ Interactions Produced by 8B Solar Neutrinos at the Sudbury Neutrino Observatory”, *Physical Review Letters* **87** (2001) 071301, doi:10.1103/PhysRevLett.87.071301.
- [43] Y. e. a. S.-K. C. Fukuda, “Evidence for Oscillation of Atmospheric Neutrinos”, *Physical Review Letters* **81** (1998) 1562, doi:10.1103/PhysRevLett.81.1562.
- [44] K. e. a. K.-I. C. Hirata, “Observation of a Neutrino Burst from the Supernova SN1987A”, *Physical Review Letters* **58** (1988) 1490, doi:10.1103/PhysRevLett.58.1490.
- [45] K. e. a. K. C. Eguchi, “First Results from KamLAND: Evidence for Reactor Antineutrino Disappearance”, *Physical Review Letters* **90** (2003) 021802, doi:10.1103/PhysRevLett.90.021802.
- [46] F. P. e. a. D. B. C. An, “Observation of Electron-Antineutrino Disappearance at Daya

- Bay”, *Physical Review Letters* **108** (2012) 171803,
doi:10.1103/PhysRevLett.108.171803.
- [47] Y. e. a. D. C. C. Abe, “Indication for the Disappearance of Reactor Electron Antineutrinos in the Double Chooz Experiment”, *Physical Review Letters* **108** (2012) 131801, doi:10.1103/PhysRevLett.108.131801.
- [48] J. K. e. a. R. C. Ahn, “Observation of Reactor Electron Antineutrino Disappearance in the RENO Experiment”, *Physical Review Letters* **108** (2012) 191802, doi:10.1103/PhysRevLett.108.191802.
- [49] M. H. e. a. K. C. Ahn, “Evidence for Muon Neutrino Oscillation in an Accelerator-Based Experiment”, *Physical Review Letters* **93** (2004) 101801, doi:10.1103/PhysRevLett.93.101801.
- [50] D. G. e. a. M. C. Michael, “Observation of Muon Neutrino Disappearance with the MINOS Detectors and the NuMI Neutrino Beam”, *Physical Review Letters* **97** (2006) 191801, doi:10.1103/PhysRevLett.97.191801.
- [51] K. e. a. T. C. Abe, “Indication of Electron Neutrino Appearance from an Accelerator-Produced Off-Axis Muon Neutrino Beam”, *Physical Review Letters* **107** (2011) 041801, doi:10.1103/PhysRevLett.107.041801.
- [52] M. A. e. a. N. C. Acero, “First Measurement of Electron Neutrino Appearance in NOvA”, *Physical Review Letters* **118** (2017) 231801, doi:10.1103/PhysRevLett.118.231801.
- [53] P. Minkowski, “ $\mu \rightarrow e\gamma \rightarrow$ at a Rate of One Out of 109 Muon Decays?”, *Physics Letters B* **67** (1977) 421, doi:10.1016/0370-2693(77)90435-X.
- [54] T. Yanagida, “Horizontal gauge symmetry and masses of neutrinos”,.
- [55] M. Gell-Mann, P. Ramond, and R. Slansky, “Complex spinors and unified theories”,.
- [56] R. N. Mohapatra and G. Senjanovic, “Neutrino Mass and Spontaneous Parity Nonconservation”, *Physical Review Letters* **44** (1980) 912, doi:10.1103/PhysRevLett.44.912.
- [57] M. Magg and C. Wetterich, “Neutrino mass problem and gauge hierarchy”, *Physics Letters B* **94** (1980) 61, doi:10.1016/0370-2693(80)90825-4.
- [58] J. Schechter and J. W. F. Valle, “Neutrino masses in $SU(2) \times U(1)$ theories”, *Physical Review D* **22** (1980) 2227, doi:10.1103/PhysRevD.22.2227.
- [59] B. Pontecorvo, “Mesonium and anti-mesonium”, *Soviet Physics JETP* **6** (1957) 429.
- [60] K. N. e. a. Abazajian, “Light Sterile Neutrinos: A White Paper”, *arXiv preprint arXiv:1204.5379* (2012).
- [61] C. e. a. L. C. Athanassopoulos, “Evidence for neutrino oscillations from the observation of $\bar{\nu}_e$ appearance in a $\bar{\nu}_\mu$ beam”, *Physical Review C* **64** (1998) 112007, doi:10.1103/PhysRevC.64.112007.
- [62] A. A. e. a. M. C. Aguilar-Arevalo, “Improved Search for $\bar{\nu}_\mu \rightarrow \bar{\nu}_e$ Oscillations in the MiniBooNE Experiment”, *Physical Review Letters* **110** (2013) 161801, doi:10.1103/PhysRevLett.110.161801.
- [63] J. Schechter and J. W. F. Valle, “Neutrinoless double- β decay in $SU(2) \times U(1)$ theories”,

- Physical Review D* **25** (1982) 2951, doi:10.1103/PhysRevD.25.2951.
- [64] M. e. a. Doi, “Neutrinoless double beta decay and Majorana neutrino”, *Progress of Theoretical Physics* **83** (1985) 1, doi:10.1143/PTP.83.1.
 - [65] M. e. a. G. C. Agostini, “Results on Neutrinoless Double- β Decay of ^{76}Ge from Phase I of the GERDA Experiment”, *Physical Review Letters* **111** (2013) 122503, doi:10.1103/PhysRevLett.111.122503.
 - [66] K.-Z. Collaboration, “Search for Majorana Neutrinos near the Inverted Mass Hierarchy Region with KamLAND-Zen”, *Physical Review Letters* **117** (2016) 082503, doi:10.1103/PhysRevLett.117.082503.
 - [67] V. C. Rubin and W. K. Ford, Jr., “Rotation of the Andromeda Nebula from a Spectroscopic Survey of Emission Regions”, *Astrophys. J.* **159** (1970) 379–403, doi:10.1086/150317.
 - [68] V. C. Rubin, N. Thonnard, and W. K. Ford, Jr., “Rotational properties of 21 SC galaxies with a large range of luminosities and radii, from NGC 4605 / $R = 4\text{kpc}$ / to UGC 2885 / $R = 122\text{ kpc}$ /”, *Astrophys. J.* **238** (1980) 471, doi:10.1086/158003.
 - [69] K. G. Begeman, A. H. Broeils, and R. H. Sanders, “Extended rotation curves of spiral galaxies: Dark haloes and modified dynamics”, *Mon. Not. Roy. Astron. Soc.* **249** (1991) 523, doi:10.1093/mnras/249.3.523.
 - [70] D. Clowe, A. Gonzalez, and M. Markevitch, “Weak lensing mass reconstruction of the interacting cluster 1E0657-558: Direct evidence for the existence of dark matter”, *Astrophys. J.* **604** (2004) 596–603, doi:10.1086/381970, arXiv:astro-ph/0312273.
 - [71] M. Markevitch et al., “Direct constraints on the dark matter self-interaction cross-section from the merging galaxy cluster 1E0657-56”, *Astrophys. J.* **606** (2004) 819–824, doi:10.1086/383178, arXiv:astro-ph/0309303.
 - [72] D. Clowe et al., “A direct empirical proof of the existence of dark matter”, *Astrophys. J. Lett.* **648** (2006) L109–L113, doi:10.1086/508162, arXiv:astro-ph/0608407.
 - [73] **WMAP** Collaboration, “First year Wilkinson Microwave Anisotropy Probe (WMAP) observations: Parameter estimation methodology”, *Astrophys. J. Suppl.* **148** (2003) 195, doi:10.1086/377335, arXiv:astro-ph/0302218.
 - [74] **Planck** Collaboration, “Planck 2018 results. VI. Cosmological parameters”, *Astron. Astrophys.* **641** (2020) A6, doi:10.1051/0004-6361/201833910, arXiv:1807.06209. [Erratum: *Astron. Astrophys.* 652, C4 (2021)].
 - [75] V. Springel et al., “Simulations of the formation, evolution and clustering of galaxies and quasars”, *nature* **435** (2005), no. 7042, 629–636.
 - [76] C. L. Sarazin, “X-ray emission from clusters of galaxies”, *Rev. Mod. Phys.* **58** (Jan, 1986) 1–115, doi:10.1103/RevModPhys.58.1.
 - [77] N. Arkani-Hamed, S. Dimopoulos, and G. Dvali, “The hierarchy problem and new dimensions at a millimeter”, *Physics Letters B* **429** (1998), no. 3, 263–272, doi:https://doi.org/10.1016/S0370-2693(98)00466-3.
 - [78] D. Abercrombie et al., “Dark Matter benchmark models for early LHC Run-2 Searches:

- Report of the ATLAS/CMS Dark Matter Forum”, *Physics of the Dark Universe* **27** (2020) 100371, doi:<https://doi.org/10.1016/j.dark.2019.100371>.
- [79] **LZ** Collaboration, “Projected WIMP sensitivity of the LUX-ZEPLIN dark matter experiment”, *Phys. Rev. D* **101** (2020), no. 5, 052002, doi:[10.1103/PhysRevD.101.052002](https://doi.org/10.1103/PhysRevD.101.052002), arXiv:1802.06039.
- [80] **XENON** Collaboration, “First Dark Matter Search with Nuclear Recoils from the XENONnT Experiment”, *Phys. Rev. Lett.* **131** (2023), no. 4, 041003, doi:[10.1103/PhysRevLett.131.041003](https://doi.org/10.1103/PhysRevLett.131.041003), arXiv:2303.14729.
- [81] **PICO** Collaboration, “Dark Matter Search Results from the Complete Exposure of the PICO-60 C₃F₈ Bubble Chamber”, *Phys. Rev. D* **100** (2019), no. 2, 022001, doi:[10.1103/PhysRevD.100.022001](https://doi.org/10.1103/PhysRevD.100.022001), arXiv:1902.04031.
- [82] **SuperCDMS** Collaboration, “First Dark Matter Constraints from a SuperCDMS Single-Charge Sensitive Detector”, *Phys. Rev. Lett.* **121** (2018), no. 5, 051301, doi:[10.1103/PhysRevLett.121.051301](https://doi.org/10.1103/PhysRevLett.121.051301), arXiv:1804.10697. [Erratum: *Phys. Rev. Lett.* **122**, 069901 (2019)].
- [83] S. Perlmutter et al., “Measurements of Ω and Λ from 42 High-Redshift Supernovae”, *The Astrophysical Journal* **517** (jun, 1999) 565, doi:[10.1086/307221](https://doi.org/10.1086/307221).
- [84] A. G. Riess et al., “Observational Evidence from Supernovae for an Accelerating Universe and a Cosmological Constant”, *The Astronomical Journal* **116** (sep, 1998) 1009, doi:[10.1086/300499](https://doi.org/10.1086/300499).
- [85] **DESI** Collaboration, “DESI 2024 VI: Cosmological Constraints from the Measurements of Baryon Acoustic Oscillations”, arXiv:2404.03002.
- [86] B. A. Reid et al., “Cosmological constraints from the clustering of the Sloan Digital Sky Survey DR7 luminous red galaxies”, *Monthly Notices of the Royal Astronomical Society* (March, 2010) doi:[10.1111/j.1365-2966.2010.16276.x](https://doi.org/10.1111/j.1365-2966.2010.16276.x).
- [87] C. L. Reichardt et al., “A MEASUREMENT OF SECONDARY COSMIC MICROWAVE BACKGROUND ANISOTROPIES WITH TWO YEARS OF SOUTH POLE TELESCOPE OBSERVATIONS”, *The Astrophysical Journal* **755** (July, 2012) 70, doi:[10.1088/0004-637x/755/1/70](https://doi.org/10.1088/0004-637x/755/1/70).
- [88] C. L. Reichardt, R. de Putter, O. Zahn, and Z. Hou, “NEW LIMITS ON EARLY DARK ENERGY FROM THE SOUTH POLE TELESCOPE”, *The Astrophysical Journal* **749** (March, 2012) L9, doi:[10.1088/2041-8205/749/1/19](https://doi.org/10.1088/2041-8205/749/1/19).
- [89] M. Cvetič, P. Langacker, and G. Shiu, “Phenomenology of a three-family standardlike string model”, *Phys. Rev. D* **66** (Sep, 2002) 066004, doi:[10.1103/PhysRevD.66.066004](https://doi.org/10.1103/PhysRevD.66.066004).
- [90] N. Arkani-Hamed, S. Dimopoulos, and S. Kachru, “Predictive landscapes and new physics at a TeV”, arXiv:hep-th/0501082.
- [91] Z. Chacko, H.-S. Goh, and R. Harnik, “The Twin Higgs: Natural electroweak breaking from mirror symmetry”, *Phys. Rev. Lett.* **96** (2006) 231802, doi:[10.1103/PhysRevLett.96.231802](https://doi.org/10.1103/PhysRevLett.96.231802), arXiv:hep-ph/0506256.
- [92] L. Randall and R. Sundrum, “Large Mass Hierarchy from a Small Extra Dimension”, *Phys. Rev. Lett.* **83** (Oct, 1999) 3370–3373, doi:[10.1103/PhysRevLett.83.3370](https://doi.org/10.1103/PhysRevLett.83.3370).

- [93] L. Randall and R. Sundrum, “An Alternative to Compactification”, *Phys. Rev. Lett.* **83** (Dec, 1999) 4690–4693, doi:10.1103/PhysRevLett.83.4690.
- [94] S. Knapen, S. Pagan Griso, M. Papucci, and D. J. Robinson, “Triggering Soft Bombs at the LHC”, *JHEP* **08** (2017) 076, doi:10.1007/JHEP08(2017)076, arXiv:1612.00850.
- [95] J. Barron et al., “Unsupervised hadronic SUEP at the LHC”, *JHEP* **12** (2021) 129, doi:10.1007/JHEP12(2021)129, arXiv:2107.12379.
- [96] “BSM Higgs production cross sections at $\sqrt{s} = 13$ TeV (update in CERN Report4 2016)”. https://twiki.cern.ch/twiki/bin/view/LHCPhysics/CERNYellowReportPageBSMAT13TeV#Point_like_effective_interaction. Accessed: 2024-11-24.
- [97] L. Evans and P. Bryant, “LHC Machine”, *JINST* **3** (2008), no. 08, S08001, doi:10.1088/1748-0221/3/08/S08001.
- [98] L. Forthomme (Wikimedia Commons), “File:Cern-accelerator-complex.svg — Wikimedia Commons, the free media repository”, <https://commons.wikimedia.org/wiki/File:Cern-accelerator-complex.svg>, 2016. (Retrieved Jul 24, 2017).
- [99] W. Herr and B. Muratori, “Concept of luminosity”,.
- [100] **CMS** Collaboration, “Public CMS Luminosity Information”. <https://twiki.cern.ch/twiki/bin/view/CMSPublic/LumiPublicResults>. (Retrieved Dec 6, 2022).
- [101] “How CMS Works”. <http://cms.cern/detector>. Accessed: 2020-02-27.
- [102] Neutelings, Izaak, “CMS coordinate system – TikZ.net”, https://tikz.net/axis3d_cms/, 2022. (Retrieved Dec 2, 2022).
- [103] Neutelings, Izaak, “Pseudorapidity – TikZ.net”, https://tikz.net/axis2d_pseudorapidity/, 2022. (Retrieved Dec 2, 2022).
- [104] **CMS** Collaboration, “The CMS experiment at the CERN LHC”, *JINST* **3** (2008) S08004, doi:10.1088/1748-0221/3/08/S08004.
- [105] **CMS** Collaboration, “Performance of the CMS Drift Tube Chambers with Cosmic Rays”, *JINST* **5** (2010) T03015, doi:10.1088/1748-0221/5/03/T03015, arXiv:0911.4855.
- [106] **CMS** Collaboration, “Description and performance of track and primary-vertex reconstruction with the CMS tracker”, *JINST* **9** (2014), no. 10, P10009, doi:10.1088/1748-0221/9/10/P10009, arXiv:1405.6569.
- [107] **CMS Tracker** Group, “The CMS Phase-1 Pixel Detector Upgrade”, *JINST* **16** (2021), no. 02, P02027, doi:10.1088/1748-0221/16/02/P02027, arXiv:2012.14304.
- [108] **CMS** Collaboration, “CMS Tracker Detector Performance Results”, <https://twiki.cern.ch/twiki/bin/view/CMSPublic/DPGResultsTRK>, 2022. (Retrieved Dec 2, 2022).
- [109] **CMS** Collaboration, “The CMS electromagnetic calorimeter project: Technical Design Report”,.
- [110] **CMS** Collaboration V. Karimäki, et al., “The CMS tracker system project: Technical

- Design Report”. Technical design report. CMS. CERN, Geneva, 1997.
- [111] **CMS** Collaboration, “The Phase-1 upgrade of the CMS pixel detector”, *JINST* **12** (2017), no. 07, C07009, doi:10.1088/1748-0221/12/07/C07009.
 - [112] **CMS** Collaboration, “Description and performance of track and primary-vertex reconstruction with the CMS tracker”, *JINST* **9** (2014) P10009, doi:10.1088/1748-0221/9/10/P10009, arXiv:1405.6569.
 - [113] **CMS** Collaboration, “CMS Tracking POG Performance Plots For 2017 with PhaseI pixel detector”, https://twiki.cern.ch/twiki/bin/view/CMSPublic/TrackingPOGPerformance2017MC#Vertex_Resolutions, 2022. (Retrieved Dec 8, 2022).
 - [114] **CMS** Collaboration, “The CMS muon project : Technical Design Report”, Technical Design Report CMS. CERN, Geneva, 1997.
 - [115] **CMS** Collaboration, “The CMS trigger system”, *JINST* **12** (2017) P01020, doi:10.1088/1748-0221/12/01/P01020, arXiv:1609.02366.
 - [116] **CMS** Collaboration, “Enriching the Physics Program of the CMS Experiment via Data Scouting and Data Parking”, arXiv:2403.16134.
 - [117] **CMS** Collaboration, “Description and performance of track and primary-vertex reconstruction with the CMS tracker”, *JINST* **9** (2014) P10009, doi:10.1088/1748-0221/9/10/P10009, arXiv:1405.6569.
 - [118] K. Rose, “Deterministic annealing for clustering, compression, classification, regression, and related optimization problems”, *Proceedings of the IEEE* **86** (1998), no. 11, 2210, doi:10.1109/5.726788.
 - [119] W. Waltenberger, R. Frühwirth, and P. Vanlaer, “Adaptive vertex fitting”, *Journal of Physics G: Nuclear and Particle Physics* **34** (2007), no. 12, N343, doi:10.1088/0954-3899/34/12/N01.
 - [120] R. Frühwirth, “Application of Kalman filtering to track and vertex fitting”, *Nuclear Instruments and Methods in Physics Research Section A: Accelerators, Spectrometers, Detectors and Associated Equipment* **262** (1987), no. 2-3, 444–450, doi:10.1016/0168-9002(87)90887-4.
 - [121] P. Billoir, “Progressive track recognition with a Kalman-like fitting procedure”, *Computer Physics Communications* **57** (1989), no. 1-3, 390–394, doi:10.1016/0010-4655(89)90249-X.
 - [122] P. Billoir and S. Qian, “Simultaneous pattern recognition and track fitting by the Kalman filtering method”, *Nuclear Instruments and Methods in Physics Research Section A: Accelerators, Spectrometers, Detectors and Associated Equipment* **294** (1990), no. 1-2, 219–228, doi:10.1016/0168-9002(90)91835-Y.
 - [123] R. Mankel, “A concurrent track evolution algorithm for pattern recognition in the HERA-B main tracking system”, *Nuclear Instruments and Methods in Physics Research Section A: Accelerators, Spectrometers, Detectors and Associated Equipment* **395** (1997), no. 2, 169–184, doi:10.1016/S0168-9002(97)00705-5.
 - [124] **CMS** Collaboration, “Commissioning of the Particle-flow Event Reconstruction with the first LHC collisions recorded in the CMS detector”, technical report, 2010.

- [125] **CMS** Collaboration, “Particle-flow reconstruction and global event description with the CMS detector”, *JINST* **12** (2017), no. 10, P10003, doi:10.1088/1748-0221/12/10/P10003, arXiv:1706.04965.
- [126] M. Cacciari, G. P. Salam, and G. Soyez, “The anti- k_t jet clustering algorithm”, *JHEP* **04** (2008) 063, doi:10.1088/1126-6708/2008/04/063, arXiv:0802.1189.
- [127] **CMS** Collaboration, “Measurement of long-range near-side two-particle angular correlations in pp collisions at $\sqrt{s}=13$ TeV”, *Phys. Rev. Lett.* **116** (2016), no. 17, 172302, doi:10.1103/PhysRevLett.116.172302, arXiv:1510.03068.
- [128] **CMS** Collaboration, “Observation of enhanced long-range elliptic anisotropies inside high-multiplicity jets in pp collisions at $\sqrt{s}=13$ TeV”, *Phys. Rev. Lett.* **133** (2024) 142301, doi:10.1103/PhysRevLett.133.142301, arXiv:2312.17103.
- [129] **ALICE** Collaboration, “Multiplicity dependence of π , K, and p production in pp collisions at $\sqrt{s}=13$ TeV”, *Eur. Phys. J. C* **80** (2020), no. 8, 693, doi:10.1140/epjc/s10052-020-8125-1, arXiv:2003.02394.
- [130] **ATLAS** Collaboration, “Underlying-event studies with strange hadrons in pp collisions at $\sqrt{s}=13$ TeV with the ATLAS detector”, *Eur. Phys. J. C* **84** (2024), no. 12, 1335, doi:10.1140/epjc/s10052-024-13243-1, arXiv:2405.05048.
- [131] S. Brandt and H. Dahmen, “Axes and scalar measures of two-jet and three-jet events”, *Zeitschrift für Physik C Particles and Fields* **1** (1979) 61, doi:10.1007/BF01450381.
- [132] P. T. Komiske, E. M. Metodiev, and J. Thaler, “Energy flow networks: deep sets for particle jets”, *JHEP* **01** (2019) 121, doi:10.1007/JHEP01(2019)121, arXiv:1603.05567.
- [133] C. Cesarotti and J. Thaler, “A Robust Measure of Event Isotropy at Colliders”, *JHEP* **08** (2020) 084, doi:10.1007/JHEP08(2020)084, arXiv:1810.05165.
- [134] C. Cesarotti, M. Reece, and M. J. Strassler, “The efficacy of event isotropy as an event shape observable”, *JHEP* **07** (2021) 215, doi:10.1007/jhep07(2021)215, arXiv:2011.06599.
- [135] T. Sjöstrand, P. Edén, C. Friberg, L. Lönnblad, G. Miu, S. Mrenna and E. Norrbin, “High-energy-physics event generation with Pythia 6.1”, *Computer Physics Communications* **135** (2001), no. 2, 238–259, doi:https://doi.org/10.1016/S0010-4655(00)00236-8.
- [136] P. . Team, “PYTHIA 8 Online Manual”. <https://pythia.org/manuals/pythia8305/Welcome.html>. Accessed 2022 Jan 19.
- [137] G. Corcella, I. G. Knowles, G. Marchesini, S. Moretti, K. Odagiri, P. Richardson, M. H. Seymour and B. R. Webber, “HERWIG 6: an event generator for hadron emission reactions with interfering gluons (including supersymmetric processes)”, *Journal of High Energy Physics* **2001** (2001), no. 01, 010, doi:10.1088/1126-6708/2001/01/010.
- [138] T. Pierog et al., “EPOS LHC: Test of collective hadronization with data measured at the CERN Large Hadron Collider”, *Phys. Rev. C* **92** (2015), no. 3, 034906, doi:10.1103/PhysRevC.92.034906, arXiv:1306.0121.
- [139] S. Agostinelli et al., “Geant4—a simulation toolkit”, *Nuclear Instruments and Methods*

- in *Physics Research Section A: Accelerators, Spectrometers, Detectors and Associated Equipment* **506** (2003), no. 3, 250–303,
doi:[https://doi.org/10.1016/S0168-9002\(03\)01368-8](https://doi.org/10.1016/S0168-9002(03)01368-8).
- [140] J. Allison et al., “Geant4 developments and applications”, *IEEE Transactions on Nuclear Science* **53** (2006), no. 1, 270–278, doi:[10.1109/TNS.2006.869826](https://doi.org/10.1109/TNS.2006.869826).
 - [141] J. Allison et al., “Recent developments in Geant4”, *Nuclear Instruments and Methods in Physics Research Section A: Accelerators, Spectrometers, Detectors and Associated Equipment* **835** (2016) 186–225, doi:<https://doi.org/10.1016/j.nima.2016.06.125>.
 - [142] **CMS** Collaboration, “Extraction and validation of a new set of CMS PYTHIA8 tunes from underlying-event measurements”, *Eur. Phys. J. C* **80** (2020), no. 1, 4, doi:[10.1140/epjc/s10052-019-7499-4](https://doi.org/10.1140/epjc/s10052-019-7499-4), arXiv:1903.12179.
 - [143] **ATLAS** Collaboration, “The Pythia 8 A3 tune description of ATLAS minimum bias and inelastic measurements incorporating the Donnachie-Landshoff diffractive model”, technical report, CERN, Geneva, 2016. All figures including auxiliary figures are available at <https://atlas.web.cern.ch/Atlas/GROUPS/PHYSICS/PUBNOTES/ATL-PHYS-PUB-2016-017>.
 - [144] **CMS** Collaboration, “Development and validation of HERWIG 7 tunes from CMS underlying-event measurements”, *Eur. Phys. J. C* **81** (2021) 312, doi:[10.1140/epjc/s10052-021-08949-5](https://doi.org/10.1140/epjc/s10052-021-08949-5), arXiv:2011.03422.
 - [145] **CMS** Collaboration, “Event generator tunes obtained from underlying event and multiparton scattering measurements”, *Eur. Phys. J. C* **76** (2016), no. 3, 155, doi:[10.1140/epjc/s10052-016-3988-x](https://doi.org/10.1140/epjc/s10052-016-3988-x), arXiv:1512.00815.
 - [146] The ATLAS Collaboration, “ATLAS Pythia 8 tunes to 7 TeV data”, technical report, CERN, Geneva, 2014. All figures including auxiliary figures are available at <https://atlas.web.cern.ch/Atlas/GROUPS/PHYSICS/PUBNOTES/ATL-PHYS-PUB-2014-021>.
 - [147] **CMS** Collaboration, “CMS pythia 8 colour reconnection tunes based on underlying-event data”, *Eur. Phys. J. C* **83** (2023), no. 7, 587, doi:[10.1140/epjc/s10052-023-11630-8](https://doi.org/10.1140/epjc/s10052-023-11630-8), arXiv:2205.02905.
 - [148] A. Andreassen et al., “OmniFold: A method to simultaneously unfold all observables”, *Phys. Rev. Lett.* **124** (May, 2020) 182001, doi:[10.1103/PhysRevLett.124.182001](https://doi.org/10.1103/PhysRevLett.124.182001).
 - [149] A. Andreassen et al., “Scaffolding Simulations with Deep Learning for High-dimensional Deconvolution”, <https://arxiv.org/abs/2105.04448>, 2021.
 - [150] G. D’Agostini, “A Multidimensional unfolding method based on Bayes’ theorem”, *Nucl. Instrum. Meth. A* **362** (1995) 487–498, doi:[10.1016/0168-9002\(95\)00274-X](https://doi.org/10.1016/0168-9002(95)00274-X).
 - [151] P. T. Komiske, E. M. Metodiev, and J. Thaler, “Energy Flow Networks: Deep Sets for Particle Jets”, *JHEP* **01** (2019) 121, doi:[10.1007/JHEP01\(2019\)121](https://doi.org/10.1007/JHEP01(2019)121), arXiv:1810.05165.
 - [152] M. Zaheer et al., “Deep sets”, *Advances in neural information processing systems* **30** (2017).
 - [153] G. D’Agostini, “A multidimensional unfolding method based on Bayes’ theorem”,

Nuclear Instruments and Methods in Physics Research Section A: Accelerators, Spectrometers, Detectors and Associated Equipment **362** (1995), no. 2, 487–498, doi:[https://doi.org/10.1016/0168-9002\(95\)00274-X](https://doi.org/10.1016/0168-9002(95)00274-X).

- [154] **CMS** Collaboration, “Tracking performance for charged pions with Run2 Legacy data”,.
- [155] C. Collaboration et al., “Muon Tracking Efficiency for 2018 dataset using Tag and Probe method, CMS Detector Performance Summary CMS-DP-2020-013, 2019”, *URL*: <https://cds.cern.ch/record/2712742>.
- [156] **Particle Data** Group, “Review of particle physics”, *Phys. Rev. D* **110** (2024), no. 3, 030001, doi:10.1103/PhysRevD.110.030001.
- [157] **ALEPH** Collaboration, “Studies of QCD at e^+e^- centre-of-mass energies between 91-GeV and 209-GeV”, *Eur. Phys. J. C* **35** (2004) 457, doi:10.1140/epjc/s2004-01891-4.
- [158] **BRAHMS** Collaboration, “Quark gluon plasma and color glass condensate at RHIC? The Perspective from the BRAHMS experiment”, *Nucl. Phys. A* **757** (2005) 1, doi:10.1016/j.nuclphysa.2005.02.130, arXiv:nucl-ex/0410020.
- [159] **PHOBOS** Collaboration, “The PHOBOS perspective on discoveries at RHIC”, *Nucl. Phys. A* **757** (2005) 28, doi:10.1016/j.nuclphysa.2005.03.084, arXiv:nucl-ex/0410022.
- [160] **STAR** Collaboration, “Experimental and theoretical challenges in the search for the quark gluon plasma: The STAR Collaboration’s critical assessment of the evidence from RHIC collisions”, *Nucl. Phys. A* **757** (2005) 102, doi:10.1016/j.nuclphysa.2005.03.085, arXiv:nucl-ex/0501009.
- [161] **PHENIX** Collaboration, “Formation of dense partonic matter in relativistic nucleus-nucleus collisions at RHIC: Experimental evaluation by the PHENIX collaboration”, *Nucl. Phys. A* **757** (2005) 184, doi:10.1016/j.nuclphysa.2005.03.086, arXiv:nucl-ex/0410003.
- [162] **CMS** Collaboration, “Observation of Long-Range Near-Side Angular Correlations in Proton-Proton Collisions at the LHC”, *JHEP* **09** (2010) 091, doi:10.1007/JHEP09(2010)091, arXiv:1009.4122.
- [163] **ATLAS** Collaboration, “Observation of Long-Range Elliptic Azimuthal Anisotropies in $\sqrt{s}=13$ and 2.76 TeV pp Collisions with the ATLAS Detector”, *Phys. Rev. Lett.* **116** (2016), no. 17, 172301, doi:10.1103/PhysRevLett.116.172301, arXiv:1509.04776.
- [164] **ALICE** Collaboration, “Long- and short-range correlations and their event-scale dependence in high-multiplicity pp collisions at $\sqrt{s}=13$ TeV”, *JHEP* **05** (2021) 290, doi:10.1007/JHEP05(2021)290, arXiv:2101.03110.
- [165] S. Amoroso, D. Kar, and M. Schott, “How to discover QCD Instantons at the LHC”, *Eur. Phys. J. C* **81** (2021) 624, doi:10.1140/epjc/s10052-021-09412-1, arXiv:2012.09120.
- [166] M. Mangano, “Remarks on the numerical impact of potential theoretical systematics in the prediction of QCD instanton cross sections”, 2021. arXiv:2101.02719.
- [167] R. Kleiss, W. J. Stirling, and S. D. Ellis, “A New Monte Carlo Treatment of

- Multiparticle Phase Space at High-energies”, *Comput. Phys. Commun.* **40** (1986) 359, doi:10.1016/0010-4655(86)90119-0.
- [168] A. Bermudez Martinez et al., “The transverse momentum spectrum of low mass Drell–Yan production at next-to-leading order in the parton branching method”, *Eur. Phys. J. C* **80** (2020) 598, doi:10.1140/epjc/s10052-020-8136-y, arXiv:2001.06488.
 - [169] I. Bujanja et al., “The small k_T region in Drell–Yan production at next-to-leading order with the parton branching method”, *Eur. Phys. J. C* **84** (2024) 154, doi:10.1140/epjc/s10052-024-12507-0, arXiv:2312.08655.
 - [170] M. Mendizabal, F. Guzman, H. Jung, and S. Taheri Monfared, “On the role of soft gluons in collinear parton densities and parton shower event generators”, 2023. arXiv:2309.11802.
 - [171] P. Hägler, B. U. Musch, J. W. Negele, and A. Schäfer, “Intrinsic quark transverse momentum in the nucleon from lattice QCD”, *Euro. Phys. Lett.* **88** (2009) 61001, doi:10.1209/0295-5075/88/61001, arXiv:0908.1283.
 - [172] B. U. Musch et al., “Transverse momentum distributions of quarks in the nucleon from lattice QCD”, *PoS LC2008* (2008) 053, doi:10.22323/1.061.0053, arXiv:0811.1536.
 - [173] B. U. Musch, P. Hägler, J. W. Negele, and A. Schäfer, “Exploring quark transverse momentum distributions with lattice QCD”, *Phys. Rev. D* **83** (2011) 094507, doi:10.1103/PhysRevD.83.094507, arXiv:1011.1213.
 - [174] C. Bierlich et al., “A comprehensive guide to the physics and usage of PYTHIA 8.3”, *SciPost Phys. Codeb.* **2022** (2022) 8, doi:10.21468/SciPostPhysCodeb.8, arXiv:2203.11601.
 - [175] T. Sjöstrand and P. Z. Skands, “Multiple interactions and the structure of beam remnants”, *JHEP* **03** (2004) 053, doi:10.1088/1126-6708/2004/03/053, arXiv:hep-ph/0402078.
 - [176] J. Bellm et al., “Herwig 7.0/Herwig++ 3.0 release note”, *Eur. Phys. J. C* **76** (2016) 196, doi:10.1140/epjc/s10052-016-4018-8, arXiv:1512.01178.
 - [177] **Sherpa** Collaboration, “Event Generation with Sherpa 2.2”, *SciPost Phys.* **7** (2019) 034, doi:10.21468/SciPostPhys.7.3.034, arXiv:1905.09127.
 - [178] C. T. H. Davies, B. R. Webber, and W. J. Stirling, “Drell–Yan Cross-Sections at Small Transverse Momentum”, *Nucl. Phys. B* **256** (1985) 413, doi:10.1016/0550-3213(85)90402-X.
 - [179] M. Guzzi, P. M. Nadolsky, and B. Wang, “Nonperturbative contributions to a resummed leptonic angular distribution in inclusive neutral vector boson production”, *Phys. Rev. D* **90** (2014) 014030, doi:10.1103/PhysRevD.90.014030, arXiv:1309.1393.
 - [180] S.-Y. Wei, “Exploring the non-perturbative Sudakov factor via Z^0 -boson production in pp collisions”, *Phys. Lett. B* **817** (2021) 136356, doi:10.1016/j.physletb.2021.136356, arXiv:2009.06514.
 - [181] **NuSea** Collaboration, “Absolute Drell–Yan dimuon cross-sections in 800 GeV/c pp and pd collisions”, 2003. arXiv:hep-ex/0302019.

- [182] J. C. Webb, “Measurement of continuum dimuon production in 800-GeV/ c proton nucleon collisions”. PhD thesis, New Mexico State U., 2003. [arXiv:hep-ex/0301031](#). FERMILAB-THESIS-2002-56, [doi:10.2172/1155678](#).
- [183] D. Antreasyan et al., “Dimuon Scaling Comparison at 44 GeV and 62 GeV”, *Phys. Rev. Lett.* **48** (1982) 302, [doi:10.1103/PhysRevLett.48.302](#).
- [184] **PHENIX** Collaboration, “Measurements of $\mu\mu$ pairs from open heavy flavor and Drell–Yan in $p + p$ collisions at $\sqrt{s} = 200$ GeV”, *Phys. Rev. D* **99** (2019) 072003, [doi:10.1103/PhysRevD.99.072003](#), [arXiv:1805.02448](#).
- [185] **D0** Collaboration, “Measurement of the inclusive differential cross section for Z bosons as a function of transverse momentum in $\bar{p}p$ collisions at $\sqrt{s} = 1.8$ TeV”, *Phys. Rev. D* **61** (2000) 032004, [doi:10.1103/PhysRevD.61.032004](#), [arXiv:hep-ex/9907009](#).
- [186] **CDF** Collaboration, “The transverse momentum and total cross section of e^+e^- pairs in the Z boson region from $p\bar{p}$ collisions at $\sqrt{s} = 1.8$ TeV”, *Phys. Rev. Lett.* **84** (2000) 845, [doi:10.1103/PhysRevLett.84.845](#), [arXiv:hep-ex/0001021](#).
- [187] **D0** Collaboration, “Measurement of the normalized $Z/\gamma^* \rightarrow \mu^+\mu^-$ Transverse Momentum Distribution in $p\bar{p}$ Collisions at $\sqrt{s} = 1.96$ TeV”, *Phys. Lett. B* **693** (2010) 522, [doi:10.1016/j.physletb.2010.09.012](#), [arXiv:1006.0618](#).
- [188] **CDF** Collaboration, “Transverse momentum cross section of e^+e^- pairs in the Z-boson region from $p\bar{p}$ collisions at $\sqrt{s} = 1.96$ TeV”, *Phys. Rev. D* **86** (2012) 052010, [doi:10.1103/PhysRevD.86.052010](#), [arXiv:1207.7138](#).
- [189] **CMS** Collaboration, “Study of Z production in PbPb and pp collisions at $\sqrt{s_{NN}} = 2.76$ TeV in the dimuon and dielectron decay channels”, *JHEP* **03** (2015) 022, [doi:10.1007/JHEP03\(2015\)022](#), [arXiv:1410.4825](#).
- [190] **ATLAS** Collaboration, “Measurement of the transverse momentum and ϕ_η^* distributions of Drell–Yan lepton pairs in proton–proton collisions at $\sqrt{s} = 8$ TeV with the ATLAS detector”, *Eur. Phys. J. C* **76** (2016) 291, [doi:10.1140/epjc/s10052-016-4070-4](#), [arXiv:1512.02192](#).
- [191] **CMS** Collaboration, “Study of Drell–Yan dimuon production in proton-lead collisions at $\sqrt{s_{NN}} = 8.16$ TeV”, *JHEP* **05** (2021) 182, [doi:10.1007/JHEP05\(2021\)182](#), [arXiv:2102.13648](#).
- [192] **CMS** Collaboration, “Measurement of the mass dependence of the transverse momentum of lepton pairs in Drell–Yan production in proton-proton collisions at $\sqrt{s} = 13$ TeV”, *Eur. Phys. J. C* **83** (2023) 628, [doi:10.1140/epjc/s10052-023-11631-7](#), [arXiv:2205.04897](#).
- [193] **LHCb** Collaboration, “Precision measurement of forward Z boson production in proton-proton collisions at $\sqrt{s} = 13$ TeV”, *JHEP* **07** (2022) 026, [doi:10.1007/JHEP07\(2022\)026](#), [arXiv:2112.07458](#).
- [194] J. Alwall et al., “The automated computation of tree-level and next-to-leading order differential cross sections, and their matching to parton shower simulations”, *JHEP* **07** (2014) 079, [doi:10.1007/JHEP07\(2014\)079](#), [arXiv:1405.0301](#).
- [195] **CMS** Collaboration, “Extraction and validation of a new set of CMS PYTHIA8 tunes

- from underlying-event measurements”, *Eur. Phys. J. C* **80** (2020) 4, doi:10.1140/epjc/s10052-019-7499-4, arXiv:1903.12179.
- [196] A. Buckley et al., “Rivet user manual”, *Comput. Phys. Commun.* **184** (2013) 2803–2819, doi:10.1016/j.cpc.2013.05.021, arXiv:1003.0694.
- [197] A. Buckley et al., “Systematic event generator tuning for the LHC”, *Eur. Phys. J. C* **65** (2010) 331, doi:10.1140/epjc/s10052-009-1196-7, arXiv:0907.2973.
- [198] F. James and M. Roos, “Minuit - a system for function minimization and analysis of the parameter errors and correlations”, *Computer Physics Communications* **10** (1975), no. 6, 343, doi:https://doi.org/10.1016/0010-4655(75)90039-9.
- [199] H. Cramér, “Mathematical methods of statistics”, volume 26. Princeton university press, 1999.
- [200] C. R. Rao, “Information and the accuracy attainable in the estimation of statistical parameters”, in *Breakthroughs in Statistics: Foundations and basic theory*, pp. 235–247. Springer, 1992.
- [201] M. Fréchet, “Sur l’extension de certaines évaluations statistiques au cas de petits échantillons”, *Revue de l’Institut International de Statistique* (1943) 182–205.
- [202] G. Darmais, “Sur les limites de la dispersion de certaines estimations”, *Revue de l’Institut International de Statistique* (1945) 9–15.
- [203] A. Aitken and H. Silverstone, “Xv.—on the estimation of statistical parameters”, *Proceedings of the Royal Society of Edinburgh Section A: Mathematics* **61** (1942), no. 2, 186–194.
- [204] S. Baranov et al., “CASCADE3 A Monte Carlo event generator based on TMDs”, *Eur. Phys. J. C* **81** (2021) 425, doi:10.1140/epjc/s10052-021-09203-8, arXiv:2101.10221.
- [205] E. Gross and O. Vitells, “Trial factors for the look elsewhere effect in high energy physics”, *Eur. Phys. J. C* **70** (2010) 525, doi:10.1140/epjc/s10052-010-1470-8, arXiv:1005.1891.
- [206] C. Balázs and C.-P. Yuan, “Soft gluon effects on lepton pairs at hadron colliders”, *Phys. Rev. D* **56** (1997) 5558, doi:10.1103/PhysRevD.56.5558, arXiv:hep-ph/9704258.
- [207] **CMS** Collaboration, “Particle-Flow Event Reconstruction in CMS and Performance for Jets, Taus, and MET”,.
- [208] S. Knapen, S. Pagan Griso, M. Papucci, and D. J. Robinson, “Triggering Soft Bombs at the LHC”, *JHEP* **08** (2017) 076, doi:10.1007/JHEP08(2017)076, arXiv:1612.00850.
- [209] J. Alwall et al., “The automated computation of tree-level and next-to-leading order differential cross sections, and their matching to parton shower simulations”, *JHEP* **07** (2014) 079, doi:10.1007/JHEP07(2014)079, arXiv:1405.0301.
- [210] T. Sjostrand, S. Mrenna, and P. Z. Skands, “PYTHIA 6.4 Physics and Manual”, *JHEP* **05** (2006) 026, doi:10.1088/1126-6708/2006/05/026, arXiv:hep-ph/0603175.
- [211] T. Sjöstrand et al., “An introduction to PYTHIA 8.2”, *Comput. Phys. Commun.* **191** (2015) 159–177, doi:10.1016/j.cpc.2015.01.024, arXiv:1410.3012.

- [212] **NNPDF** Collaboration, “Parton distributions from high-precision collider data”, *Eur. Phys. J. C* **77** (2017), no. 10, 663, doi:10.1140/epjc/s10052-017-5199-5, arXiv:1706.00428.
- [213] **CMS** Collaboration, “Jet Identification for the 13 TeV UL data”. https://twiki.cern.ch/twiki/bin/view/CMS/JetID13TeVUL#Preliminary_Recommendations_for.
- [214] S. Choi and H. Oh, “Improved extrapolation methods of data-driven background estimations in high energy physics”, *Eur. Phys. J. C* **81** (2021), no. 7, 643, doi:10.1140/epjc/s10052-021-09404-1, arXiv:1906.10831.
- [215] **CMS** Collaboration, “Jet energy scale and resolution performance with 13 TeV data collected by CMS in 2016-2018”,.
- [216] K. Becker et al., “Precise predictions for boosted Higgs production”, *SciPost Phys. Core* **7** (2024) 001, doi:10.21468/SciPostPhysCore.7.1.001, arXiv:2005.07762.
- [217] A. L. Read, “Presentation of search results: The CL_s technique”, *J. Phys. G* **28** (2002) 2693–2704, doi:10.1088/0954-3899/28/10/313.
- [218] A. L. Read, “Modified frequentist analysis of search results (The CL(s) method)”, in *Workshop on Confidence Limits*, pp. 81–101. 8, 2000.
- [219] T. Junk, “Confidence level computation for combining searches with small statistics”, *Nucl. Instrum. Meth. A* **434** (1999) 435–443, doi:10.1016/S0168-9002(99)00498-2, arXiv:hep-ex/9902006.
- [220] **CMS** Collaboration, “Search for Soft Unclustered Energy Patterns in Proton-Proton Collisions at 13 TeV”, *Phys. Rev. Lett.* **133** (2024), no. 19, 191902, doi:10.1103/PhysRevLett.133.191902, arXiv:2403.05311.
- [221] **CMS** Collaboration, “Underlying event measurements with leading particles and jets in pp collisions at $\sqrt{s} = 13$ TeV”, CMS Physics Analysis Summary CMS-PAS-FSQ-15-007, 2015.

A Additional material for the measurement of event shapes in minimum bias events

A.1 Generator settings

In this section, the specific generator settings used for various Monte Carlo samples used in the analysis are given.

Many of the different simulations rely on some common simulation settings. In particular, CMS uses a set of common PYTHIA 8 settings, which are:

```
Tune:preferLHAPDF = 2
Main:timesAllowErrors = 10000
Check:epTolErr = 0.01
Beams:setProductionScalesFromLHEF = off
SLHA:keepSM = on
SLHA:minMassSM = 1000.
ParticleDecays:limitTau0 = on
ParticleDecays:tau0Max = 10
ParticleDecays:allowPhotonRadiation = on
```

A.1.1 PYTHIA A3 tune

This is a tune initially performed by ATLAS, with the settings shown below. In addition to these settings, taken directly from the A3 tune, the CMS common PYTHIA settings given above are also applied.

```
SoftQCD:inelastic = on
```

```
Tune:pp 14
Tune:ee 7
```

```
MultipartonInteractions:pT0Ref 2.45
MultipartonInteractions:ecmPow 0.21
MultipartonInteractions:coreRadius 0.55
MultipartonInteractions:coreFraction 0.90
```

```
ColourReconnection:range 1.8
```

```
Diffraction:PomFlux 4
Diffraction:PomFluxEpsilon 0.07
Diffraction:PomFluxAlphaPrime 0.25
```

A.1.2 PYTHIA CP1

SoftQCD:inelastic = on

Tune:pp 14

Tune:ee 7

PDF:pSet=17

MultipartonInteractions:bProfile=2

MultipartonInteractions:ecmPow=0.1543

MultipartonInteractions:pT0Ref=2.40

MultipartonInteractions:coreRadius=0.5436

MultipartonInteractions:coreFraction=0.6836

ColourReconnection:range=2.633

SigmaTotal:zeroAXB=off

SpaceShower:rapidityOrder=off

A.1.3 EPOS-LHC

A.1.4 PYTHIA CP5

SoftQCD:inelastic = on

Tune:pp 14

Tune:ee 7

MultipartonInteractions:ecmPow=0.03344

PDF:pSet=20

MultipartonInteractions:bProfile=2

MultipartonInteractions:pT0Ref=1.41

MultipartonInteractions:coreRadius=0.7634

MultipartonInteractions:coreFraction=0.63

ColourReconnection:range=5.176

SigmaTotal:zeroAXB=off

SpaceShower:alphaSorder=2

SpaceShower:alphaSvalue=0.118

SigmaProcess:alphaSvalue=0.118

SigmaProcess:alphaSorder=2

MultipartonInteractions:alphaSvalue=0.118

MultipartonInteractions:alphaSorder=2

TimeShower:alphaSorder=2

TimeShower:alphaSvalue=0.118

A.1.5 PYTHIA CUEPT8M1

SoftQCD:inelastic = on

Tune:pp 14

Tune:ee 7

PDF:pSet=17

MultipartonInteractions:ecmPow=0.25208

MultipartonInteractions:expPow=1.6

MultipartonInteractions:pT0Ref=2.4024

A.1.6 PYTHIA A14 Tunes

Because the A14 tune set, including the eigenvariations, as well as the tune run with different PDF sets, are included directly in PYTHIA, the setting changes required for each of the different samples are minimal.

Each sample uses the inelastic collision setting:

SoftQCD:inelastic = on

along with simply the tune settings, which for the nominal A14 tune is:

Tune:pp 21

Tune:ee 7

and, as with the A3P tune, the common CMS PYTHIA settings described above are always included.

The table of tune values for each of the variations is given in Table A.1.

Table A.1: Settings for variations of the A14 tune that were tested. These tune settings are built directly into PYTHIA 8, and therefore require only changing a single setting.

| Sample | Tune:pp Value |
|--------------|---------------|
| Nominal | 21 |
| CTEQL1 | 19 |
| MSTW2008LO | 20 |
| HERAPDF1p5LO | 22 |
| var1 up | 23 |
| var1 down | 24 |
| var2 up | 25 |
| var2 down | 26 |
| var3a up | 27 |
| var3a down | 28 |
| var3b up | 29 |
| var3b down | 30 |
| var3c up | 31 |
| var3c down | 32 |

A.2 Systematic weighting plots

As described in Section 4.6, we weight the nominal simulation towards several alternative templates which are used to define the systematic variations.

This section shows distributions from the weighting procedure. They are comparisons of the weighted nominal sample to the initial alternative samples that define the corresponding uncertainties. These plots and comparisons validate the weighting procedure. The nominal MC sample from the PYTHIA 8 A3 tune and the systematic variation sample generated by EPOS-LHC are chosen to validate the weighting method. Because of the different models in PYTHIA and EPOS-LHC in describing the minimum bias events, both the gen-level distributions and the migration functions of the EPOS-LHC samples are expected to be distinct from the nominal sample. In addition, the weighting from the PYTHIA 8 A3 tune to the CP1 tune and the HERWIG 7 CH3 tune is also tested.

A.2.1 Truth-level weighting to estimate the bias

Figure A.1 shows the results of the gen-level weighting, comparing the nominal MC, the nominal MC weighted to the EPOS-LHC samples, and the EPOS-LHC samples in the distributions of particle-level observables. The weighted MC is more compatible with the alternative MC from EPOS-LHC as expected.

The truth-level weighting results for the nominal A3 tune samples and the systematic variation of CP1 samples are shown in Figures A.2 and A.3.

The truth-level weighting results for the nominal PYTHIA 8 A3 tune samples and the systematic variation of HERWIG 7 CH3 samples are shown in Figures A.4 and A.5.

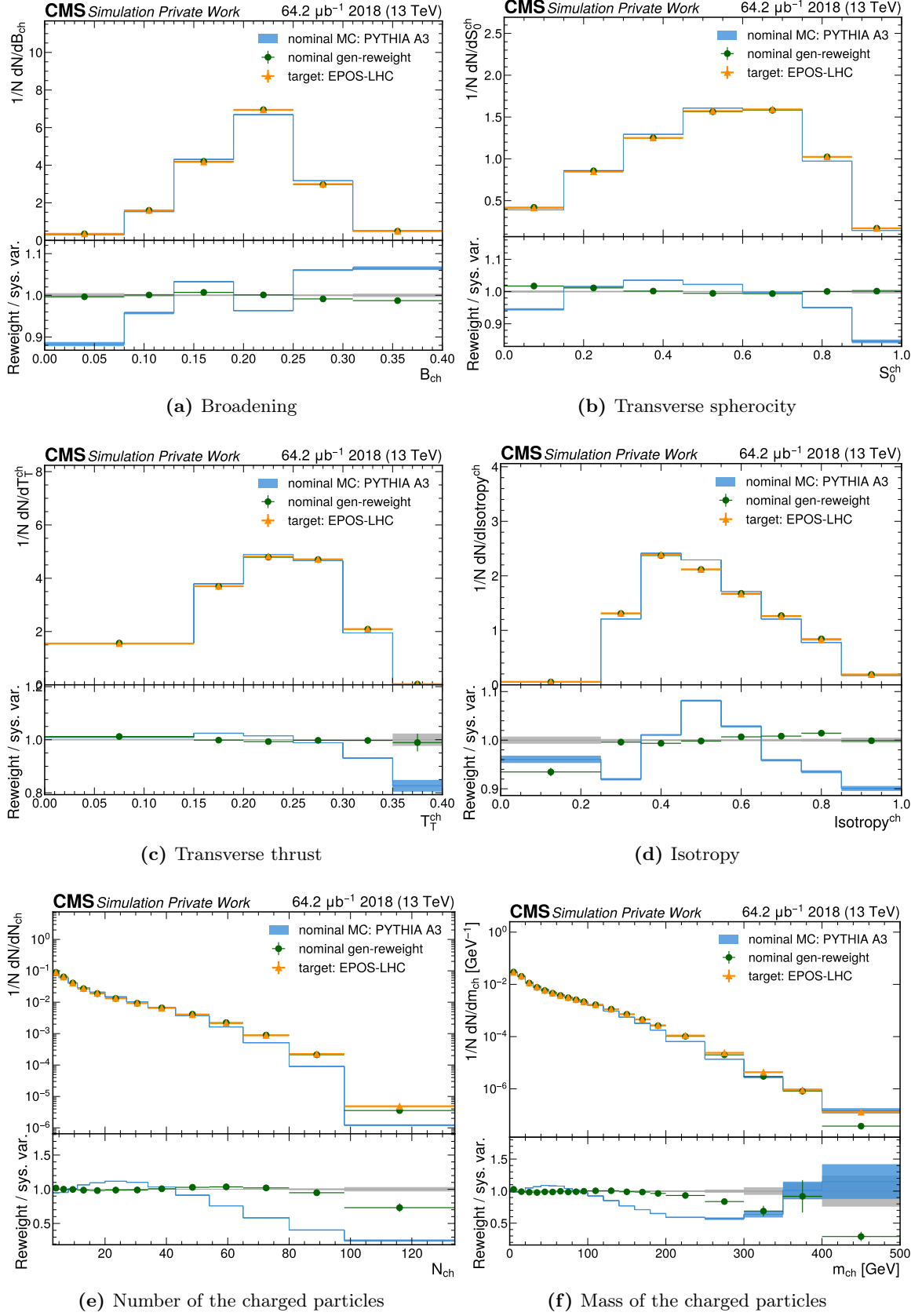


Figure A.1: The event shape distributions of the target for truth-level weight from EPOS-LHC, the PYTHIA 8 A3 tune (nominal MC), and the results after weighting.

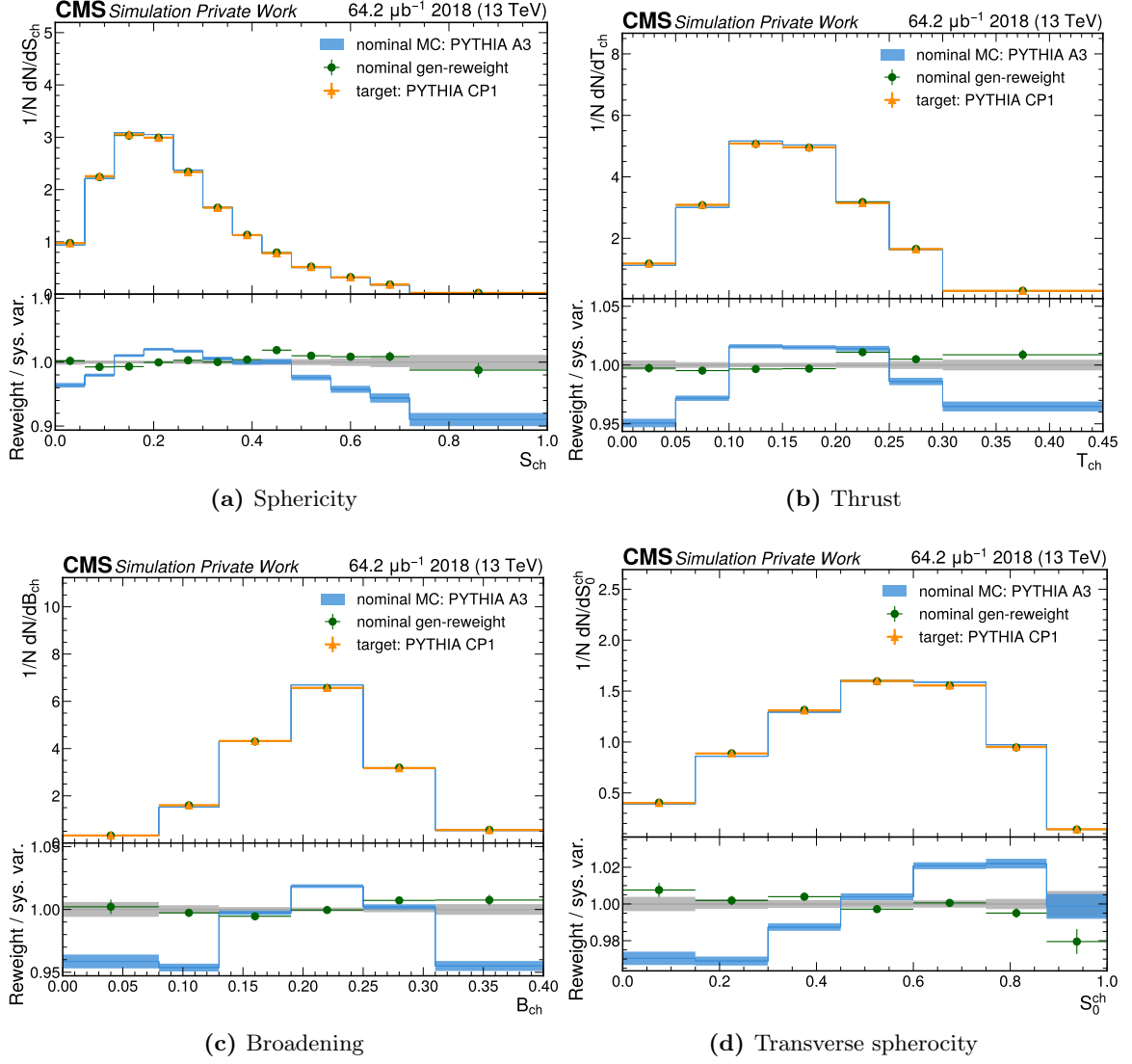


Figure A.2: The event shape distributions of the target for truth-level weight from CP1 tune, the A3 tune (nominal MC), and the results after weighting.

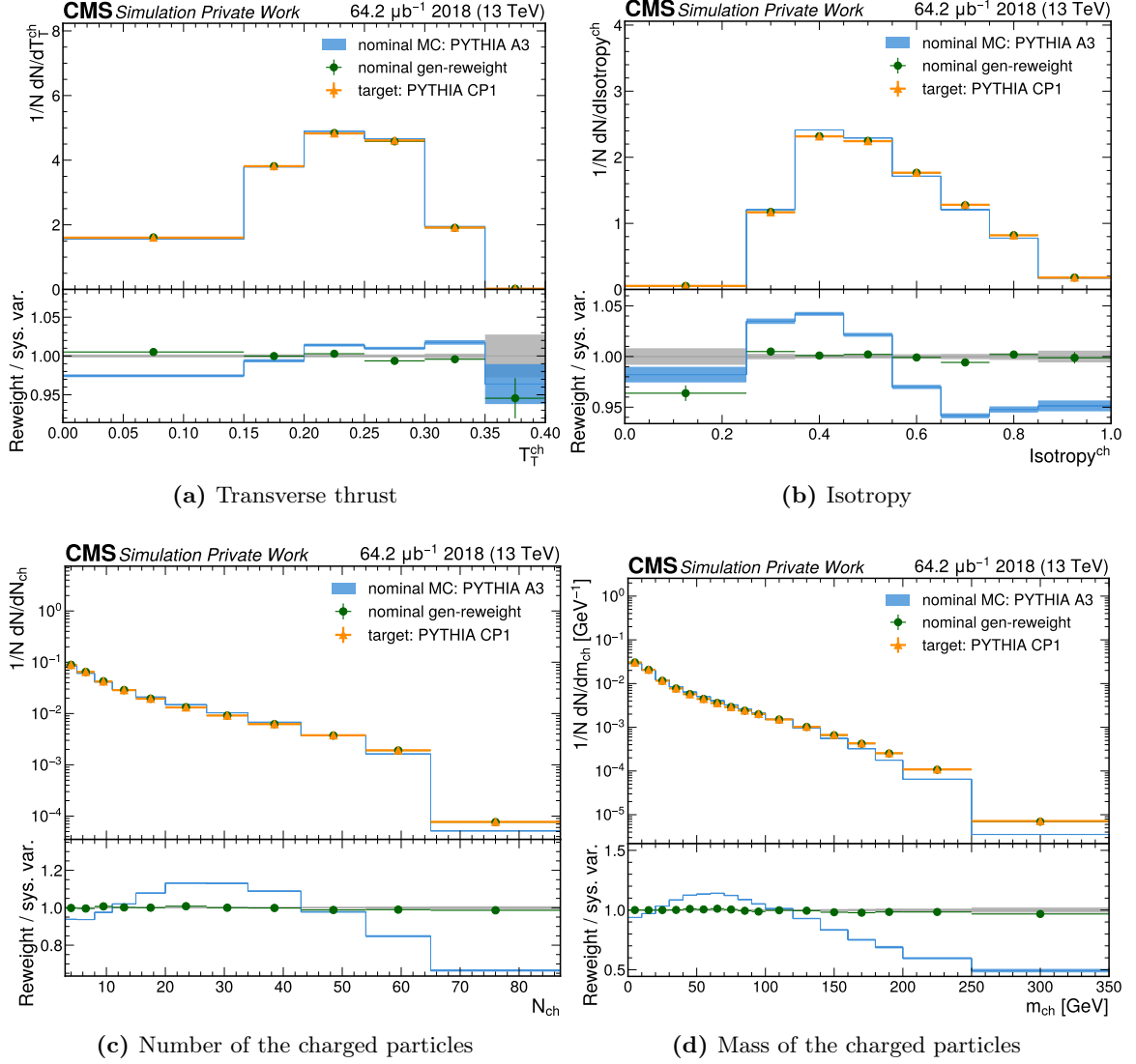


Figure A.3: The event shape distributions of the target for truth-level weight from CP1 tune, the A3 tune (nominal MC), and the results after weighting.

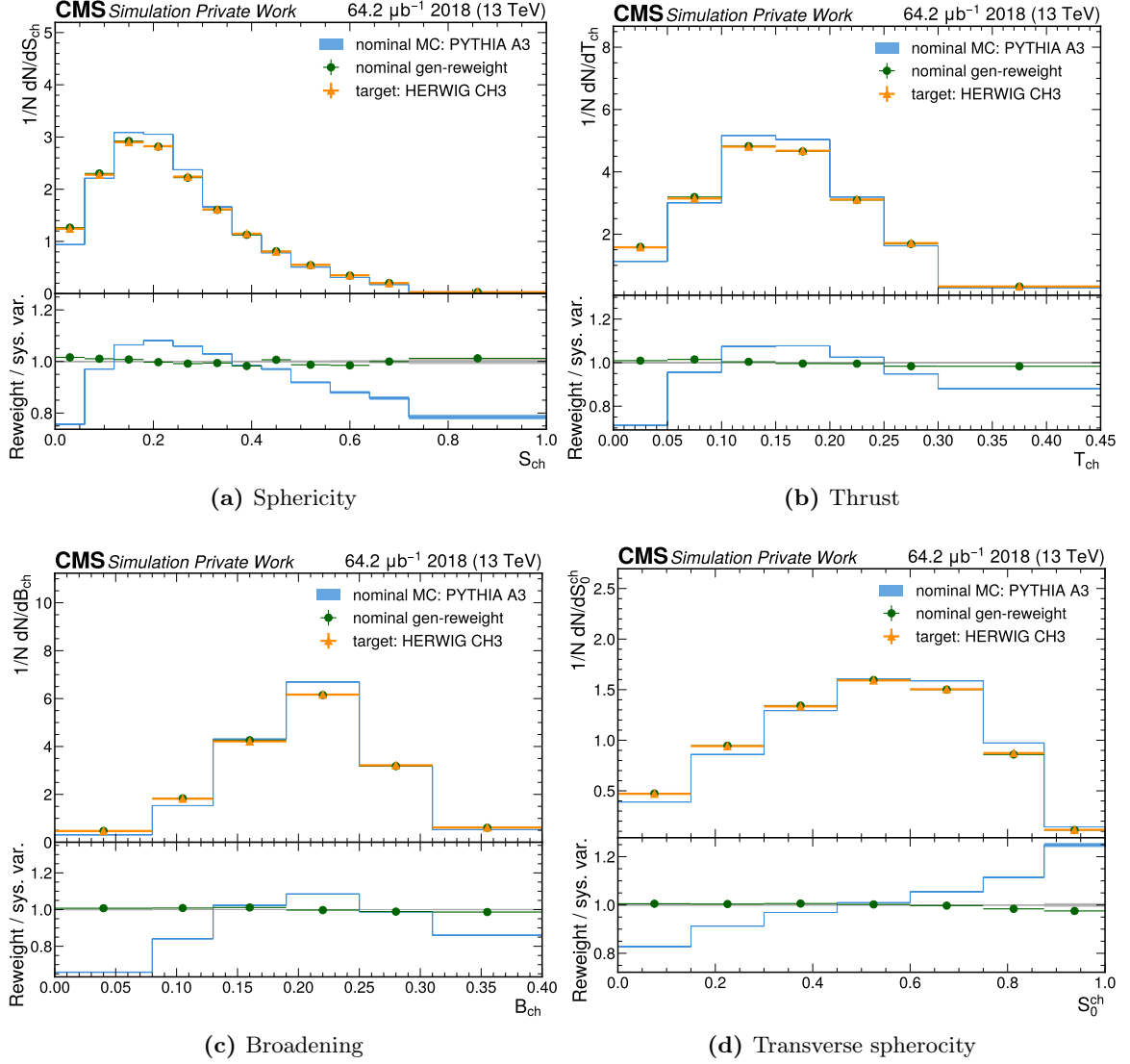


Figure A.4: The event shape distributions of the target for truth-level weight from HERWIG 7 CH3 tune, the PYTHIA 8 A3 tune (nominal MC) and the results after weighting.

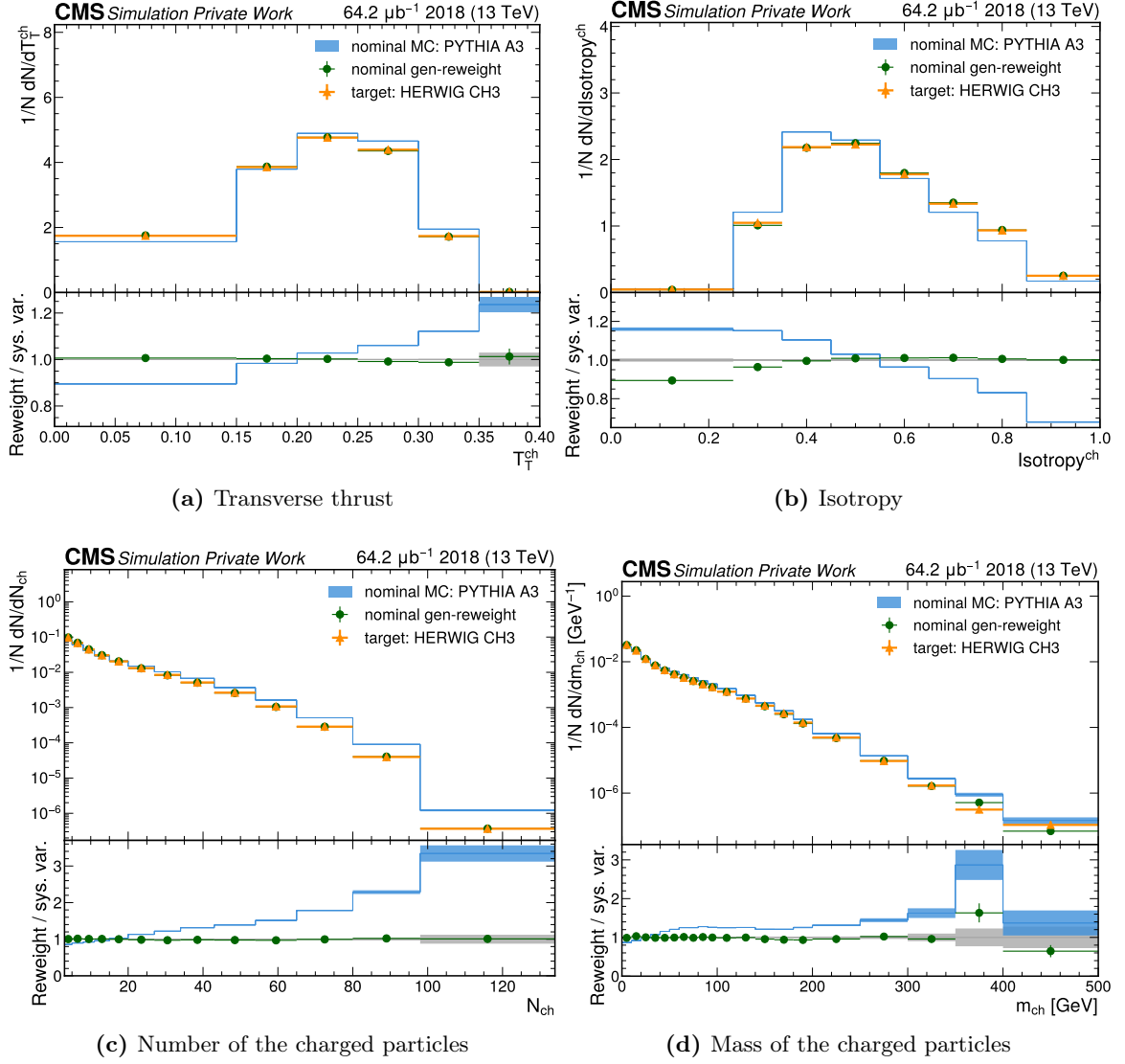
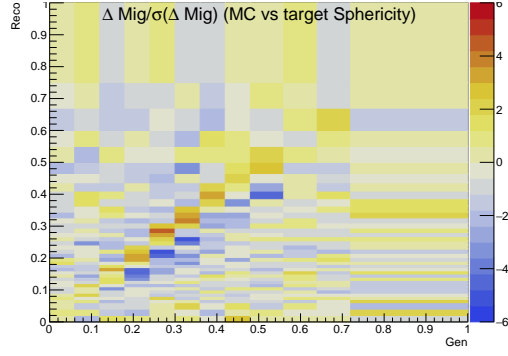


Figure A.5: The event shape distributions of the target for truth-level weight from HERWIG 7 CH3 tune, the PYTHIA 8 A3 tune (nominal MC), and the results after weighting.

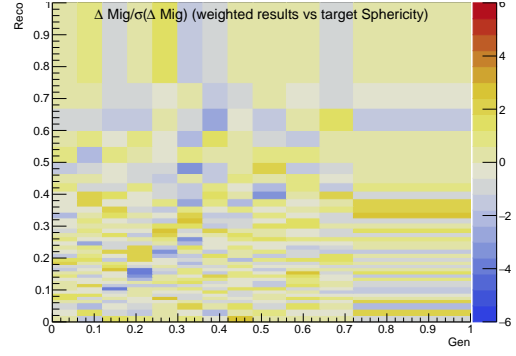
A.2.2 Two-step weighting to estimate the uncertainty of migration between different MC models

To estimate the uncertainty from migration, the alternative MC sample from the EPOS-LHC is first weighted to the nominal PYTHIA 8 A3 sets at the truth level with a procedure similar to Section A.2.1. After this step, the weighted EPOS-LHC sample and the nominal MC have similar truth-level distributions but distinct migration functions. Then as the second step, the nominal PYTHIA 8 A3 events are weighted at the truth and detector level to the alternative EPOS-LHC events with weights from the previous step. This step does not change the truth level distributions much. Instead, it alters the migration function in the space of the observables input into the weighting.

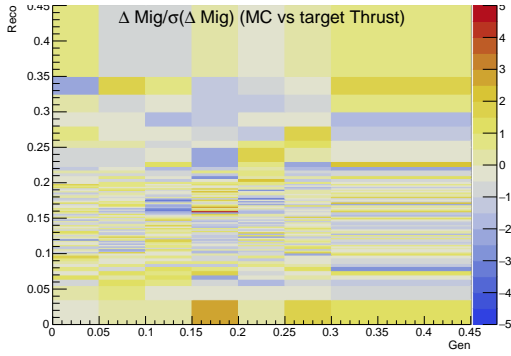
Figures A.6, A.7, and A.8 show the differences of migration matrices (1D projections of the detector response) between the nominal sample and the target (left column), and the differences between the results after weighting and the target (right column), both weighted by their statistical uncertainties. The lighter colors of the matrices in the right column indicate the migration matrices' difference closer to zero. Therefore, the weighting procedure on the second step produces the weighted PYTHIA A3 events with a detector response similar to that of the EPOS-LHC sample.



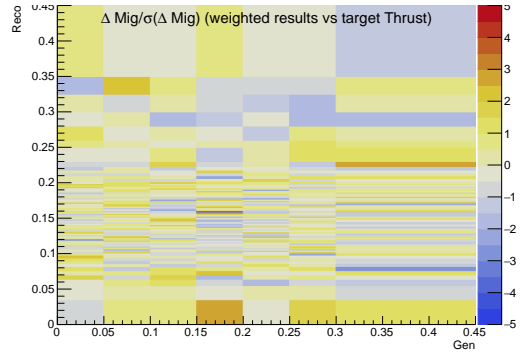
(a) Sphericity migration matrix difference between the nominal MC and the target



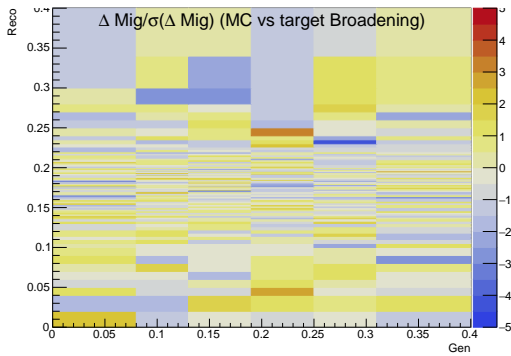
(b) Sphericity migration matrix difference between the weighted results and the target



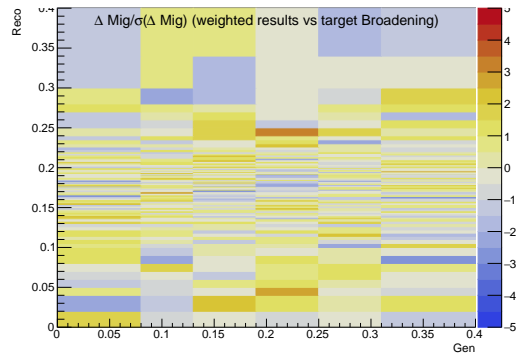
(c) Thrust migration matrix difference between the nominal MC and the target



(d) Thrust migration matrix difference between the weighted results and the target

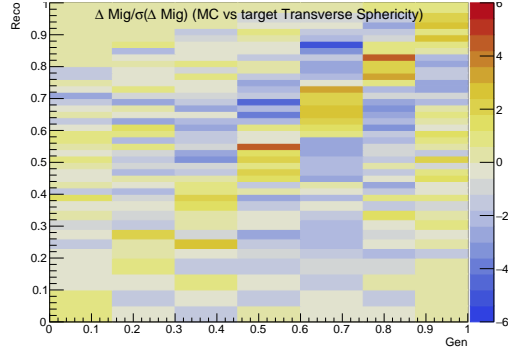


(e) Broadening migration matrix difference between the nominal MC and the target

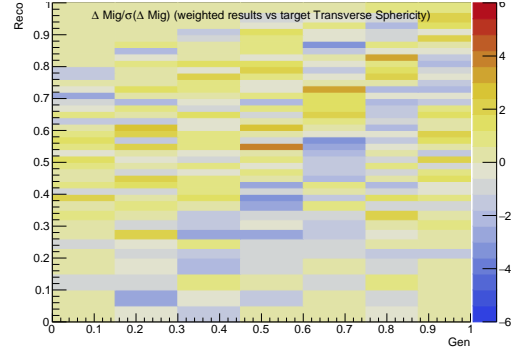


(f) Broadening migration matrix difference between the weighted results and the target

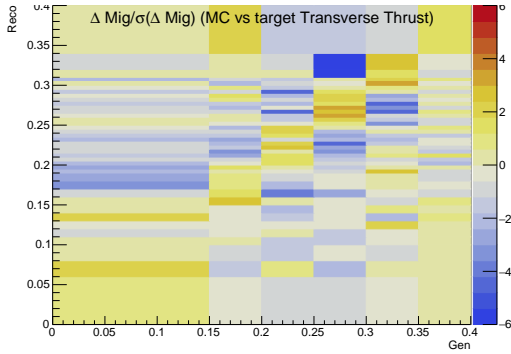
Figure A.6: The closure of migration matrices between the nominal MC/weighted results and the target EPOS-LHC sample.



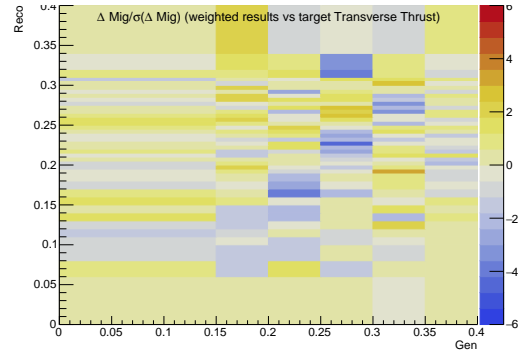
(a) Transverse sphericity migration matrix difference between the nominal MC and the target



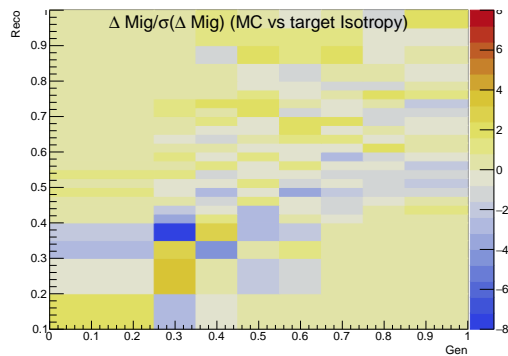
(b) Transverse sphericity migration matrix difference between the weighted results and the target



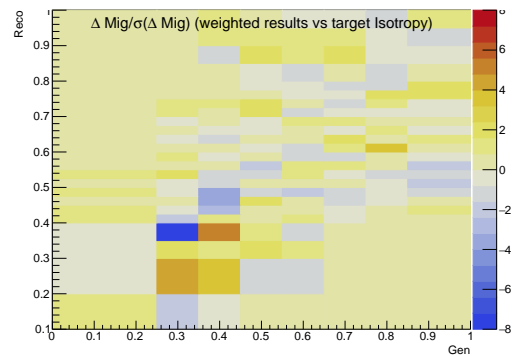
(c) Transverse thrust migration matrix difference between the nominal MC and the target



(d) Transverse thrust migration matrix difference between the weighted results and the target

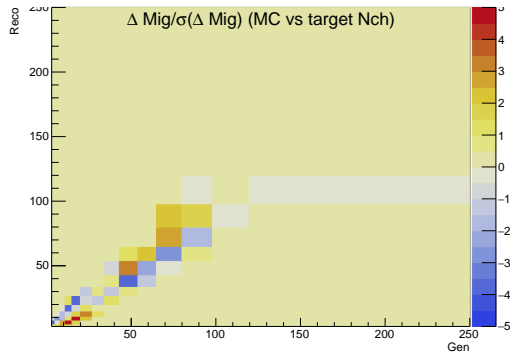


(e) Isotropy migration matrix difference between the nominal MC and the target

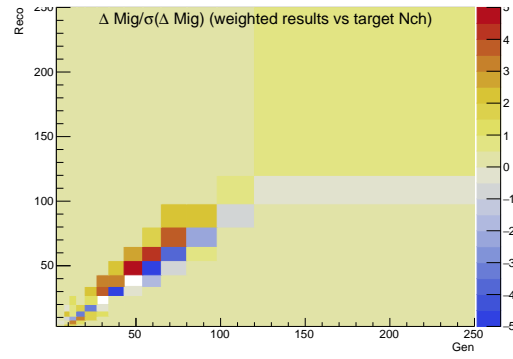


(f) Isotropy migration matrix difference between the weighted results and the target

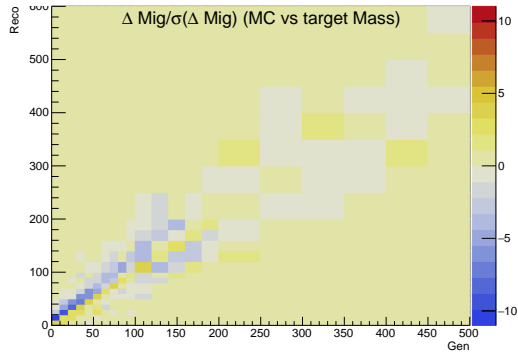
Figure A.7: The closure of migration matrices between the nominal MC/weighted results and the target EPOS-LHC sample.



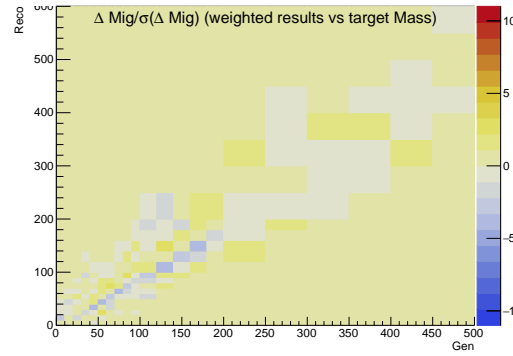
(a) Charged particle/track multiplicity migration matrix difference between the nominal MC and the target EPOS-LHC sample



(b) Charged particle/track multiplicity migration matrix difference between the weighted results and the target EPOS-LHC sample



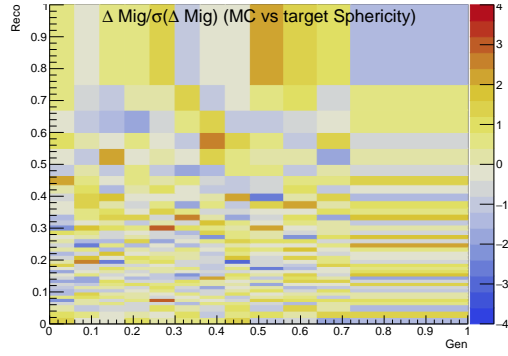
(c) Charged particle/track center of mass energy migration matrix difference between the nominal MC and the target EPOS-LHC sample



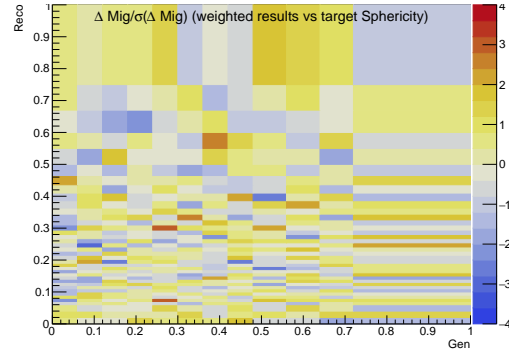
(d) Charged particle/track center of mass energy migration matrix difference between the weighted results and the target EPOS-LHC sample

Figure A.8: The closure of migration matrices between the nominal MC/weighted results and the target EPOS-LHC sample.

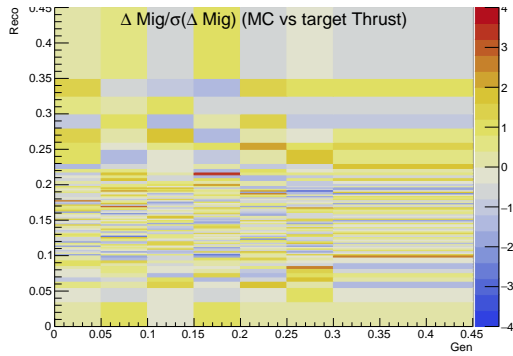
The variations of the migration function from the PYTHIA 8 A3 tune to the PYTHIA 8 CP1 tune and HERWIG 7 CH3 are estimated in the same way. The CP1 (CH3) sample was first weighted to the A3 sample at the truth level at the first step, then the nominal A3 sample was weighted at the truth and detector level to the CP1 (CH3) sample weight at the first step. Figures A.9 to A.14 show the migration matrices before (left column) and after (right column) the second step of weighting.



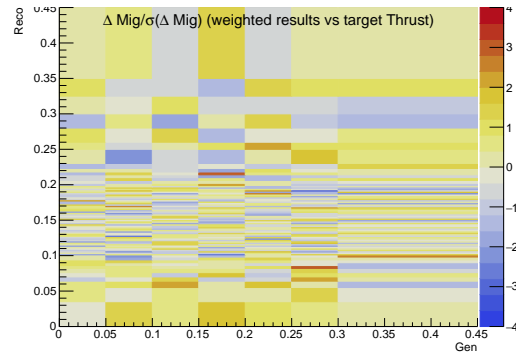
(a) Sphericity migration matrix difference between the nominal MC and the target



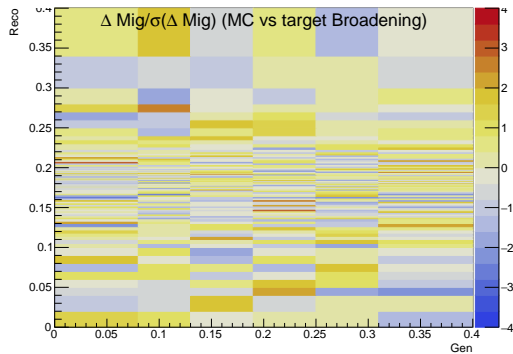
(b) Sphericity migration matrix difference between the weighted results and the target



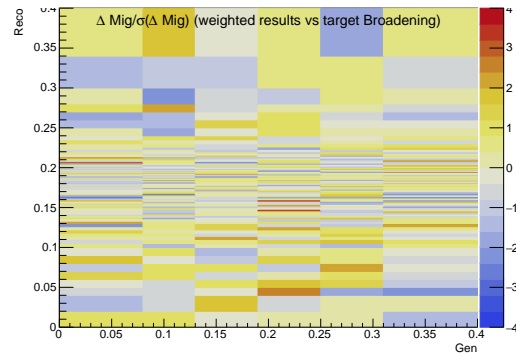
(c) Thrust migration matrix difference between the nominal MC and the target



(d) Thrust migration matrix difference between the weighted results and the target

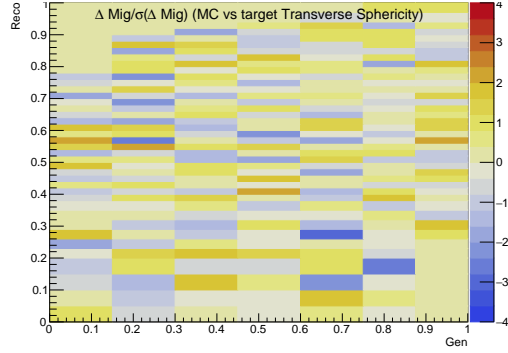


(e) Broadening migration matrix difference between the nominal MC and the target

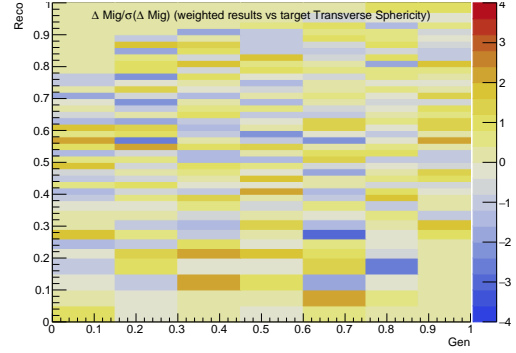


(f) Broadening migration matrix difference between the weighted results and the target

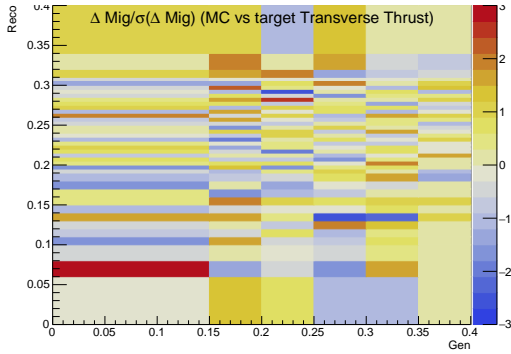
Figure A.9: The closure of migration matrices between the nominal MC/weighted results and the target CP1 sample.



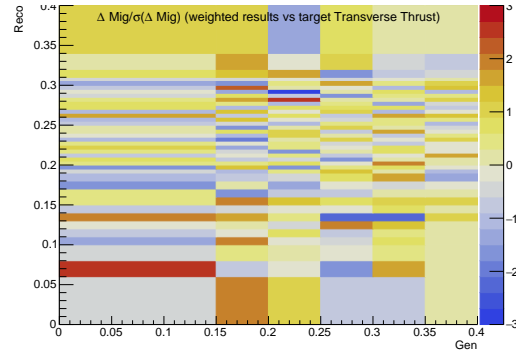
(a) Transverse sphericity migration matrix difference between the nominal MC and the target



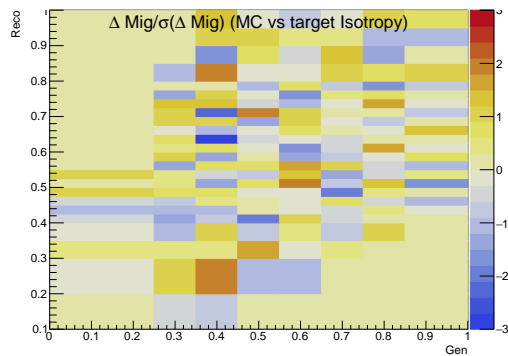
(b) Transverse sphericity migration matrix difference between the weighted results and the target



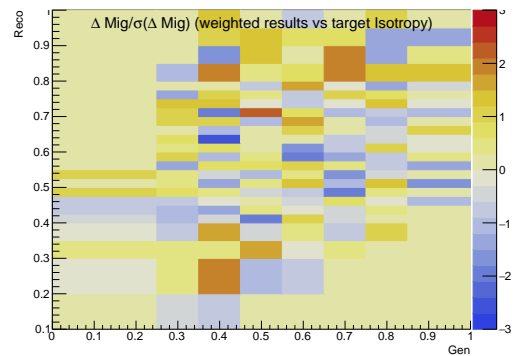
(c) Transverse thrust migration matrix difference between the nominal MC and the target



(d) Transverse thrust migration matrix difference between the weighted results and the target

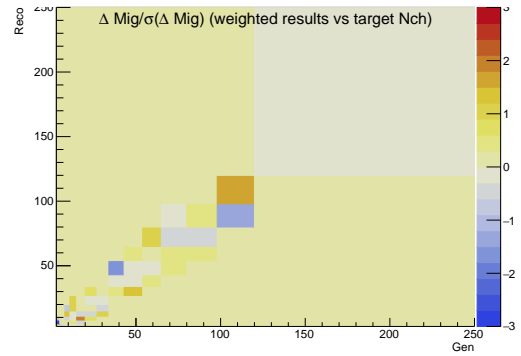
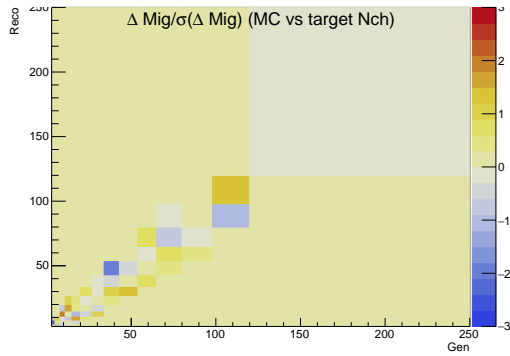


(e) Isotropy migration matrix difference between the nominal MC and the target

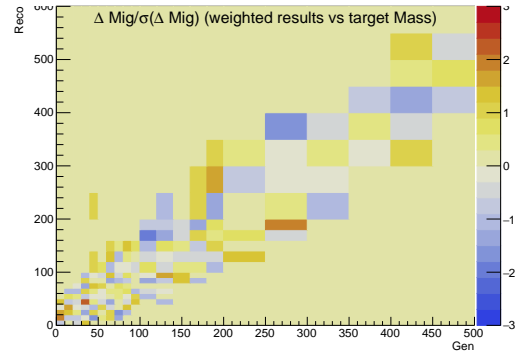
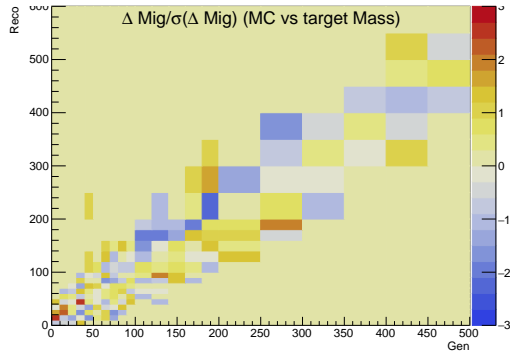


(f) Isotropy migration matrix difference between the weighted results and the target

Figure A.10: The closure of migration matrices between the nominal MC/weighted results and the target CP1 sample.

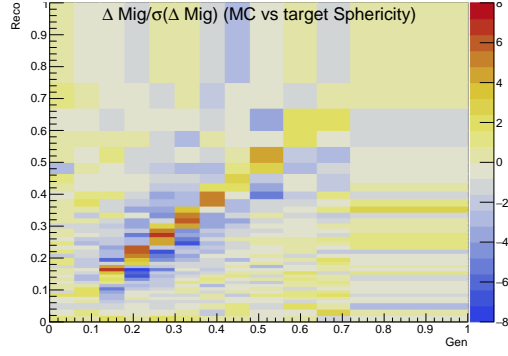


(a) Charged particle/track multiplicity migration matrix difference between the nominal MC and the target CP1 sample. (b) Charged particle/track multiplicity migration matrix difference between the weighted results and the target

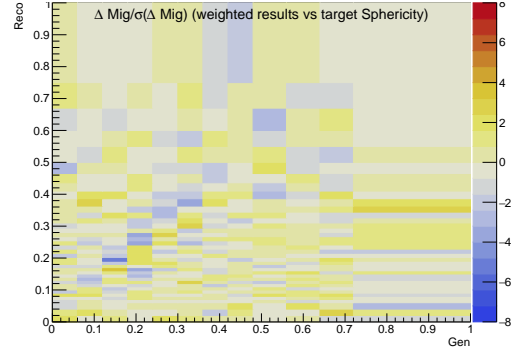


(c) Charged particle/track center of mass energy migration matrix difference between the nominal MC and the target CP1 sample. (d) Charged particle/track center of mass energy migration matrix difference between the weighted results and the target

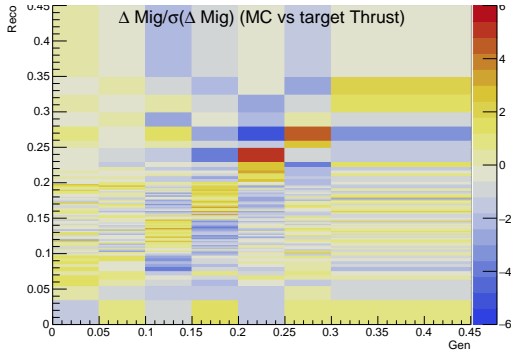
Figure A.11: The closure of migration matrices between the nominal MC/weighted results and the target CP1 sample.



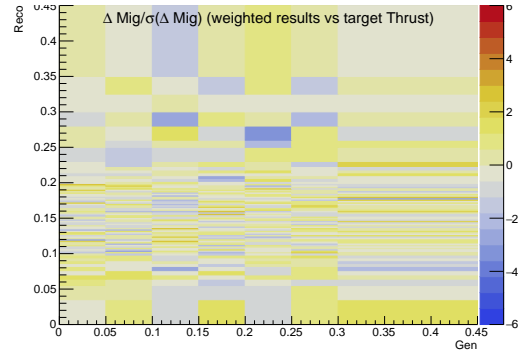
(a) Sphericity migration matrix difference between the nominal MC and the target



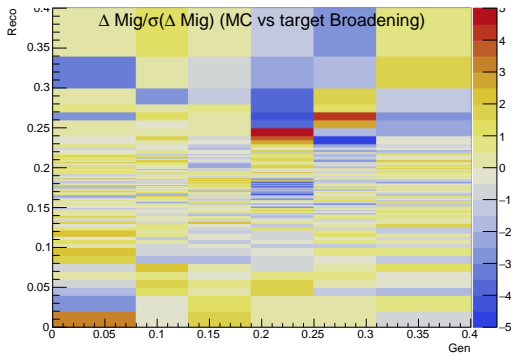
(b) Sphericity migration matrix difference between the weighted results and the target



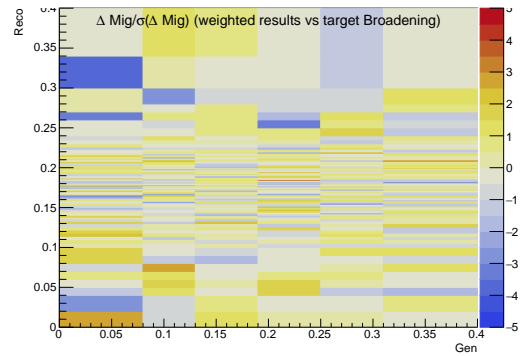
(c) Thrust migration matrix difference between the nominal MC and the target



(d) Thrust migration matrix difference between the weighted results and the target

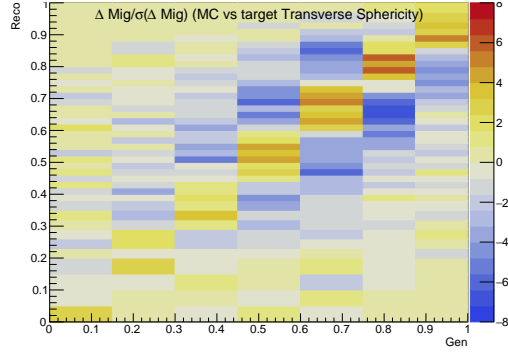


(e) Broadening migration matrix difference between the nominal MC and the target

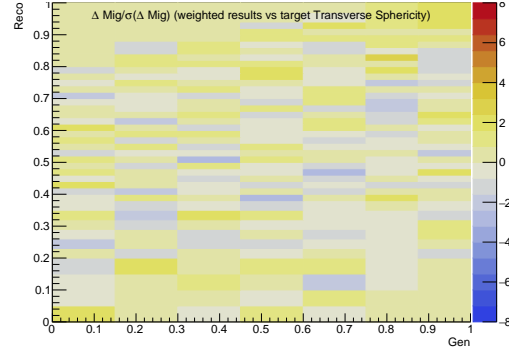


(f) Broadening migration matrix difference between the weighted results and the target

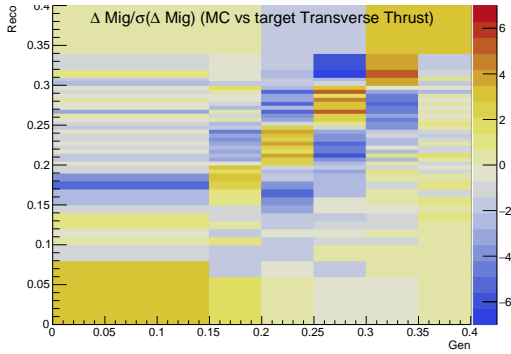
Figure A.12: The closure of migration matrices between the nominal MC/weighted results and the target HERWIG 7 CH3 sample.



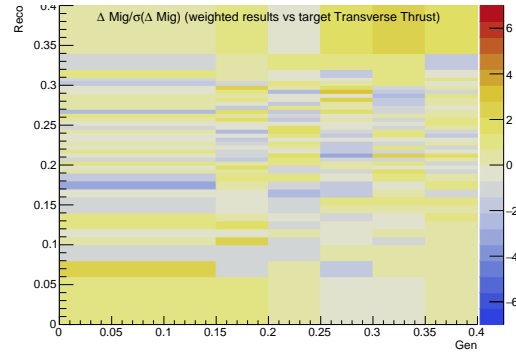
(a) Transverse sphericity migration matrix difference between the nominal MC and the target



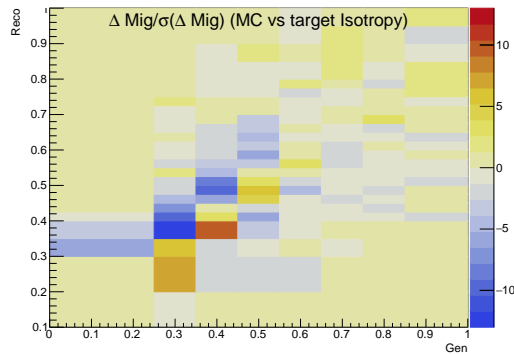
(b) Transverse sphericity migration matrix difference between the weighted results and the target



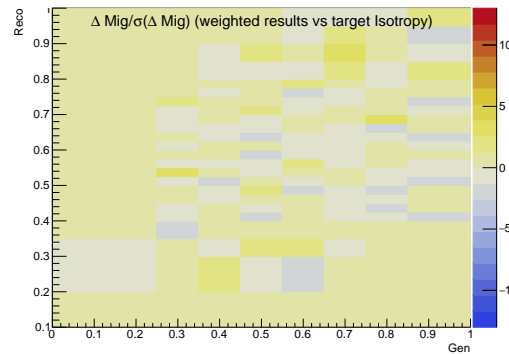
(c) Transverse thrust migration matrix difference between the nominal MC and the target



(d) Transverse thrust migration matrix difference between the weighted results and the target

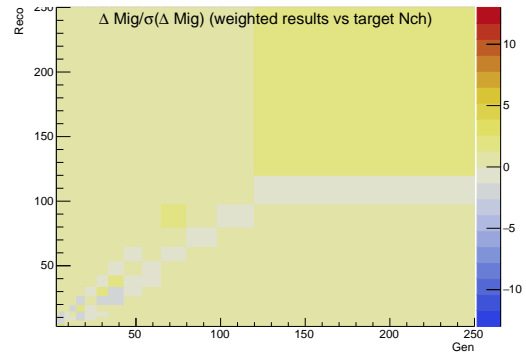
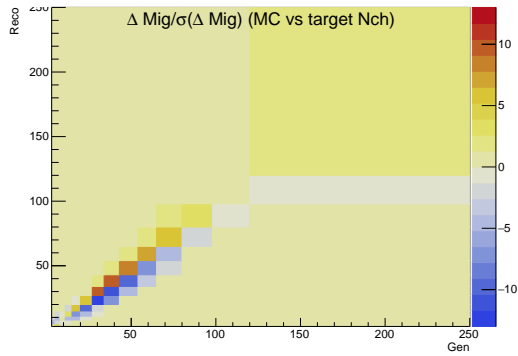


(e) Isotropy migration matrix difference between the nominal MC and the target

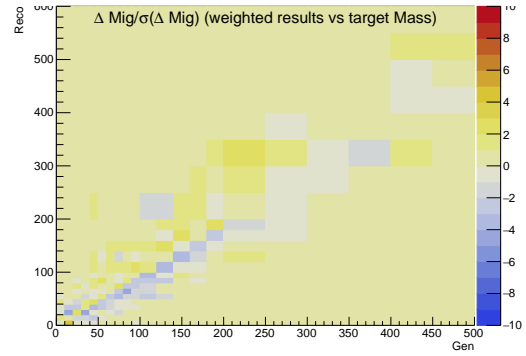
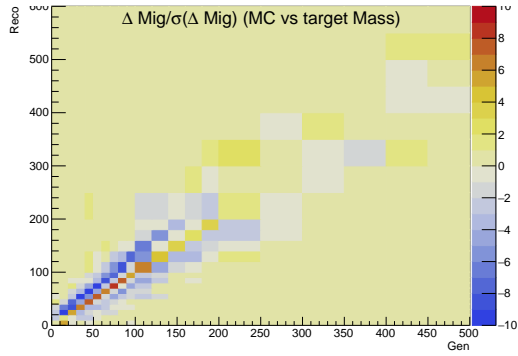


(f) Isotropy migration matrix difference between the weighted results and the target

Figure A.13: The closure of migration matrices between the nominal MC/weighted results and the target HERWIG 7 CH3 sample.



(a) Charged particle/track multiplicity migration matrix difference between the nominal MC and the target
(b) Charged particle/track multiplicity migration matrix difference between the weighted results and the target



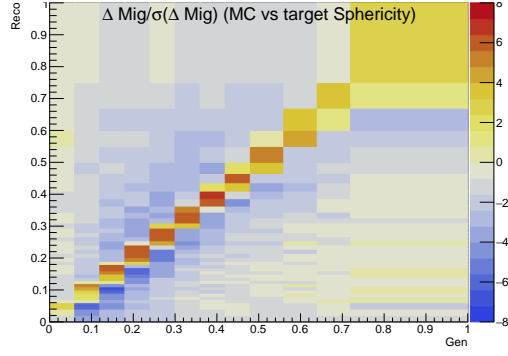
(c) Charged particle/track center of mass energy migration matrix difference between the nominal MC and the target
(d) Charged particle/track center of mass energy migration matrix difference between the weighted results and the target

Figure A.14: The closure of migration matrices between the nominal MC/weighted results and the target HERWIG 7 CH3 sample.

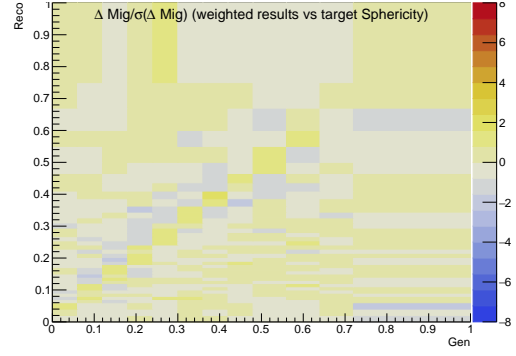
A.2.3 Truth and detector level weighting to estimate the track reconstruction efficiency uncertainty

The systematic variation of the uncertainty in the track reconstruction efficiency is estimated by removing 2.1% tracks with $p_T < 20$ GeV and 1% tracks with $p_T > 20$ GeV in the nominal MC, which alters the event kinematics at the detector level. The truth level event kinematics are the same as the nominal MC. The systematic template is extracted by weighting the nominal MC to the systematic variation at both levels simultaneously, to obtain the weighted sample with a detector response similar to the one with alternative track reconstruction efficiency.

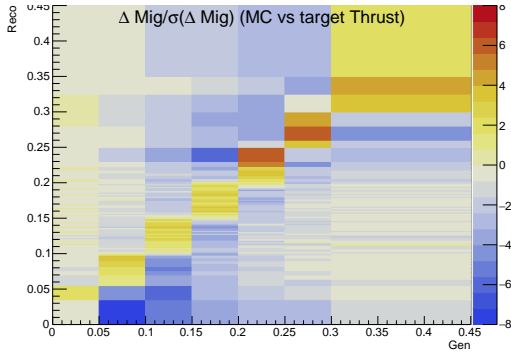
Figures A.15, A.16 and A.17 show the differences between the migration matrices of the target and the nominal MC (results after weighting) in the left (right) column. The weighting on the nominal MC sample gives events with a similar detector response to those with randomly dropped tracks.



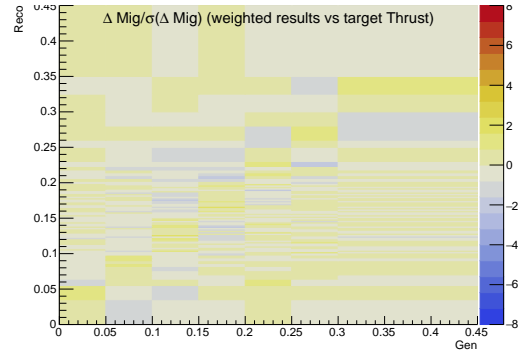
(a) Sphericity migration matrix difference between the nominal MC and the target



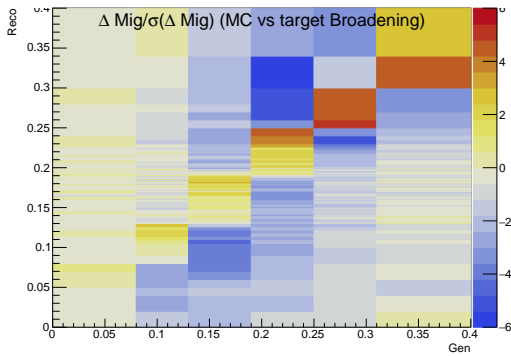
(b) Sphericity migration matrix difference between the weighted results and the target



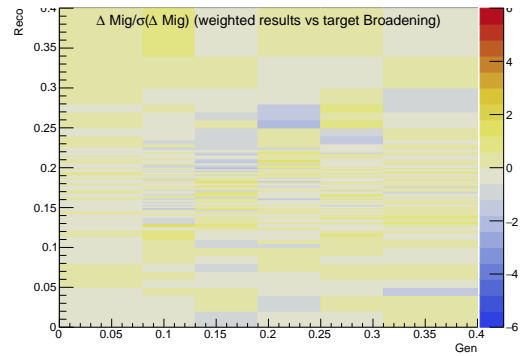
(c) Thrust migration matrix difference between the nominal MC and the target



(d) Thrust migration matrix difference between the weighted results and the target

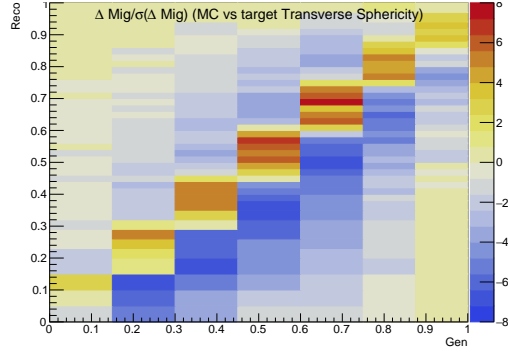


(e) Broadening migration matrix difference between the nominal MC and the target

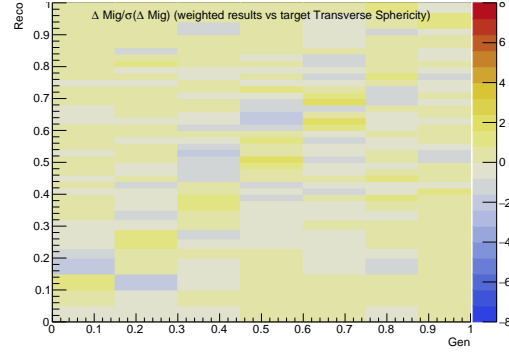


(f) Broadening migration matrix difference between the weighted results and the target

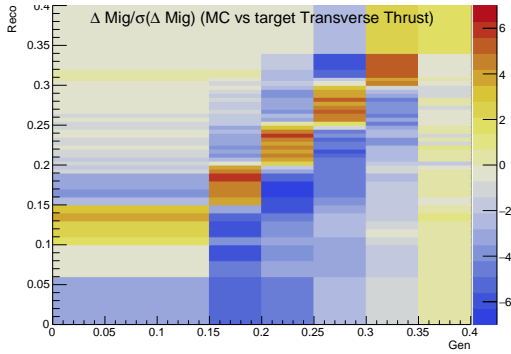
Figure A.15: The closure of migration matrices between the nominal MC/weighted results and the target PYTHIA 8 A3 sample with randomly dropped tracks.



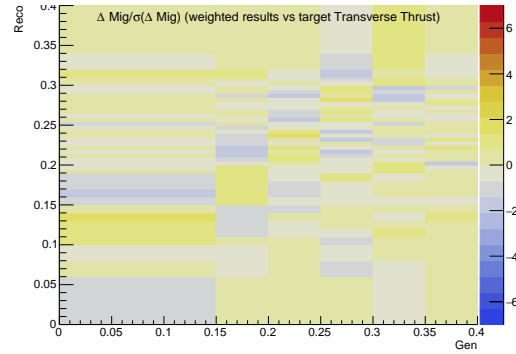
(a) Transverse sphericity migration matrix difference between the nominal MC and the target



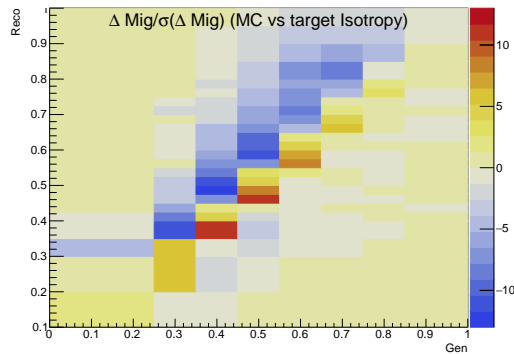
(b) Transverse sphericity migration matrix difference between the weighted results and the target



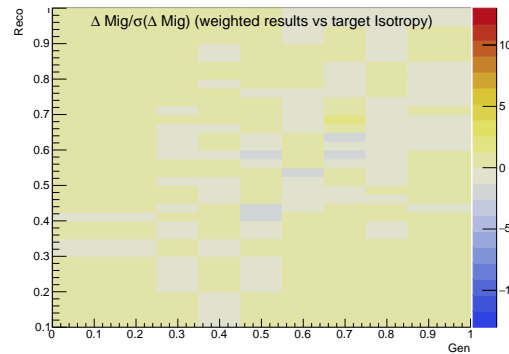
(c) Transverse thrust migration matrix difference between the nominal MC and the target



(d) Transverse thrust migration matrix difference between the weighted results and the target

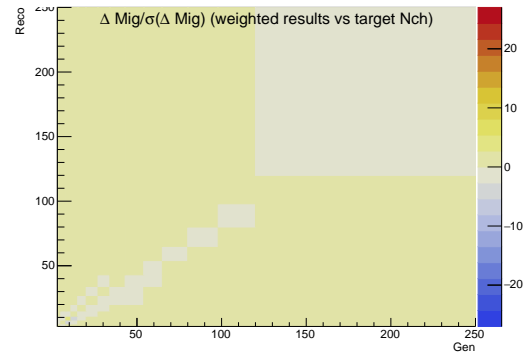
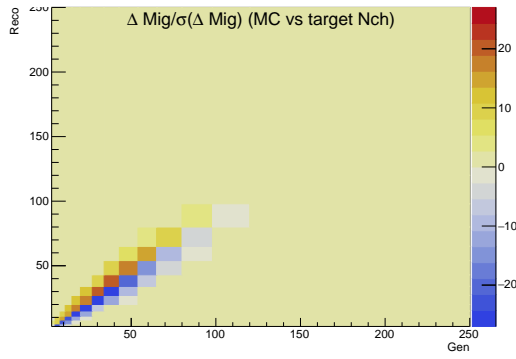


(e) Isotropy migration matrix difference between the nominal MC and the target

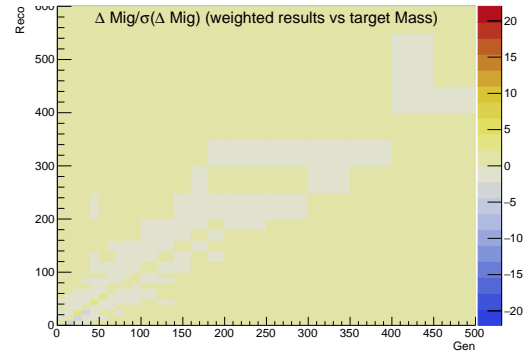
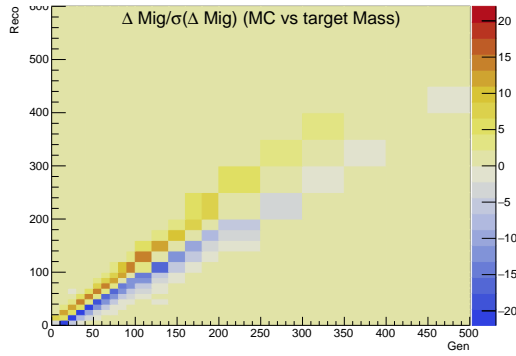


(f) Isotropy migration matrix difference between the weighted results and the target

Figure A.16: The closure of migration matrices between the nominal MC/weighted results and the target PYTHIA 8 A3 sample with randomly dropped tracks.



(a) Charged particle/track multiplicity migration matrix difference between the nominal MC and the target
(b) Charged particle/track multiplicity migration matrix difference between the weighted results and the target



(c) Charged particle/track center of mass energy migration matrix difference between the nominal MC and the target
(d) Charged particle/track center of mass energy migration matrix difference between the weighted results and the target

Figure A.17: The closure of migration matrices between the nominal MC/weighted results and the target PYTHIA 8 A3 sample with randomly dropped tracks.

A.3 More Validation Tests of Unfolding Pseudo-data

This section includes the validation plots for the other observables besides the ones shown in Section 4.6.4 for unfolding the pseudodata from the PYTHIA 8 CUETP8M1 tune, as well as the plots for unfolding the PYTHIA 8 CP5 and A14 samples as pseudodata.

Figure A.18 and A.19 show the truth and detector level comparisons among the unfolded results, the pseudodata, and the nominal MC in distributions of thrust, broadening, transverse thrust, isotropy, charged particle multiplicity, and their invariant mass. Figure A.20 and A.21 show the comparisons in 2-dimensional distributions.

The plots of acceptance and efficiency are used to validate the unfolding performance considering the detector artifacts and inefficiency. The acceptance is defined as the fraction of events passing the truth-level selection among those passing the detector-level selection in a given bin. The efficiency is defined as the fraction of events passing the detector-level selection among those passing the truth-level selection in a given bin.

Figure A.22-A.23 show the unfolded efficiency as functions of the truth-level observables compared to the pseudodata truth from the PYTHIA 8 CUETP8M1 sample and the nominal MC. Figure A.24-A.25 are the unfolded acceptance as functions of reconstructed observables compared to the pseudodata truth from the PYTHIA 8 CUETP8M1 sample and the nominal MC. Due to the minimal selections applied to the events for the inclusive measurement, both acceptance and efficiency are close to unity, as expected.

Figure A.26 and A.27 show the χ^2 difference and the ks-distance for the closure between the unfolding results with the nominal MC from PYTHIA 8 A3 tune and the CP5 pseudodata at the truth and detector level, respectively. The uncertainty in the χ^2 calculation includes only the pseudodata statistical uncertainty. The values of the χ^2 and ks-distance are normalized to their values before unfolding, so that only the relative change in the goodness-of-fit measure is shown, not their absolute values.

Figures A.28, A.29 and A.30, A.31 are the unfolding results using the nominal MC and its systematic variations to the CP5 pseudodata at the second iteration. Figures A.34, A.35 and A.32, A.33 are the acceptance and efficiency given by the unfolding results for the CP5 pseudodata, compared to the nominal MC and the pseudodata truth.

A similar test was performed for the pseudodata from the A14 tune, as shown in Figure A.36, A.37, A.38, A.39, A.40, A.41, A.44 and A.45.

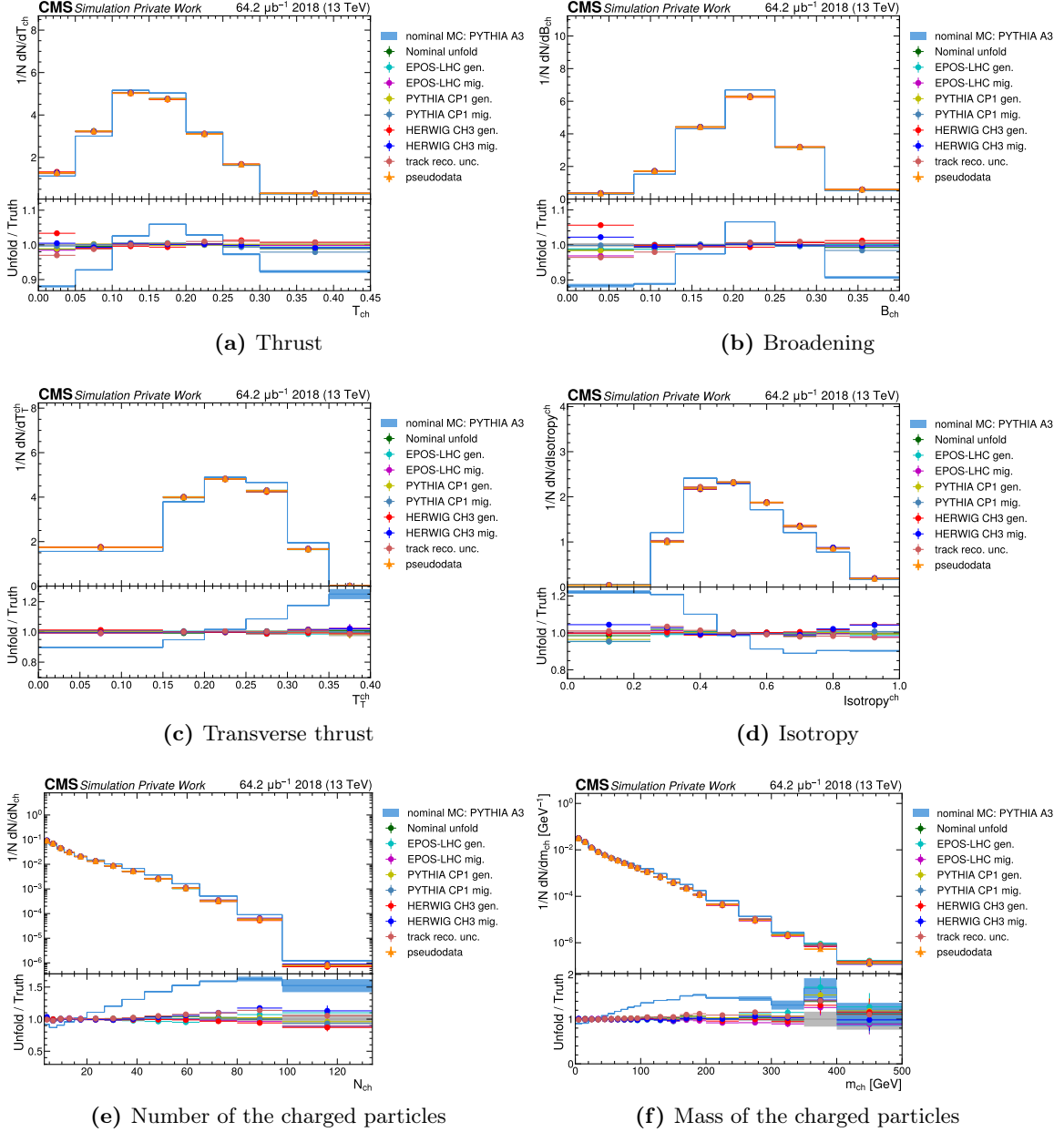


Figure A.18: The thrust, broadening, transverse thrust, isotropy, charged particle multiplicity and invariant mass distributions of the PYTHIA 8 CUETP8M1 (NNPDF3.1LO) tune (pseudodata), the A3 tune (nominal MC) and the unfolding results at the truth level. The unfolding results using the systematic deviations of the MC are also shown in the plots.

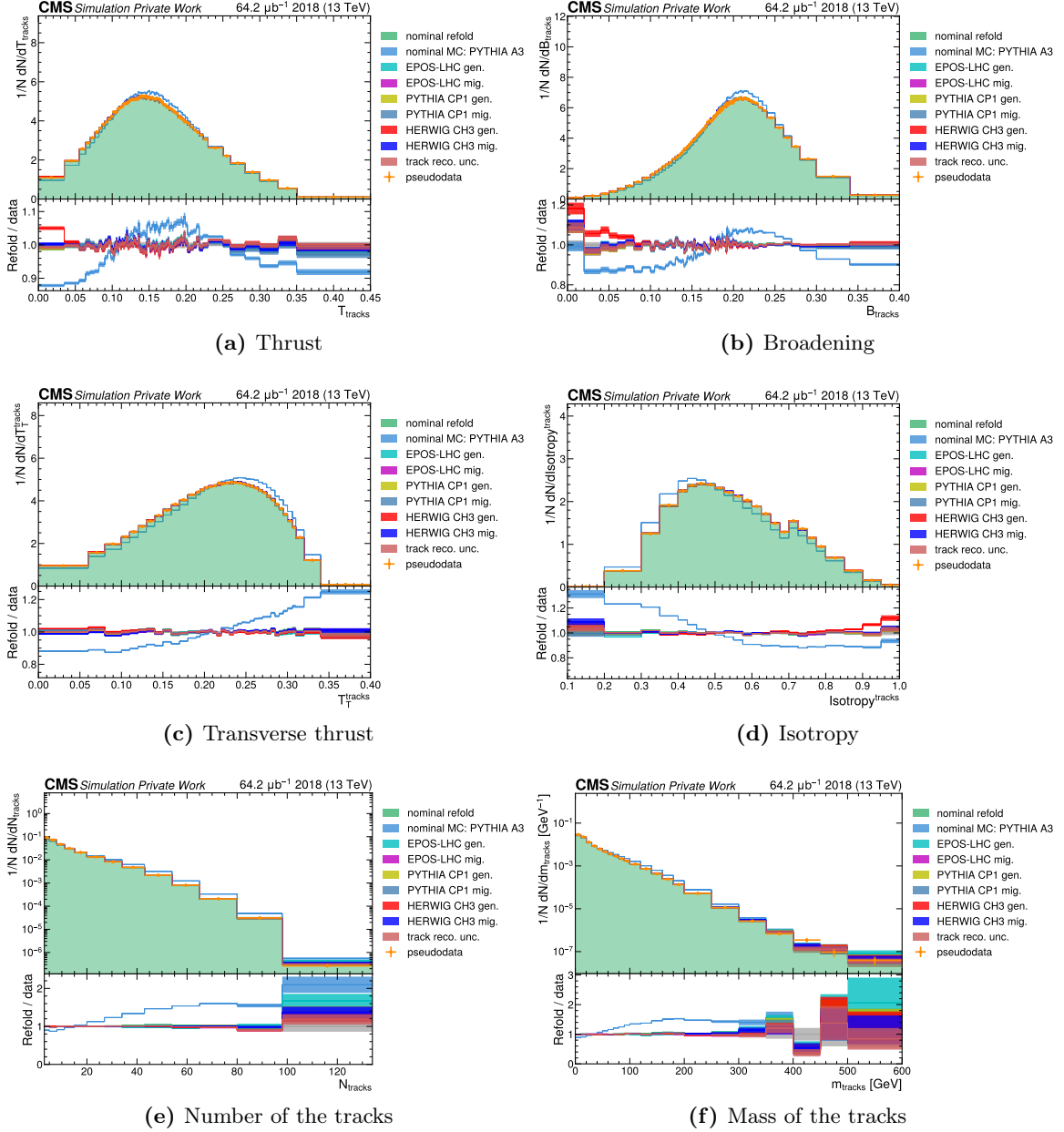


Figure A.19: The thrust, broadening, transverse thrust, isotropy, track multiplicity and invariant mass distributions of the PYTHIA 8 CUETP8M1 (NNPDF3.1LO) tune (pseudodata), the A3 tune (nominal MC) and the unfolding results at the detector level. The refolded results using the systematic deviations of the MC are also shown in the plots.

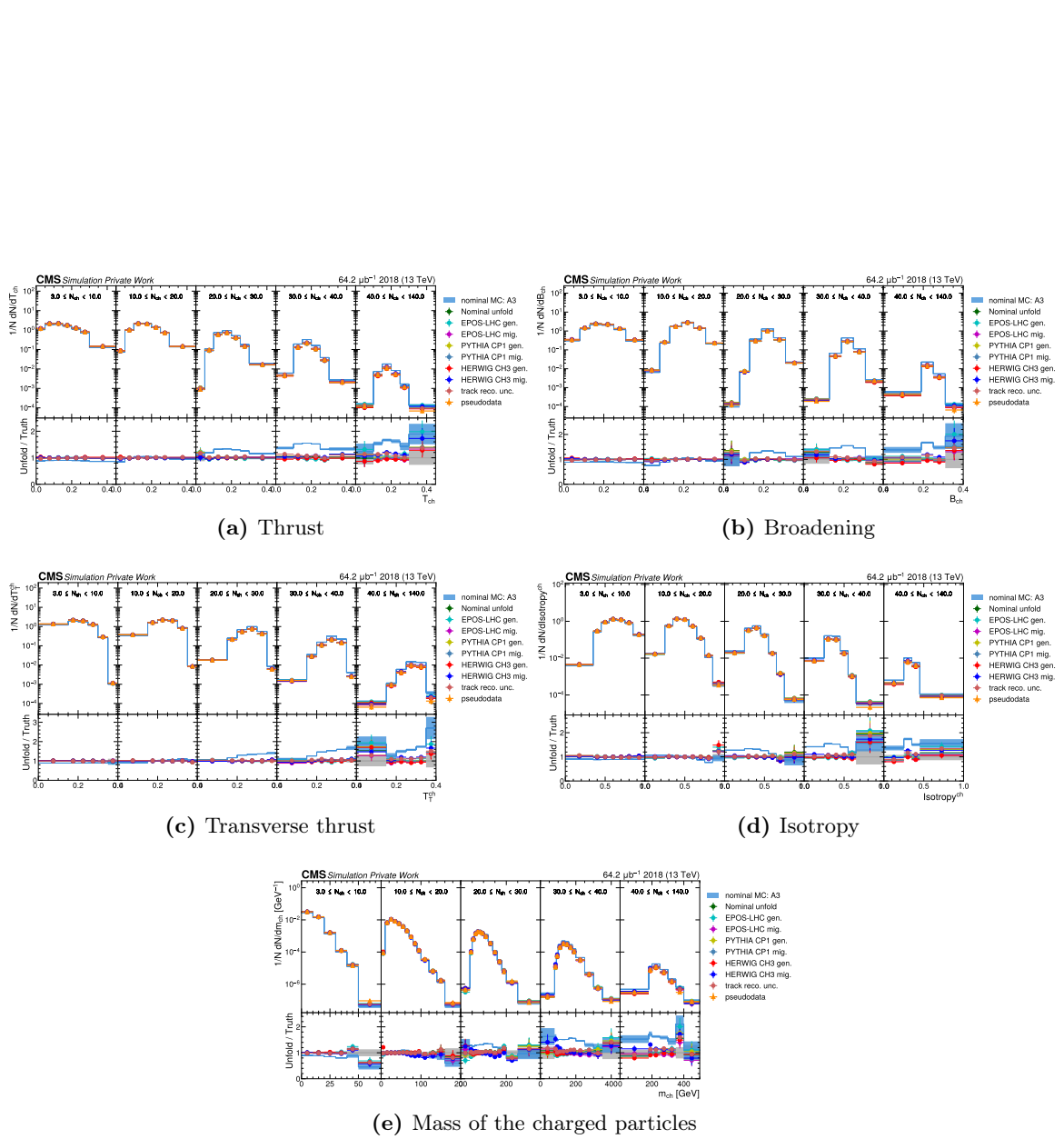


Figure A.20: The event shape and invariant mass distributions of the PYTHIA 8 CUETP8M1 (NNPDF3.1LO) tune (pseudodata), the A3 tune (nominal MC) and the unfolding results in slices of charged particle multiplicity at the truth level. The unfolding results using the systematic deviations of the MC are also shown in the plots.

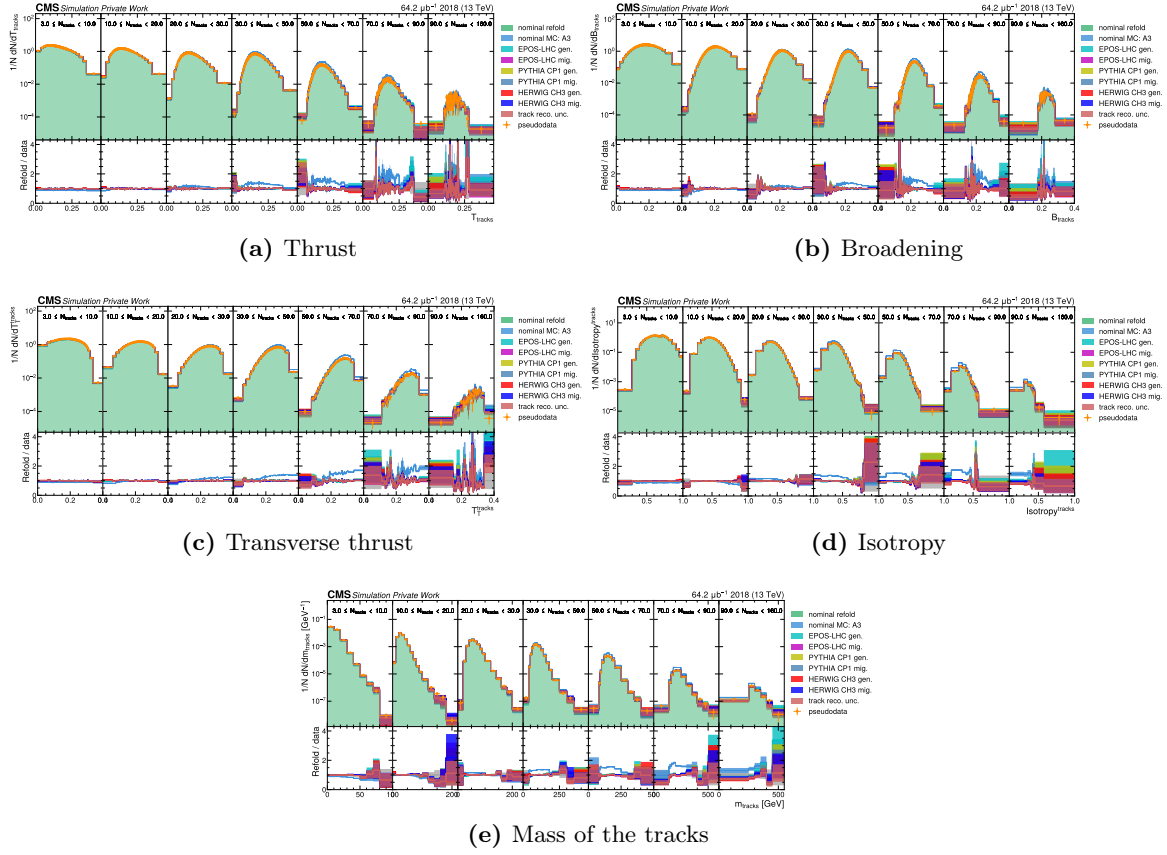


Figure A.21: The event shape and invariant mass distributions of the PYTHIA 8 CUETP8M1 (NNPDF3.1LO) tune (pseudodata), the A3 tune (nominal MC) and the unfolding results at the detector level in slices of track multiplicity at the detector level. The refolded results using the systematic deviations of the MC are also shown in the plots.

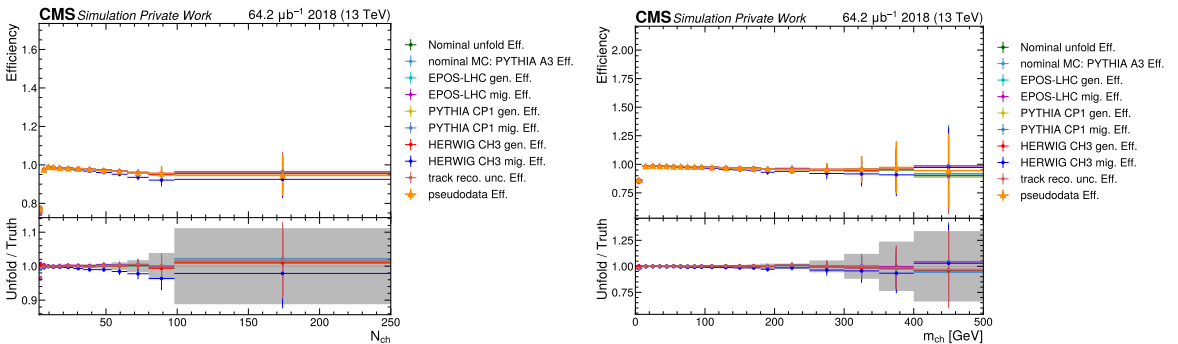


Figure A.22: The efficiency of the PYTHIA 8 CUETP8M1 (NNPDF3.1LO) tune (pseudodata), the A3 tune (nominal MC) and the unfolding results as functions of the charged particle multiplicity and invariant mass of the charged particles. The efficiency results from the unfolding using the systematic deviations of the MC are also shown in the plots.

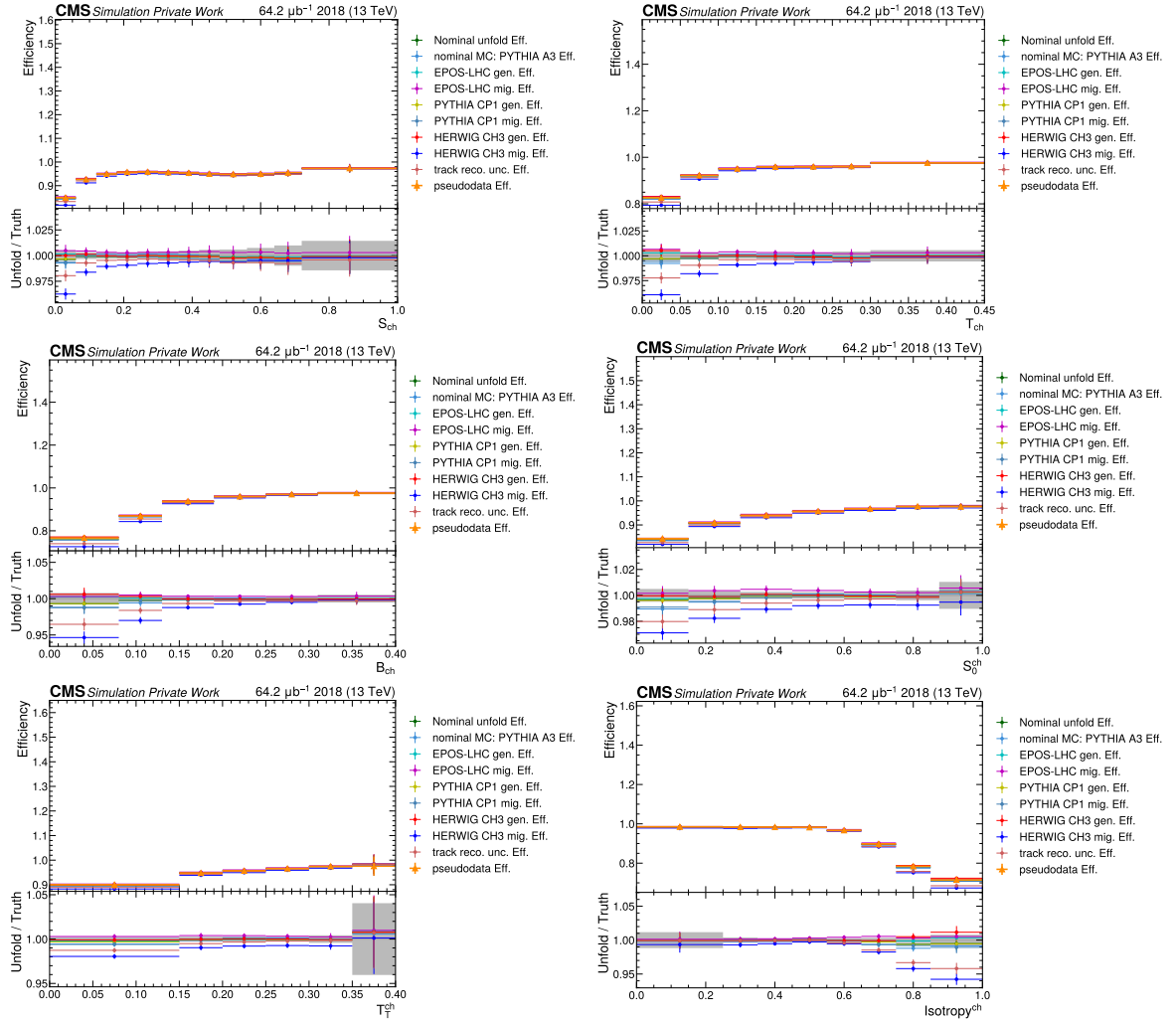


Figure A.23: The efficiency of the PYTHIA 8 CUETP8M1 (NNPDF3.1LO) tune (pseudodata), the A3 tune (nominal MC) and the unfolding results as functions of the event shape observables at the particle level. The efficiency results from the unfolding using the systematic deviations of the MC are also shown in the plots.

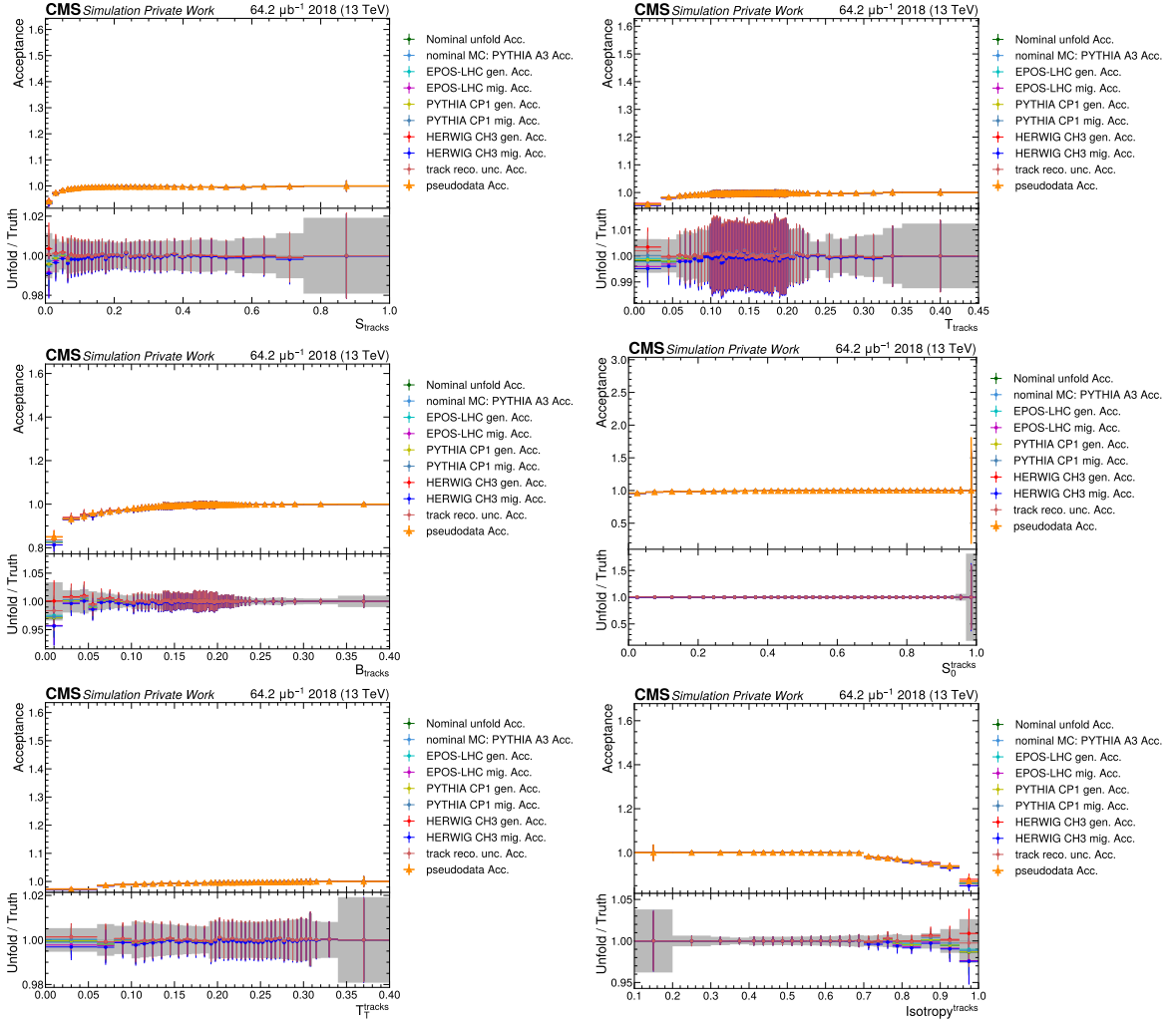


Figure A.24: The acceptance of the PYTHIA 8 CUETP8M1 (NNPDF3.1LO) tune (pseudodata), the A3P tune (nominal MC) and the unfolding results as functions of the event shape observables at the reconstructed level. The acceptance results from the unfolding using the systematic deviations of the MC are also shown in the plots.

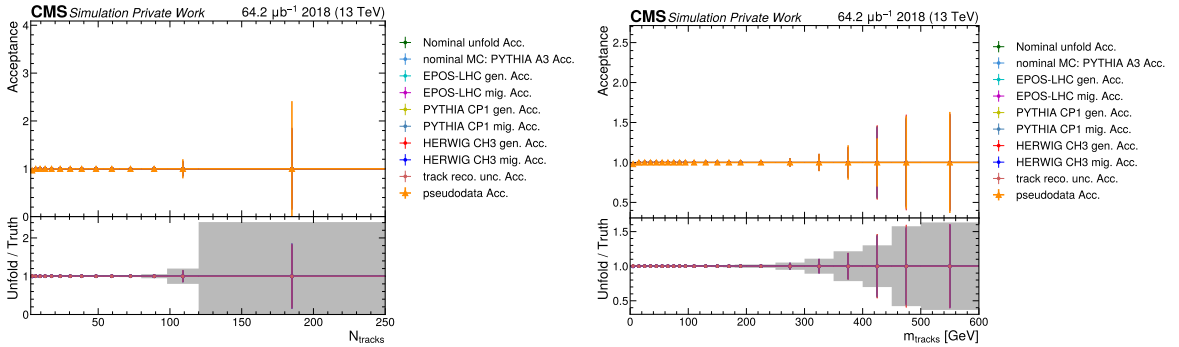


Figure A.25: The acceptance of the PYTHIA 8 CUETP8M1 (NNPDF3.1LO) tune (pseudodata), the A3 tune (nominal MC) and the unfolding results as functions of the track multiplicity and invariant mass of the tracks. The acceptance results from the unfolding using the systematic deviations of the MC are also shown in the plots.

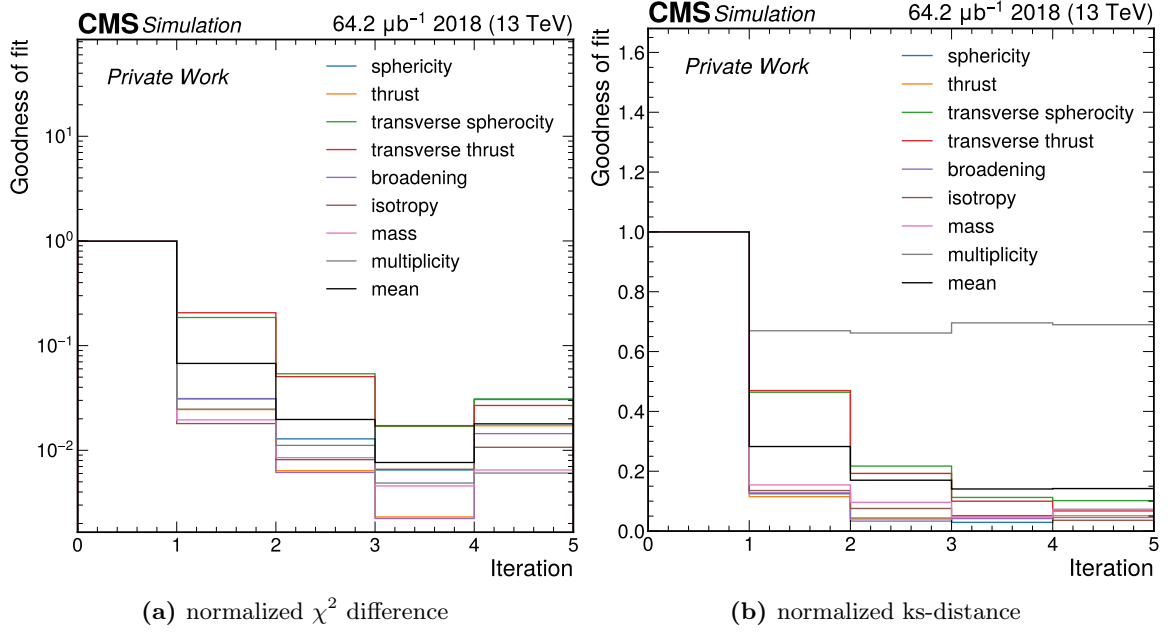


Figure A.26: The unfolding closure to the pseudodata from PYTHIA 8 CP5 tune for the truth level observables. The uncertainty in the χ^2 calculation includes only the pseudodata statistical uncertainty. The χ^2 and ks-distance values for each observable are normalized to the corresponding values between the initial nominal MC and pseudodata samples before unfolding.

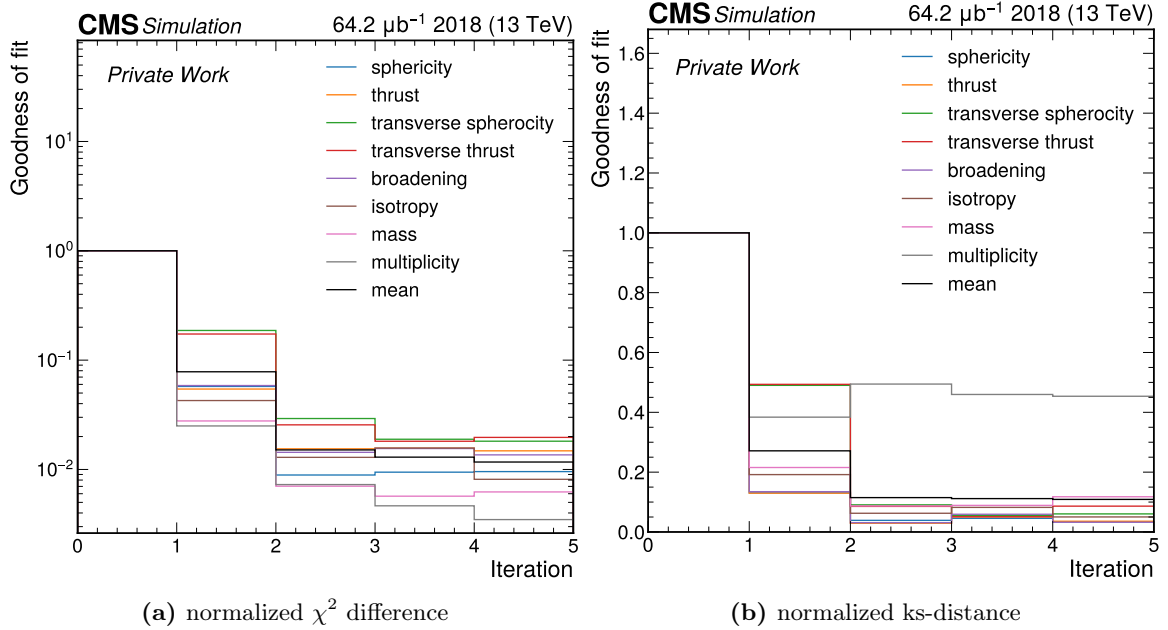
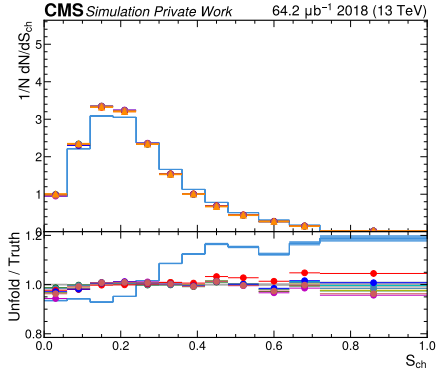
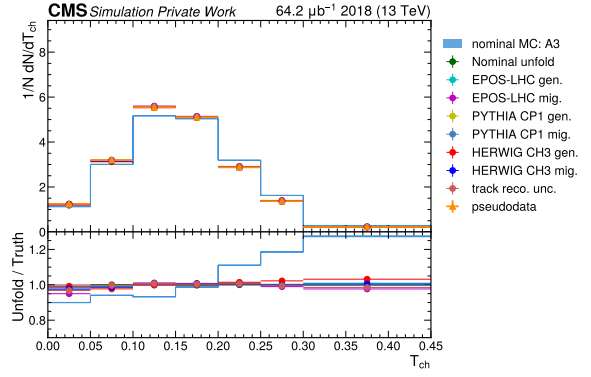


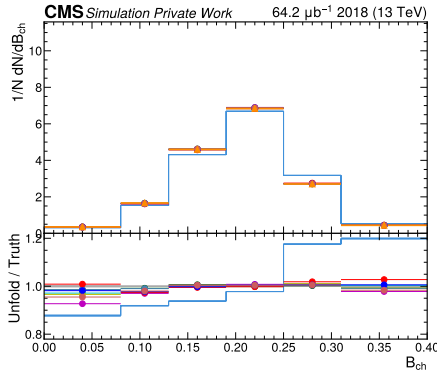
Figure A.27: The unfolding closure to the pseudodata from PYTHIA 8 CP5 tune for the detector level observables. The uncertainty in the χ^2 calculation includes only the pseudodata statistical uncertainty. The χ^2 and ks-distance values for each observable are normalized to the corresponding values between the initial nominal MC and pseudodata samples before unfolding.



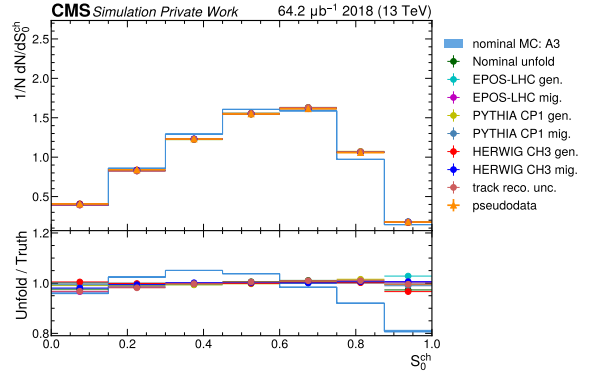
(a) Sphericity



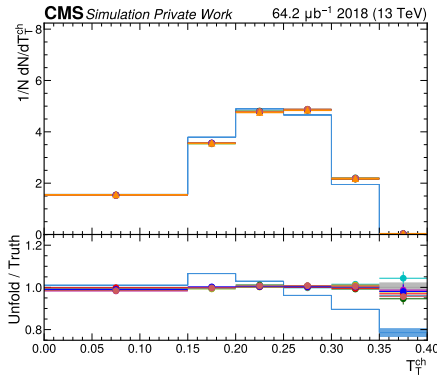
(b) Thrust



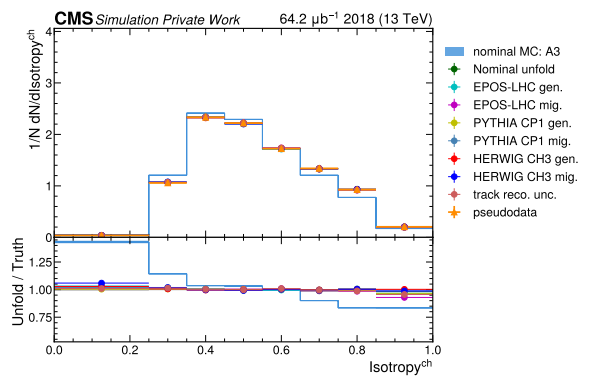
(c) Broadening



(d) Transverse sphericity

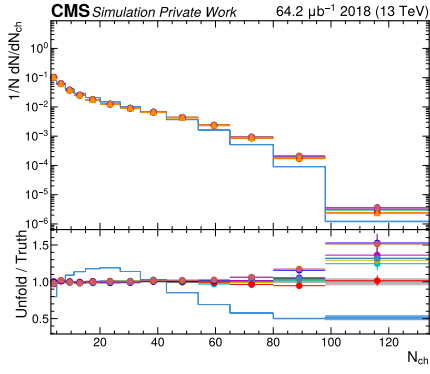


(e) Transverse thrust

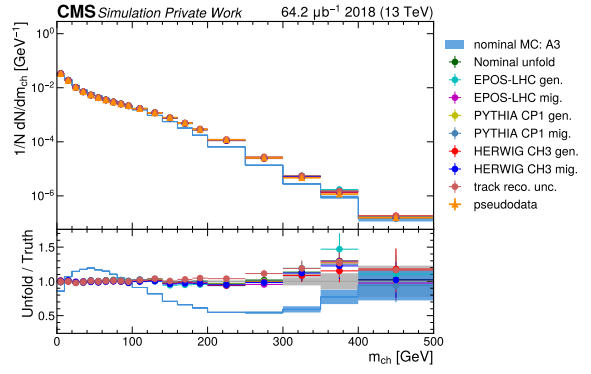


(f) Isotropy

Figure A.28: The event shape distributions of the CP5 tune (pseudodata), the A3 tune (nominal MC), and the unfolding results at the truth level.

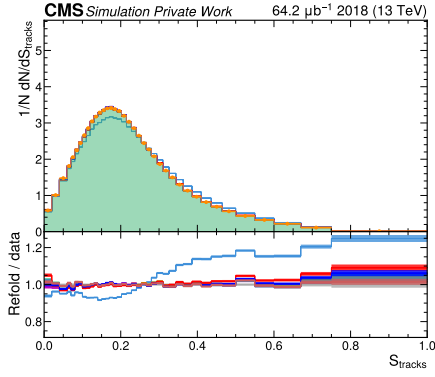


(a) Number of the charged particles

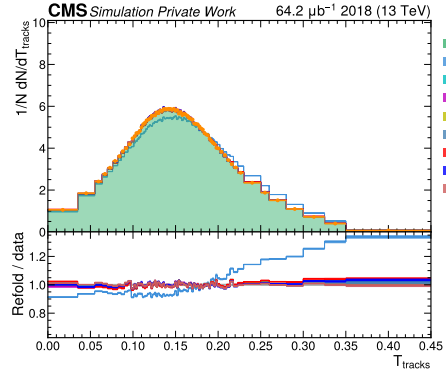


(b) Mass of the charged particles

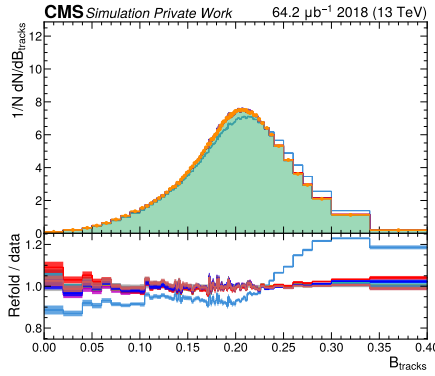
Figure A.29: The charged particle multiplicity and invariant mass distributions of the CP5 tune (pseudodata), the A3 tune (nominal MC), and the unfolding results at the truth level.



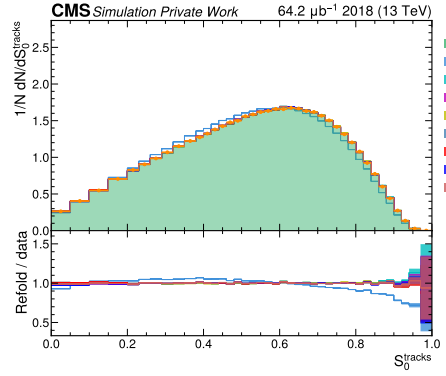
(a) Sphericity



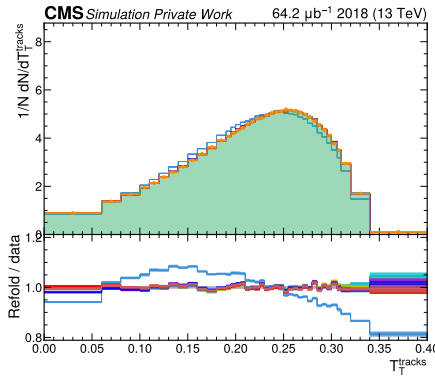
(b) Thrust



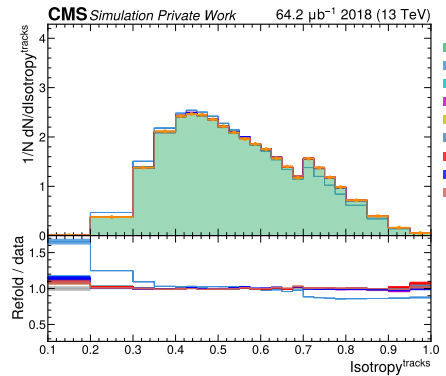
(c) Broadening



(d) Transverse sphericity



(e) Transverse thrust



(f) Isotropy

Figure A.30: The event shape distributions of the CP5 tune (pseudodata), the A3 tune (nominal MC), and the unfolding results at the detector level.

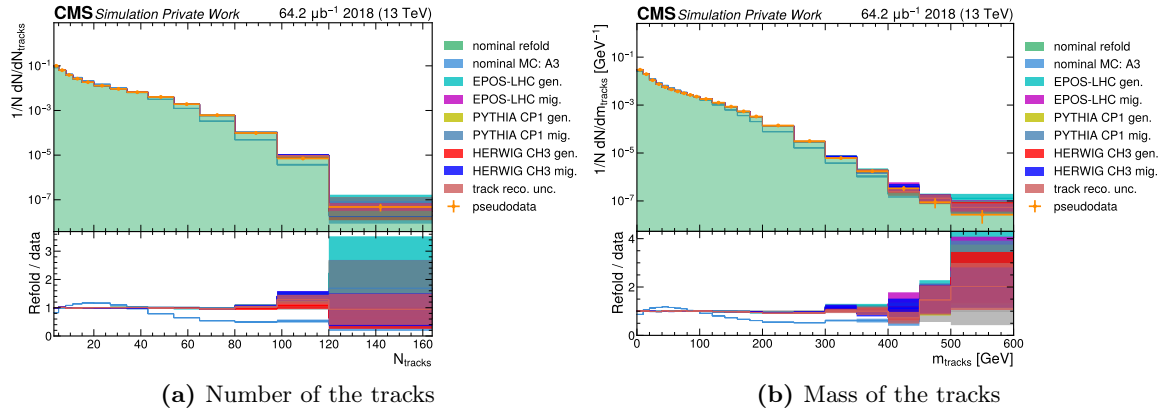


Figure A.31: The track multiplicity and invariant mass distributions of the CP5 tune (pseudodata), the A3 tune (nominal MC), and the unfolding results at the detector level.

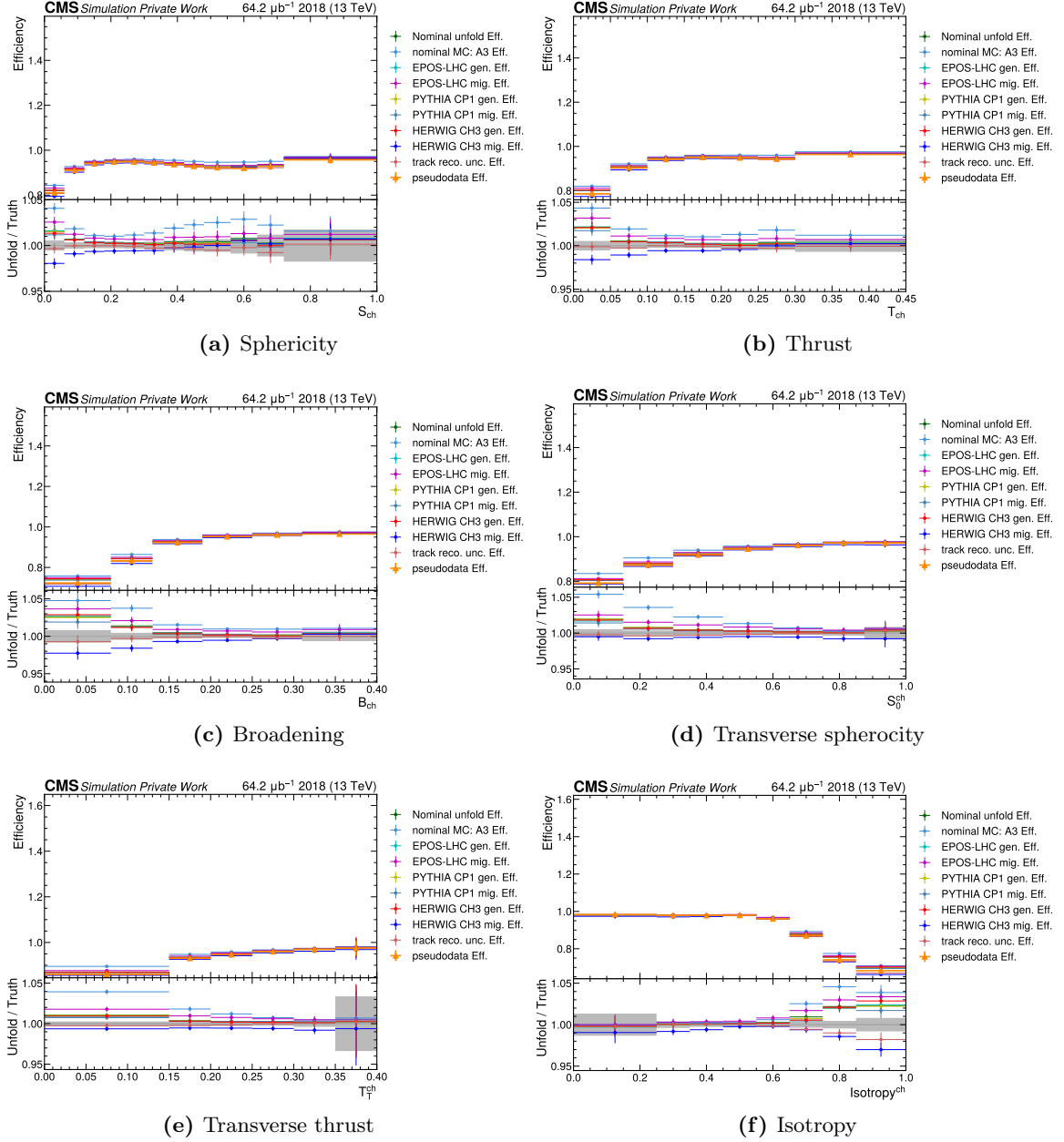
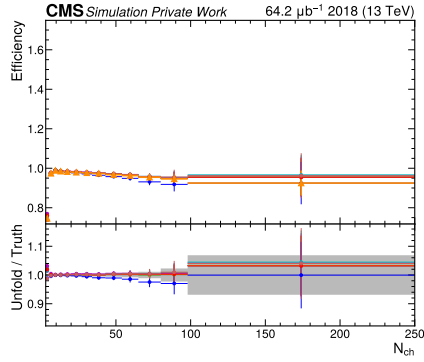
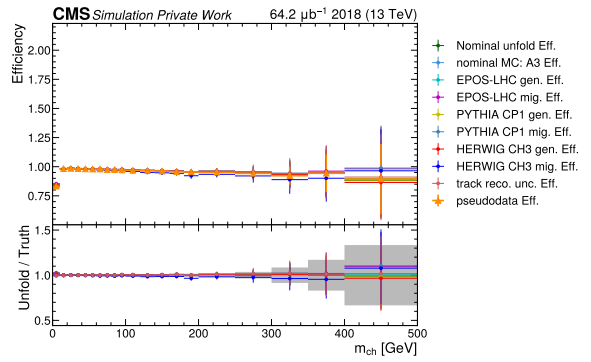


Figure A.32: The efficiency of the CP5 tune (pseudodata), the A3 tune (nominal MC), and the unfolding results as functions of the event shape observables at the truth level. The efficiency results from the unfolding using the systematic deviations of the MC are also shown in the plots.



(a) Number of the tracks



(b) Mass of the tracks

Figure A.33: The efficiency of the CP5 tune (pseudodata), the A3 tune (nominal MC), and the unfolding results as functions of the charged particle multiplicity and invariant mass of the charged particles. The efficiency results from the unfolding using the systematic deviations of the MC are also shown in the plots.

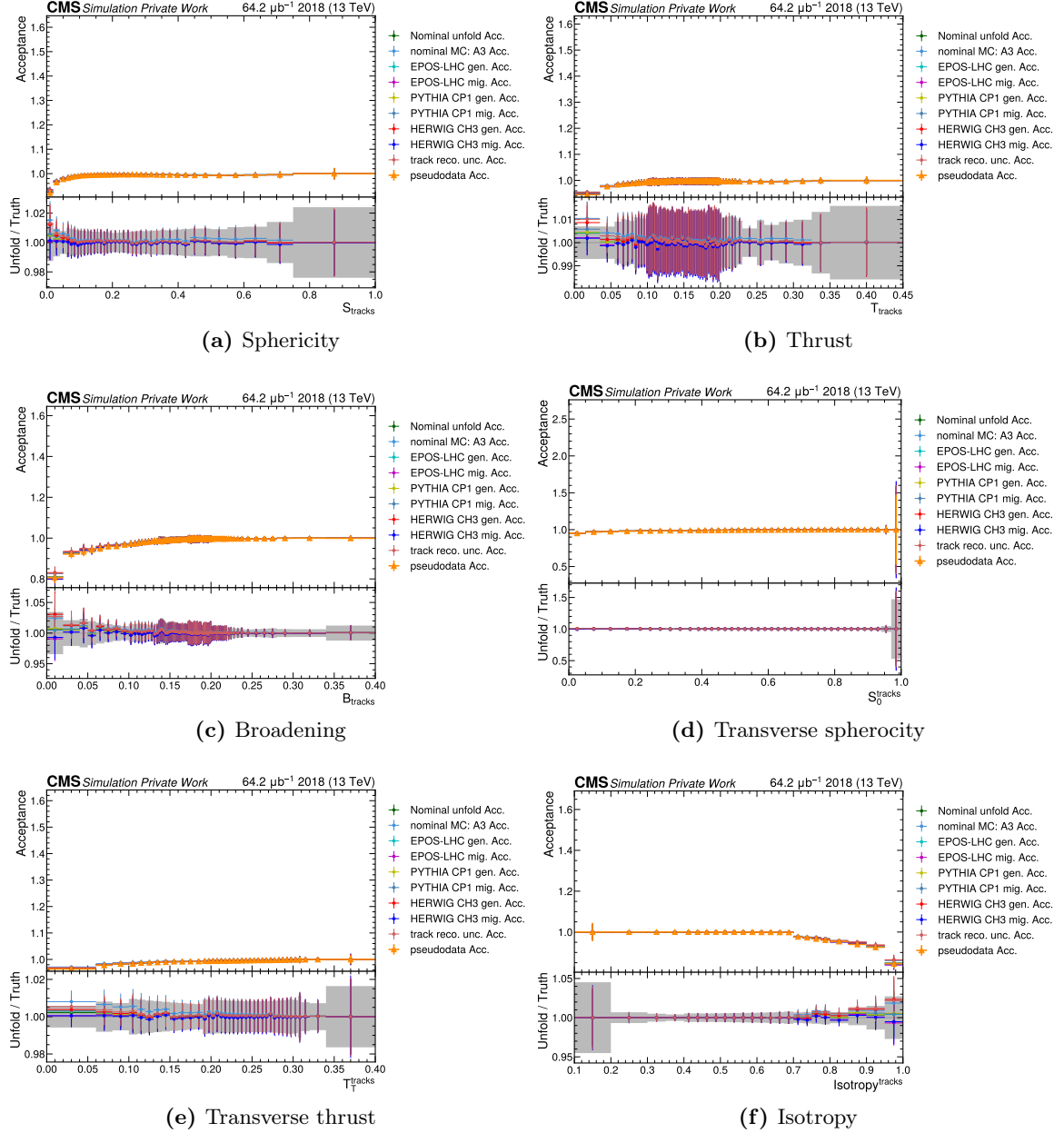


Figure A.34: The acceptance of the CP5 tune (pseudodata), the A3 tune (nominal MC), and the unfolding results as functions of the event shape observables at the detector level. The acceptance results from the unfolding using the systematic deviations of the MC are also shown in the plots.

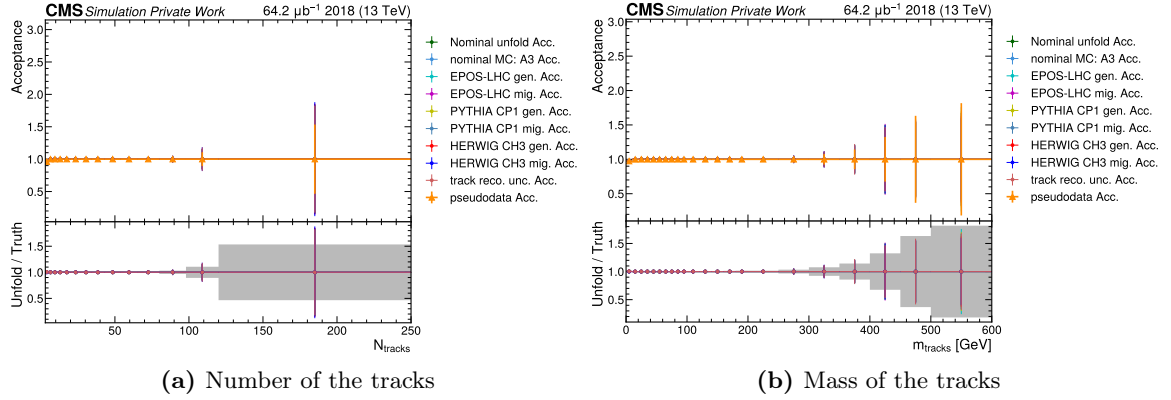


Figure A.35: The acceptance of the CP5 tune (pseudodata), the A3 tune (nominal MC), and the unfolding results as functions of the track multiplicity and invariant mass of the tracks. The acceptance results from the unfolding using the systematic deviations of the MC are also shown in the plots.

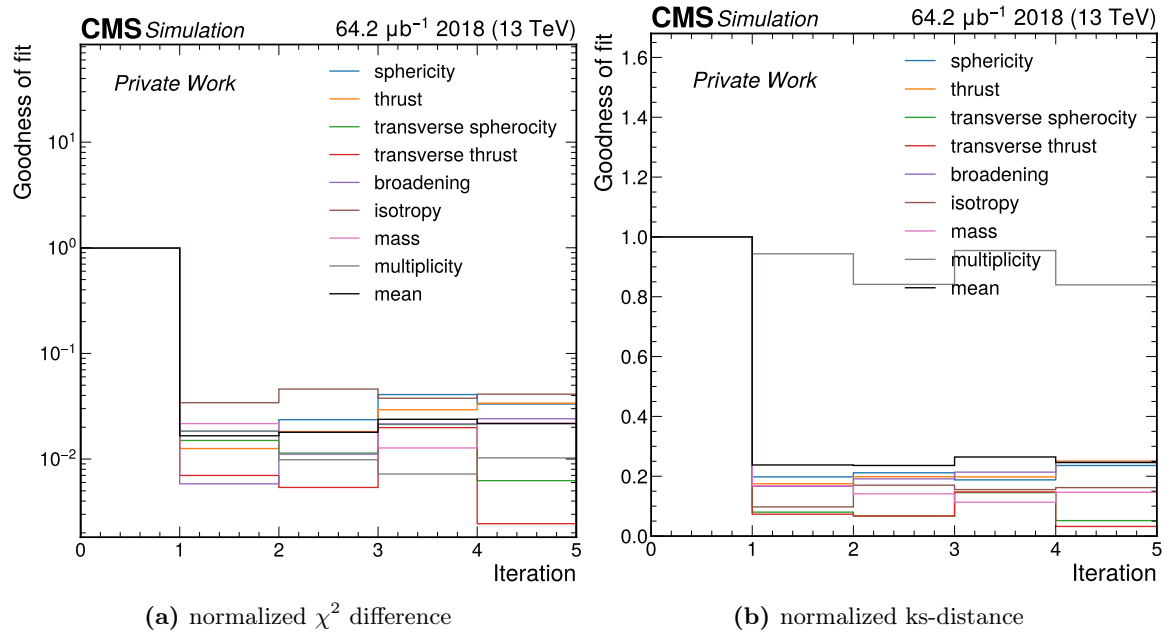


Figure A.36: The unfolding closure to the pseudo-data from PYTHIA 8 A14 tune for the gen-level observables. The uncertainty in the χ^2 calculation includes only the pseudodata statistical uncertainty. The χ^2 and ks-distance values for each observable are normalized to the χ^2 of the initial nominal MC and pseudodata samples before unfolding.

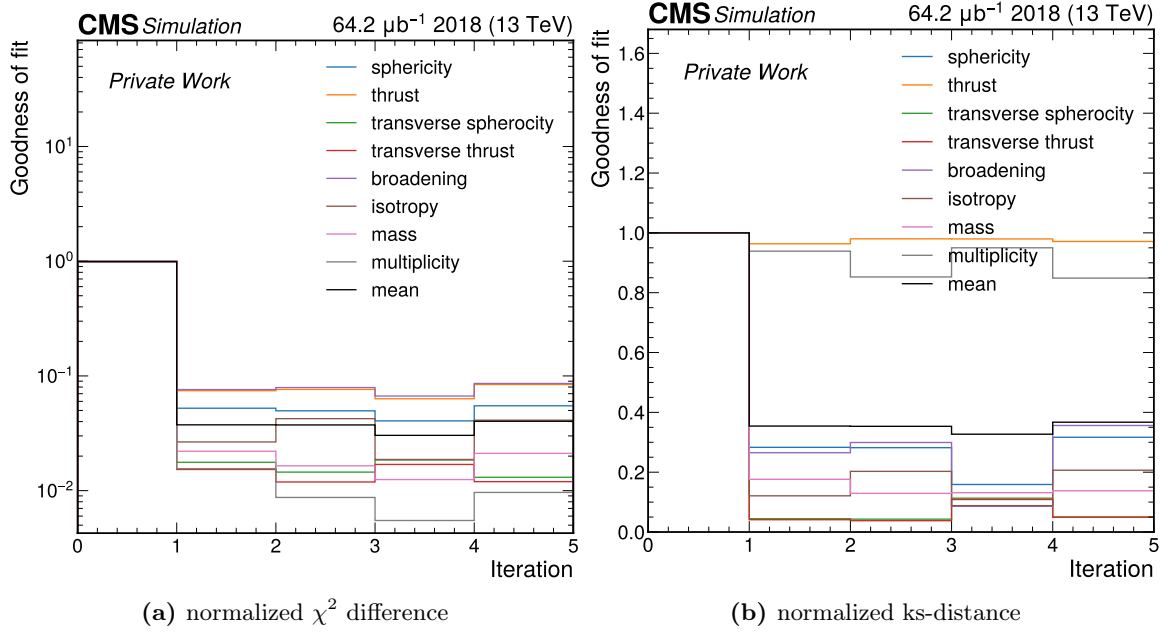


Figure A.37: The unfolding closure to the pseudo-data from PYTHIA 8 A14 tune for the reco-level observables. The uncertainty in the χ^2 calculation includes only the pseudodata statistical uncertainty. The χ^2 and ks-distance values for each observable are normalized to the χ^2 of the initial nominal MC and pseudodata samples before unfolding.

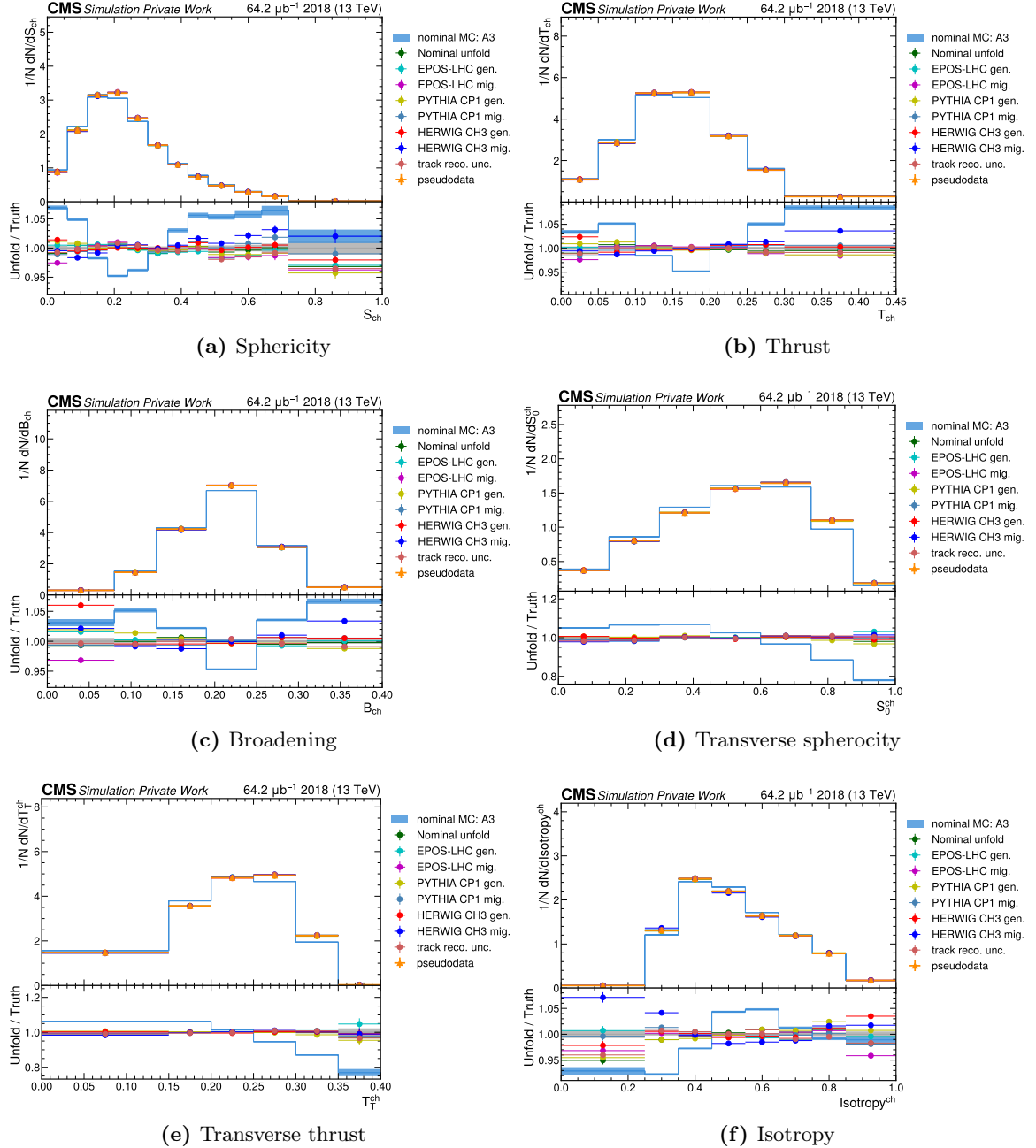
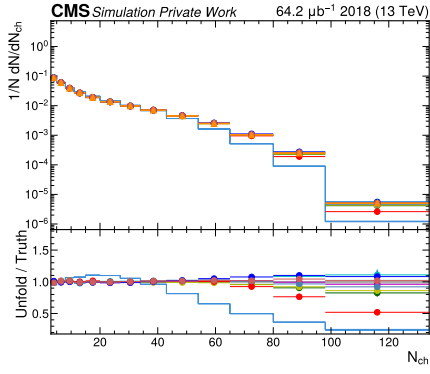
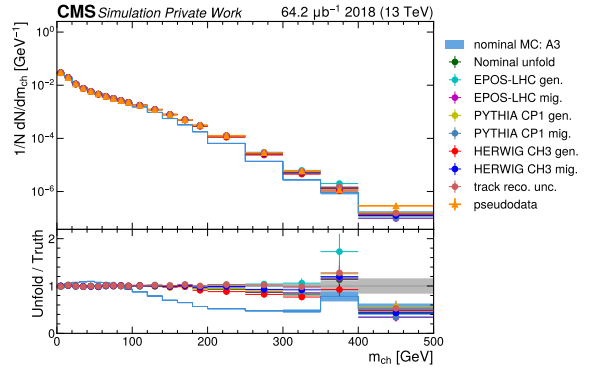


Figure A.38: The event shape distributions of the A14 tune(pseudo-data), the A3P tune (nominal MC), and the unfolding results at the particle level.

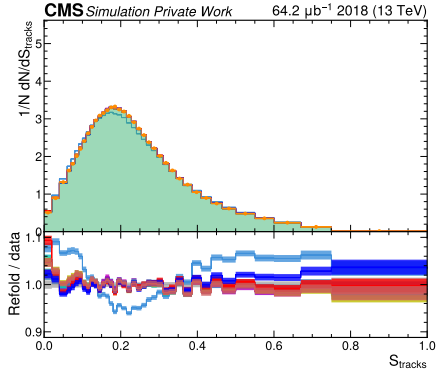


(a) Number of the charged particles

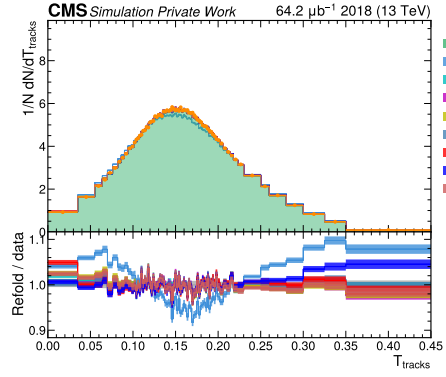


(b) Mass of the charged particles

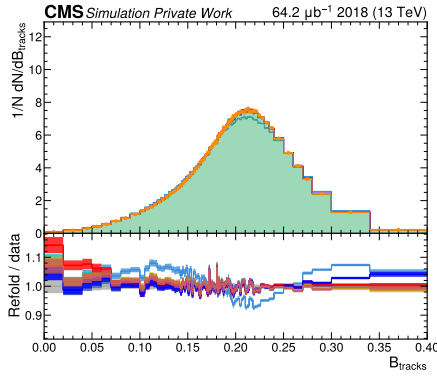
Figure A.39: The charged particle multiplicity and invariant mass distributions of the A14 tune(pseudo-data), the A3P tune (nominal MC) and the unfolding results.



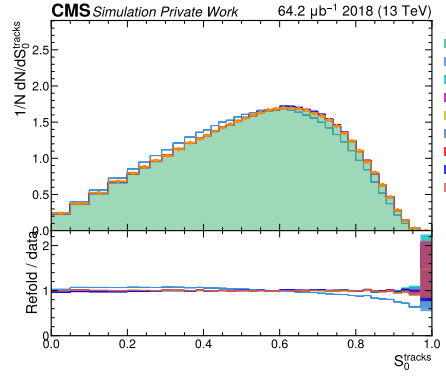
(a) Sphericity



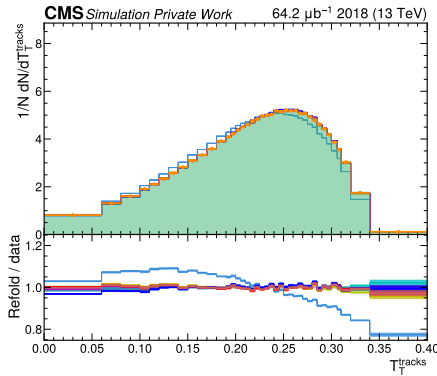
(b) Thrust



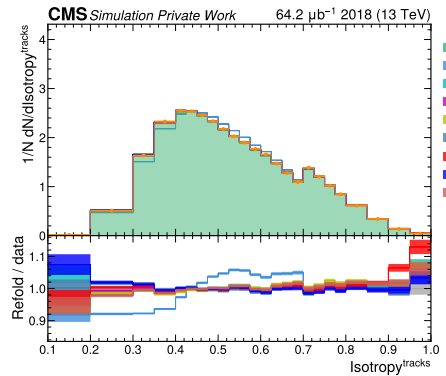
(c) Broadening



(d) Transverse sphericity

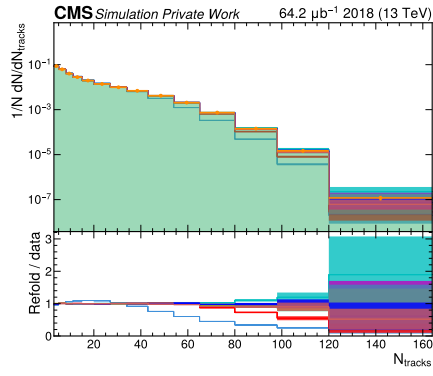


(e) Transverse thrust

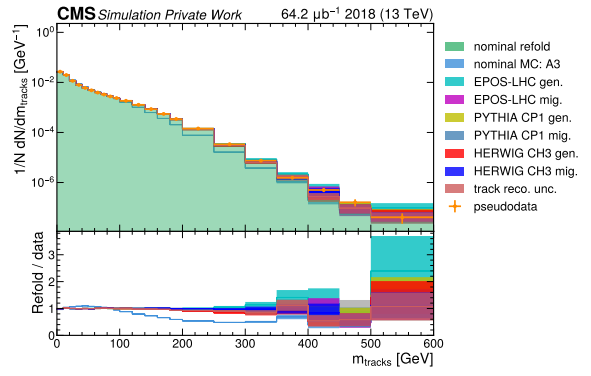


(f) Isotropy

Figure A.40: The event shape distributions of the A14 tune(pseudo-data), the A3P tune (nominal MC), and the unfolding results at the reconstructed level.

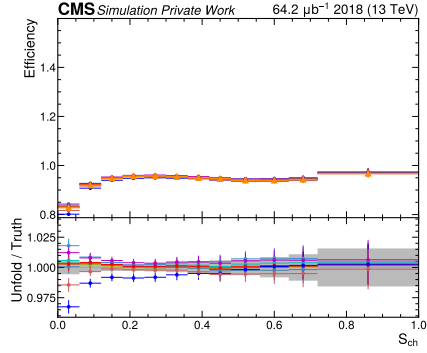


(a) Number of the tracks

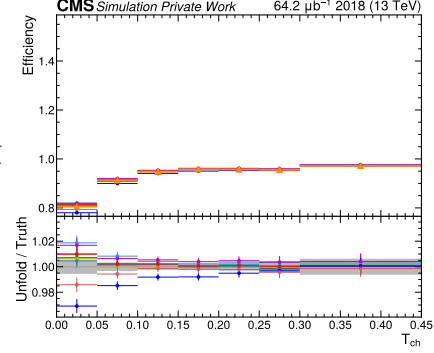


(b) Mass of the tracks

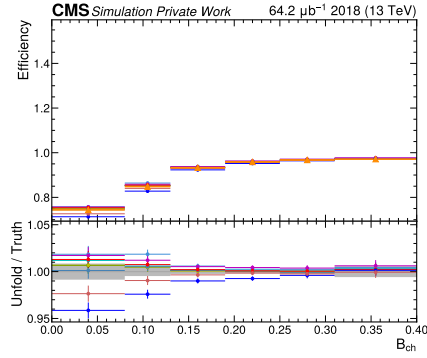
Figure A.41: The track multiplicity and invariant mass distributions of the A14 tune(pseudo-data), the A3P tune (nominal MC) and the unfolding results.



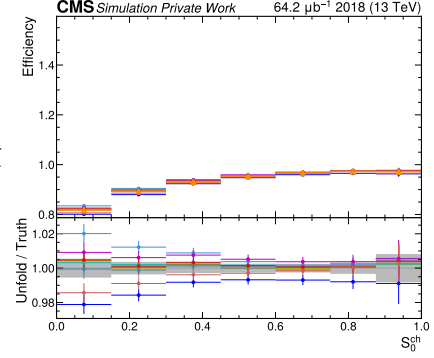
(a) Sphericity



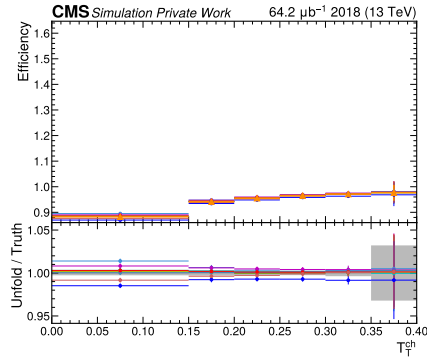
(b) Thrust



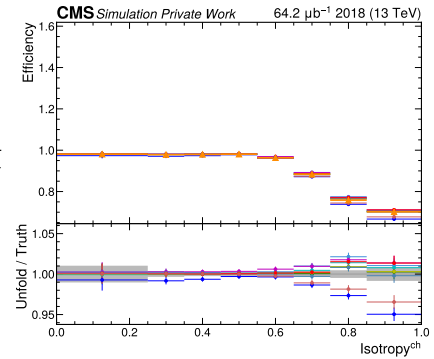
(c) Broadening



(d) Transverse sphericity

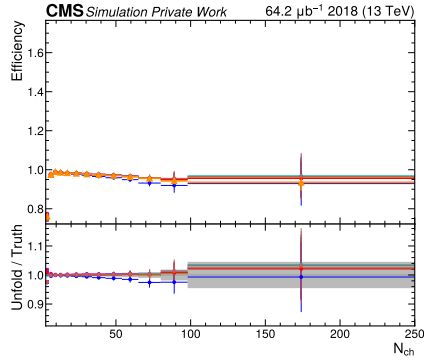


(e) Transverse thrust

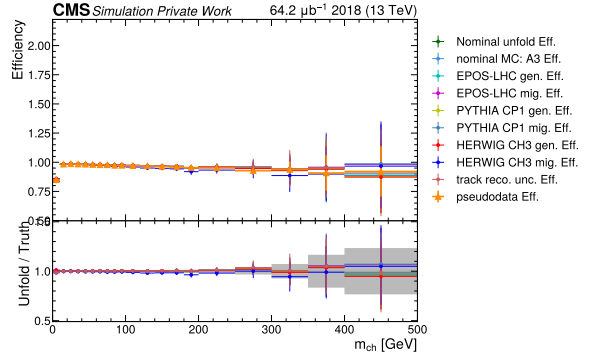


(f) Isotropy

Figure A.42: The efficiency of the A14 tune(pseudo-data), the A3P tune (nominal MC), and the unfolding results as functions of the event shape observables at the particle level. The efficiency results from the unfolding using the systematic deviations of the MC are also shown in the plots.

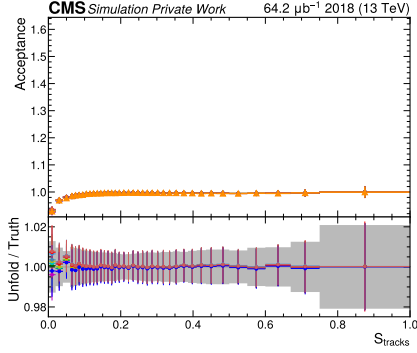


(a) Number of the tracks

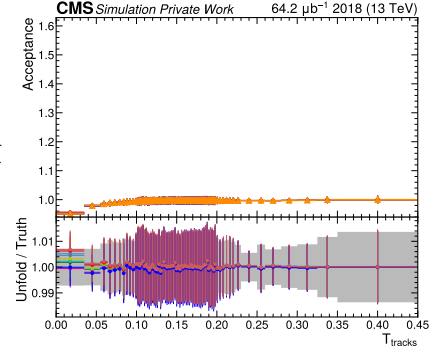


(b) Mass of the tracks

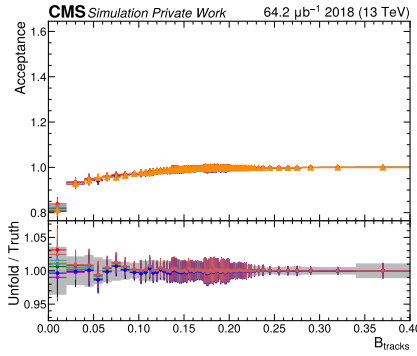
Figure A.43: The efficiency of the A14 tune(pseudo-data), the A3P tune (nominal MC), and the unfolding results as functions of the charged particle multiplicity and invariant mass of the charged particles. The efficiency results from the unfolding using the systematic deviations of the MC are also shown in the plots.



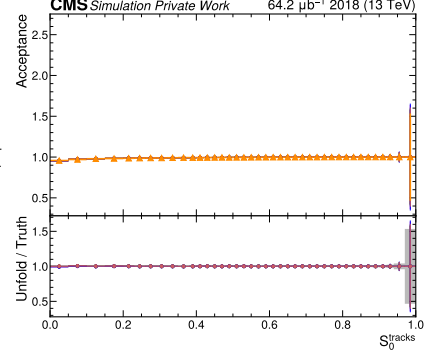
(a) Sphericity



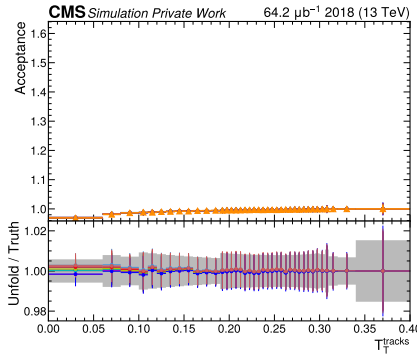
(b) Thrust



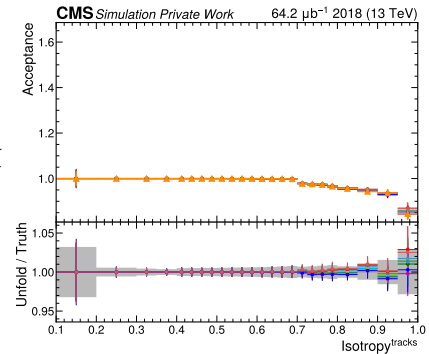
(c) Broadening



(d) Transverse sphericity

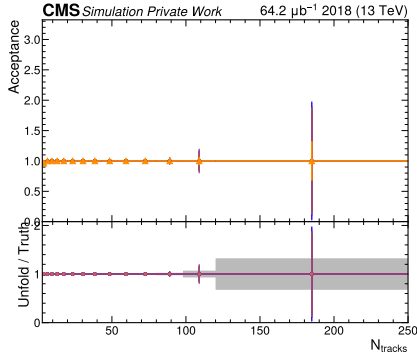


(e) Transverse thrust

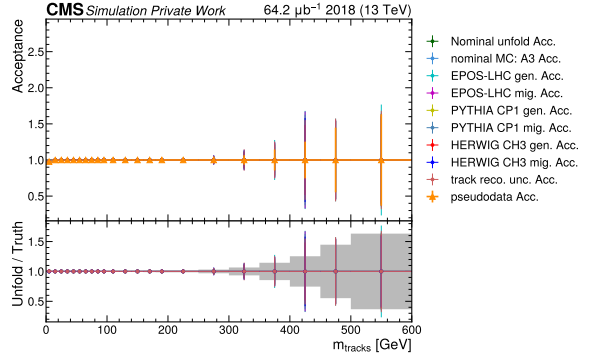


(f) Isotropy

Figure A.44: The acceptance of the A14 tune(pseudo-data), the A3P tune (nominal MC), and the unfolding results as functions of the event shape observables at the reconstructed level. The acceptance results from the unfolding using the systematic deviations of the MC are also shown in the plots.



(a) Number of the tracks



(b) Mass of the tracks

Figure A.45: The acceptance of the A14 tune(pseudo-data), the A3P tune (nominal MC), and the unfolding results as functions of the track multiplicity and invariant mass of the tracks. The acceptance results from the unfolding using the systematic deviations of the MC are also shown in the plots.

A.4 More plots of bias and coverage test

Results of the bias and coverage tests as outlined in Section 4.6.4 are shown below for the rest of the observables.

Results of bias tests are shown in Figure A.46. Results of the coverage tests are shown in Figures A.47.

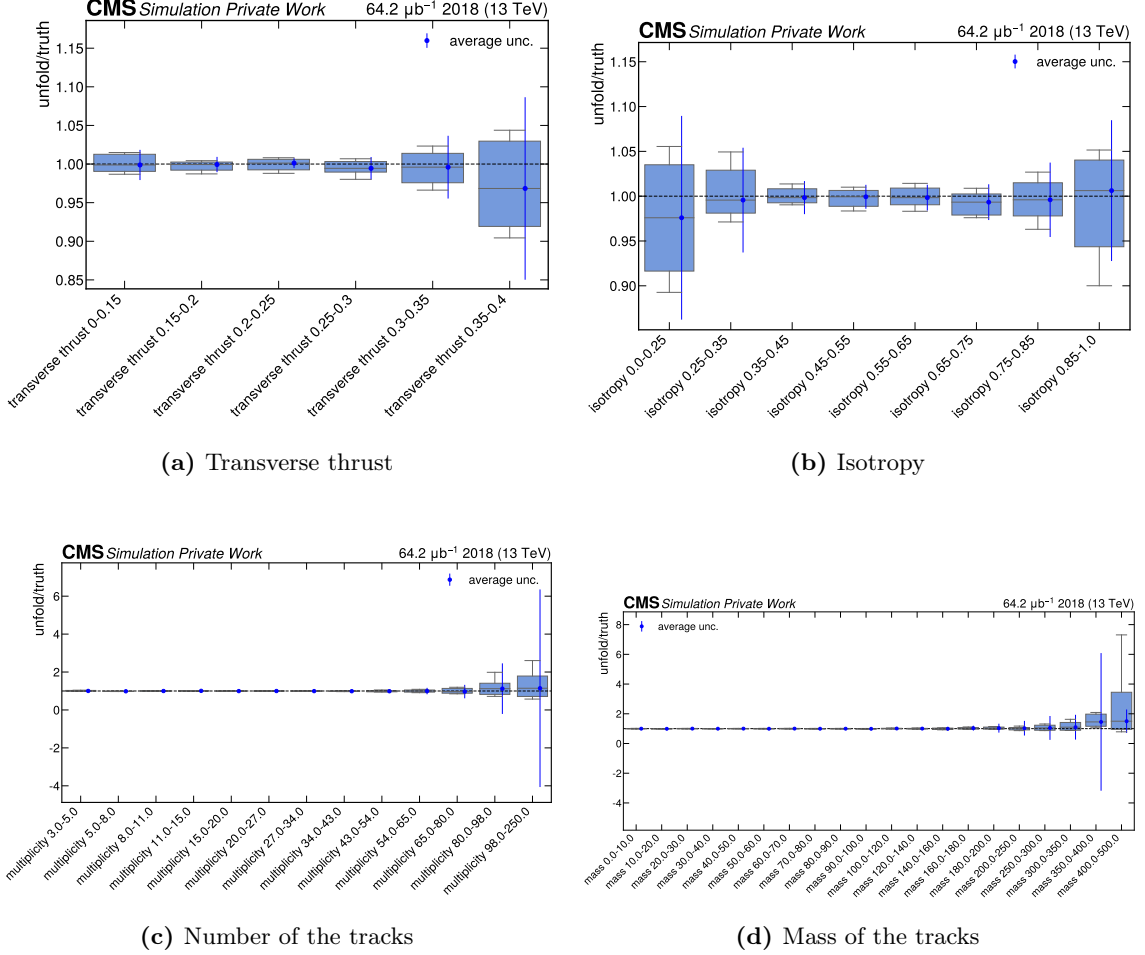
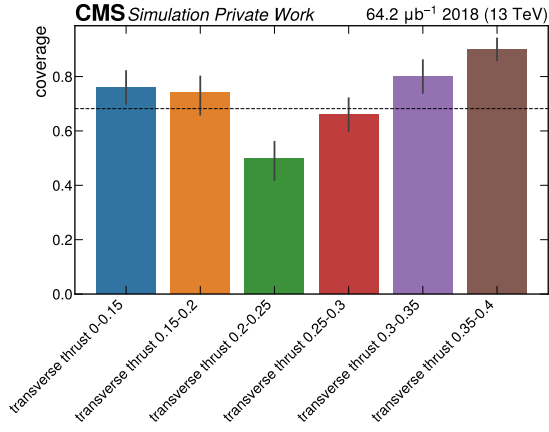
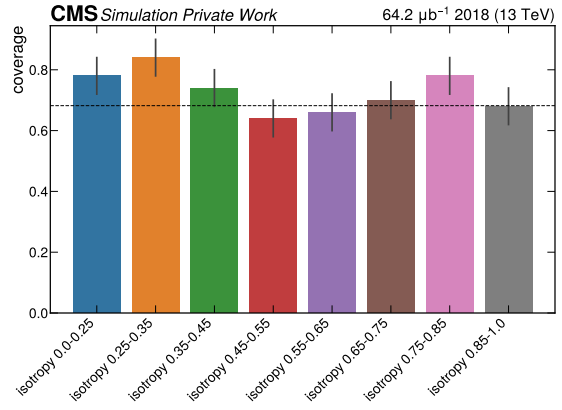


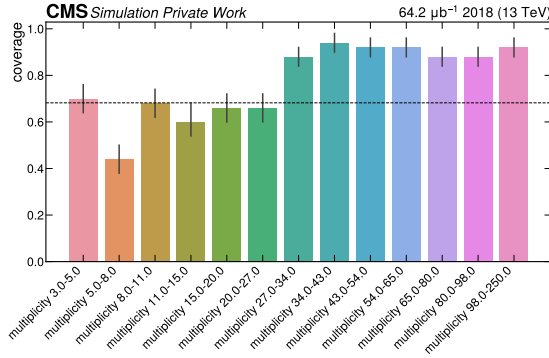
Figure A.46: The bias of the unfolded results after 2 iterations, when unfolding the pseudo-data from PYTHIA 8 CUETP8M1 tune with the nominal MC from the A3 tune. The boxplot shows the 25%, 50% and 75% quantiles of the ratio of the unfolded result over the corresponding pseudodata; the whiskers show the standard deviation. The average uncertainty of the unfolding result in each bin is overlaid so that the size of the bias can be compared directly to the measurement uncertainty. The bias is estimated by 50 toy experiments with resampling of the systematic templates. The unfolding uncertainty of each toy experiment is approximated by the uncertainty of unfolding the data.



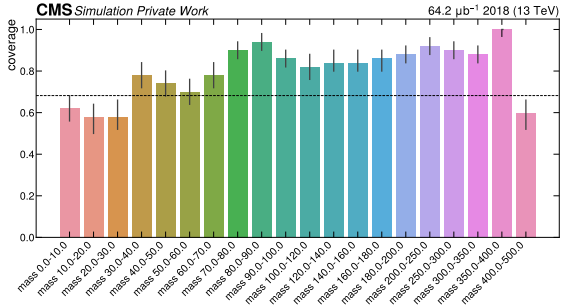
(a) Transverse thrust



(b) Isotropy



(c) Number of the tracks



(d) Mass of the tracks

Figure A.47: The coverage of the unfolded results after 2 iterations, when unfolding the pseudo-data from PYTHIA 8 CUETP8M1 tune with the nominal MC from the A3 tune. The coverage is estimated by 50 toy experiments with resampling of the systematic templates. The unfolding uncertainty of each toy experiment is approximated by the uncertainty of unfolding the data.

A.5 Correlation matrices

The correlations matrices of the unfolding uncertainty are given in Figure A.48, A.49, A.50 and A.51, corresponding to the one-dimensional histograms shown in Section 4.7.1.

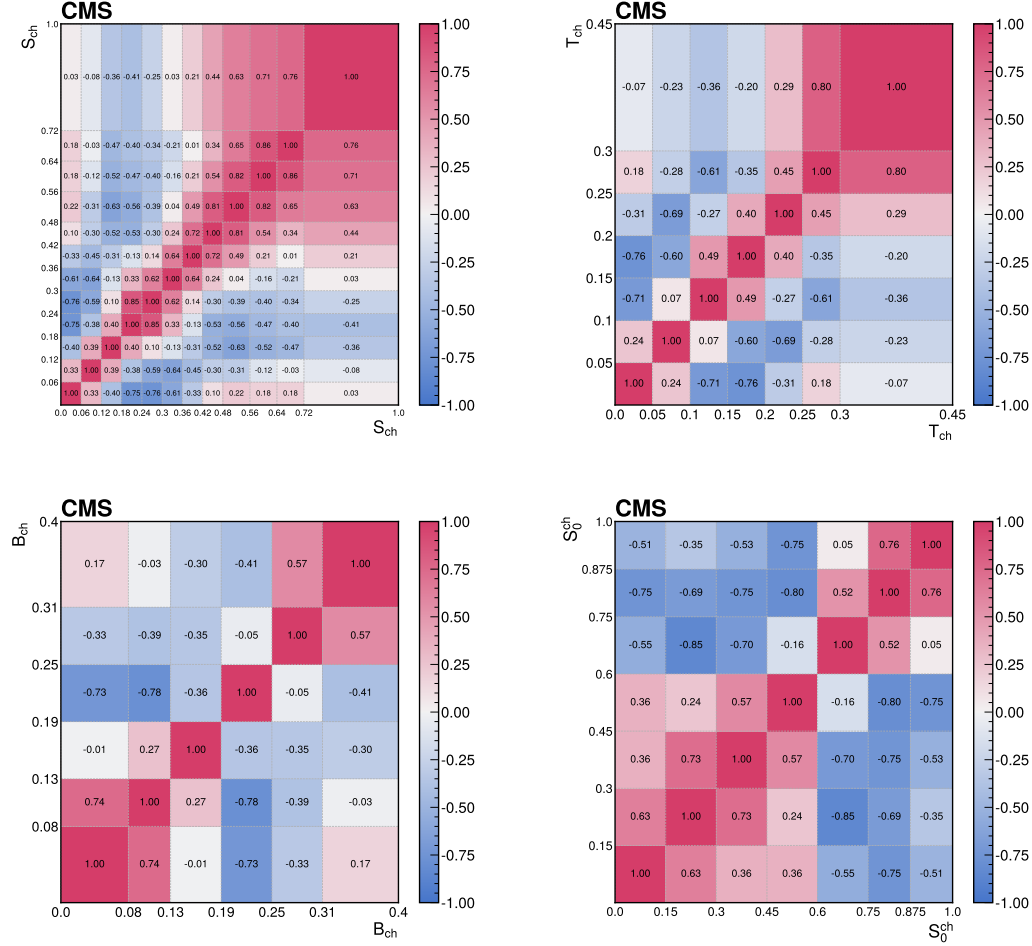


Figure A.48: The correlations of the unfolding systematic uncertainty between bins of the event shape observables shown for (upper left) sphericity, (upper right) thrust, (lower left) broadening, and (lower right) transverse sphericity.

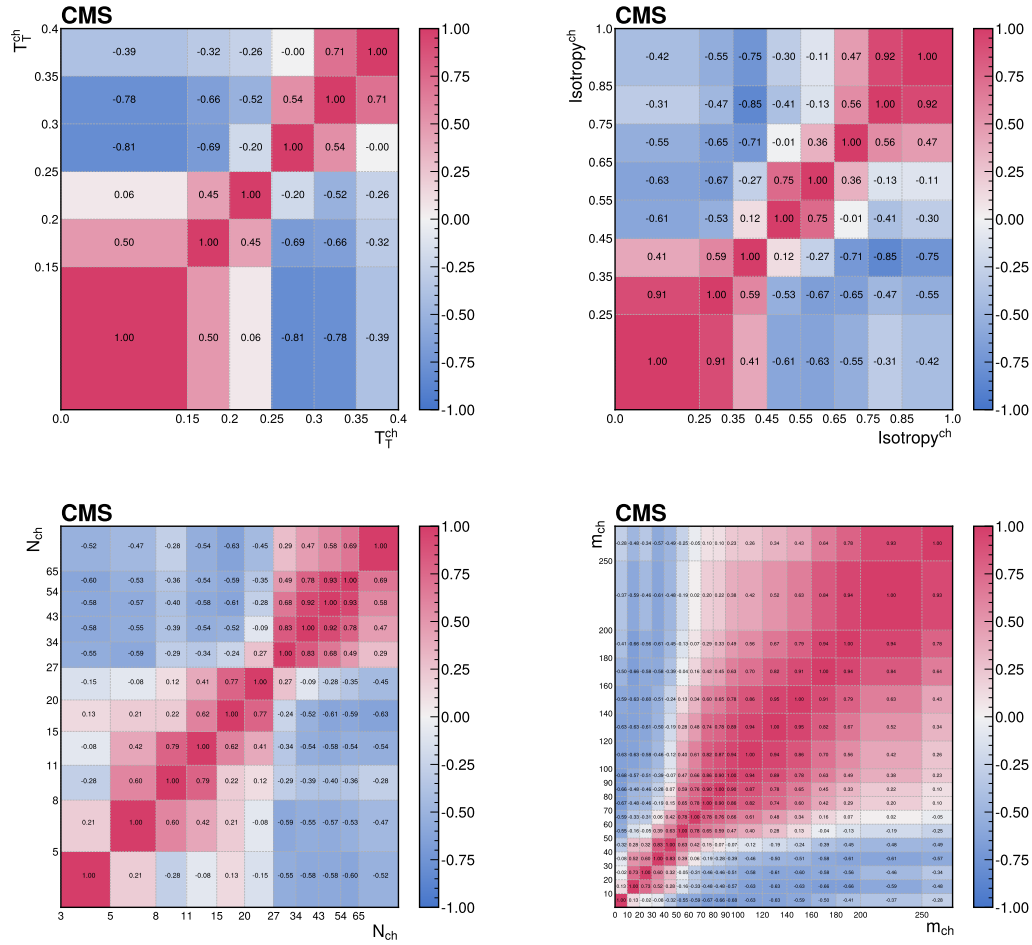


Figure A.49: The correlations of the unfolding systematic uncertainty between bins of the event shape observables shown for (upper left) transverse thrust, (upper right) isotropy, (lower left) particle multiplicity, (lower right) invariant mass.

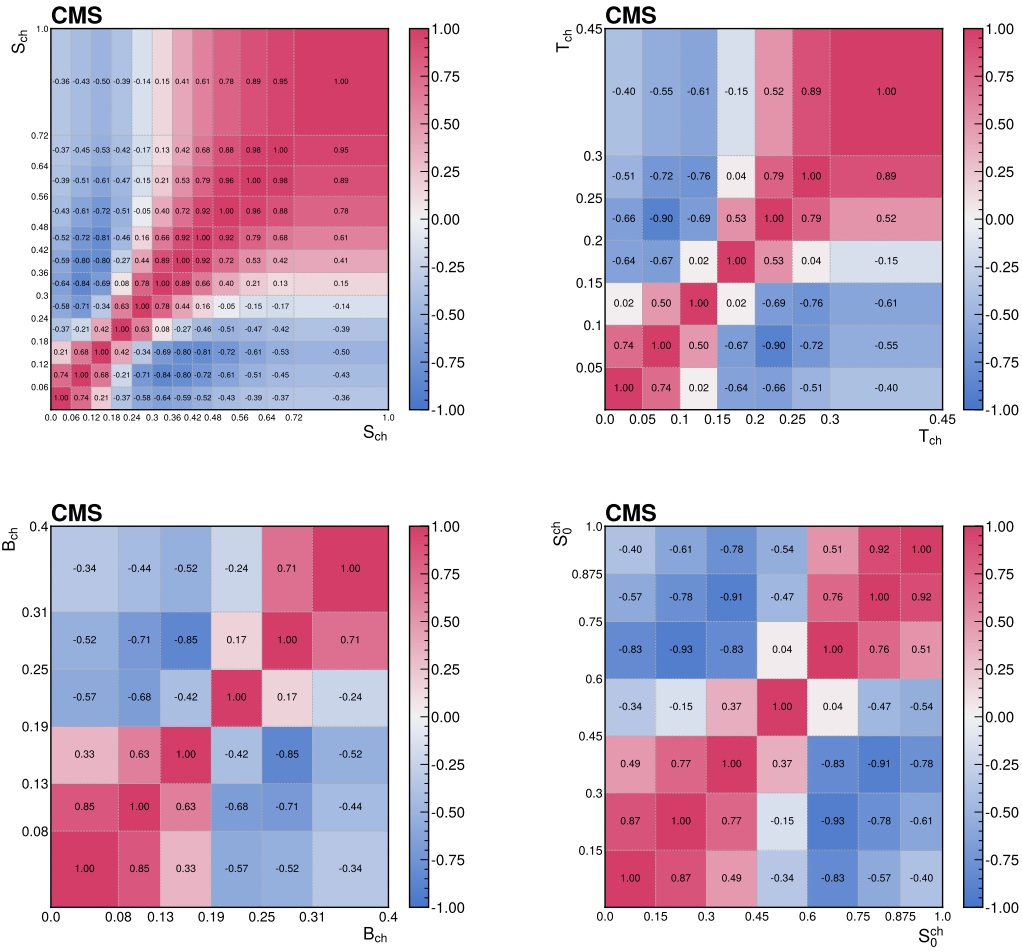


Figure A.50: The correlations of the unfolding statistical uncertainty between bins of the event shape observables shown for (upper left) sphericity, (upper right) thrust, (lower left) broadening, and (lower right) transverse sphericity.

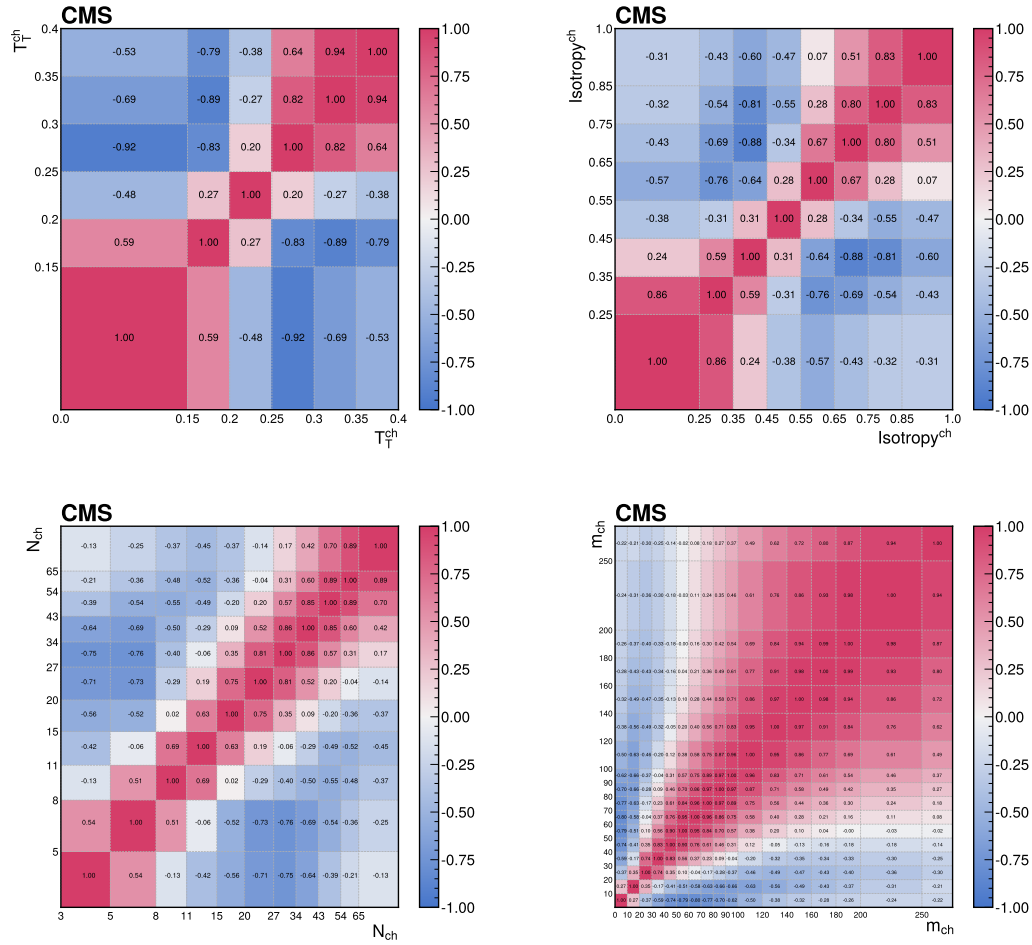


Figure A.51: The correlations of the unfolding statistical uncertainty between bins of the event shape observables shown for (upper left) transverse thrust, (upper right) isotropy, (lower left) particle multiplicity, (lower right) invariant mass.

A.6 Uncertainty breakdown

The contributions from individual uncertainty sources are analysed in the uncertainty breakdown plots in Figure A.52 and A.53 corresponding to the one-dimensional histograms shown in Section 4.7.1. The figures show the unfolding uncertainties relative to the values in the bins. The component from each source of MC modeling uncertainty is estimated as the difference between the unfolding result using the corresponding template and the central result using the nominal MC sample. The MC statistic uncertainty is estimated as the square root of the sum of the squared weights for all the events in each bin. The total systematic uncertainty is estimated either by quadrature sum of all these components (black solid line labeled as "Total sys. unc."), or by using toy experiments (black dash-dotted line labeled as "Total sys. unc. (pseudo-experiment)"). Due to the correlations among the components, the estimation from their quadrature sum is different from the more accurate estimation with toy experiments, but in similar order and trend. The statistical uncertainty from data statistics is estimated by toy experiments (orange dash-dotted line labeled as "Stat. unc. (pseudo-experiment)") and compared with the systematic uncertainty components.

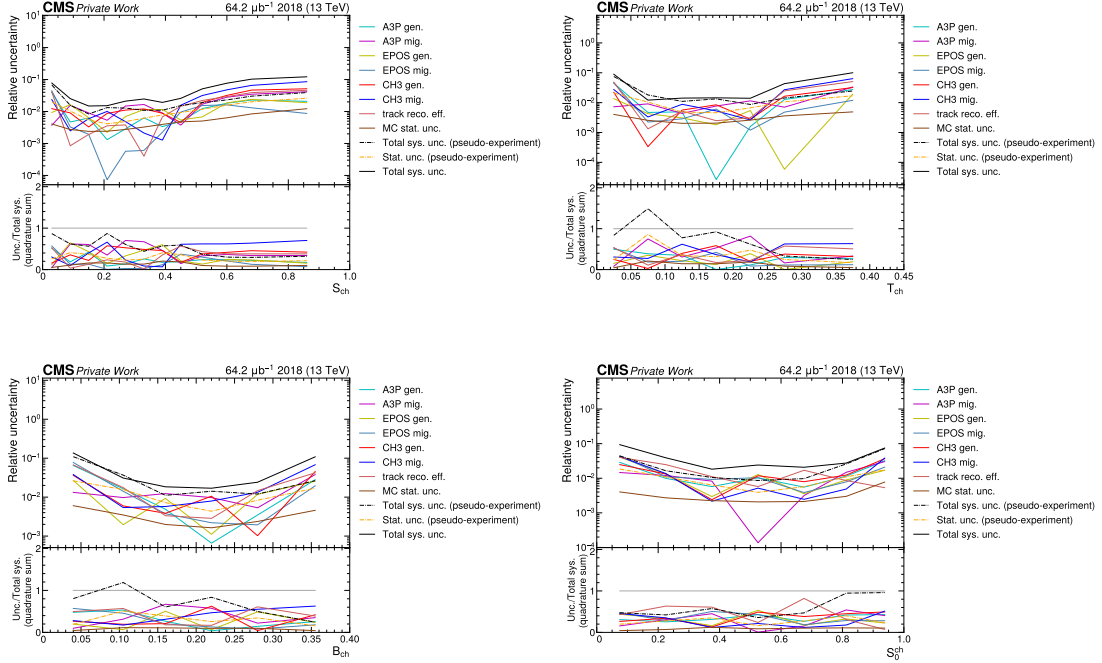


Figure A.52: The uncertainty breakdown of unfolding shown for (upper left) sphericity, (upper right) thrust, (lower left) broadening, and (lower right) transverse sphericity.

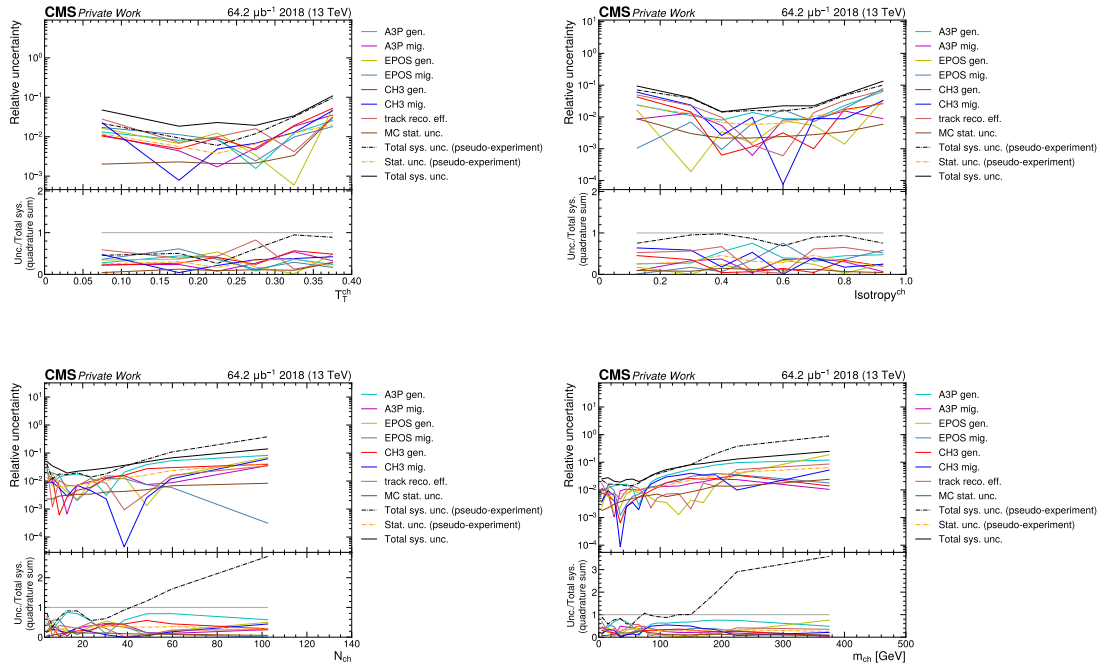


Figure A.53: The uncertainty breakdown of unfolding shown for (upper left) transverse thrust, (upper right) isotropy, (lower left) particle multiplicity, (lower right) invariant mass.

B Additional material for the energy scaling

Behaviour of intrinsic k_T in Drell–Yan events

B.1 Decoupling the underlying-event and Drell–Yan dilepton transverse momentum descriptions

The analysis in this chapter shows the mutual influence of the intrinsic k_T tune on the underlying-event (UE) description, and vice versa. The results of the approximate decoupling of the two parts rationalize the studies in the main text of tuning the intrinsic k_T using fixed UE tunes. Our baseline is the PYTHIA CP5 UE tune [195], recently developed by the CMS Collaboration, for which five parameters controlling multiple-parton interactions (MPI) and color reconnection were varied. This tune was obtained using UE data measured by CDF and CMS at center-of-mass energies of 1.96, 7, and 13 TeV.

To assess the impact of the UE parameterization on the Drell–Yan (DY) dilepton transverse momentum ($p_T(\ell^+\ell^-)$) spectrum, we generated DY samples and their $p_T(\ell^+\ell^-)$ distributions with the intrinsic k_T parameter fixed to the tuned result and the UE parameters set to either the CP5 tune-up or tune-down variation. The difference between the two predictions reflects the effects of the UE-tune uncertainty on the DY $p_T(\ell^+\ell^-)$ spectrum, shown as red bands in Fig. B.1 (upper), which are much smaller than the uncertainty from the intrinsic k_T variations shown as violet bands.

Similarly, we studied the impact of the intrinsic k_T variation on observables that are sensitive to the UE models and have been used to obtain the CP5 tune. With the UE parameters fixed to the CP5 tune, we generated minimum-bias events with the tuned intrinsic k_T parameter, shown as violet markers in Fig. B.1 (lower). The intrinsic k_T tune uncertainty was estimated from the difference between the tune-up and -down variations, represented as the violet band in Fig. B.1 (lower). Compared with the UE tune uncertainty represented by the red band, the impact of the intrinsic k_T variations on UE-sensitive observables is small. The results shown in Fig. B.1 imply that the parameter space for UE and intrinsic k_T can be factorized.

Besides the intrinsic k_T model, also the lower cutoff scale of initial state radiation (ISR) (SPACESHOWER:PT0REF in PYTHIA) affects the DY $p_T(\ell^+\ell^-)$ distribution, as indicated in the main text and shown in Fig. 5.6. However, the UE observables are sensitive to the ISR cutoff scale. The combined tune of the intrinsic k_T parameter and the cutoff scale of ISR to the DY $p_T(\ell^+\ell^-)$ distribution alters the UE observable, which is shown as the blue markers in Fig. B.1 (lower). To decouple the intrinsic k_T study from the UE modeling when investigating its scaling behavior with the collision energy and hard-scattering scale, the parameter for the ISR cutoff is fixed to its default value in the studies shown in Figs. 5.5 and 5.7.

In summary, the study assesses the mutual impacts of the variation of the intrinsic k_T tune on the UE, and that of the UE tune on the DY transverse momentum, and concludes that the impacts are negligible, which supports our approach of tuning the intrinsic k_T parameters with

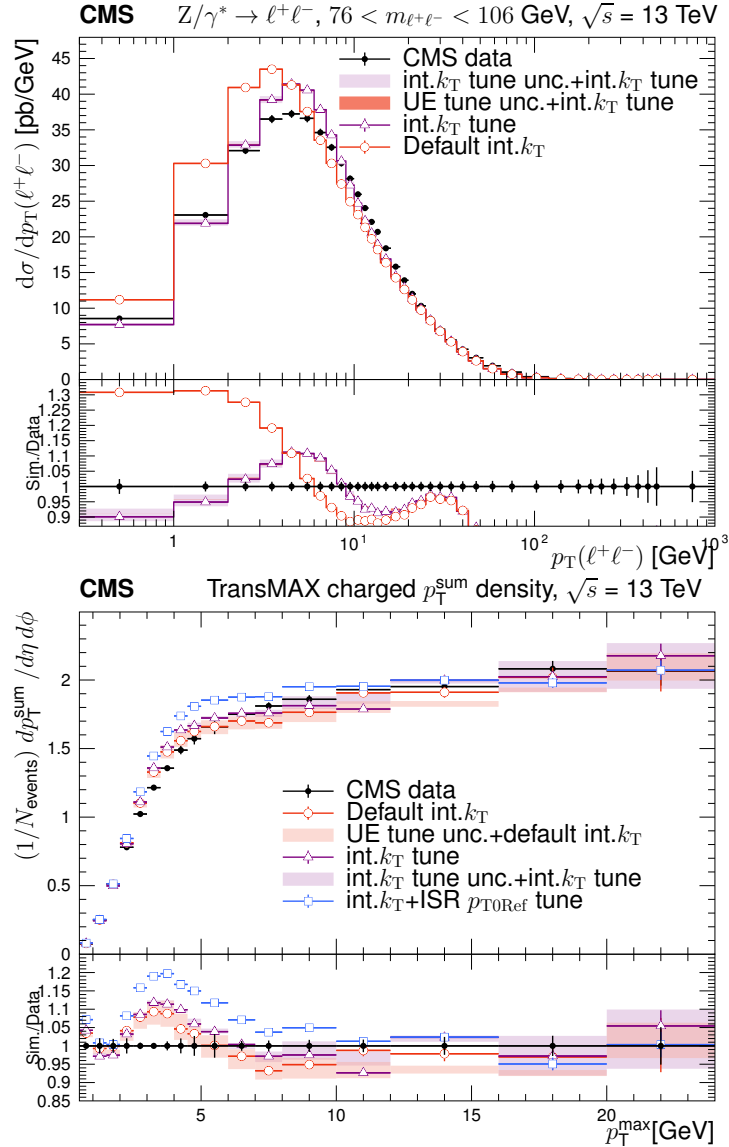


Figure B.1: Effects of the variation of the UE parameters on the DY $p_T(\ell^+\ell^-)$ spectrum (up), and of the variation of the intrinsic k_T parameter on the density of the scalar sum of the charged-particle transverse momenta (p_T^{sum}) on the rapidity (η) - azimuthal angle (ϕ) space as a function of the transverse momentum of the leading charged particle (p_T^{max}) in the transMAX region averaged over N_{events} generated events [221] in the minimum bias (MB) process (down), which is one of the observables used for UE tuning. For each event, the transMAX region is defined by the direction of the leading charged particle in the space transverse to the proton beams. Assuming ϕ as the azimuthal angle of the leading charged particle, the ranges of ϕ_1 satisfying $60^\circ < |\phi - \phi_1| < 120^\circ$ define the two transverse regions, in which transMAX is the one with a higher activity. The red and violet shaded areas represent the predictions from the up and down variations of the UE tune and the intrinsic k_T tune, respectively. In the upper plot, both shaded areas are based on the prediction of tuned intrinsic k_T parameter on top of PYTHIA CP5 (“int. k_T tune”). In the lower plot, the red shaded area is based on the prediction of the intrinsic k_T parameter set to the default 1.8 and the UE tune set to PYTHIA CP5 (“Default int. k_T ”), while the violet shaded area is based on the “int. k_T tune” prediction. The error bars represent the statistical uncertainty in the simulated events. The upper distribution also includes the UE prediction of the combined tune of the intrinsic k_T and the ISR cutoff scale to the DY $p_T(\ell^+\ell^-)$ distribution (“int. k_T +ISR $p_{T0\text{Ref}}$ tune”).

fixed UE parameters.

B.2 Validation of the tunes

B.3 Tuning results

Table B.1 gives the tuning results shown in Fig. 5.5. Tables B.2 and B.3 give the tuning results corresponding to the entries “CP5 SpaceShower:pT0Ref = 1 GeV” and “CH3 Sudakov-Common:pTmin = 0.7 GeV” in Fig. 5.6, respectively. Table B.4 gives the tuning results shown in Fig. 5.7.

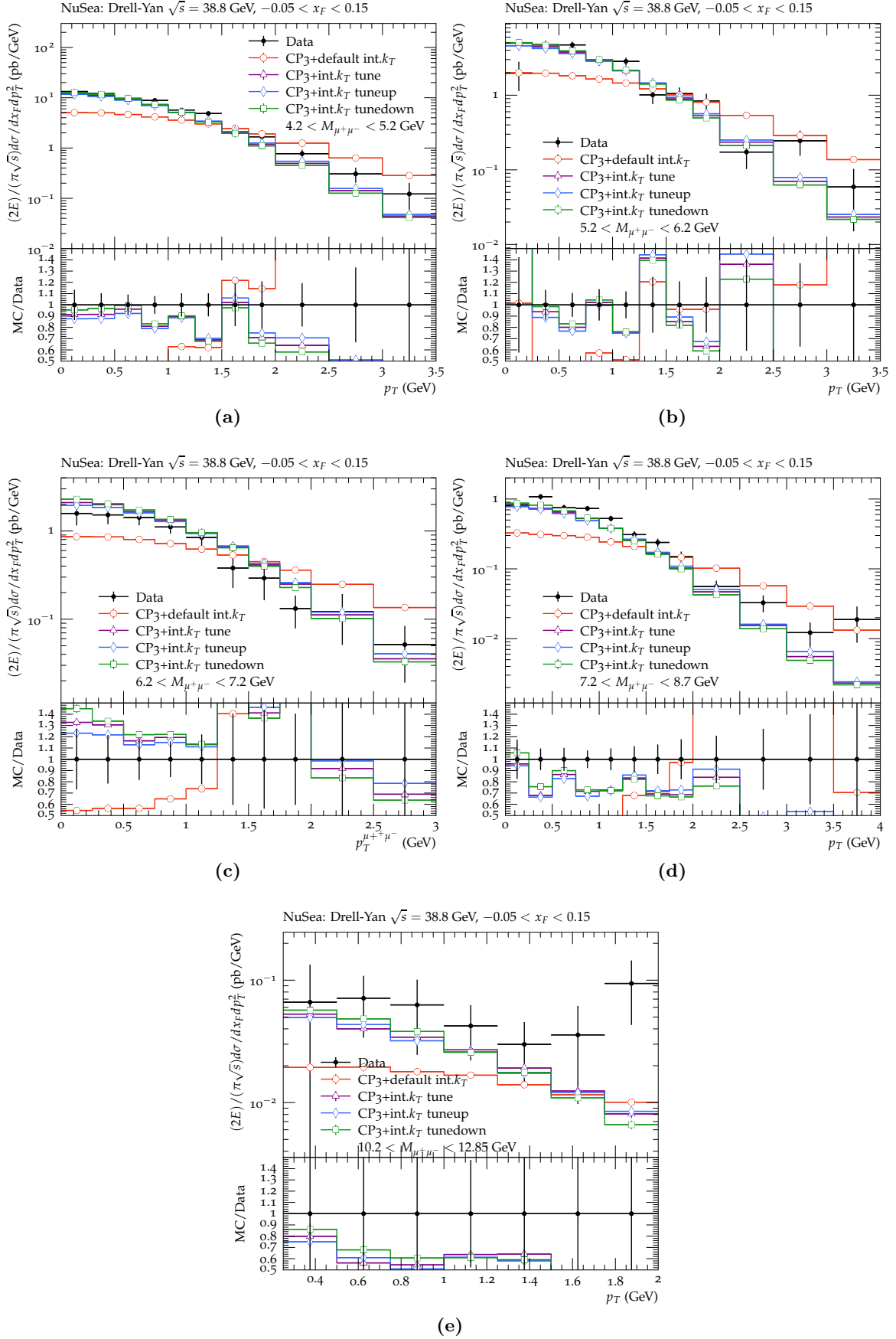


Figure B.2: The predictions of the intrinsic k_T tunes of the Drell-Yan $p_T(\ell^+\ell^-)$ under PYTHIA CP3 tune at 38.8 GeV.

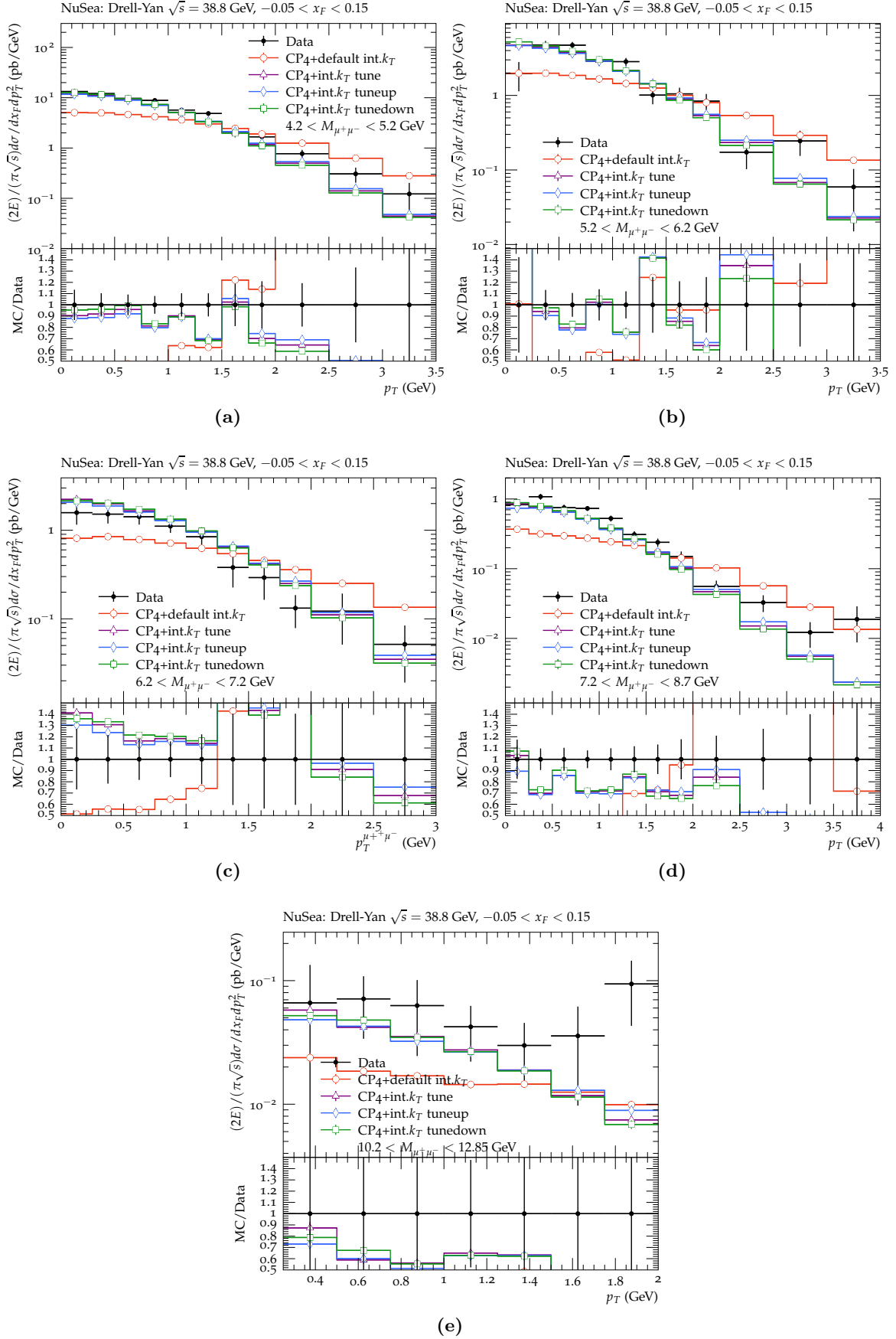


Figure B.3: The predictions of the intrinsic k_T tunes of the Drell-Yan $p_T(\ell^+\ell^-)$ under PYTHIA CP4 tune at 38.8 GeV.

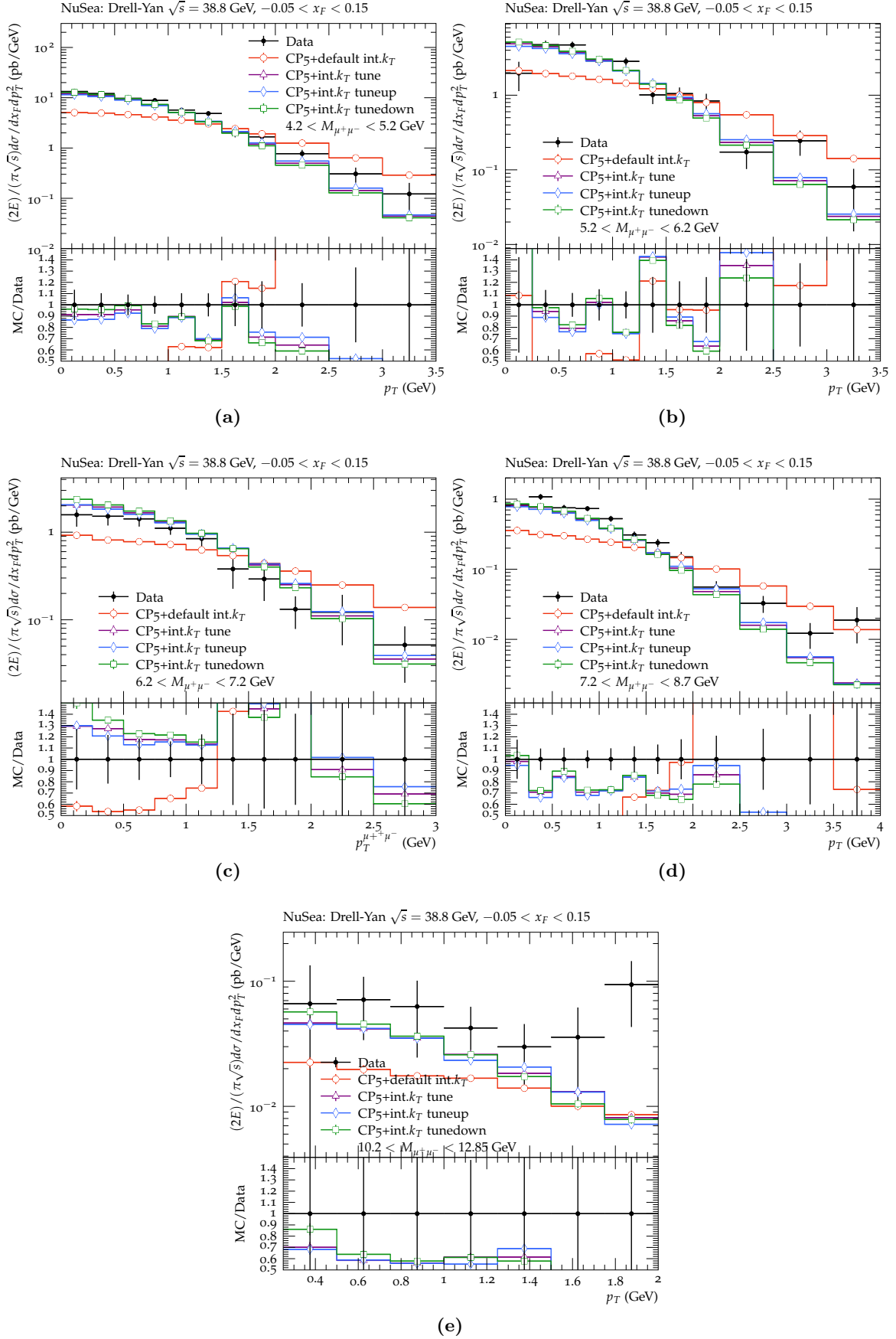


Figure B.4: The predictions of the intrinsic k_T tunes of the Drell-Yan $p_T(\ell^+\ell^-)$ under PYTHIA CP5 tune at 38.8 GeV.

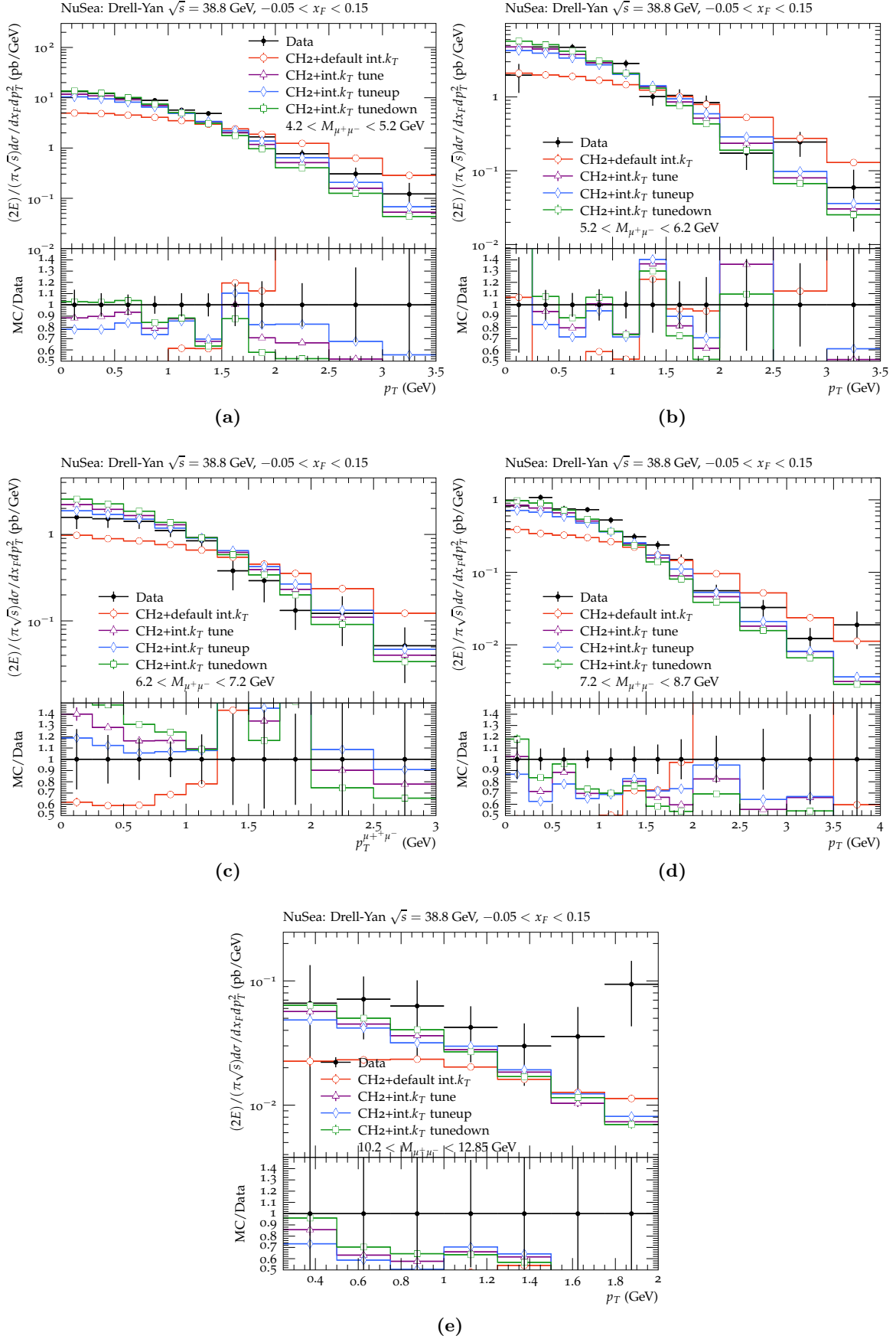


Figure B.5: The predictions of the intrinsic k_T tunes of the Drell-Yan $p_T(\ell^+\ell^-)$ under HERWIG CH2 tune at 38.8 GeV.

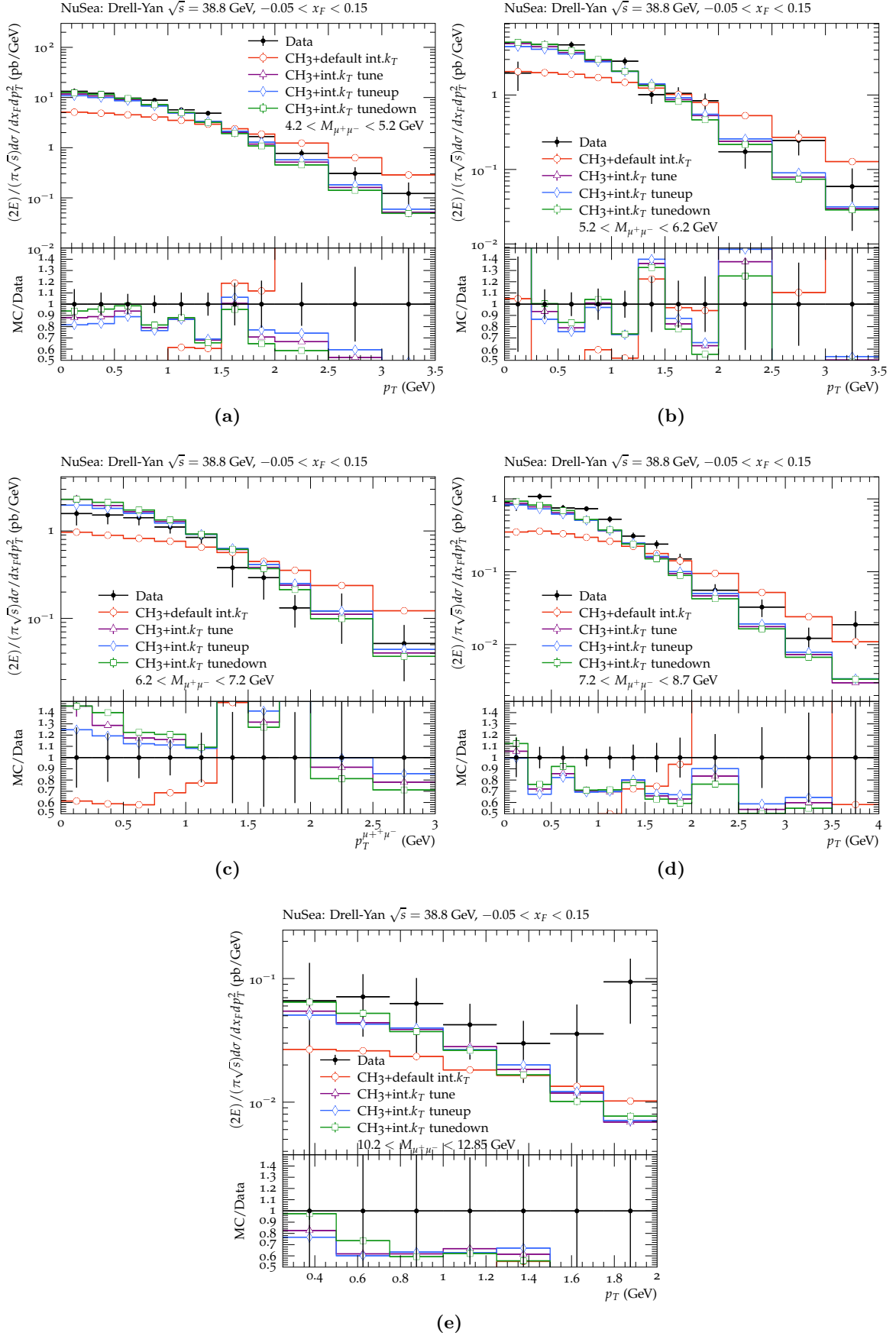


Figure B.6: The predictions of the intrinsic k_T tunes of the Drell-Yan $p_T(\ell^+\ell^-)$ under HERWIG CH3 tune at 38.8 GeV.

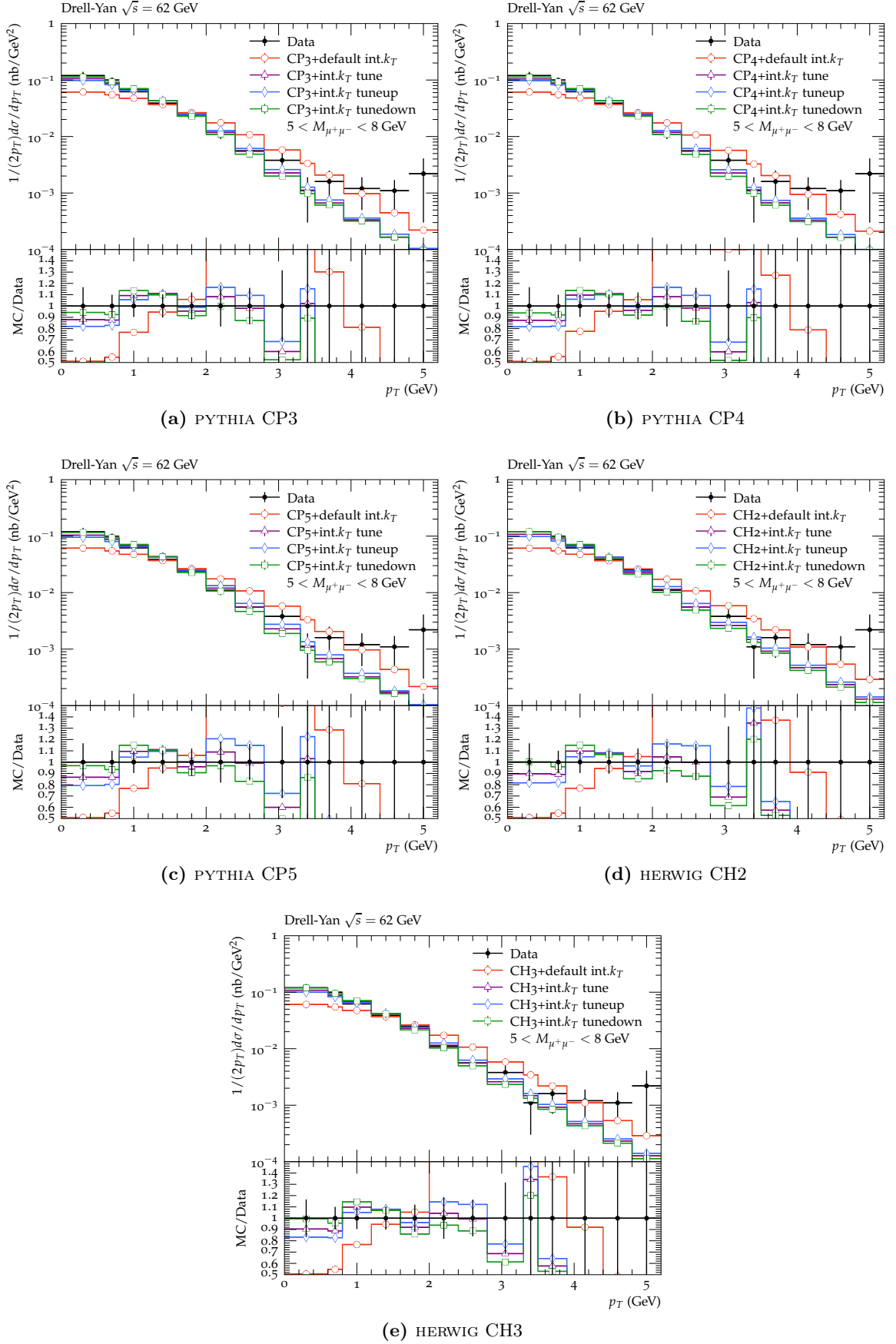


Figure B.7: The predictions of the intrinsic k_T tunes of the Drell-Yan $p_T(\ell^+\ell^-)$ under CP3, CP4 or CP5 tunes in PYTHIA or CH2, CH3 tunes in HERWIG at 62 GeV.

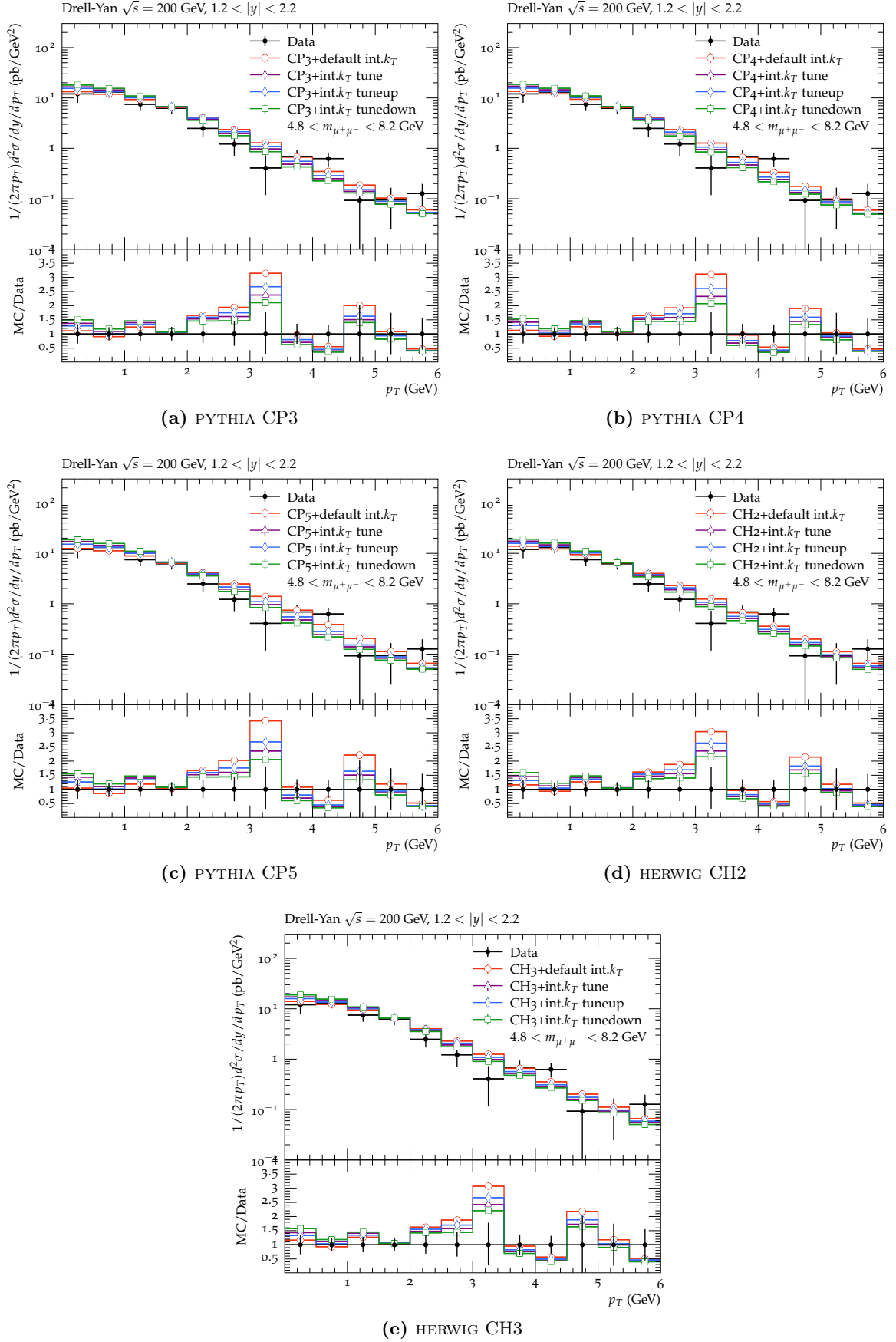


Figure B.8: The predictions of the intrinsic k_T tunes of the Drell-Yan $p_T(\ell^+\ell^-)$ under CP3, CP4 or CP5 tunes in PYTHIA or CH2, CH3 tunes in HERWIG at 200 GeV.

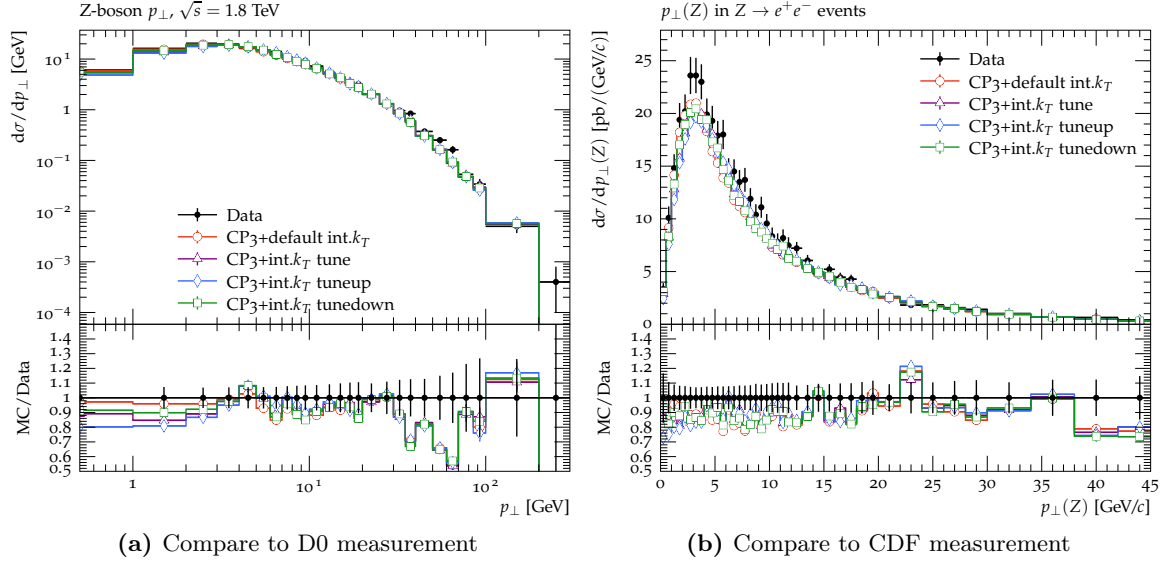


Figure B.9: The predictions of the intrinsic k_T tunes of the Drell-Yan $p_T(\ell^+\ell^-)$ under PYTHIA CP3 tune at 1.8 TeV.

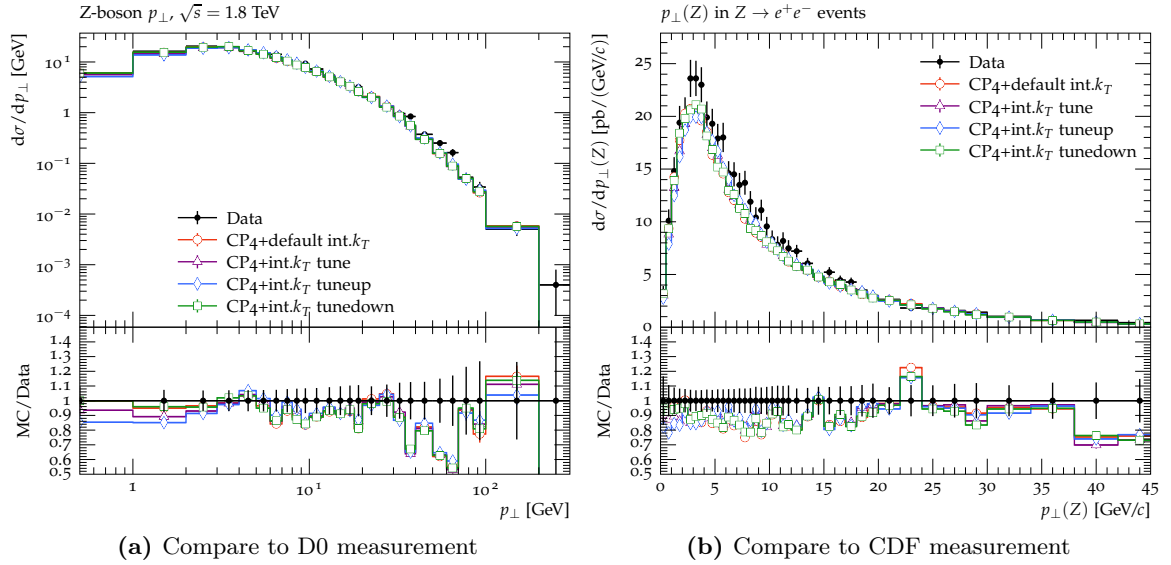


Figure B.10: The predictions of the intrinsic k_T tunes of the Drell-Yan $p_T(\ell^+\ell^-)$ under PYTHIA CP4 tune at 1.8 TeV.

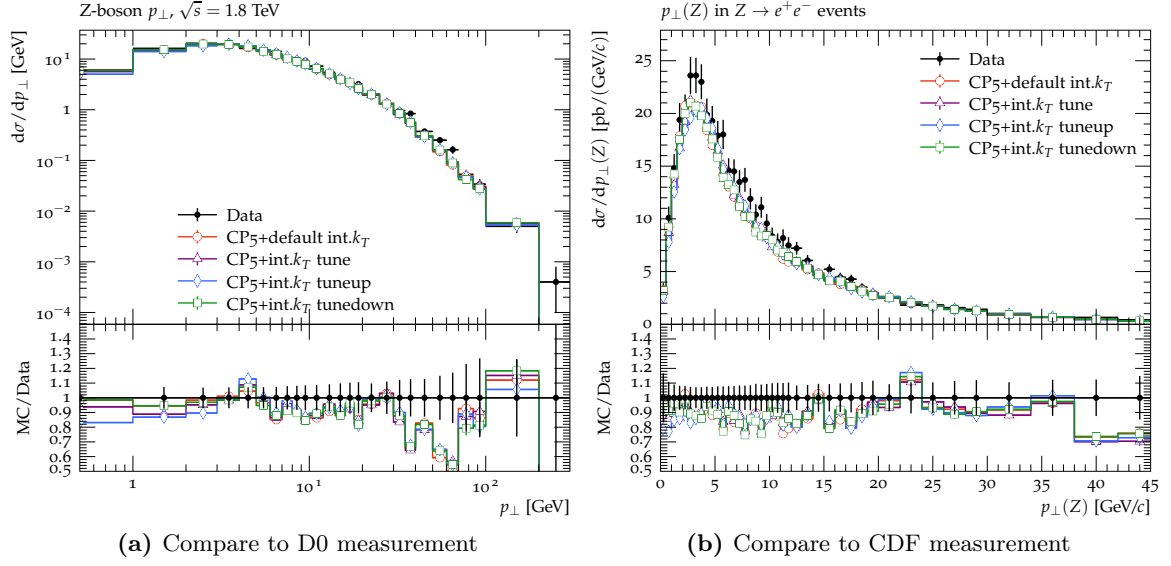


Figure B.11: The predictions of the intrinsic k_T tunes of the Drell-Yan $p_T(\ell^+\ell^-)$ under PYTHIA CP5 tune at 1.8 TeV.

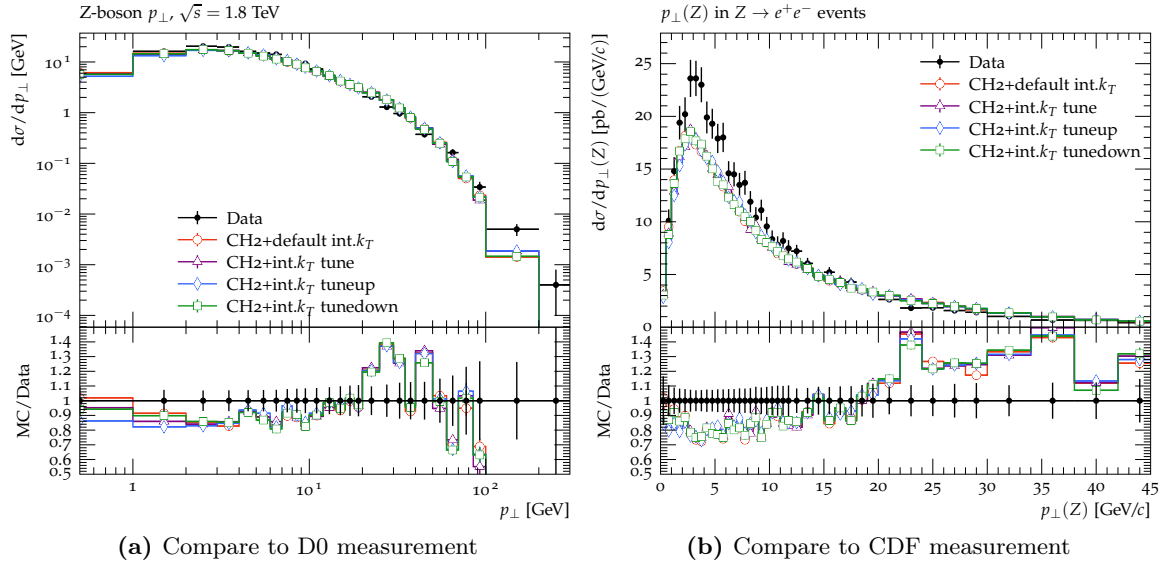


Figure B.12: The predictions of the intrinsic k_T tunes of the Drell-Yan $p_T(\ell^+\ell^-)$ under HERWIG CH2 tune at 1.8 TeV.

Table B.1: Tune results for the BEAMREMNANTS:PRIMORDIALKTHARD parameter in PYTHIA 8 and the SHOWERHANDLER:INTRINSICPTGAUSSIAN parameter in HERWIG 7, taking into account the uncertainty from tune ranges (range) and the functions for interpolation (int.).

| \sqrt{s} | Generator setup | Tune result \pm MC stat. \pm data unc. \pm range \pm int. |
|------------------|-----------------|---|
| 38.8 GeV | PYTHIA 8 CP5 | $0.988 \pm 0.0008 \pm 0.029 \pm 0.022 \pm 0.015$ |
| | PYTHIA 8 CP4 | $0.993 \pm 0.0008 \pm 0.029 \pm 0.017 \pm 0.009$ |
| | PYTHIA 8 CP3 | $0.990 \pm 0.004 \pm 0.03 \pm 0.017 \pm 0.020$ |
| | HERWIG 7 CH2 | $0.829 \pm 0.0005 \pm 0.017 \pm 0.010 \pm 0.06$ |
| | HERWIG 7 CH3 | $0.830 \pm 0.0005 \pm 0.017 \pm 0.010 \pm 0.026$ |
| 62 GeV | PYTHIA 8 CP5 | $1.24 \pm 0.0008 \pm 0.07 \pm 0.0015 \pm 0.06$ |
| | PYTHIA 8 CP4 | $1.24 \pm 4 \times 10^{-8} \pm 0.06 \pm 0.0012 \pm 0.006$ |
| | PYTHIA 8 CP3 | $1.23 \pm 0.0009 \pm 0.06 \pm 0.0010 \pm 0.012$ |
| | HERWIG 7 CH2 | $0.94 \pm 0.0006 \pm 0.05 \pm 0.0012 \pm 0.024$ |
| | HERWIG 7 CH3 | $0.93 \pm 0.0006 \pm 0.04 \pm 0.0014 \pm 0.019$ |
| 200 GeV | PYTHIA 8 CP5 | $1.47 \pm 0.0022 \pm 0.08 \pm 0.005 \pm 0.06$ |
| | PYTHIA 8 CP4 | $1.54 \pm 0.0024 \pm 0.09 \pm 0.003 \pm 0.004$ |
| | PYTHIA 8 CP3 | $1.54 \pm 0.0024 \pm 0.09 \pm 0.003 \pm 0.022$ |
| | HERWIG 7 CH2 | $1.14 \pm 0.0014 \pm 0.06 \pm 0.003 \pm 0.018$ |
| | HERWIG 7 CH3 | $1.15 \pm 0.0015 \pm 0.06 \pm 0.005 \pm 0.004$ |
| 1.8 TeV | PYTHIA 8 CP5 | $1.93 \pm 0.012 \pm 0.11 \pm 0.02 \pm 0.015$ |
| | PYTHIA 8 CP4 | $1.94 \pm 0.013 \pm 0.12 \pm 0.04 \pm 0.0005$ |
| | PYTHIA 8 CP3 | $2.09 \pm 0.013 \pm 0.12 \pm 0.03 \pm 0.007$ |
| | HERWIG 7 CH2 | $1.52 \pm 0.014 \pm 0.12 \pm 0.03 \pm 0.0024$ |
| | HERWIG 7 CH3 | $1.52 \pm 0.014 \pm 0.13 \pm 0.03 \pm 0.010$ |
| 1.96 TeV | PYTHIA 8 CP5 | $1.88 \pm 0.017 \pm 0.08 \pm 0.10 \pm 0.009$ |
| | PYTHIA 8 CP4 | $1.93 \pm 0.018 \pm 0.08 \pm 0.03 \pm 0.009$ |
| | PYTHIA 8 CP3 | $2.03 \pm 0.019 \pm 0.08 \pm 0.03 \pm 0.008$ |
| | HERWIG 7 CH2 | $1.41 \pm 0.023 \pm 0.10 \pm 0.08 \pm 0.0019$ |
| | HERWIG 7 CH3 | $1.42 \pm 0.021 \pm 0.09 \pm 0.024 \pm 0.021$ |
| 2.76 TeV | PYTHIA 8 CP5 | $2.36 \pm 0.022 \pm 0.3 \pm 0.005 \pm 0.005$ |
| | PYTHIA 8 CP4 | $2.39 \pm 0.020 \pm 0.3 \pm 0.024 \pm 0.013$ |
| | PYTHIA 8 CP3 | $2.35 \pm 0.023 \pm 0.3 \pm 0.004 \pm 0.007$ |
| | HERWIG 7 CH2 | $1.87 \pm 0.03 \pm 0.5 \pm 0.06 \pm 0.003$ |
| | HERWIG 7 CH3 | $1.9 \pm 0.03 \pm 0.4 \pm 0.18 \pm 0.018$ |
| 8 TeV | PYTHIA 8 CP5 | $2.64 \pm 0.006 \pm 0.0251 \pm 0.06 \pm 0.0016$ |
| | PYTHIA 8 CP4 | $2.62 \pm 0.008 \pm 0.022 \pm 0.04 \pm 0.006$ |
| | PYTHIA 8 CP3 | $2.50 \pm 0.008 \pm 0.012 \pm 0.03 \pm 0.026$ |
| | HERWIG 7 CH2 | $1.89 \pm 0.008 \pm 0.015 \pm 0.05 \pm 0.007$ |
| | HERWIG 7 CH3 | $1.89 \pm 0.007 \pm 0.009 \pm 0.05 \pm 0.007$ |
| 8.16 TeV | PYTHIA 8 CP5 | $2.66 \pm 0.029 \pm 0.14 \pm 0.02 \pm 0.015$ |
| | PYTHIA 8 CP4 | $2.63 \pm 0.029 \pm 0.16 \pm 0.023 \pm 0.013$ |
| | PYTHIA 8 CP3 | $2.62 \pm 0.029 \pm 0.13 \pm 0.015 \pm 0.007$ |
| | HERWIG 7 CH2 | $1.96 \pm 0.03 \pm 0.19 \pm 0.06 \pm 0.027$ |
| | HERWIG 7 CH3 | $1.96 \pm 0.03 \pm 0.17 \pm 0.09 \pm 0.02$ |
| 13 TeV (CMS) | PYTHIA 8 CP5 | $2.648 \pm 0.006 \pm 0.027 \pm 0.028 \pm 0.04$ |
| | PYTHIA 8 CP4 | $2.654 \pm 0.006 \pm 0.027 \pm 0.08 \pm 0.004$ |
| | PYTHIA 8 CP3 | $2.619 \pm 0.006 \pm 0.028 \pm 0.05 \pm 0.009$ |
| | HERWIG 7 CH2 | $2.05 \pm 0.03 \pm 0.04 \pm 0.03 \pm 0.035$ |
| | HERWIG 7 CH3 | $2.03 \pm 0.03 \pm 0.04 \pm 0.021 \pm 0.010$ |
| 13 TeV (LHCb) | PYTHIA 8 CP5 | $2.66 \pm 0.009 \pm 0.06 \pm 0.13 \pm 0.0007$ |
| | PYTHIA 8 CP4 | $2.67 \pm 0.009 \pm 0.06 \pm 0.10 \pm 0.003$ |
| | PYTHIA 8 CP3 | $2.62 \pm 0.009 \pm 0.06 \pm 0.11 \pm 0.00007$ |
| | HERWIG 7 CH2 | $1.99 \pm 0.04 \pm 0.06 \pm 0.05 \pm 0.04$ |
| | HERWIG 7 CH3 | $1.99 \pm 0.06 \pm 0.14 \pm 0.16 \pm 0.06$ |

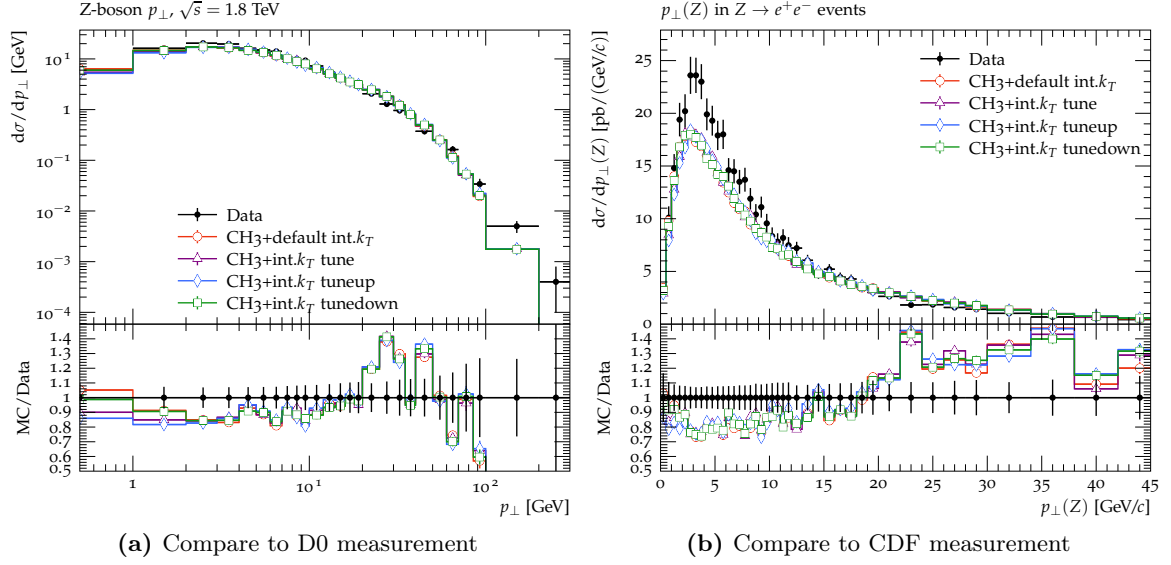


Figure B.13: The predictions of the intrinsic k_T tunes of the Drell-Yan $p_T(\ell^+\ell^-)$ under HERWIG CH3 tune at 1.8 TeV.

Table B.2: Tune results for the BEAMREMNANTS:PRIMORDIALKTHARD parameter in PYTHIA 8 with the CP5 tune setup. The parameter SPACESHOWER:PT0REF was set to 1 GeV.

| \sqrt{s} | Tune result \pm MC stat. \pm data unc. \pm range \pm int. |
|---------------|---|
| 38.8 GeV | $0.929 \pm 0.001 \pm 0.03 \pm 0.015 \pm 0.0005$ |
| 62 GeV | $1.16 \pm 1.8 \times 10^{-10} \pm 0.07 \pm 0.0014 \pm 0.00018$ |
| 200 GeV | $1.37 \pm 0.003 \pm 0.09 \pm 0.006 \pm 0.003$ |
| 1.8 TeV | $1.66 \pm 0.013 \pm 0.08 \pm 0.007 \pm 0.016$ |
| 1.96 TeV | $1.51 \pm 0.016 \pm 0.11 \pm 0.18 \pm 0.08$ |
| 2.76 TeV | $2.2 \pm 0.026 \pm 0.3 \pm 0.006 \pm 0.025$ |
| 8 TeV | $2.51 \pm 0.04 \pm 0.03 \pm 0.008 \pm 0.04$ |
| 8.16 TeV | $2.51 \pm 0.05 \pm 0.20 \pm 0.021 \pm 0.14$ |
| 13 TeV (CMS) | $2.54 \pm 0.008 \pm 0.04 \pm 0.09 \pm 0.0024$ |
| 13 TeV (LHCb) | $2.52 \pm 0.014 \pm 0.09 \pm 0.17 \pm 0.0021$ |

Table B.3: Tune results for the SHOWERHANDLER:INTRINSICPTGAUSSIAN parameter in HERWIG 7 with the CH3 tune setup. The parameter SUDAKOVCOMMON:PTMIN was set to 0.7 GeV.

| \sqrt{s} | Tune result \pm MC stat. \pm data unc. \pm range \pm int. |
|---------------|---|
| 38.8 GeV | $0.742 \pm 0.0010 \pm 0.024 \pm 0.0010 \pm 0.004$ |
| 62 GeV | $0.80 \pm 0.00021 \pm 0.04 \pm 0.0020 \pm 0.00024$ |
| 200 GeV | $1.00 \pm 0.0018 \pm 0.06 \pm 0.004 \pm 0.0023$ |
| 1.8 TeV | $1.16 \pm 0.024 \pm 0.18 \pm 0.06 \pm 0.07$ |
| 1.96 TeV | $0.95 \pm 0.025 \pm 0.10 \pm 0.012 \pm 0.005$ |
| 2.76 TeV | $1.60 \pm 0.018 \pm 0.23 \pm 0.10 \pm 0.24$ |
| 8 TeV | $1.395 \pm 0.07 \pm 0.17 \pm 0.14 \pm 0.08$ |
| 8.16 TeV | $1.47 \pm 0.028 \pm 0.17 \pm 0.03 \pm 0.04$ |
| 13 TeV (CMS) | $1.71 \pm 0.025 \pm 0.016 \pm 0.00017 \pm 0.07$ |
| 13 TeV (LHCb) | $1.60 \pm 0.06 \pm 0.08 \pm 0.13 \pm 0.05$ |

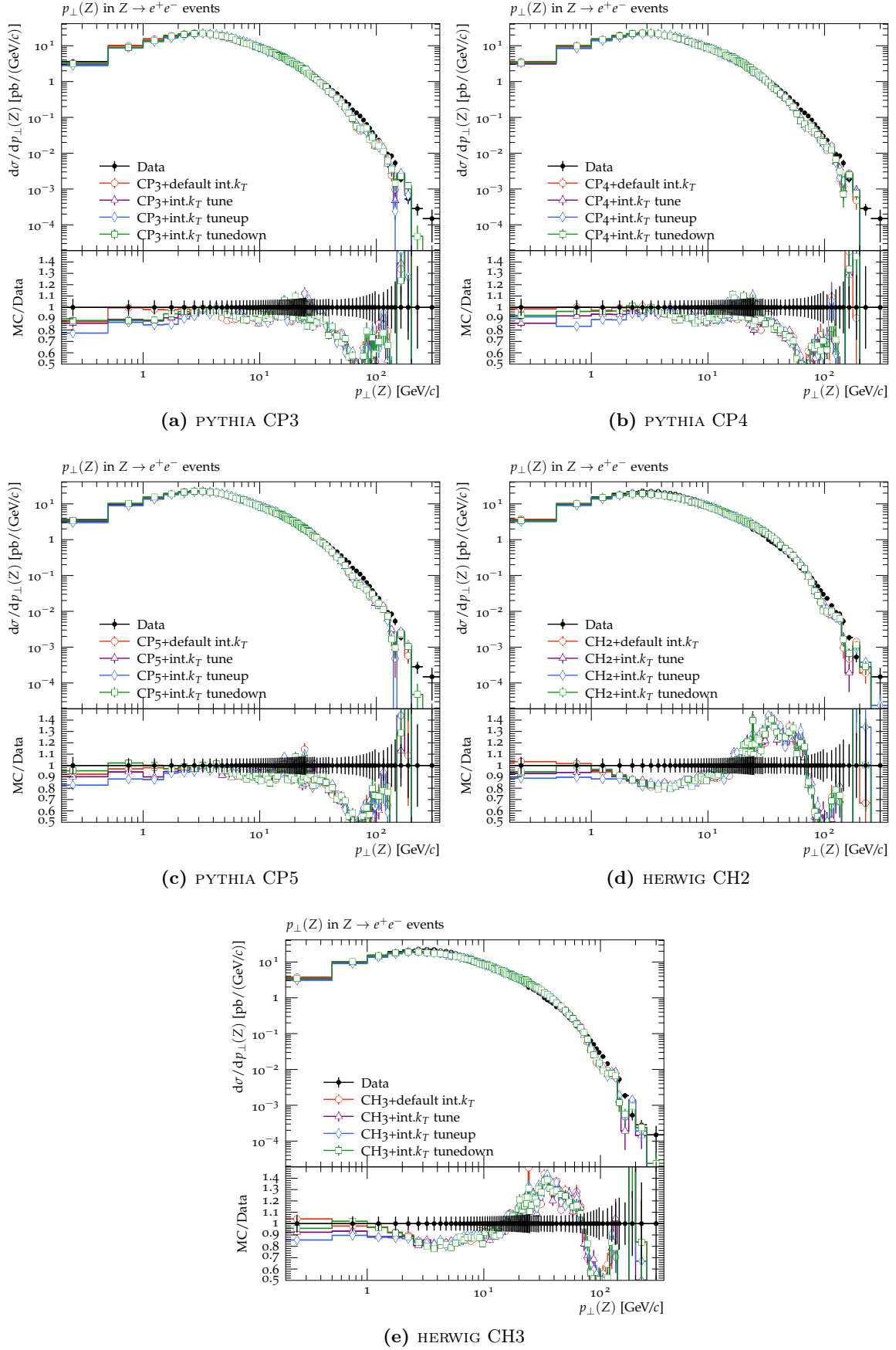


Figure B.14: The predictions of the intrinsic k_T tunes of the Drell-Yan $p_T(\ell^+\ell^-)$ under CP3, CP4 or CP5 tunes in PYTHIA or CH2, CH3 tunes in HERWIG at 1.96 TeV.

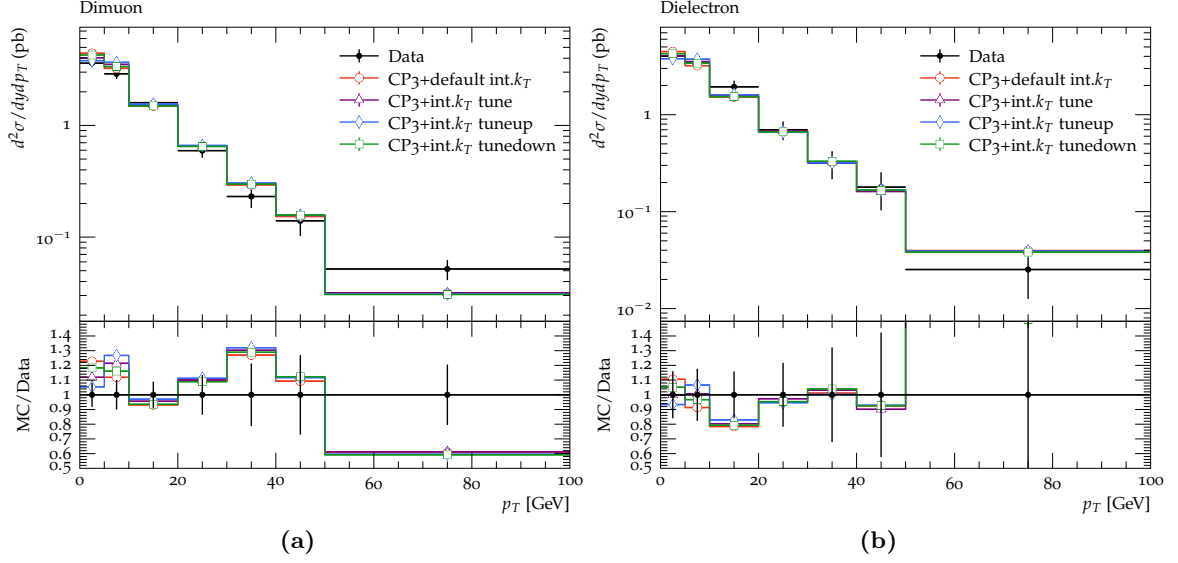


Figure B.15: The predictions of the intrinsic k_T tunes of the Drell-Yan $p_T(\ell^+\ell^-)$ under PYTHIA CP3 tune at 2.76 TeV.

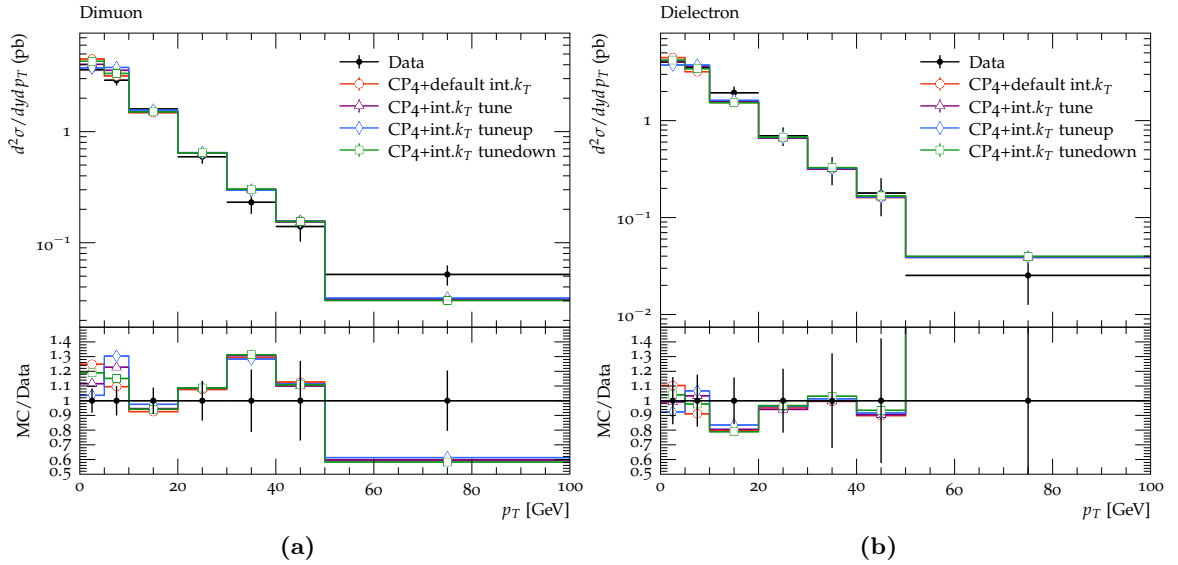


Figure B.16: The predictions of the intrinsic k_T tunes of the Drell-Yan $p_T(\ell^+\ell^-)$ under PYTHIA CP4 tune at 2.76 TeV.

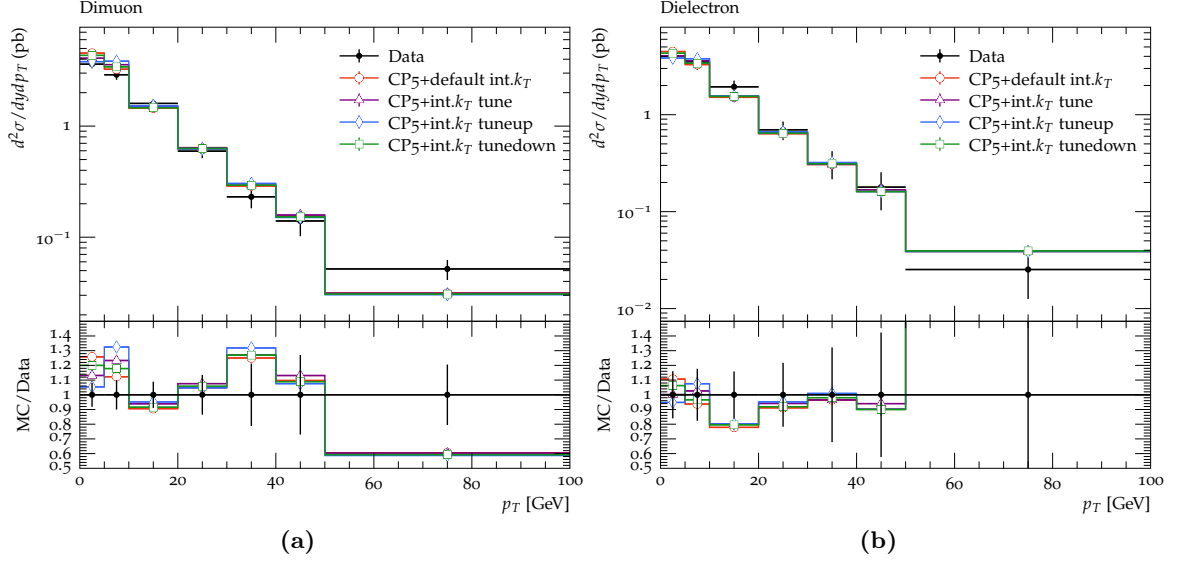


Figure B.17: The predictions of the intrinsic k_T tunes of the Drell–Yan $p_T(\ell^+\ell^-)$ under PYTHIA CP5 tune at 2.76 TeV.

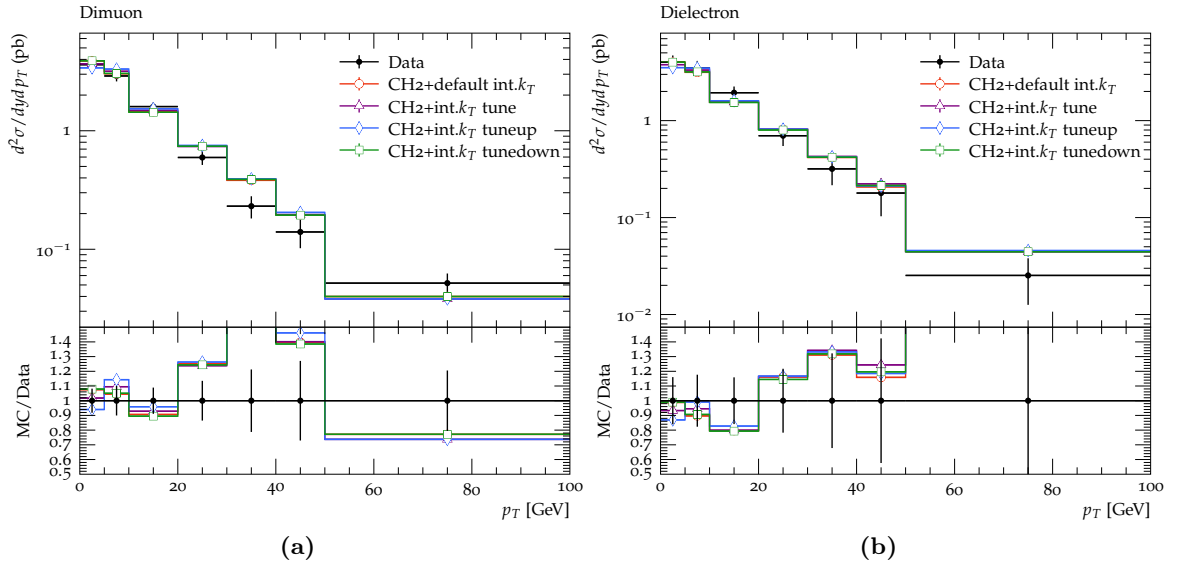


Figure B.18: The predictions of the intrinsic k_T tunes of the Drell–Yan $p_T(\ell^+\ell^-)$ under HERWIG CH2 tune at 2.76 TeV.

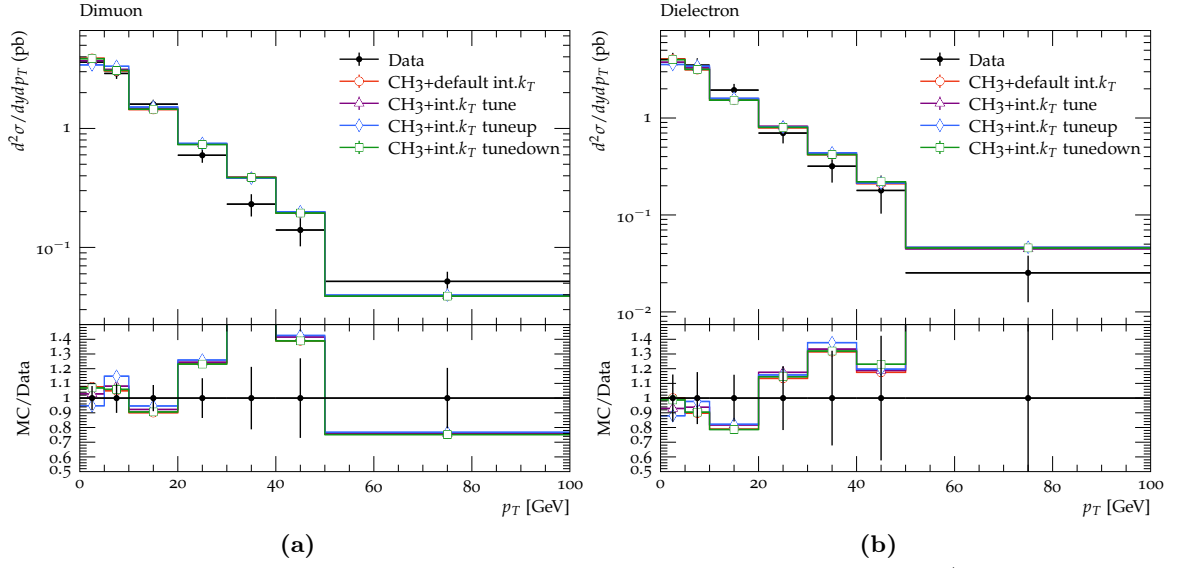


Figure B.19: The predictions of the intrinsic k_T tunes of the Drell-Yan $p_T(\ell^+\ell^-)$ under HERWIG CH3 tune at 2.76 TeV.

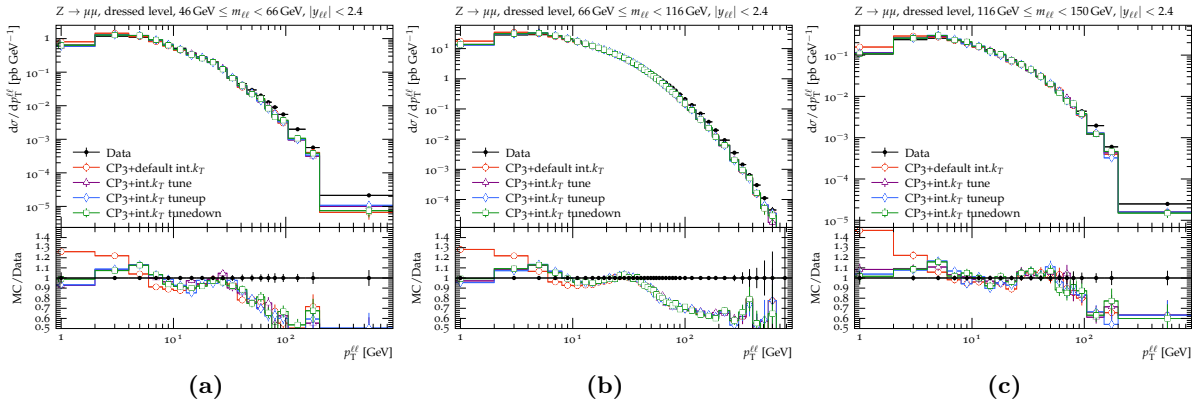


Figure B.20: The predictions of the intrinsic k_T tunes of the Drell-Yan $p_T(\ell^+\ell^-)$ under PYTHIA CP3 tune at 8 TeV.

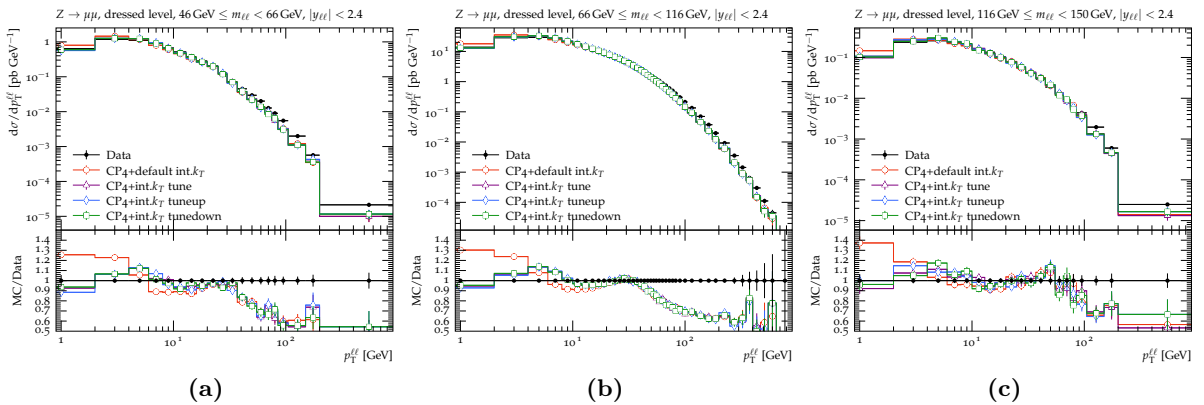


Figure B.21: The predictions of the intrinsic k_T tunes of the Drell-Yan $p_T(\ell^+\ell^-)$ under PYTHIA CP4 tune at 8 TeV.

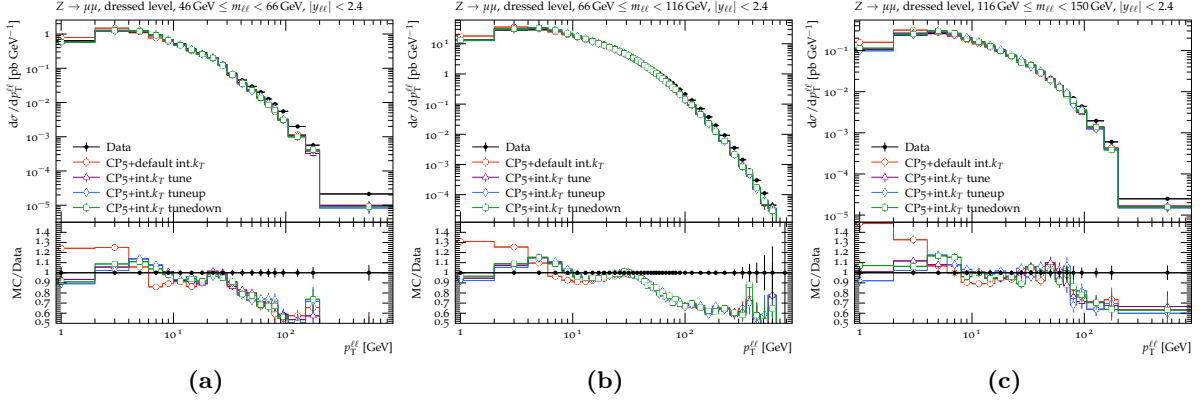


Figure B.22: The predictions of the intrinsic k_T tunes of the Drell-Yan $p_T(\ell^+\ell^-)$ under PYTHIA CP5 tune at 8 TeV.

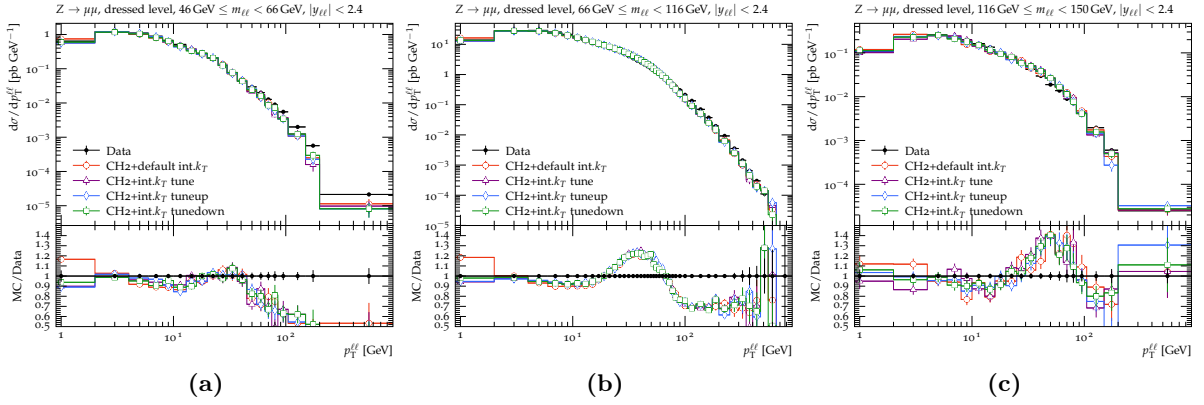


Figure B.23: The predictions of the intrinsic k_T tunes of the Drell-Yan $p_T(\ell^+\ell^-)$ under HERWIG CH2 tune at 8 TeV.

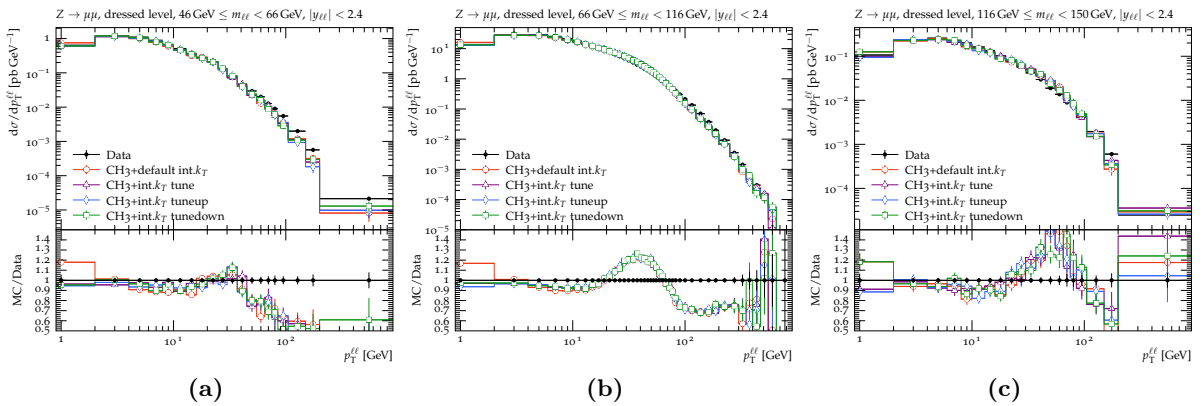


Figure B.24: The predictions of the intrinsic k_T tunes of the Drell-Yan $p_T(\ell^+\ell^-)$ under HERWIG CH3 tune at 8 TeV.

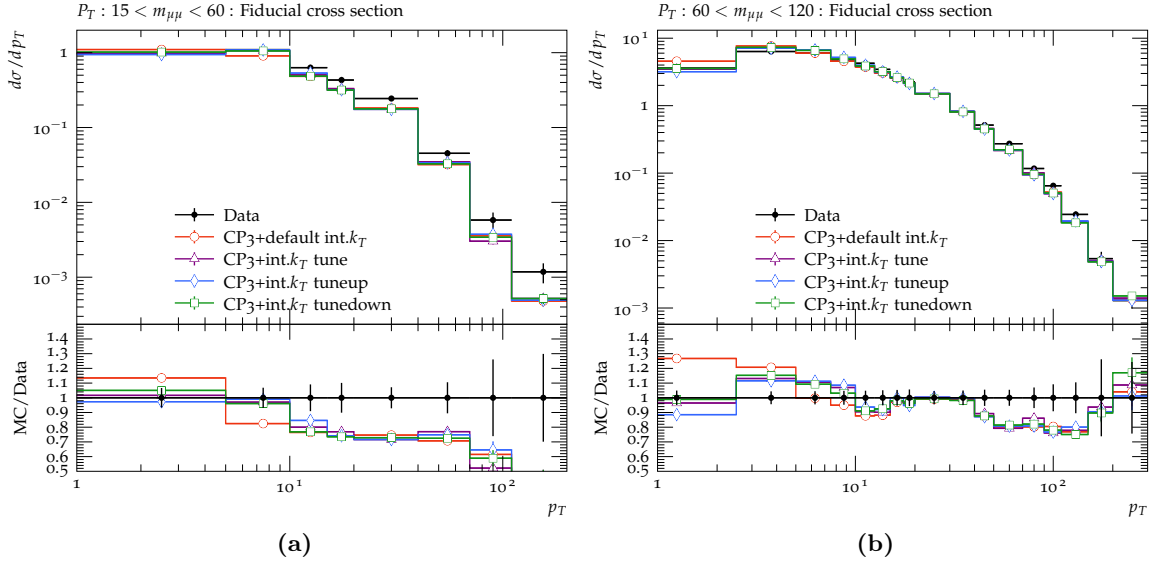


Figure B.25: The predictions of the intrinsic k_T tunes of the Drell-Yan $p_T(\ell^+\ell^-)$ under PYTHIA CP3 tune at 8.16 TeV.

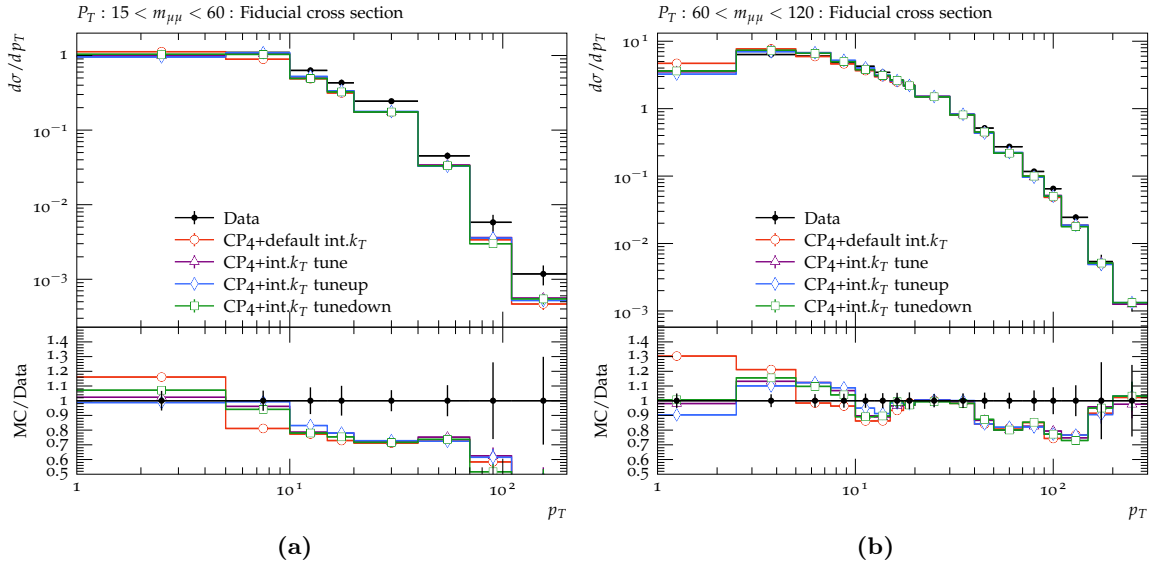


Figure B.26: The predictions of the intrinsic k_T tunes of the Drell-Yan $p_T(\ell^+\ell^-)$ under PYTHIA CP4 tune at 8.16 TeV.

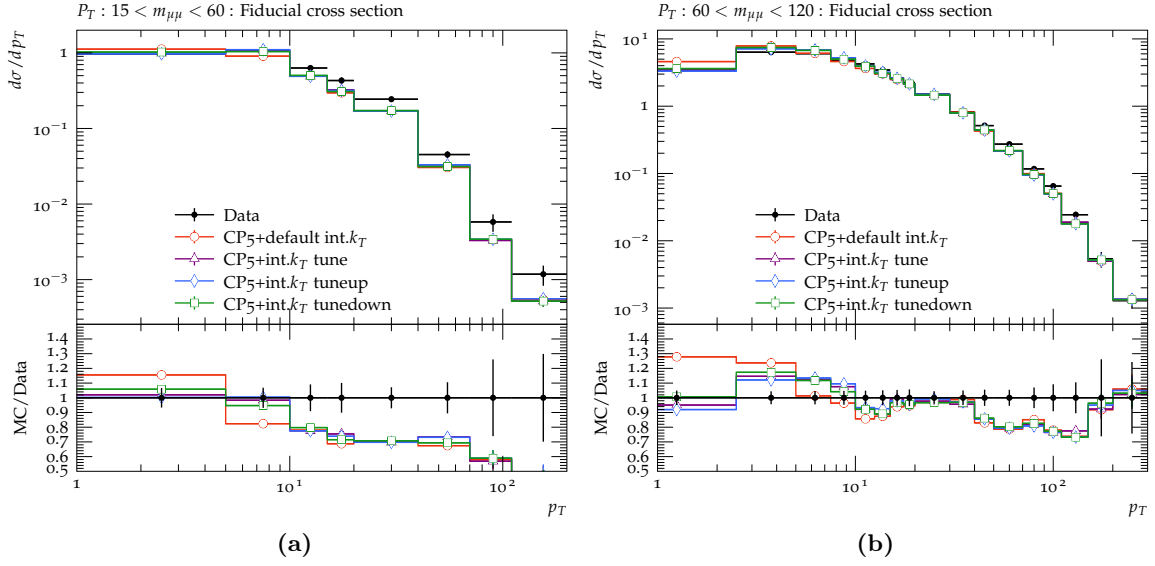


Figure B.27: The predictions of the intrinsic k_T tunes of the Drell-Yan $p_T(\ell^+\ell^-)$ under PYTHIA CP5 tune at 8.16 TeV.

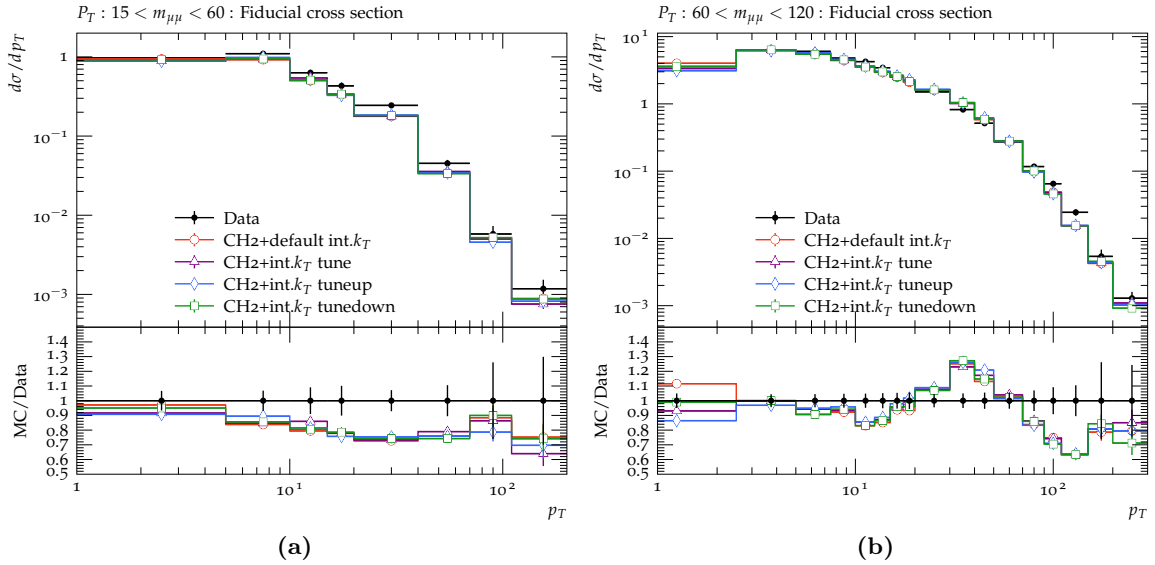


Figure B.28: The predictions of the intrinsic k_T tunes of the Drell-Yan $p_T(\ell^+\ell^-)$ under HERWIG CH2 tune at 8.16 TeV.

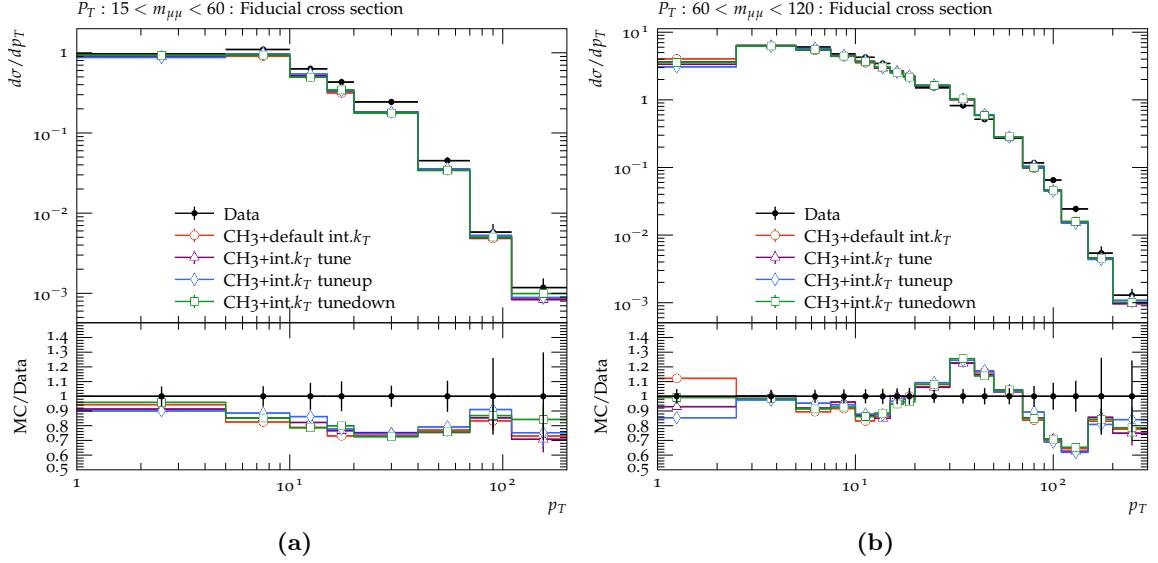


Figure B.29: The predictions of the intrinsic k_T tunes of the Drell-Yan $p_T(\ell^+\ell^-)$ under HERWIG CH3 tune at 8.16 TeV.

Table B.4: Results of the tune to various ranges of the $m_{\ell\ell}$ for values of \sqrt{s} of 38.8 GeV and 8, 8.16, and 13 TeV.

| \sqrt{s} | $m_{\ell\ell}$ range | Tune result \pm MC stat. and data unc. \pm range \pm int. | |
|------------|----------------------|---|------------------------------------|
| | | PYTHIA CP5 | HERWIG CH2 |
| 38.8 GeV | 4.2 – 5.2 GeV | $0.99 \pm 0.05 \pm 0.020 \pm 0.010$ | $0.82 \pm 0.03 \pm 0.011 \pm 0.05$ |
| | 5.2 – 6.2 GeV | $1.03 \pm 0.06 \pm 0.020 \pm 0.025$ | $0.85 \pm 0.03 \pm 0.010 \pm 0.09$ |
| | 6.2 – 7.2 GeV | $1.07 \pm 0.08 \pm 0.010 \pm 0.20$ | $0.88 \pm 0.05 \pm 0.010 \pm 0.11$ |
| | 7.2 – 8.7 GeV | $0.92 \pm 0.04 \pm 0.025 \pm 0.005$ | $0.80 \pm 0.03 \pm 0.016 \pm 0.05$ |
| | 10.2 – 12.85 GeV | $0.87 \pm 0.31 \pm 0.18 \pm 0.16$ | $0.81 \pm 0.23 \pm 0.09 \pm 0.06$ |
| 8 TeV | 46 – 66 GeV | $2.36 \pm 0.17 \pm 0.0016 \pm 0.05$ | $2.15 \pm 0.27 \pm 0.03 \pm 0.07$ |
| | 66 – 116 GeV | $2.51 \pm 0.07 \pm 0.017 \pm 0.05$ | $1.95 \pm 0.05 \pm 0.04 \pm 0.011$ |
| | 116 – 150 GeV | $2.70 \pm 0.33 \pm 0.13 \pm 0.17$ | $2.1 \pm 0.4 \pm 0.0005 \pm 0.006$ |
| 8.16 TeV | 15 – 60 GeV | $3.0 \pm 0.4 \pm 0.19 \pm 0.10$ | $2.2 \pm 0.3 \pm 0.10 \pm 0.11$ |
| | 60 – 120 GeV | $2.61 \pm 0.13 \pm 0.033 \pm 0.009$ | $1.89 \pm 0.18 \pm 0.08 \pm 0.003$ |
| 13 TeV | 50 – 76 GeV | $2.65 \pm 0.07 \pm 0.06 \pm 0.017$ | $1.91 \pm 0.14 \pm 0.02 \pm 0.007$ |
| | 76 – 106 GeV | $2.66 \pm 0.03 \pm 0.08 \pm 0.003$ | $2.05 \pm 0.05 \pm 0.02 \pm 0.01$ |
| | 106 – 170 GeV | $2.59 \pm 0.07 \pm 0.11 \pm 0.03$ | $2.34 \pm 0.23 \pm 0.07 \pm 0.16$ |
| | 170 – 350 GeV | $2.65 \pm 0.16 \pm 0.07 \pm 0.007$ | $1.90 \pm 0.16 \pm 0.16 \pm 0.02$ |
| | 350 – 1000 GeV | $2.17 \pm 0.4 \pm 0.018 \pm 0.017$ | $1.8 \pm 0.4 \pm 0.13 \pm 0.03$ |

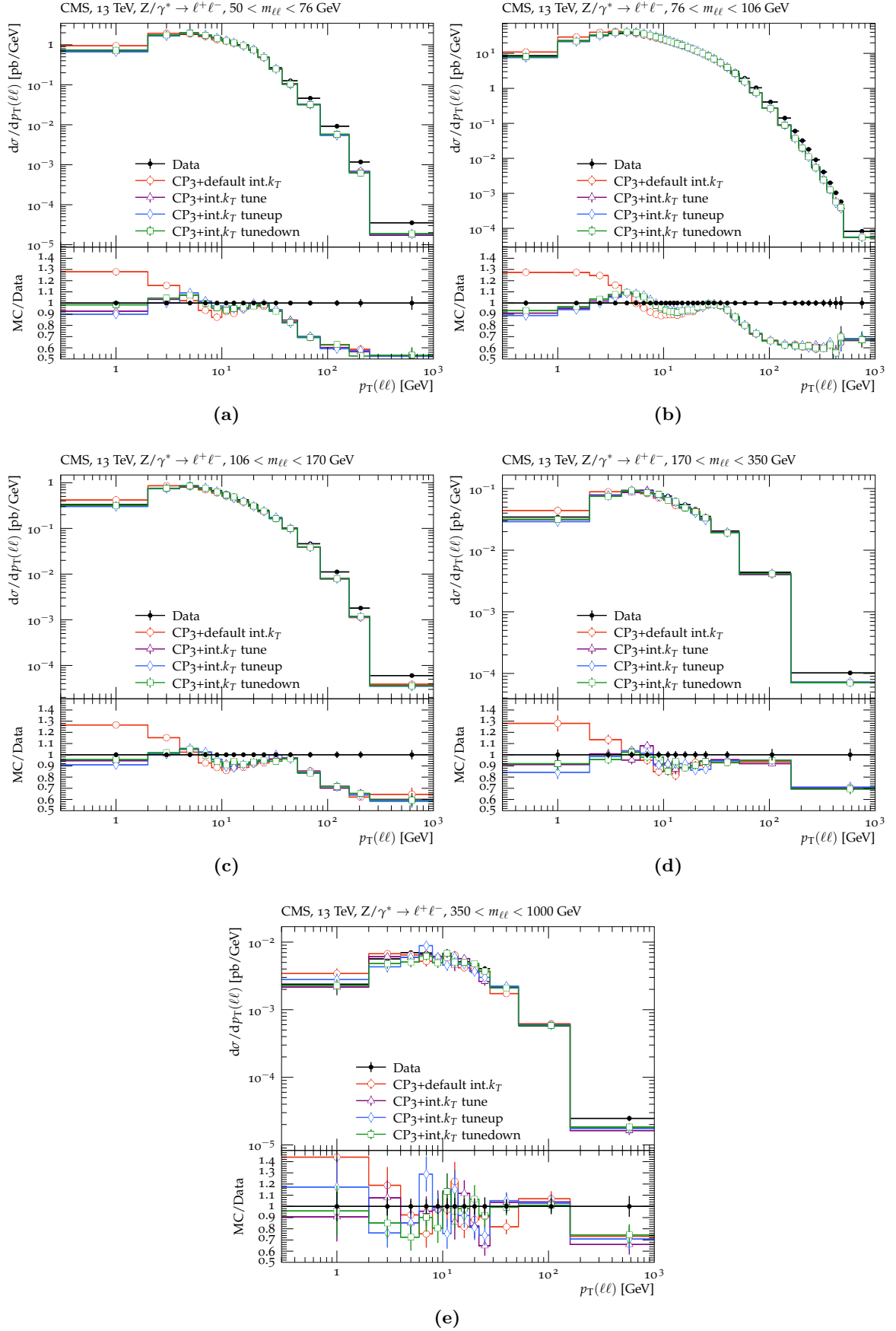


Figure B.30: The predictions of the intrinsic k_T tunes of the Drell-Yan $p_T(\ell^+\ell^-)$ under PYTHIA CP3 tune at 13 TeV compared to CMS measurement.

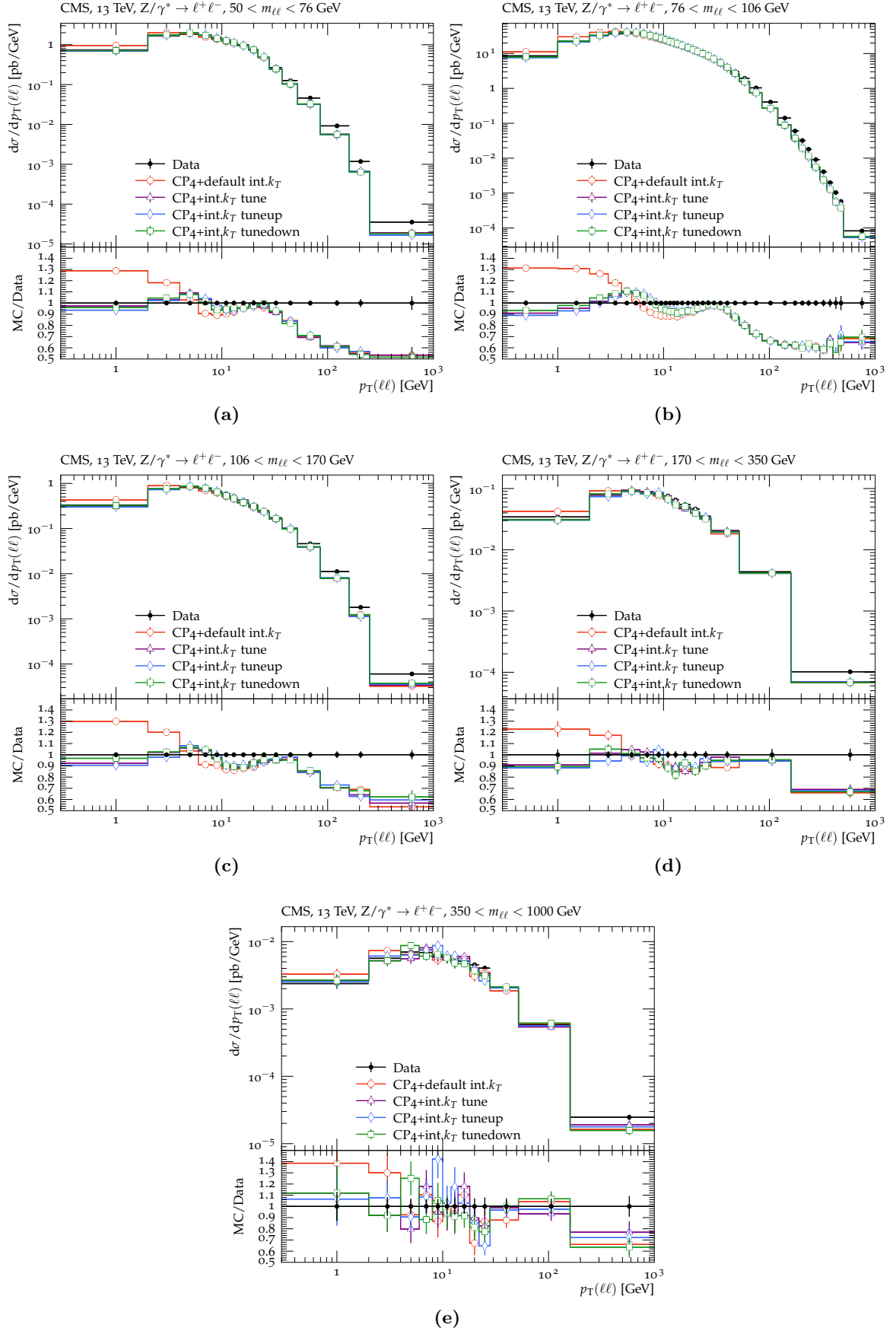


Figure B.31: The predictions of the intrinsic k_T tunes of the Drell-Yan $p_T(\ell^+\ell^-)$ under PYTHIA CP4 tune at 13 TeV compared to CMS measurement.

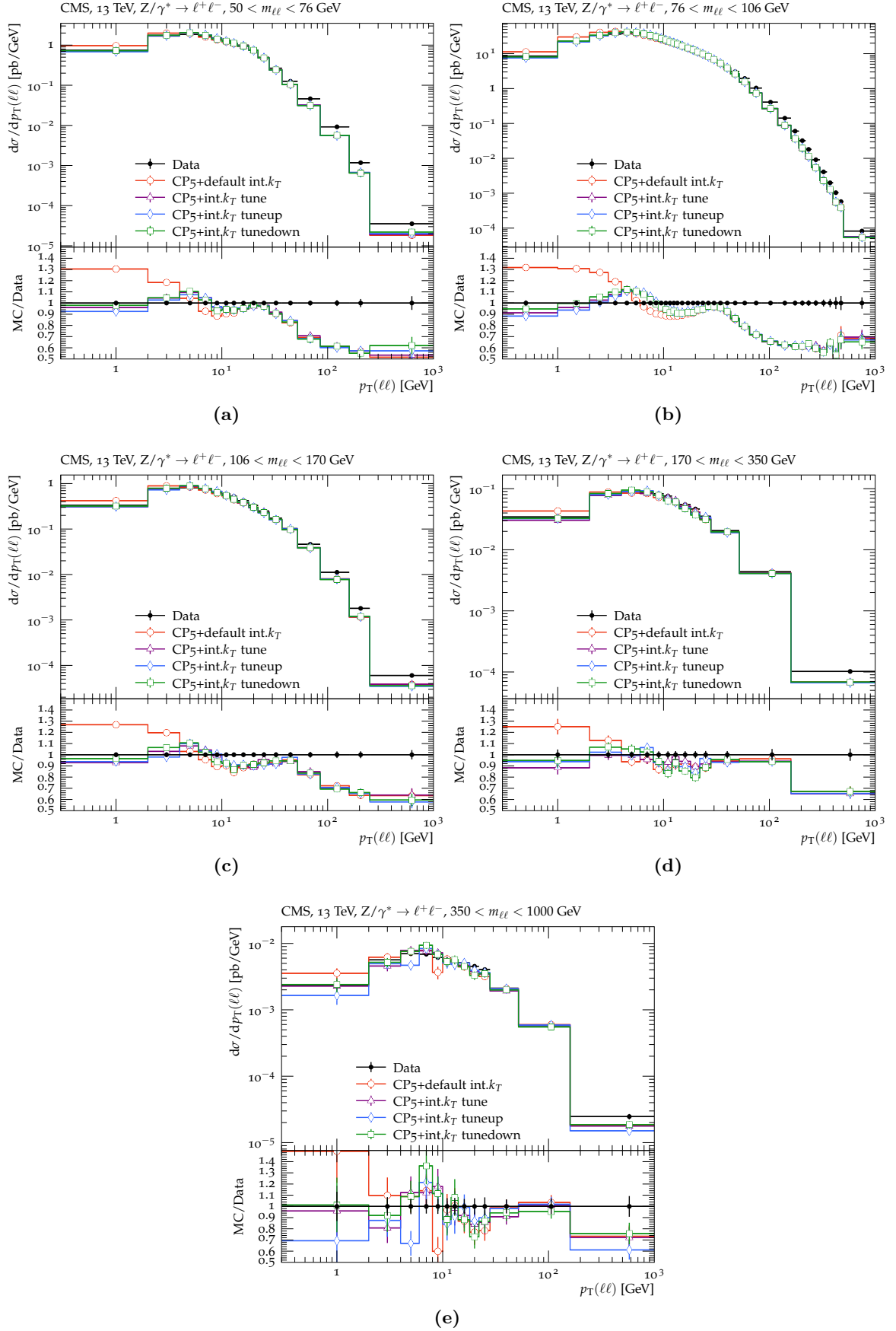


Figure B.32: The predictions of the intrinsic k_T tunes of the Drell-Yan $p_T(\ell^+\ell^-)$ under PYTHIA CP5 tune at 13 TeV compared to CMS measurement.

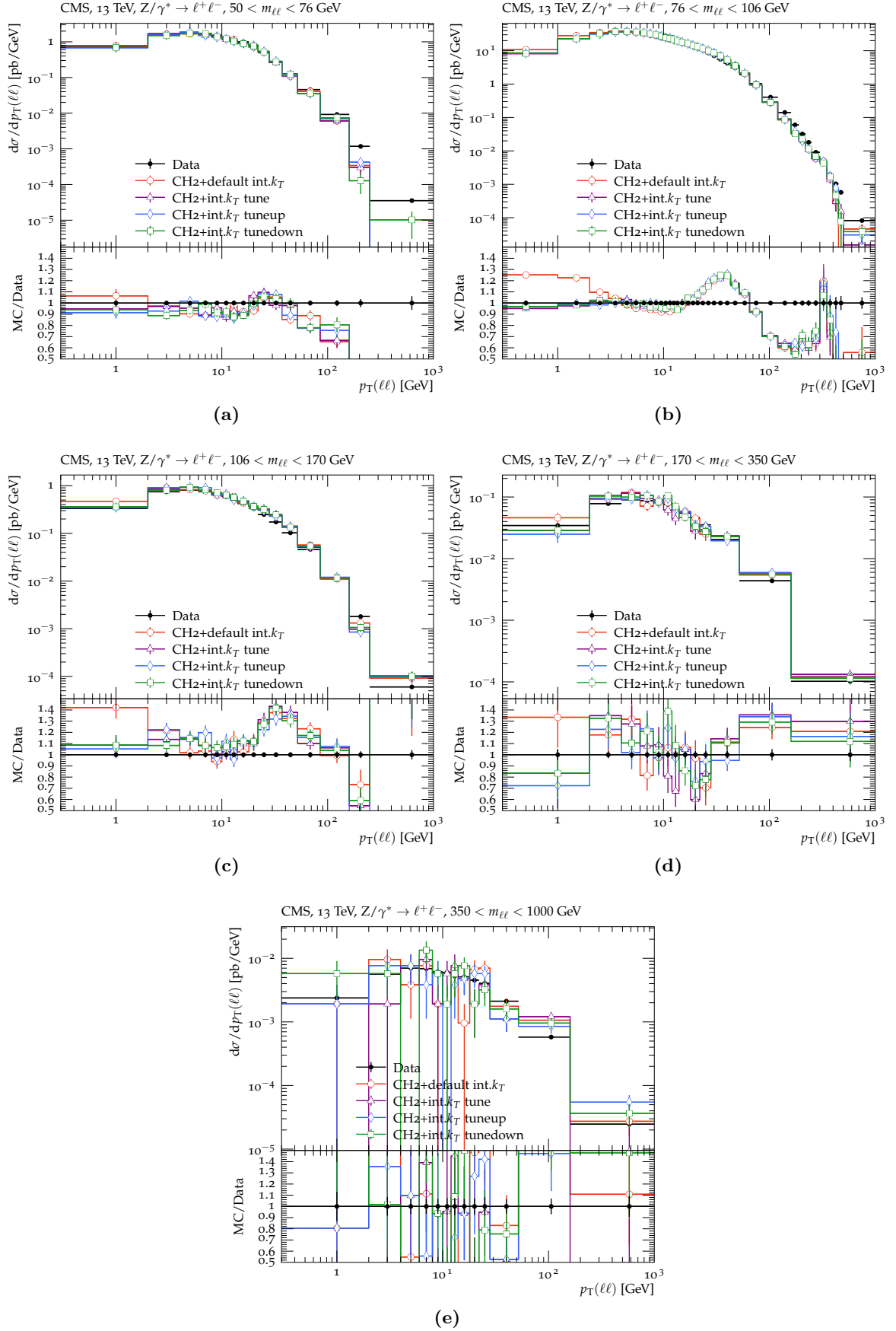


Figure B.33: The predictions of the intrinsic k_T tunes of the Drell-Yan $p_T(\ell^+\ell^-)$ under HERWIG CH2 tune at 13 TeV compared to CMS measurement.

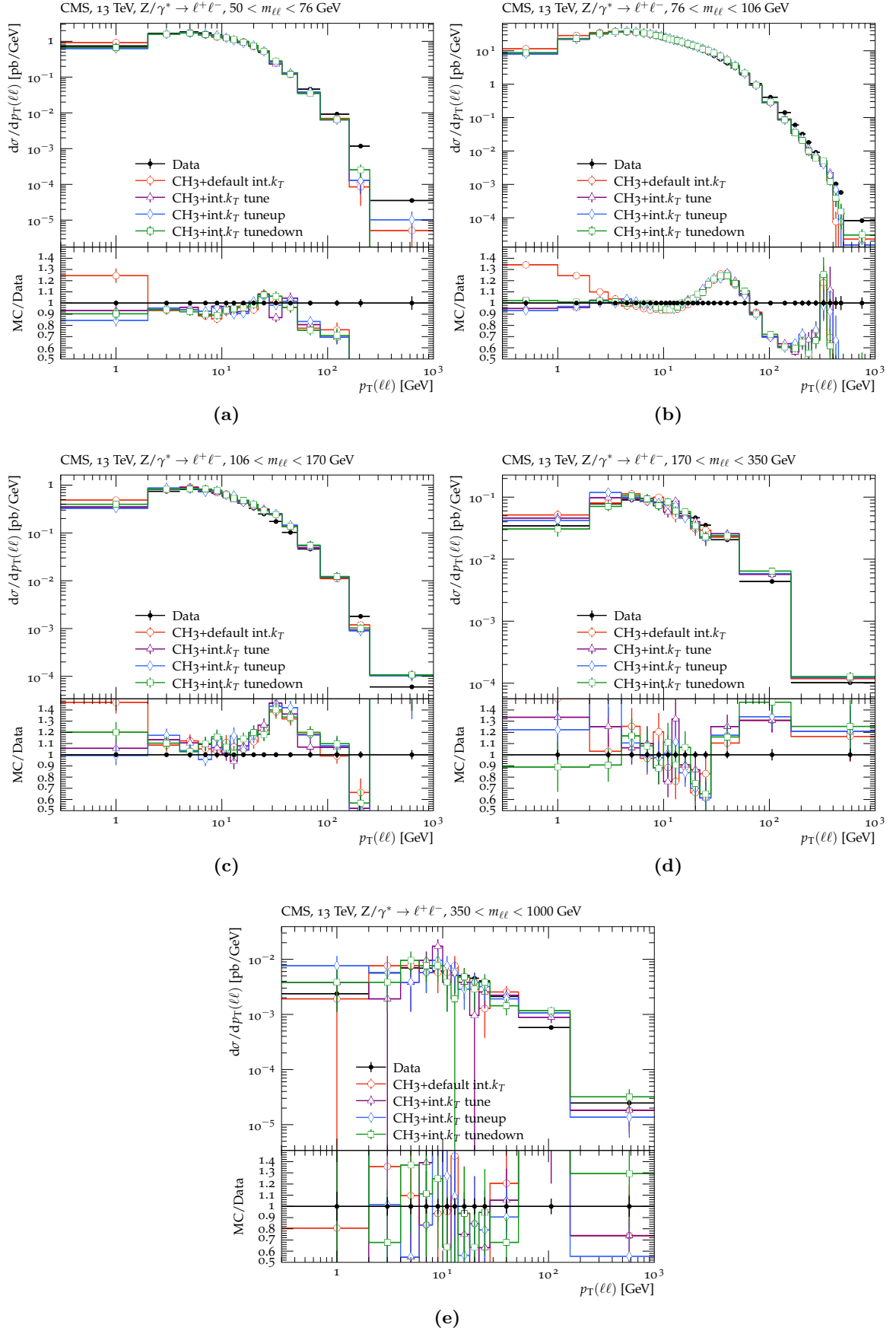


Figure B.34: The predictions of the intrinsic k_T tunes of the Drell-Yan $p_T(\ell^+\ell^-)$ under HERWIG CH3 tune at 13 TeV compared to CMS measurement.

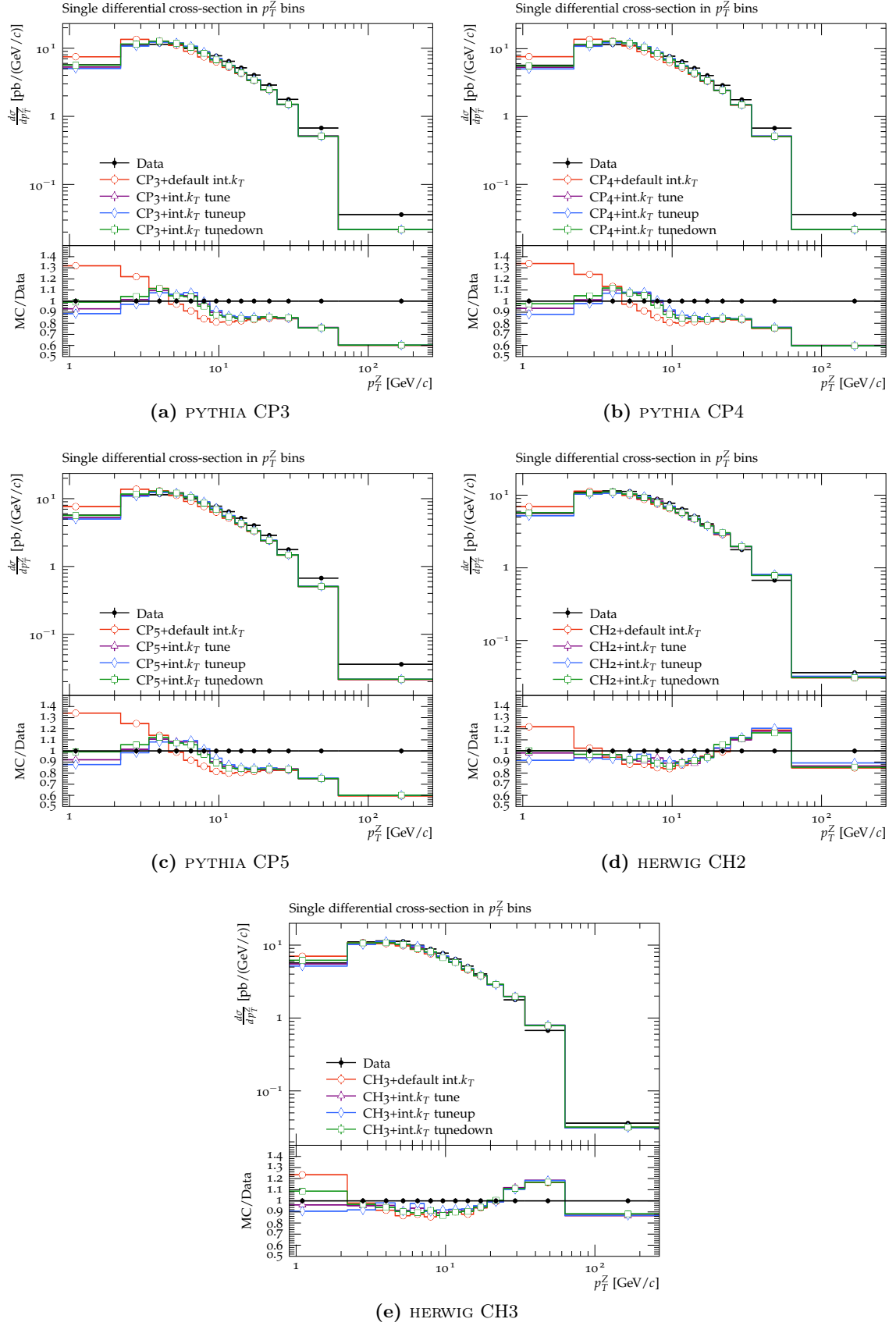


Figure B.35: The predictions of the intrinsic k_T tunes of the Drell-Yan $p_T(\ell^+\ell^-)$ under CP3, CP4 or CP5 tunes in PYTHIA or CH2, CH3 tunes in HERWIG at 13 TeV compared to LHCb data.

C Additional material for the SUEP search

The Monte Carlo simulations of the QCD background and signals in 2017 are tested and validated similarly to those in 2018. Figure C.1 shows the offline-emulated H_T distributions of the 2017 background and signals before and after the trigger selection. Figure C.2 shows the trigger efficiency as a function of H_T , comparing the data in the `ScoutingPFCommissioning` selected by the reference trigger `DST_DoubleMu3_noVtx_CaloScouting_v*`, the QCD background, and the signals. The trigger turn-on curve of the background matches that of the reference data well above the analysis selection threshold $H_T > 560$ GeV. The trigger turn-on curves of signals have similar behaviors as observed in 2018 signals (Figure 6.2).

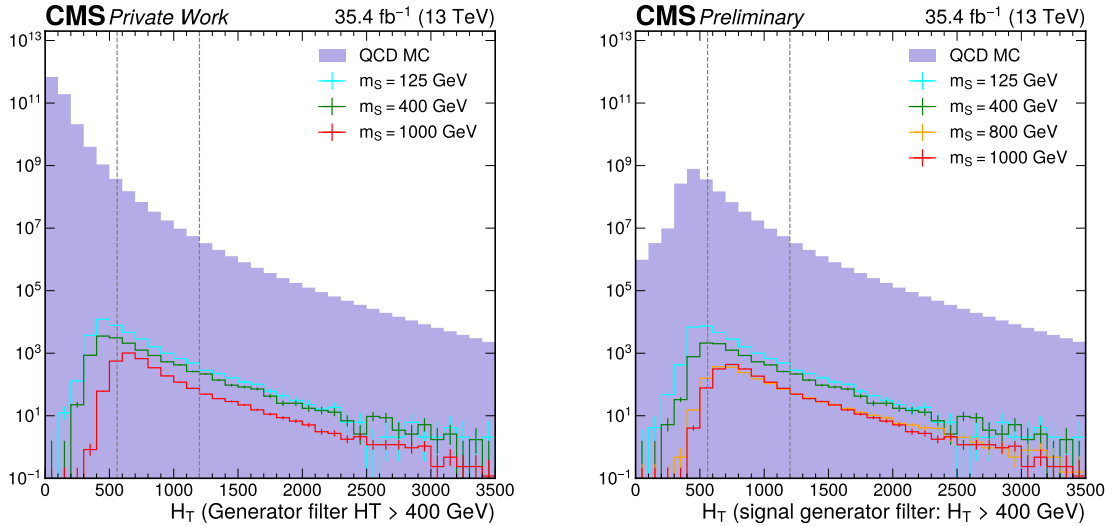


Figure C.1: Left: H_T distributions of signals with various mediator masses passing the generator level selection $H_T > 400$ GeV and the QCD background. No trigger or offline cuts are applied. The requirement of $H_T > 560(1200)$ GeV is shown as a vertical gray line for the offline H_T cut for the scouting (offline) analysis. Right: H_T distributions of the QCD background and signals passing the trigger. The requirement of $H_T > 560(1200)$ GeV is shown as a vertical gray line.

C.0.1 Bias test of the signal extraction

Bias tests are performed for some representative signal models with the expected limits near the theoretical upper bound of the signal cross section. In each test, 1000 toy experiments are performed to fit the signal rates to the toy data of expected background plus injected signals. Before the toy data generation, an initial fit is used to determine the best fit values of the nuisance parameters under the nominal background expectation and signals. Then the toy data is produced with observations sampled from Poisson distributions with expectations equal to the post-fit results, and the auxiliary observables of the systematic uncertainties are

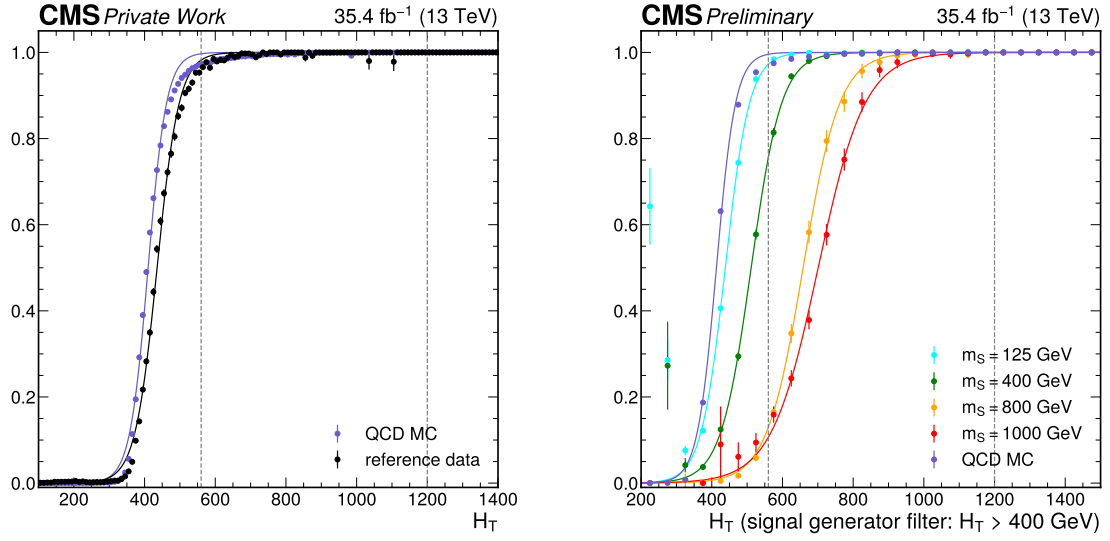


Figure C.2: Left: Trigger efficiency for QCD MC (purple) and reference data (black) in 2017. Right: Trigger efficiency of QCD MC (purple) and signals in 2017. The fluctuations and large uncertainties at low H_T for signal samples are due to the inefficiency from the generator level filter $H_T > 400$ GeV.

sampled from their probability density distributions with expectations equal to the nuisance parameters given by the initial fit. The toy experiments test the distributions of the fit results under the fluctuations according to the background estimation uncertainty and signal systematic uncertainty, as shown in Figure C.3. The fits to toy data approximately recover the values of injected signals as expected.

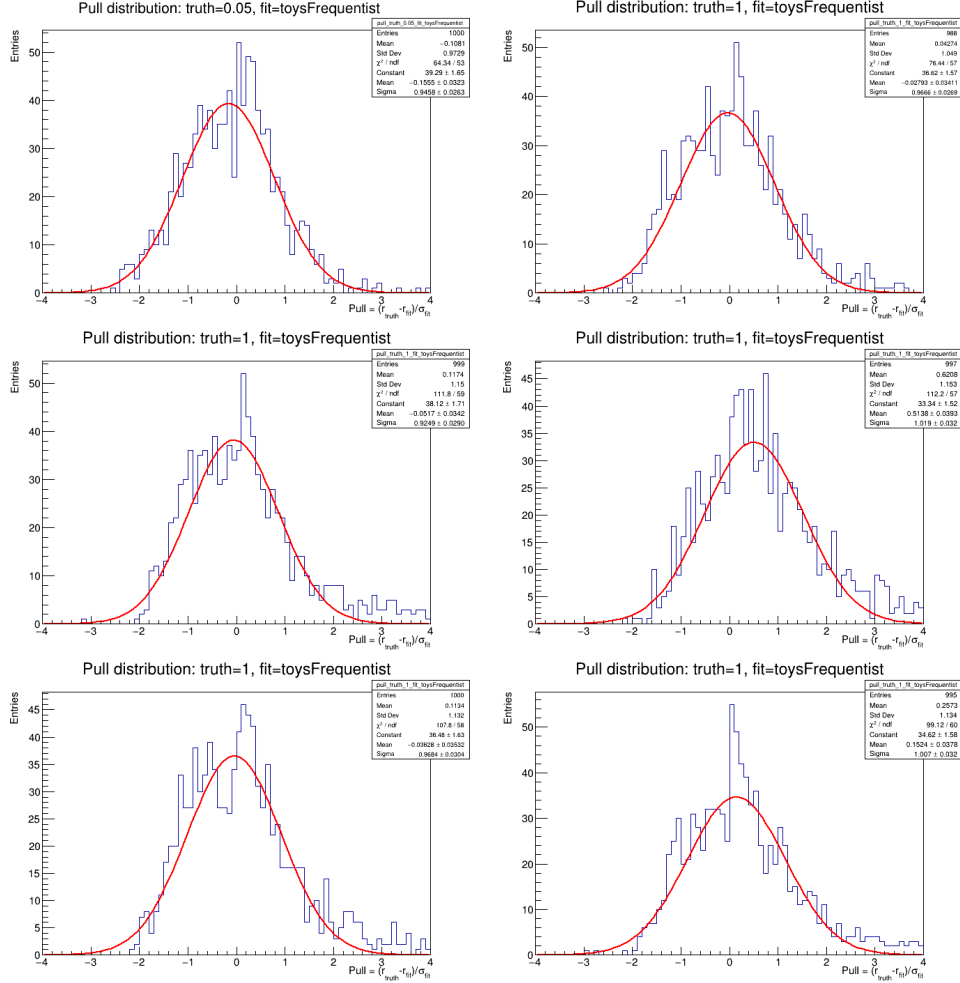


Figure C.3: Distributions of the difference between the fitted signal rates and the truth, normalized by the uncertainty of the fits. The bias test is performed for a few signal models with $A' \rightarrow \pi^+ \pi^-$ BR = 100 %: upper left: $m_S = 125$ GeV, $T = 0.75$ GeV, $m_\Phi = 3$ GeV; upper right: $m_S = 400$ GeV, $T = 4$ GeV, $m_\Phi = 8$ GeV; middle left: $m_S = 700$ GeV, $T = 8$ GeV, $m_\Phi = 4$ GeV; middle right: $m_S = 1000$ GeV, $T = 8$ GeV, $m_\Phi = 8$ GeV; lower left: $m_S = 1200$ GeV, $T = 12$ GeV, $m_\Phi = 3$ GeV; lower right: $m_S = 2000$ GeV, $T = 16$ GeV, $m_\Phi = 4$ GeV.